From High-throughput Systems to Serum Vials : Mathematical Modelling to Accelerate the Development of Freeze-Dried Vaccines

Juan Buceta Correa de Borba

université PARIS-SACLAY

From High-throughput Systems to Serum Vials: Mathematical Modelling to Accelerate the Development of Freeze-Dried Vaccines

Des systèmes à haut débit aux flacons à sérum : modélisation mathématique pour accélérer le développement des vaccins lyophilisés

Thèse de doctorat de l'université Paris-Saclay

École doctorale n° 581 : Agriculture, Alimentation, Biologie, Environnement et Santé (ABIES)
Spécialité de doctorat : Génie des procédés
Graduate School : Biosphera. Référent : AgroParisTech

Thèse préparée dans l'UMR SayFood
(Université Paris-Saclay, INRAE, AgroParisTech),
sous la direction de **Cristian TRELEA**, Professeur (AgroParisTech),
la co-direction de **Fernanda FONSECA**, Directrice de recherche (INRAE),
le co-encadrement de **Stéphanie PASSOT**, Professeure (AgroParisTech),
la co-supervision de **Erwan BOURLES**, Senior manager (GSK)
et de **Bernadette SCUTELLA**, Expert scientist (GSK)

Thèse soutenue à Paris-Saclay, le 19 mai 2022, par

Juan Patricio BUCETA CORREA DE BORBA

Composition du Jury

Guillaume DELAPLACE Directeur de recherche, INRAE (Centre Hauts de France)	Président & Rapporteur
Maria Elena GALVEZ Maîtresse de conférences (HDR), Sorbonne Université	Rapporteur & Examinatrice
Gilles TRYSTRAM Professeur, AgroParisTech (Université Paris-Saclay)	Examinateur
Carlos VILAS FERNANDEZ Chercheur, Spanish National Research Council (CSIC) (Espagne)	Examinateur
Cristian TRELEA Professeur, AgroParisTech (Université Paris-Saclay)	Directeur de thèse
Erwan BOURLES Chercheur, GlaxoSmithKline Vaccines	Invité
Bernadette SCUTELLA Chercheure, GlaxoSmithKline Vaccines	Invitée

THÈSE DE DOCTORAT

NNT: 2022UPASB018

université PARIS-SACLAY

ÉCOLE DOCTORALE
Agriculture, alimentation, biologie, environnement, santé (ABIES)

Titre : Des systèmes à haut débit aux flacons à sérum : modélisation mathématique pour accélérer le développement des vaccins lyophilisés

Mots clés : Lyophilisation ; Vaccins ; Modélisation mathématique ; Transfert de chaleur ; Transfert de matière

Résumé : Le processus de lyophilisation est largement utilisé pour stabiliser les produits pharmaceutiques sensibles à la chaleur (par exemple, les vaccins). L'apparence du produit séché est l'un des critères de qualité les plus importants et dépend de la température du produit pendant l'étape de sublimation. Des petits flacons "à haut débit" (< 1 mL) à l'intérieur de plaques à 96 puits pourraient accélérer le développement de vaccins en testant plus de formulations par cycle de lyophilisation par rapport aux grands flacons "à sérum" (> 3 mL) - qui sont utilisés pour la production. Cette thèse a étudié l'utilisation des flacons à haut débit en se concentrant sur : (*Q1*) comment identifier les conditions opératoires dans les flacons à sérum qui entraînent la même température de produit que dans les flacons à haut débit ?, et (*Q2*) comment les variations entre les flacons à haut débit pourraient affecter la température du produit ?
En ce qui concerne *Q1*, un outil graphique a été proposé pour "traduire" les conditions opératoires entre les flacons à haut débit et les flacons à sérum, en se basant sur un modèle de transfert de chaleur et de matière (à paramètres concentrés, en régime permanent) pour une solution de saccharose à 5%. Le transfert de chaleur vers les flacons à haut débit était plus efficace que vers les flacons à sérum grâce à la plaque à puits en aluminium, et le transfert de matière du front de sublimation vers la chambre de séchage tend à être plus efficace avec les flacons à haut débit en raison de la forme du front de sublimation.
Concernant *Q2*, le fond du flacon à haut débit, le fond de la plaque à puits et les surfaces des puits, ainsi que la position de la plaque à puits sur l'étagère ont entraîné des variations significatives de la température du produit (jusqu'à 2 °C). La position du flacon à haut débit dans la plaque à puits et la température de nucléation n'ont pas affecté de manière significative la température du produit en cours de lyophilisation.

Title: From High-throughput Systems to Serum Vials: Mathematical Modelling to Accelerate the Development of Freeze-Dried Vaccines

Keywords: Freeze-drying; Vaccines; Mathematical modelling; Heat transfer; Mass transfer

Abstract: The freeze-drying process is widely used to stabilize heat-sensitive pharmaceutical products (e.g. vaccines). The dried product appearance is one of the most relevant quality criteria and depends on the product temperature during the sublimation step. Small "high-throughput" vials (< 1 mL) inside 96-well plates could accelerate the development of vaccines by testing more formulations per freeze-drying cycle than larger "serum" vials (> 3 mL) – which are used for production. This PhD project studied the use of high-throughput vials focusing on: (*Q1*) how to identify the operating conditions in serum vials that entail the same product temperature obtained in high-throughput vials?; and (*Q2*) how variations between high-throughput vials could affect the product temperature?
Regarding *Q1*, a graphic tool was proposed to "translate" the operating conditions between high-throughput and serum vials, based on a heat and mass transfer model (lumped-parameter, steady-state) for a 5% sucrose solution. The heat transfer to high-throughput vials was more efficient than to the serum vials thanks to the aluminum well plate, and the mass transfer from the sublimation front to the drying chamber tended to be more efficient in high-throughput vials due to the shape of the sublimation front.
Concerning *Q2*, the high-throughput vial bottom, the well plate bottom and well surfaces, and the position of the well plate on the shelf entailed significant variations in the product temperature (up to 2 °C). The position of the high-throughput vial in the well plate (studied by 3D modelling) and the nucleation temperature did not significantly affect the product temperature in primary drying.

DISCLOSURE STATEMENT

Juan Patricio Buceta participated in a postgraduate Ph.D. program at GSK Vaccines. This work was funded by GlaxoSmithKline Biologicals S.A., under a Cooperative Research and Development Agreement with the Institut National de la Recherche pour l'Agriculture, l'Alimentation et l'Environnement (INRAE) via the intermediary of the Unité Mixte de Recherche (UMR), Paris Saclay Food and Bioproducts Engineering (SayFood) at the INRAE, Versailles-Grignon Research Centre.

PARTS OF THIS THESIS THAT HAVE BEEN PRESENTED OR PUBLISHED:

Publications in peer-reviewed journals:

- **Buceta, J.P.**, Trelea I.C., Scutellà B., Fonseca F., Bourles E., Passot, P. (2021). "Heat transfer during freeze-drying using a high-throughput vial system in view of process scale-up to serum vials". *Journal of Pharmaceutical Sciences, 110 (3), pp. 1323-1336, (https://doi.org/10.1016/j.xphs.2020.11.029).*

- **Buceta, J.P.**, Passot, P., Scutellà B., Fonseca F., Bourles E., Trelea I.C. (2022). "Use of 3D mathematical modelling to understand the heat transfer mechanisms during freeze-drying using high-throughput vials". *Applied Thermal Engineering, 207, 118099. (https://doi.org/10.1016/j.applthermaleng.2022.118099).*

Posters and oral communications in international conferences:

- **Buceta, J.P.**, Passot, P., Scutellà B., Fonseca F., Bourles E., Trelea I.C. (2021). "Mathematical modelling of heat and mass transfer during freeze-drying using high-throughput vial systems to accelerate the development of new vaccines". *Oral presentation at the 2nd European Federation of Chemical Engineering Spotlight Talks, May 2021, online.*

- **Buceta, J.P.**, Passot, P., Scutellà B., Fonseca F., Bourles E., Trelea I.C. (2019). "Freeze-drying in atypical vials: how to model heat transfer during sublimation by using 3D mathematical modelling". *Poster presented at the 9th International Symposium on Lyophilization and Pharmaceutics ISLFD, September 2019, Ghent, Belgium.*

Other communications:

- 1st prize as best presenter at "Ph.D. days" organized by the ABIES Doctoral School (2021).

- Finialist of the Université Paris Saclay at the contest "Ma these en 180 secondes" (2021).

Contents

Abbreviations

Latin alphabet

A	Transfer area	m^2
A_{in}	Inner cross-sectional area of the vial	m^2
A_V	Outer cross-sectional area of the vial	m^2
A^{cc}	Vial bottom contact area	m^2
C_1	Coefficient describing pressure-independent apparent heat transfer between the shelves and the vial, K_V	$W.m^{-2}.K^{-1}$
C_2	Coefficient describing pressure-dependent apparent heat transfer between the shelves and the vial, K_V	$W.m^{-2}.K^{-1}.Pa^{-1}$
C_3	Coefficient describing pressure-dependent apparent heat transfer between the shelves and the vial, K_V	Pa^{-1}
d_C	Distance between the shelves and the chamber surface	m
d_E	Distance between the edge of the bottom shelf and the well plate	m
d_{gas}	Molecular diameter of the trapped gas	m
$\overline{D}_{H20}^{Kn}$	Knudsen diffusivity for the vapour	$m^2.s^{-1}$
d_S	Separation between shelves	m
d_{VE}	Outer bottom diameter of the vial	m
d_{VI}	Inner bottom diameter of the vial	m
DGM	Dusty-gas model	
F	Visualisation factor	Dimensionless
F_b	Visualisation factor from the vial bottom to the bottom shelf	Dimensionless
F_t	Visualisation factor from the vial to the top shelf	Dimensionless
G	Irradiation	$W.m^{-2}$
h_{HV}	Vial height	m
h_{well}	Depth of the wells	m
J	Radiosity	$W.m^{-2}$
K	Heat transfer coefficient	$W.m^{-2}.K^{-1}$
K_V	Apparent heat transfer coefficient between the shelf and the vial	$W.m^{-2}.K^{-1}$
k	Empirical constant of proportionality	$W.m^{-4}.K^{-1}$
$K_{shelf-tray}$	Apparent heat transfer coefficient between the shelf and the tray	$W.m^{-2}.K^{-1}$
$K_{tray-vial}$	Apparent heat transfer coefficient between the tray and the vial	$W.m^{-2}.K^{-1}$

Kn	Knudsen number	Dimensionless
l	Gas layer thickness	m
l_d	Dried product layer thickness	m
l_f	Frozen product layer thickness	m
l_{fp}	Mean free path	m
$\dot{m}$	Sublimation mass flow leaving the container	$kg.s^{-1}$
m_{final}	Mass of the vial after ice sublimation experiments	kg
$m_{initial}$	Mass of the vial before ice sublimation experiments	kg
M_L	Mass loss factor for mass flows estimated using the pressure rise tests	Dimensionless
$\dot{m}_{PRT}$	Vial-averaged sublimation mass flow rate determined by a pressure rise test method	$kg.s^{-1}$
$\dot{M}_{H2O}$	Mass flux rate of the vapour through the dried product	$kg.s^{-1}.m^{-2}$
$\dot{M}_I$	Mass flux rate of the inert gas through the dried product	$kg.s^{-1}.m^{-2}$
$\dot{m}_{total}$	Total mass flow from the chamber to the condenser	$kg.s^{-1}$
n_V	Number of vials in the drying chamber	vials
P	Pressure	Pa
$\dot{P}_0$	Initial derivate of the pressure during the pressure rise tests	$Pa.s^{-1}$
P_C	Pressure inside the drying chamber	Pa
P_{CD}	Pressure inside the condenser	Pa
P_{H2O}	Partial pressure of the water vapour	Pa
P_I	Partial pressure of the inert gas	Pa
P_{sat}	Ice-vapour equilibrium pressure, pressure at the sublimation front	Pa
P_{triple}	Triple point pressure	Pa
P_V	Pressure in the main gas volume inside the vials	Pa
$\dot{q}$	Heat flux	$W.m^{-2}$
$\dot{Q}$	Heat flow	W
$\dot{Q}_b$	Heat flow from the bottom shelf to the container	W
$\dot{Q}_{exp}$	Experimental heat flow rate	W
$\dot{Q}_t$	Heat flow from the top shelf to the container	W
R	Ideal gas constant	$J.K^{-1}.mol^{-1}$
R_{CD}	Mass transfer resistance due to the duct between the drying chamber and the condenser	$Pa.s.kg^{-1}$
R_P	Area-normalised dried product resistance to the mass transfer	$Pa.s.m^2.kg^{-1}$

$R_{P,0}$	Coefficient of the area-normalised dried product resistance to the mass transfer, R_P	$Pa.s.m^2.kg^{-1}$
$R_{P,1}$	Coefficient of the area-normalised dried product resistance to the mass transfer, R_P	$Pa.s.m.kg^{-1}$
$R_{P,2}$	Coefficient of the area-normalised dried product resistance to the mass transfer, R_P	m^{-1}
r_{pore}	Average pore radius	m
R_S	Mass transfer resistance between the main gas volume inside the vial and the drying chamber	$Pa.s.kg^{-1}$
t	Time	s
t_{final}	Time when sublimation is finished	s
$t_{initial}$	Time when sublimation begins	s
T	Temperature	K
T_b	Temperature at the bottom of the container	K
T_c	Collapse temperature	K
T_{door}	Surface temperature of the chamber door	K
T_e	Eutectic temperature	K
T_g	Glass transition temperature	K
T_j	Freezing-point depression temperature	K
T_n	Nucleation temperature	K
T_p	Product temperature	K
T_{shelf}	Shelf temperature	K
T_t	Temperature at the top of the container	K
T_{triple}	Triple point temperature	K
T_{wall}	Surface temperature of the chamber wall	K
V_C	Volume of the drying chamber	m^3
V_{fill}	Filling volume	m^3
V_i	Ice volume	m^3
V_p	Product volume (sum of dried and frozen product volumes)	m^3
W_{gas}	Molar mass of a gas	$kg.mol^{-1}$
W_{H2O}	Molar mass of water	$kg.mol^{-1}$
W_I	Molar mass of inert gas	$kg.mol^{-1}$

Greek alphabet

α	Thermal accommodation coefficient for gas conduction	Dimensionless
α_V	Thermal accommodation coefficient for gas conduction between the bottom shelf and the vial	Dimensionless
Δm_{total}	Total water mass removed during a freeze-drying cycle	kg
ΔH_{sub}	Mass latent heat of sublimation	$J.kg^{-1}$
$\widetilde{\Delta H_{sub}}$	Molar latent heat of sublimation	$J.mol^{-1}$
ε	Emissivity	Dimensionless
ε_{ice}	Emissivity of the ice	Dimensionless
ε_{shelf}	Emissivity of the shelf	Dimensionless
ε_{vial}	Emissivity of the vial	Dimensionless
ε_{wall}	Emissivity of the chamber wall	Dimensionless
ε_{wp}	Emissivity of the well plate	Dimensionless
Θ_{gas}	Number of gas molecules per volume	n° $molecules.m^{-3}$
κ	Boltzmann constant	$J.K^{-1}$
λ	Thermal conductivity	$W.m^{-1}.K^{-1}$
λ_{gas}^{fm}	Gas thermal conductivity in a free molecular regime	$W.m^{-1}.K^{-1}$
λ_{gas}^{cont}	Gas thermal conductivity in a continuous regime	$W.m^{-1}.K^{-1}$
ρ	Density	$kg.m^{-3}$
Λ_0	Free molecular heat conductivity of the gas at 0 °C	$W.m^{-1}.K^{-1}.Pa^{-1}$
σ	Stephan-Boltzmann constant	$W.m^{-2}.K^{-4}$
τ	Tortuosity	Dimensionless
ϕ	Porosity	Dimensionless
ψ_B	Self-diffusivity for two gases	$m^4.N^{-1}.s^{-1}$
ψ_{H20}	Bulk diffusivity for vapour	$m.s^{-1}$
ψ_I	Bulk diffusivity for inert gas	$m.s^{-1}$
ω	Surface reflectivity	Dimensionless

Superscript

B	Referring to the heat transfer between the well and the vial bottom
c	Conduction within a body
cc	Contact conduction contribution
gc	Gas conduction contribution
HT	Refers to high-throughput vials and well plate system
rad	Radiation contribution
ser	Refers to serum vials
V	Refers to the heat transfer between the shelf and the vial bottom
cc	Contact conduction contribution
gc	Gas conduction contribution
HT	Refers to high-throughput vials and well plate system
S	Referring to the heat transfer between the well and the vial lateral side

Subscript

$1,2$	Refers to the heat transfer between surfaces 1 and 2
bb	Refers to a black body
d	Refers to the dried product layer
f	Refers to the frozen product layer
HV	Refers to the heat transfer to high-throughput vials
ser	Refers to serum vials
V	Refers to the heat transfer between the shelves and the vial
V,b	Refers to the heat transfer between the bottom shelf and the vial
V,t	Refers to the heat transfer between the top shelf and the vial
WP	Refers to the heat transfer to well plates

1. Introduction

1.1. Motivation for This Work

1.1.1. Freeze-Drying of Vaccines

Infectious diseases are caused by organisms (e.g. virus, bacteria) known as “pathogens” (Smith et al., 2009). When a pathogen enters a subject’s body, the immune system produces “antibodies” that recognise and neutralise the pathogen. Live-attenuated viral vaccines contain weakened or inactive pathogens capable of triggering the production of antibodies without causing the disease, so a vaccinated subject’s immune system is prepared for future exposures to the pathogen (US Department of Health and Human Services, 2008). The part of the inactivated pathogen that prompts antibodies is known as “antigen” (Siegrist, 2008). For an effective vaccination, the antigen needs to be stabilised to preserve its therapeutic effect during storage and transportation (World Health Organization, 2011). In the case of live-attenuated viral vaccines, most formulations on the market require a drying step at the end of the process to stabilise the antigen, ensuring the vaccine's functionality when rehydrated and administered to a subject (Hansen et al., 2015; Oslan et al., 2017; Patel et al., 2018; Yang et al., 2007).

Freeze-drying or lyophilisation is a drying process that entails particularly low product temperatures (less than 0 °C), which is why it is widely used in the pharmaceutical industry to dry temperature-sensitive products, such as live-attenuated viral vaccines. The freeze-drying process consists of three steps, which are: (i) freezing, (ii) primary drying, and (iii) secondary drying (Adams, 2007). During the freezing step, over 80% of the water becomes ice crystals, and the rest of the water remains chemically bound to the product (Patel et al., 2010b). Ice crystals are removed by sublimation during primary drying, and the bound water is removed by desorption during secondary drying (Franks, 1998). Once the vaccines are dried, they could be stored and transported at temperatures commonly between 2 and 8 °C (World Health Organisation, 2000). After transportation and storage, freeze-dried vaccines are dissolved in a diluent before injection, obtaining the vaccine solution that should be dosed to the subject. This dissolution process is known as “reconstitution” (World Health Organization, 2015).

Due to the freezing and drying steps, the antigen can suffer irreversible damage during freeze-drying. Therefore, other ingredients (e.g. buffers, carbohydrates) are included in the vaccine formulation to protect the antigen and preserve the vaccine’s quality (Hansen et al., 2015). To characterize the quality of a freeze-dried vaccine, the World Health Organization (2011) referred to three attributes: (i) the potency (also denoted as biological activity), (ii) the moisture content, and (iii) the appearance.

The product potency refers to retaining the integrity of the product composition, so the vaccine continues to fulfil its biological purpose after freeze-drying. Different experimental methods (e.g. in vivo methods, Milstien and Gibson, 1990; fluorescent focus formation assay, Naik et al., 2017; ELISA-type

methods, Page et al., 2017; live cell count, Schneid et al., 2011) and reference standards are defined to evaluate the potency, varying among antigens.

The final moisture content of the product must be low enough to stabilise the antigen during storage and transportation. However, the moisture content shall not be extremely low since this can damage the antigen's chemical structure (Passot et al., 2012a). The reference standard for the moisture's range varies among products, yet values are commonly lower than 3% of the total weight of the freeze-dried product (May, 2010).

The appearance of the final dried product refers to its shape upon visual inspection. The following Section 1.1.2 details how the product appearance is more than just a mere "cosmetic" requirement.

1.1.2. The Importance of a Freeze-Dried Vaccine's Appearance

Arguably, the dried product appearance is the quality attribute involving the most subjective standards. The final dried product (commonly known as "dried cake") must present an "elegant" appearance, which refers to a non-collapsed structure (Peiren et al., 2016; Stärtzel et al., 2015). To understand the importance of product collapse and its implications for product quality, we need to understand why collapse occurs. During primary drying, the sublimation front moves through the vial content leaving a dried product layer. In this way, the dried product layer presents a series of interconnected pores that allow the water vapour to escape from the sublimation front and leave the vial. The dried product layer contains bound water during primary drying (Patel et al., 2010b), so the layer is particularly unstable and collapses when heated above a specific critical temperature (Pikal and Shah, 1990a). If a portion of the dried product collapses, the pores in the dried product layer would no longer be connected. Collapse prevents the vapour from escaping through the dried product layer; consequently, a collapsed product shall present humidity pockets that can potentially entail the deterioration of the antigen during storage and transportation. However, a direct correlation between product collapse and the loss of potency has not been proved yet (Patel et al., 2017; Wang et al., 2004).

The dried cake appearance also has practical consequences when dosing freeze-dried vaccines to subjects. During the vaccine reconstitution, the dried product and a diluent are mixed until obtaining a homogeneous solution. Porous and non-collapsed products are easier to dissolve due to their high surface-area-to-volume ratio, simplifying the obtention of a homogenous solution. Therefore, non-collapsed or elegant dried products are required to reduce human error during vaccine reconstitution (Adams and Irons, 1993; World Health Organisation, 2000). Product stability and reconstitution require an elegant non-collapsed dried cake; thus, observing the dried cake appearance is, in practice, a key routine criterion for the quality assessment of freeze-dried vaccines (World Health Organization, 2011).

1.1.3. Developing a Freeze-Dried Vaccine

Various authors frequently mentioned the dried cake appearance as a quality attribute of great importance (e.g. Adams, 2007; Barresi et al., 2009; Christensen et al., 2007; Nail and Searles, 2008; Patel and Pikal, 2013), proving to be more than a "cosmetic" requirement. The temperature at which the dried product collapses (collapse temperature) varies between formulations (e.g. from -50 to -10 °C; Fonseca et al., 2004; MacKenzie, 1975). Therefore, when developing a freeze-dried vaccine, it is important to select a vaccine formulation that is most likely to entail an elegant (non-collapsed) appearance. Selecting such a formulation requires screening several potential vaccine formulations during freeze-drying. The most common containers used for screening are tubular vials, known as "serum vials", with a total volume generally greater than 3 mL (Pisano et al., 2013a; Scutellà et al., 2017a; Sheehan and Liapis, 1998). Serum vials are the same containers used at the production scale to freeze-dry vaccines, being the final container for storage and transportation.

Selecting a vaccine formulation that protects the antigen and does not collapse during primary drying involves trial and error, being a very time-consuming and laborious task. Recently, high-throughput systems consisting of aluminium 96-well plates containing small (less than 1 mL) tubular vials (from now on referred to as "high-throughput vials") have been proposed to screen formulations more efficiently (von Graberg, 2011). To illustrate the difference between high-throughput and serum vials, Figure 1.1-1a presents picture of each vial type and Figure 1.1-1b shows a well plate containing high-throughput vials (of 500 µL). Using (small) high-throughput vials allows fitting more containers inside the equipment used to freeze-dry (freeze dryer) than when using (large) serum vials. Hence, high-throughput vials reduce the number of freeze-drying cycles required to screen candidate formulations. Moreover, the 96-well disposition is compatible with most robots employed to prepare and dose the solutions to be screened (Peterman et al., 2014; Stangegaard et al., 2011; Taylor et al., 2002), simplifying the preparation of the samples and reducing handling errors.

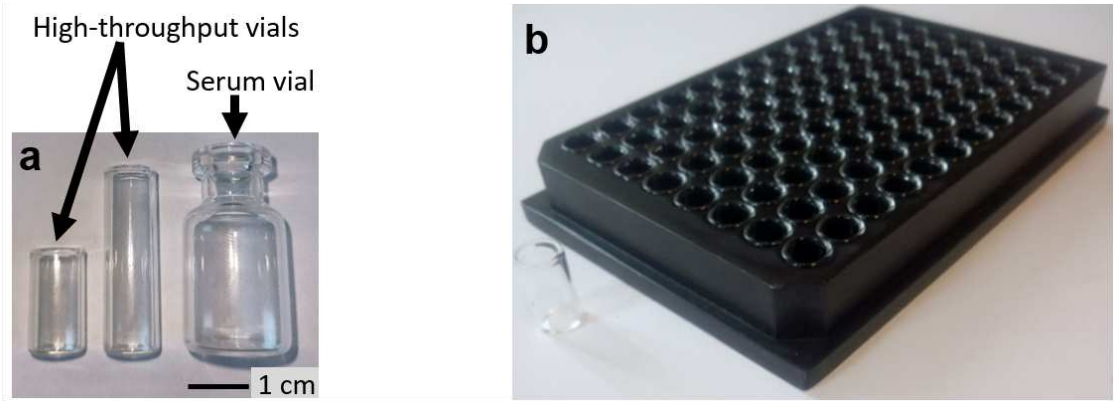

Figure 1.1-1 – (a) High-throughput and serum vials (Buceta et al., 2021). (b) Well plate with high-throughput vials with a maximal volume of 500 µL.

To obtain an elegant dried cake, the product temperature must remain lower than the collapse temperature during primary drying; notwithstanding, a freeze dryer cannot set the product temperature directly. Freeze dryers present a drying chamber with shelves where the containers with the product are placed. Shelves have internal channels where a heat-transfer fluid circulates; the temperature of this heat-transfer fluid is controlled by a cooling/heating system. The drying chamber is connected to a condenser through a duct. Moreover, the condenser is connected to a vacuum pump. A freeze dryer can set two operating conditions:

(i) the temperature of the shelves, by setting the temperature of the heat-transfer fluid, and

(ii) the pressure inside the chamber, by acting on the vacuum pump and the ventilation of the drying chamber.

The product temperature depends on the heat and mass transfer phenomena occurring simultaneously in the drying chamber (Liapis and Litchfield, 1979; Pikal, 2000). Most of the heat flow goes from the shelves to the vials (Pisano et al., 2011), and the most critical mass transfer is the water vapour moving from the sublimation front to the gas inside the drying chamber through the dried product layer (Rambhatla et al., 2004; X. C. Tang et al., 2006). Understanding the heat and mass transfer phenomena is the key to controlling the product temperature through the operating conditions, and thus, obtaining an elegant dried cake.

1.1.4. Scientific Questions

1.1.4.1. From Freeze-Drying in High-Throughput to Serum Vials

Different factors may impact the heat transfer during primary drying of a given formulation. For example, previous work put forward that the heat transfer depends on the container type (Nam and Song, 2005) and the presence of an object (e.g. a tray) between the shelf and the vial (Pisano et al., 2011). High-throughput and serum vials are considerably different in geometry, and the use of high-throughput vials requires placing an object (well plate) between the shelf and the vials. Thus, heat transfer is expected to change from high-throughput to serum vials. As a practical outcome, the product temperature during primary drying is might differ when using high-throughput vials during screening tests or serum vials during research or production. The product temperature impacts the dried cake appearance (Pikal and Shah, 1990a); hence, the product quality obtained using high-throughput vials may not be repeatable in serum vials unless the operating conditions are modified. The selection of the operating conditions for serum vials to recreate the product temperatures obtained with high-throughput vials will be referred to as "translation".

Mathematical modelling of the heat and mass transfer mechanisms (e.g. Liapis and Litchfield, 1979; Pikal, 1985; Velardi and Barresi, 2008) could be potentially used to translate the operating conditions between high-throughput and serum vials. So far, von Graberg (2011) compared the heat transfer to high-throughput and serum vials, but did not address the product temperature or any possible variation on the mass transfer due to the container type. To the best of this author's knowledge, no research on translating the operating conditions between different container types has been published. Therefore, the first scientific question of this PhD project was:

> *How could we identify the operating conditions that entail the same product temperature during primary drying in high-throughput systems and serum vials?*

1.1.4.2. Factors Affecting Freeze-Drying in High-Throughput

When considering the same vial type, inter-vial variations in the heat transfer depend on small differences in the geometry of the vial bottom (e.g., curvature and contact area; Brülls and Rasmuson, 2002; Scutellà et al., 2017a) and the vial position on the shelf with respect to the drying chamber wall or door (Rambhatla and Pikal, 2003; Sheehan and Liapis, 1998). Moreover, inter-vial variations in the mass transfer are entailed by differences during the freezing step (Oddone et al., 2016; Scutellà et al., 2018a; Searles et al., 2001a). Such inter-vial variations in the heat and mass transfer must be considered for a correct interpretation of formulation screening results and an accurate translation of the operating conditions during primary drying. Indeed, inter-vial variations may bias screening results since all the samples do not undergo the same conditions, possibly leading researchers to erroneously accept or reject a candidate formulation. In this vein, the second scientific question of this PhD project was:

> *What are the main factors responsible for product quality variations during primary drying in high-throughput systems?*

1.2. Outline of This Thesis Manuscript

Hereinafter, this thesis manuscript is divided into four main parts presenting the work carried out during this PhD project.

The first part (Chapter 2) consists of a literature review on the freeze-drying process. This literature review begins by describing how to perform the freeze-drying process (Section 2.1), underlining the importance of the critical quality parameter considered in this work: the product temperature during primary drying. Heat and mass transfer equations are the base of the mathematical models used to relate the product temperature with the operating conditions. The equations that describe the heat transfer (Section 2.2) and the mass transfer (Section 2.3) are detailed, as well as the relevant factors that affect these transfers. The literature review finishes with an overview of the modelling hypothesis used to solve the heat and mass transfer equations (Section 2.4), emphasizing the hypothesis that may be most valuable according to the scientific question to be answered.

The second part of this manuscript (Chapter 3) briefly connects the scientific questions of this thesis with the mathematical models reviewed from the literature and the laboratory work performed.

The third part of this manuscript (Chapter 4) is divided into four scientific papers that report the results obtained. The first article (Section 4.1) focuses on how the container type (i.e. high-throughput or serum vial) impacts the heat transfer during primary drying, presenting a graphic tool to identify the operating conditions that entail the same product temperature when using high-throughput and serum vials. This graphic tool is a visual representation of the solution of the heat and mass transfer equations for high-throughput and serum vials in 0D and steady-state. Moreover, the first article considers how the product temperature could be impacted by the container's design and manufacture (i.e. the height of the vial, the high-throughput vial bottom geometry, the well plate bottom geometry, and the surface finish of the well plate).

The second article (Section 4.2) investigates how the vial position in the well plate could impact the heat and mass transfer. 3D mathematical modelling for the heat and mass transfer during sublimation in high-throughput vials is used to study different vial positions (i.e. in the centre of the well plate surrounded by other vials, or at the edge of the well plate). Two 3D steady-state models are presented:

(i) one representing the beginning of primary drying when there is no dried product layer inside the vials, and

(ii) another one representing intermediate points of primary drying when a dried layer was formed inside the vials.

The notion of time passing is introduced into the results by comparing these two 3D steady-state models. In this way, the second article considers the evolution of the heat transfer variations between vial positions in the well plate during primary drying.

Similarly, the third article (Section 4.3) explores how placing a well plate near a chamber wall or door impacts the heat and mass transfer during primary drying. 3D mathematical models for the heat and mass transfer during sublimation are employed to address different well plate positions (i.e. in the centre of the shelf, near a chamber wall, or near the chamber door). Much like in Section 4.2, the concept of time passing during primary drying was introduced by comparing two 3D steady-state models representing the process's beginning and an intermediate point.

The fourth article (Section 4.4) studies how the container type impacts the mass transfer during primary drying. In this vein, the mass transfer resistance imposed by a “model” product (5% w/w sucrose aqueous solution) was determined in high-throughput and serum vials during primary drying. The effect of the nucleation temperature was evaluated by determining the mass transfer resistance using a variation of the model product that contained 0.1% (w/w) of a nucleating agent (which increased the nucleation temperature). The mass transfer resistance values were interpreted considering the pore size of the dried product (measured by X-ray micro-computed tomography) and the shape of the sublimation front.

The fourth part of this manuscript (Chapter 5) presents the general conclusions on the scientific questions addressed during this PhD project, detailing the perspectives for future research.

Finally, the fifth part of this manuscript (Chapter 6) is an excecutive summary of this PhD project in French.

2. Literature Review

2.1. Pharmaceutical Freeze-Drying

2.1.1. A Historical Perspective on Epidemics, Vaccination, and Freeze-Drying

Pustules in mummies dating from Ancient Egypt (1ST century B.C.E.) are probably the first historical evidence of the disease we know today as "smallpox" (Hopkins, 2002). Smallpox symptoms start with high fever, followed by a rash that turns into eruptions filled with pus, sometimes causing disfiguration, blindness, and death. The smallpox virus is transmitted from person to person, and several smallpox epidemics occurred worldwide throughout history (Geddes, 2006; Hays, 2005). Due to global vaccination campaigns, smallpox was declared eradicated in 1980 by the World Health Assembly (33 World Health Assembly, 1980).

The first preventive technique against smallpox was the "variolation" method, which consisted of introducing material from smallpox pustules into a healthy individual's skin (Dinc and Ulman, 2007). Variolation (usually) caused a less harmful infection than when the smallpox virus spread directly from human to human; however, the individual still obtained immunity against the disease. There are records of Emperor K'ang Hsi (China) having his children variolated in the 17th century; nevertheless, some historians assure variolation had begun before, in 200 B.C.E (The College of Physicians of Philadelphia, 2020). As promising as variolation was in Asia, Europe, and North America during the 17th and 18th centuries, many people were suspicious about the risks this procedure may involve for the subjects (Glynn and Glynn, 2004; Lombard et al., 2007).

By the 1770s, there was probably an informal public understanding that milkmen who had "cowpox" – a disease that had symptoms similar to smallpox but less severe – were immune to smallpox (Boylston, 2013; Plett and Schmidt, 2006). Between the 1770s and the 1790s, several scientists started using cowpox biologic material to immunise subjects against smallpox. This procedure was safer than variolation and was called "vaccination". As decades passed, vaccination replaced variolation, becoming a general western world procedure during the 19th century.

The spread of vaccination to tropical countries presented a challenge for scientists, since the higher temperatures damaged the vaccines throughout transportation and storage. During the first decades of the 20th century, researchers at the Vaccine Institute in Paris (France) have tried to dry smallpox vaccines to be sent to French tropical colonies. Initially, vaccines were "air-dried" by removing the moisture in an evacuated chamber (Schneider, 2009); but this method was hard to perform at industrial scales. In 1918 the Vaccine Institute produced a freeze-dried smallpox vaccine, being the first documented use of freeze-drying to preserve a vaccine formulation (The College of Physicians of Philadelphia, 2020). Freeze-drying

consisted in freezing the vaccines and removing the moisture (primarily) by sublimation in vacuum conditions, meaning that the ice crystals were taken from the solid state to the gas state (vapour) without going through a liquid state. This drying process has widely spread in the pharmaceutical industry, becoming a crucial step in the production chain for several products. The low product temperatures reached during freeze-drying make the process suitable for several thermolabile biological products such as cells, hormones, proteins, and vaccines for numerous diseases (Adams, 2007; Passot et al., 2009). Nevertheless, freeze-drying could damage the product's chemical structure if it is not performed correctly, hence the importance of selecting the vaccine formulations that are most stable during the process and the optimal operating conditions to assure the final product quality.

2.1.2. Performing Pharmaceutical Freeze-Drying

Freeze-drying consists of three successive steps: (i) freezing the product (e.g. vaccines), (ii) sublimation of the ice crystals (primary drying), and (iii) desorption of the water bound to the product (secondary drying).

To understand the pressures and temperatures required for freezing and primary drying, Figure 2.1-1 presents a state diagram of water. Throughout freezing, the product temperature is reduced (lower than 0 °C) so that water in the product solution could turn into ice crystals (from point 1 to 2 in Figure 2.1-1). During primary drying, the pressure has to be lower than the triple point pressure (600 Pa) (from point 2 to 3 in Figure 2.1-1), so that the ice crystals can be heated without melting (from point 3 to 4 in Figure 2.1-1) and removed by sublimation (point 4 in Figure 2.1-1). Desorption during secondary drying is expected to occur until the moisture content and the relative humidity of the gas phase reach an equilibrium state given by the sorption isotherm (Pikal et al., 1990).

Overall, freeze-drying involves low temperatures and pressures. The following Section 2.1.2.1 present the equipment required to reach such temperatures and pressures, and Sections 2.1.2.2 to 2.1.2.4 explain how the temperature and pressure vary throughout the process.

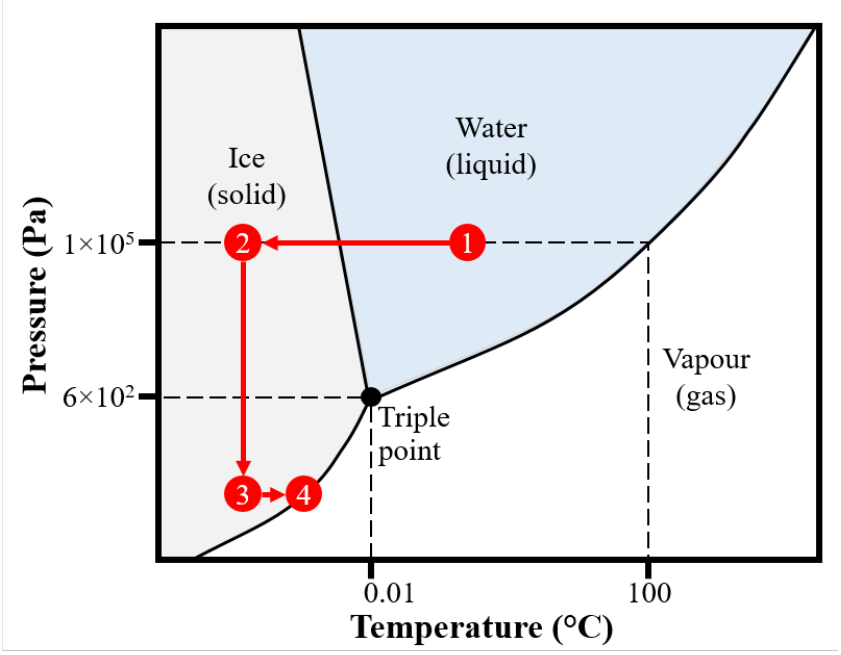

Figure 2.1-1 – Schematic of the phase diagram of water. Not in scale. Point 1 represents the initial state of the water in the product to be dried. Point 2 represents the ice crystals after freezing. Point 3 represents the ice crystals before primary drying. Point 4 represents the ice crystals during sublimation in primary drying (adapted from Ponsá et al., 2017).

2.1.2.1. Freeze-Drying Apparatus

Freeze-drying is performed in an apparatus known as a "freeze dryer" (or "lyophiliser"). A scheme of a modern freeze dryer used in the pharmaceutical industry is presented in Figure 2.1-2, consisting of a drying chamber, a condenser, a compressor, a vacuum pump, a cooling/heating system, and control systems.

Inside the drying chamber there are shelves that serve to place the product, except for the uppermost shelf, whose function is to ensure that all products have a shelf above and are thus processed in the same conditions as the other shelves. The shelves have internal channels filled with a heat-transfer fluid circulating in a closed circuit with the cooling/heating system. In this way, the temperature of the shelves is controlled by cooling or heating the heat-transfer fluid.

The drying chamber is connected to the condenser through a duct presenting a valve. A vacuum pump is connected to the condenser and creates a pressure loss from the drying chamber (through the duct) to the condenser. This pressure loss "guides" the drying mass flow from the drying chamber to the condenser. Moreover, the pressure inside the drying chamber is measured using a manometer or a Pirani gauge (Patel et al., 2010b), and is regulated through a control system acting on the vacuum pump or through the injection of inert gas into the drying chamber.

Two main operating conditions can be set in a freeze dryer: (i) the temperature of the heat-transfer fluid, commonly known as "shelf temperature", and (ii) the pressure in the drying chamber. Another condition would be the temperature at the condenser, which is considered less important as long as it is low enough to ensure vapour condensation (typically lower than -60 °C).

Before starting pharmaceutical freeze-drying, liquid formulations are filled into the selected containers (e.g. vials, syringes, microplates), which are then placed on the shelves of the freeze dryer. Glass serum vials are the most usual containers used to freeze-dry vaccines (Pikal, 1985; Pisano et al., 2011; Rambhatla et al., 2004). Once the containers are loaded in the freeze dryer, the freeze-drying protocol or cycle is started through the freeze dryer software interface. Figure 2.1-3 presents an example of a shelf temperature history (in green) during freeze-drying, a chamber pressure history (in violet/purple), and a product temperature history (in red). The following Sections 2.1.2.2 to 2.1.2.4 delve into each step, detailing the operating conditions set.

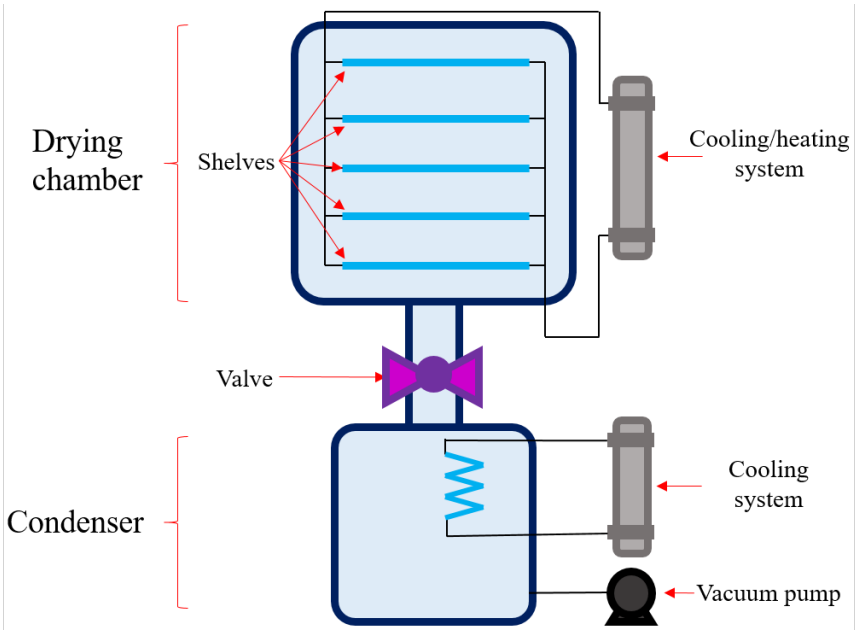

Figure 2.1-2 – Main parts of a batch freeze dryer (adapted from Millrock Technology Inc.).

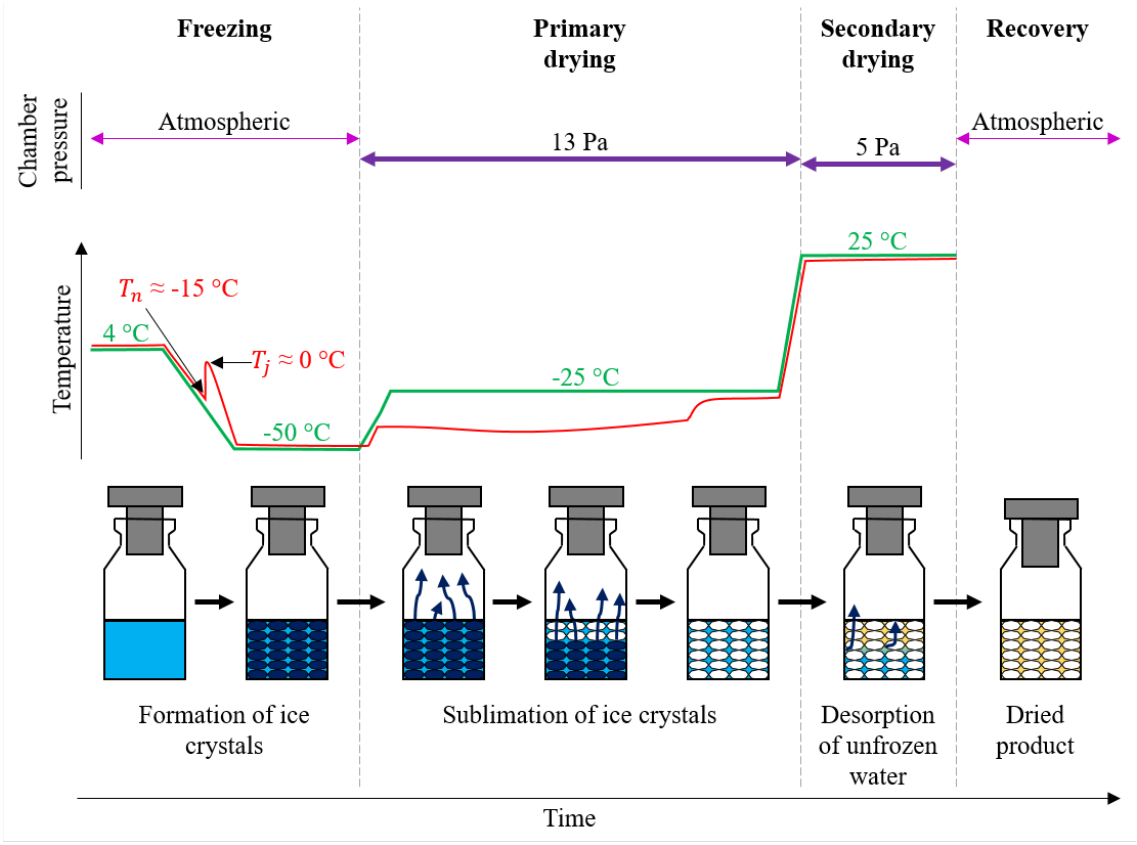

Figure 2.1-3 – Schematic illustration of the freeze-drying process. Green and red curves represent the shelf temperature and product temperature, respectively. T_n is the nucleation temperature, and T_j is the freezing-point depression temperature. Numeric values are examples of typical values. Not in scale (adapted from Kawasaki et al., 2019).

2.1.2.2. Freezing

The freezing step consists in decreasing the temperature of the product solution until the solvent (commonly water) crystallises. The shelf temperature decreases during freezing (Figure 2.1-3), and so does the product temperature until it registers a quick rise (within less than a couple of minutes) up to nearly 0 °C. This quick rise is due to the energy released when the nuclei are formed (nucleation), and ice crystals grow. The temperature when the first nuclei appear is known as "nucleation temperature" (T_n, Figure 2.1-3) (Searles et al., 2001b). Nucleation is a stochastic process, hence T_n varies between containers in the same batch and between batches (Searles et al., 2001a). Common T_n values in the pharmaceutical industry range between -20 and -1 °C (Harrison et al., 2018; Konstantinidis et al., 2011; Searles et al., 2001a). After nucleation, the product temperature rises until the freezing-point depression temperature (T_j, Figure 2.1-3), which is close to 0 °C for diluted solutions (Kiyosawa, 1988) such as vaccines. The difference between T_n and T_j is known as "supercooling" or "undercooling" (Rambhatla et al., 2004).

Water molecules in the initial product solution are commonly differentiated between (Feng et al., 2020; Moy et al., 1971; Trelea et al., 2016): (i) water molecules chemically bound to the product; and (ii) water molecules not bound to the product, also known as "free water". Crystal growth occurs when free water molecules turn into ice. What happens to the bound water during freezing depends on the characteristics of the product matrix. In the case of products that form amorphous matrices (e.g. sucrose, trehalose), bound water molecules are absorbed into the product; in contrast, when products form crystalline matrices (e.g. mannitol), bound water molecules are adsorbed on the product. In the pharmaceutical industry, most products form amorphous matrices (Barley, 2009). After the freezing step, bound water does not freeze, which is why it is referred to as "unfrozen water", while free water is referred to as "frozen water" (Fonseca et al., 2015; Roos, 2005).

The ice growth involves capturing water molecules from the solution, hence increasing the solute mass fraction and apparent viscosity of the product phase in a process known as "cryoconcentration" (Pikal, 1999). Cryoconcentration progresses during freezing until reaching a maximal solute mass fraction (e.g. 74% when freezing a 3% w/w sucrose solution; Pikal, 1999). To understand the meaning of this maximal value, Figure 2.1-4a presents a state diagram depending on the solute mass fraction and temperature for a product forming an amorphous matrix. If freezing occurs slowly enough as a succession of physicochemical pseudo-equilibria, cryoconcentration occurs as moving from "D" to "G" (Figure 2.1-4a). In contrast, if freezing occurs at a faster rate, cryoconcentration occurs as moving from "D" to "F" (Figure 2.1-4a) (Rahman, 2004). Regardless of the freezing rate, cryoconcentration continues until reaching the intersection with the glass transition curve (curve WS in Figure 2.1-4a). The maximal solute mass fraction reached through cryoconcentration (when the concentration is halted) is the value at the intersection with the glass transition curve, and it depends on the freezing rate (concentration in "G" is different to that in "F";

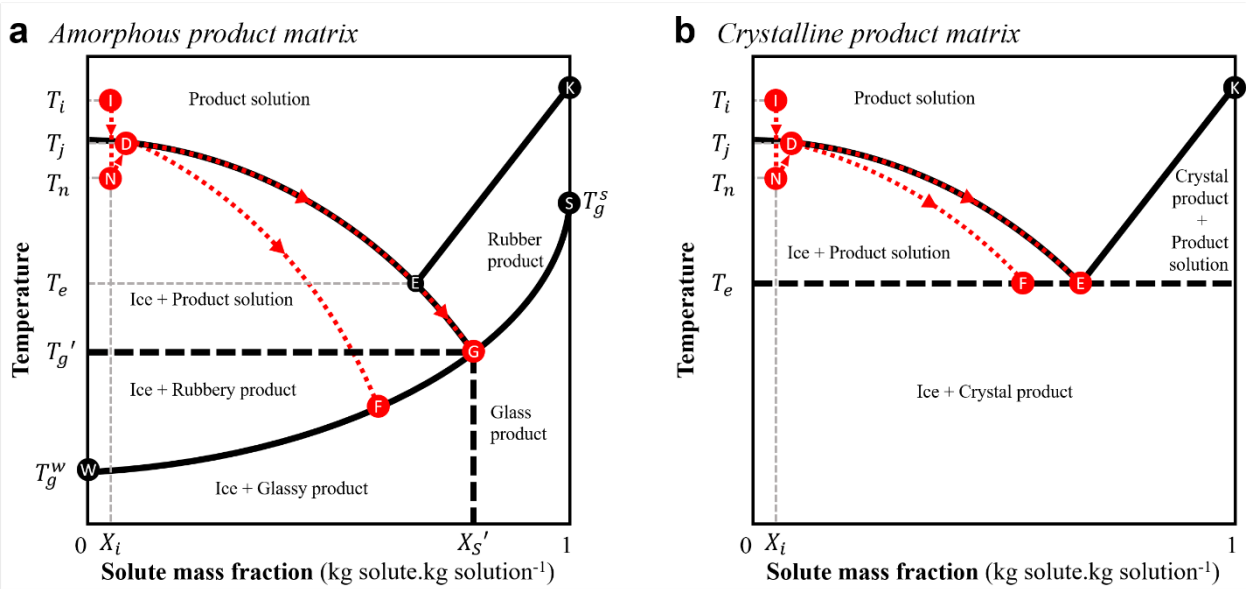

Figure 2.1-4 – State diagram for a solution. I: Initial condition before freeze-drying, N: nucleation, D: freezing point depression, E: eutectic point, DE and DG: slow freezing curve, DF: faster freezing curve, EK: solubility curve, WS: glass transition line, T_i: initial temperature, T_n: nucleation temperature, T_j: freezing-point depression, T_e: eutectic point temperature, T_g': glass transition for maximal-freeze-concentration condition, T_g^w: glass transition of water, T_g^s: glass transition temperature of solids, X_i: initial solute mass fraction, X_s': solute mass fraction at maximal-freeze-concentration condition (adapted from Rahman, 2004).

Figure 2.1-4a). The temperature at "G" and "F" is known as the "glass transition temperature" (T_g); for a certain solute mass fraction (X), T_g is the highest temperature at which the product phase obtained will remain in the glassy state. Heating the amorphous product phase above T_g would take it to a rubbery state, which is less viscous and mechanically less stable. As it can be observed in Figure 2.1-4a, freezing at slow or fast conditions entails different T_g values (the temperature in "G" is different from the temperature in "F").

Figure 2.1-4b presents a scheme of the state diagram for a product forming a crystalline phase. In this case, regardless of the freezing condition ("D" to "E" or "D" to "F"; Figure 2.1-4b), the product turns into a crystal phase at the eutectic temperature (T_e). Heating the crystalline product phase above T_e would make the product interact with the water, forming a saturated solution and making the crystalline product mechanically less stable.

The freezing step finishes when the initial solution turns into ice crystals and a glassy or crystalline product phase.

2.1.2.3. Primary Drying

Ice crystals are removed by sublimation throughout primary drying, representing a reduction of over 80% of the initial water content (Patel et al., 2010b). Primary drying is typically the most time-consuming step of the freeze-drying process, taking up to several days at industrial scale (Shukla, 2011). Once the freezing step finishes, the pressure inside the chamber is decreased, usually attaining values lower than 15 Pa. Then, the shelf temperature is increased until a set point commonly between -40 and 0 °C (Scutellà et al., 2017b) (Figure 2.1-3). In this way, a heat flow is established from the shelf to the container during primary drying. Initially, this heat flow only increases the product temperature. However, when the ice crystals in contact with the chamber gas reach the ice-vapour equilibrium temperature, this heat flow (mainly) causes ice sublimation (Pikal, 2000). The ice surface in contact with the chamber gas is known as the "sublimation front". When ice crystals sublimate, the sublimation front moves through the content (Sheehan and Liapis, 1998), leaving pores behind where the ice used to be. Vapour moves from the sublimation front to the drying chamber through the dried product layer, and then to the condenser through the duct. The condenser is a heat exchanger that is considerably colder than the drying chamber, usually at temperatures lower than -60 °C, so the vapour turns into ice. Primary drying finishes when all the ice in the containers has sublimated, only leaving unfrozen water bound to the product.

2.1.2.4. Secondary Drying

After primary drying, the product phase appears dry, even though it still contains unfrozen water. Throughout secondary drying, unfrozen water is desorbed, obtaining a final product phase with a moisture content potentially lower than 1% (Tang and Pikal, 2004). Excessively high final moistures can damage the antigen during storage and transportation; however, (World Health Organization, 2011), and excessively low final moisture contents can denature the active molecules or damage the cell structure of the biological product of interest (Passot et al., 2012a). Therefore, a limited range of final moisture content values is accepted after secondary drying so the antigen could be preserved correctly (e.g. 2.5 to 3.7% in Passot et al. (2012)), requiring a fine-tuning of the process parameters and duration of the step.

Pikal et al. (1990) concluded that it is more energetically efficient to set higher shelf temperatures to improve desorption rather than extend the secondary drying step. Therefore, shelf temperatures could be as high as 50 °C during secondary drying, so the duration of secondary drying is usually one-third of that of primary drying. Chamber pressure values during secondary drying remain similar to or lower than those in primary drying (typically lower than 15 Pa; Pikal et al., 1983).

2.1.3. Quality Management

2.1.3.1. The Advantage of Quality by Design for Process Optimisation

There are several ways to define "quality"; for pharmaceutical products, quality is commonly defined as the "fitness for use" (Woodcock, 2004). This definition is seen from the consumer's perspective and aims at complying with the therapeutic benefit promised in the label. The goal of industrial companies is to achieve a product with an acceptable quality while minimising production costs (i.e. ingredients, energy consumption, time, among others).

The traditional approach to manage quality was only based on conforming to strict specifications during physical, chemical, or clinical tests, allowing producers to detect heterogeneities between batches (Elder, 2014). This approach does not require a deep understanding of the impact of the process on the product quality attributes and envisions process design based on trial and error. So it is impossible to certainly identify the optimal operating conditions.

Juran (1992) presented a novel approach known as "Quality by Design" (QbD), which was later adopted by the US Food and Drug Administration (FDA) in 2009 for the development of new drugs (US Food and Drug Administration, 2009). The QbD approach sustains that quality must be designed into the product and the manufacturing process, claiming that most quality problems are due to how the product and process were conceived. Hence, QbD implicates understanding the "connexions" between process variables or parameters (e.g. operating conditions, equipment, disposition) and product quality attributes (Hussain, 2003). These connexions allow researchers to optimise the operating conditions, so process design is faster and more efficient than performed by simple trial and error.

2.1.3.2. Critical Quality Attributes

Freeze-drying aims at conditioning vaccines before storage and transportation to extend their shelf life, but the process could also deteriorate the product quality if not carried out correctly. For example, the antigen in the formulation could be denatured throughout freezing or drying, so the final product could lose potency and no longer immunise the subject receiving the dose (Akers, 2016). Buffers and carbohydrates (e.g. sucrose, trehalose, mannitol) are added to the formulation to protect the antigen during freeze-drying (Amorij et al., 2007). Each antigen requires a specific combination of several ingredients or excipients to be protected during the freeze-drying process.

Under the umbrella of the QbD approach, the FDA (2009) requires "identifying the potential Critical Quality Attributes (CQAs)" before "selecting the type and amount of excipients to deliver a drug product of the desired quality". In the case of freeze-dried vaccines, the CQAs are:

(i) the final product potency, to ensure the antigen was not damaged during the freezing or drying;
(ii) the final moisture content, to confirm drying was successful so the product would be stable during the prescribed shelf-life; and
(iii) the dried product appearance (Awotwe-Otoo and Khan, 2015; World Health Organization, 2011).

The reason why the dried product appearance is a CQA may not be evident at first sight. To illustrate an acceptable appearance, Figure 2.1-5 (left vial) presents a successfully dried product (also known as "dried cake"). A visually elegant dried cake presents a shape that recalls the initial filled liquid volume, as opposed to a shrunk or collapsed dried cake (Figure 2.1-5; right vial). An elegant dried cake implies that the product retained its porous structure during drying. Porous products are desired because they: (i) improve drying since the vapour can escape through the pores, and (ii) improve the solubility since there is more surface area per volume, so the dried cake could be easily dissolved (regenerated) before injection (World Health Organisation, 2000). To the best of the author's knowledge, there is no formal scientific proof confirming that an elegant dried cake guarantees that the product potency will be preserved during storage and transportation (Patel et al., 2017). However, the dried cake appearance is the most common CQA considered for process design (Nail and Searles, 2008; Nail and Gatlin, 2010; Scutellà et al., 2017b; Yu, 2008), presumably under the implicit assumption that the potency will always be preserved in cakes presenting an elegant pharmaceutical appearance.

Figure 2.1-5 – Observation of product collapse. The left vial has an acceptable appearance; the right vial does not have an acceptable appearance (collapsed).

2.1.3.3. Critical Process Parameters

The thermal history of the product during drying plays a main role in the dried cake's appearance. If a dried cake exceeds a specific critical temperature, the solid phase softens to the point at which the structure cannot hold itself, so it shrinks and collapses. Collapse is a dynamic phenomenon; therefore, the critical temperature that entails product collapse, known as "collapse temperature" (T_c), is different from the glass transition temperature (T_g, for amorphous matrices) or the eutectic temperature (T_e, for crystalline matrices) which refer to equilibrium conditions (Levi and Karel, 1995; Meister and Gieseler, 2009; Pikal and Shah, 1990a). The value of T_c varies for each formulation (ingredients and concentration), thus the dried cake appearance of each candidate vaccine formulation must be screened after freeze-drying. Selecting a final vaccine formulation that fulfils all the quality requirements is laborious and could take several months.

The European Medicines Agency (2009) defined "Critical Process Parameters" (CPPs) as "a process parameter whose variability has an impact on a critical quality attribute and therefore should be monitored or controlled to ensure the process produces the desired quality". The product is structurally fragile mostly due to the water content (adsorbed or absorbed), so the dried cake is particularly delicate during primary drying when the water content is the greatest. Therefore, the product temperature during primary drying will be the CPP considered in this thesis, impacting the dried cake appearance (CQA). The product temperature during primary drying cannot be directly set. Instead, the freeze dryer allows the user to set the shelf temperature and chamber pressure (operating conditions). According to the QbD approach, selecting the optimal operating conditions (process design) requires connecting the operating conditions with the product temperature. This "connection" is commonly established through mathematical models for heat and mass transfer during primary drying (Nail and Searles, 2008; Patel and Pikal, 2013).

2.1.4. Take-Home Message

Freeze-drying is a process widely used in the pharmaceutical industry to dry vaccines, serving to preserve their potency during storage and transportation. The process consists of three steps: (i) freezing the vaccine, (ii) removing the free water by sublimation (primary drying), and (iii) removing the bound water by desorption (secondary drying). Section 2.1 highlighted how the product temperature during primary drying is closely related to the dried cake appearance, which is a commonly monitored *critical quality attribute. In particular, the product temperature should be maintained below a critical value (collapse temperature) to ensure a non-collapsed dried cake. The collapse temperature varies for each vaccine formulation, so every candidate vaccine's appearance must be screened after freeze-drying. Moreover, the product temperature cannot be directly fixed during freeze-drying, hence the importance of using mathematical models for heat and mass transfer to understand how to control the product temperature through the operating conditions (shelf temperature and chamber pressure).*

2.2. Heat Transfer Modelling during Primary Drying

2.2.1. Heat Transfer Mechanisms

In physics, there are three mechanisms (or modes) of heat transfer: (i) conduction, (ii) radiation, and (iii) convection (Lienhard and Lienhard, 2017). On a microscopic scale, conduction is the heat transfer from a particle with a higher energy level to a contiguous particle with a lower energy level by collision (Rohsenow et al., 1998). On a larger scale, conduction refers to the heat transfer within a body from one region at a higher temperature to another region at a lower temperature, or between bodies in physical contact from the body at a higher temperature to the body at a lower temperature. Radiation is the heat transfer between surfaces through electromagnetic energy transportation (Perry and Green, 2008). Unlike conduction, radiation between surfaces does not require a medium (or body) between them. Conduction and radiation are fundamental physical modes (White, 1984), while convection is the heat transfer by moving fluids, ultimately due to conduction and radiation (Perry and Green, 2008). In other words, convection considers how fluid mechanics affect heat transfer.

During primary drying, heat transfer in the drying chamber occurs under vacuum conditions. Conduction (between and within objects) and radiation are the main heat transfer mechanisms during primary drying, so the contribution of convection in the gas inside the chamber is commonly considered negligible (Pikal et al., 2016a). Figure 2.2-1 presents the heat transfer mechanisms at an intermediate point of primary drying using a serum vial (traditional container), so there is a frozen product layer (ice crystals and product matrix with bound water) and a dried product layer (product matrix with bound water). The main heat sink is the sublimation front, where the heat is employed for the phase change from ice to vapour (sublimation), and the main heat sources are the shelves (mostly the bottom shelf) (Pikal, 1985). Other heat sources are the chamber walls and the door, which are commonly unwanted because they cause heat transfer heterogeneities between vials according to their position in the freeze dryer (Pisano et al., 2011; Scutellà et al., 2017b).

The following Sections 2.2.1.1 to 2.2.1.5 detail the physical laws that govern the heat transfer mechanisms in the drying chamber, as well as the principal heat transfer coefficients.

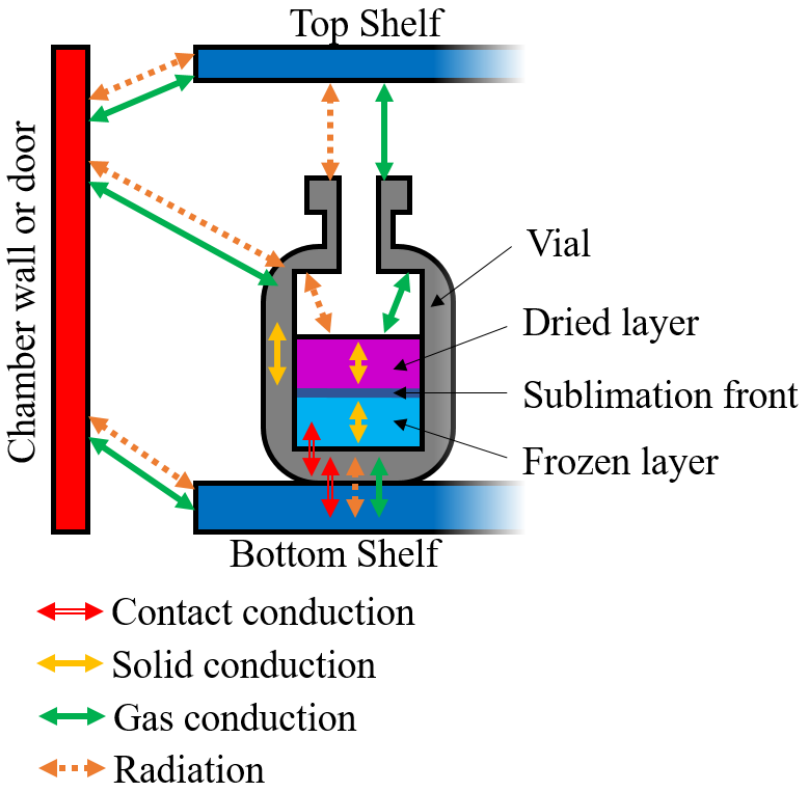

Figure 2.2-1 – Main heat transfer mechanisms (radiation and conduction) between bodies for a serum vial placed directly on the freeze dryer's shelf (adapted from Pikal, 2000).

2.2.1.1. Contact Conduction

The heat flow ($\dot{Q}_{1,2}^{cc}$, W) transferred by contact conduction from one surface (1) to another (2) is calculated as (Perry and Green, 2008):

$$\dot{Q}_{1,2}^{cc} = A_{1,2} \times K_{1,2}^{cc} \times (T_1 - T_2) \qquad \text{Equation 2.2-1}$$

where $A_{1,2}$ (m^2) is the area of both surfaces facing each other in "macroscopic" contact (different to the total area of "microscopic" contact points), $K_{1,2}^{cc}$ ($W.m^{-2}.K^{-1}$) is the heat transfer coefficient by contact conduction between the surfaces, T_1 (K) is the temperature at surface 1, and T_2 is the temperature at surface 2. When it comes to pharmaceutical freeze-drying, containers are commonly placed (directly) on the shelves. Thus, the two thermal contact conductance values between the shelf and the sublimation front (represented as red arrows in Figure 2.2-1) are those: (i) between a shelf and the container placed on it, (ii) between a container and the product. Only the thermal contact conductance between the shelf and the container has been studied in the freeze-drying literature (e.g. Pikal, 2000; Pisano et al., 2011); presumably, under the implicit hypothesis that the thermal contact conductance values between the container and the (frozen or dried) product do not limit the transfer to the sublimation front.

The empirical and semi-empirical correlations used in various fields of process engineering to estimate the thermal contact conductance between two surfaces depend on: (i) the geometry of the surfaces (e.g. roughness, flatness, asperity slope), (ii) the pressure of the gas between the surfaces, (iii) the physicochemical properties of the surfaces (e.g. thermal conductivity, specific heat capacity, surface hardness, elastic modulus, coefficient of thermal expansion), and (iv) the average temperature at the interface (Hasselstrom and Nilsson, 2012; Tariq and Asif, 2016). In pharmaceutical freeze-drying, the heat transfer coefficient by contact conduction between the shelf and the container (K_V^{cc}, $W.m^{-2}.K^{-1}$) is considered as independent of the operating conditions (i.e. shelf temperature and chamber pressure) and depends on the surface geometry and material (Fissore et al., 2011; Kuu and Nail, 2009; Patel et al., 2010c; Pikal, 2000). K_V^{cc} could be considered as a function of the total area of "microscopic" contact points between the container bottom and the shelf (A_V^{cc}, m^2; different from the "macroscopic" contact area $A_{1,2}$), as follows (Scutellà et al., 2017a):

$$K_V^{cc} = A_V^{cc} \times k_V^{cc} \qquad \text{Equation 2.2-2}$$

where k_V^{cc} ($W.m^{-4}.K^{-1}$) is the thermal conductivity per "microscopic" contact area between the shelf and the container bottom.

2.2.1.2. Conduction within Solid Bodies

The heat flux by conduction ($\dot{q}^c$, W.m^{-2}) within solid bodies is governed by Fourier's law as follows (Perry and Green, 2008):

$$\dot{q}^c = -\lambda \nabla T \qquad \text{Equation 2.2-3}$$

where λ (W.m^{-1}.K^{-1}) is the thermal conductivity of the body, and ∇T (K) is the temperature gradient within the body. λ is a measure of the body's ability to conduct heat and has a different value for each material. For solid bodies in the drying chamber (e.g. containers, frozen or dried product; represented as yellow arrows in Figure 2.2-1), λ is considered independent of the operating conditions (Scutellà et al., 2017b; Velardi and Barresi, 2008).

2.2.1.3. Conduction within Gas

Much like solid bodies, the heat flux by conduction ($\dot{q}^c$, W.m^{-2}) within a gas (represented as green arrows in Figure 2.2-1) is also governed by Fourier's law (Equation 2.2-3). Conduction occurs when molecules collide and exchange heat. In the gas phase, molecules travel distances greater than the molecule diameter until they collide and exchange energy (heat) with other molecules. The average distance travelled between collisions is known as the "mean free path" (l_{fp}, m), and is calculated as:

$$l_{fp} = \frac{1}{\sqrt{2}\pi {d_{gas}}^2 \Theta_{gas}} = \frac{\kappa \times T}{\sqrt{2}\pi {d_{gas}}^2 \times P} \qquad \text{Equation 2.2-4}$$

where d_{gas} (m), is the gas molecule diameter, Θ_{gas} (n° of molecules per m^3) is the number of gas molecules per volume, κ (J.K^{-1}) is the Boltzmann constant, T (K) is the gas temperature (Pikal, 2000), and P (Pa) is the gas pressure. When considering the heat conduction through the gas phase from one surface (1) to another parallel surface (2), the effective thermal conductivity depends on the ratio of l_{fp} to the distance between surfaces ($l_{1,2}$, m), also known as "Knudsen number" (Kn = $l_{fp}/l_{1,2}$). If l_{fp} is much greater than $l_{1,2}$ (Kn much greater than 1; Perry and Green, 2008) gas molecules are more likely to interact with the surfaces than with other molecules; this condition is known as "free molecular regime". Under a free molecular regime, an increase in the gas pressure entails a direct increase in the possibility of molecule collision, hence the thermal conductivity of the gas (λ_{gas}^{fm}, W.m^{-1}.K^{-1}) is directly proportional to the pressure and can be calculated as:

$$\lambda_{gas}^{fm} = \alpha \Lambda_0 P l_{1,2} \qquad \text{Equation 2.2-5}$$

where α is a thermal accommodation coefficient related to the quality of momentum exchange between the gas molecules and the surfaces, and Λ_0 (W.m^{-2}.K^{-1}.Pa^{-1}) is the heat transfer coefficient of the gas under a

free molecular regime (Scutellà et al., 2017b). If l_f is much smaller than $l_{1,2}$ (Kn much smaller than 1; Perry and Green, 2008), gas molecules are more likely to interact with each other than with the surfaces. This heat transfer condition is known as "continuous regime", and in this case, the thermal conductivity (λ_{gas}^{cont}, W.m^{-1}.K^{-1}) is almost independent of the gas pressure.

Due to the low pressure during primary drying, the regime of the gas inside the drying chamber is commonly somewhere between the free molecular and continuous. This transition regime between free molecular and continuous has been particularly studied in the heat flow through the gas trapped between two parallel surfaces (1 and 2), e.g. the gas trapped between the bottom shelf and the vial bottom. The following expression was derived by Pikal et al. (1984) based on the kinetic theory of gases:

$$\dot{Q}_{1,2}^{gc} = A_{1,2} \times \left(\frac{l_{1,2}}{\lambda_{gas}^{fm}} + \frac{l_{1,2}}{\lambda_{gas}^{cont}} \right)^{-1} \times (T_1 - T_2) = A_1 \times K_{1,2}^{gc} \times (T_1 - T_2) \qquad \text{Equation 2.2-6}$$

where $\dot{Q}_{1,2}^{gc}$ (W) is the conductive heat flow through the gas from surface 1 to surface 2, $A_{1,2}$ (m^2) is the area of both parallel surfaces, and $K_{1,2}^{gc}$ (W.m^{-2}.K^{-1}) is the heat transfer coefficient by gas conduction between the surfaces. The term $l_{1,2}/\lambda_{gas}^{fm}$ represents the resistance to the heat transfer through a free molecular flow, and the term $l_{1,2}/\lambda_{gas}^{cont}$ represents the resistance through a continuous flow. $K_{1,2}^{gc}$ can be calculated based on Equation 2.2-6 as:

$$K_{1,2}^{gc} = \left(\frac{l_{1,2}}{\lambda_{gas}^{fm}} + \frac{l_{1,2}}{\lambda_{gas}^{cont}} \right)^{-1} = \frac{\alpha \Lambda_0 P}{1 + \alpha \Lambda_0 P l_{1,2}/\lambda_{gas}^{cont}} \qquad \text{Equation 2.2-7}$$

2.2.1.4. Radiation between Surfaces

All objects in the drying chamber emit electromagnetic radiation (represented as orange arrows in Figure 2.2-1) (Howell et al., 2020). When radiation reaches a surface, the energy can be: (i) absorbed by the surface, (ii) reflected to other surfaces, or (iii) transmitted deeper into the body. A *black body* emits the maximal energy possible at its surface temperature, and the heat flux by radiation emitted ($\dot{q}_{bb}^{rad}$, W.m^{-2}) follows the Stefan-Boltzmann law (Perry and Green, 2008):

$$\dot{q}_{bb}^{rad} = \sigma T^4 \qquad \text{Equation 2.2-8}$$

where σ (W.m^{-2}.K^{-4}) is the Stefan-Boltzmann constant. Real surfaces emit less energy than a *black body*, and the ratio of the radiation emitted by real surfaces to the *black body* radiation (at the same temperature) is known as "emissivity" (ε, dimensionless). Surfaces inside the drying chamber are considered diffuse grey bodies in the freeze-drying literature (Pikal, 2000), which means that ε is equal to the fraction of energy absorbed (absorptivity) and does not depend on the radiation's wavelength and angle. Emissivity values of common non-metallic materials used during freeze-drying (e.g. glass, ice) are close to 1 (*black-body*

emissivity), and polished metallic surfaces have lower emissivity values (lower than 0.3) than rough metallic surfaces (greater than 0.6) (Perry and Green, 2008; Pikal, 2000). The heat flow by radiation between two *diffuse grey-bodies* surfaces (1 and 2) is usually calculated as (Pisano et al., 2011; Scutellà et al., 2017a; von Graberg, 2011):

$$\dot{Q}_{1,2}^{rad} = A_1 \times F_{1,2}\sigma \times \left({T_1}^4 - {T_2}^4\right) = A_1 \times K_{1,2}^{rad} \times (T_1 - T_2) \qquad \text{Equation 2.2-9}$$

where $\dot{Q}_{1,2}^{rad}$ (W) is the heat flow by radiation from surface 1 to surface 2, A_1 (m^2) is the area of surface 1, $F_{1,2}$ (dimensionless) is the visualisation factor (or view factor) from surface 1 to 2, and $K_{1,2}^{rad}$ ($W.m^{-2}.K^{-1}$) is the heat transfer coefficient by radiation between the surfaces. $F_{1,2}$ is a geometrical parameter that considers the effects of the surfaces' position, orientation and emissivity on $Q_{1,2}^{rad}$. $K_{1,2}^{rad}$ can be calculated based on Equation 2.2-9 as:

$$K_{1,2}^{rad} = F_{1,2}\sigma(T_1 + T_2)\left({T_1}^2 + {T_2}^2\right) \cong 4F_{1,2}\sigma\bar{T}^3 \quad ; \quad \bar{T} = \frac{(T_1 + T_2)}{2} \qquad \text{Equation 2.2-10}$$

where $\bar{T}$ (K) is the average surface temperature, which is often considered a constant value within the range of temperatures reached during freeze-drying applications (Pikal, 2000).

2.2.1.5. Heat Transfer Coefficient to the Container

The total heat flow ($\dot{Q}$, W) received by a serum vial placed directly on the shelf (without a tray) and surrounded by other identical vials during primary drying can be calculated as:

$$\dot{Q} = \dot{Q}_b + \dot{Q}_t \qquad \text{Equation 2.2-11}$$

where $\dot{Q}_b$ (W) is the heat flow from the bottom shelf (Figure 2.2-1) to the vial, and $\dot{Q}_t$ (W) is the heat flow from the top shelf (Figure 2.2-1) to the vial. Equation 2.2-11 neglects the heat reaching the vial from any object but the shelves (e.g. chamber wall and door, other vials). Thus, this equation is valid for the so-called "central vials" – i.e. vials surrounded by other identical vials for which the net exchanged heat is zero by symmetry.

Heat Transfer Coefficient between the Bottom Shelf and the Container

$\dot{Q}_b$ is commonly considered proportional to the temperature difference between the vial surface and the shelf surface (e.g. Pikal, 2000; Pisano et al., 2011), and is calculated as:

$$\dot{Q}_b = A_V \times K_{V,b} \times \left(T_{shelf} - T_b\right) \qquad \text{Equation 2.2-12}$$

where A_V (m^2) is the outer cross-sectional area, $K_{V,b}$ ($W.m^{-2}.K^{-1}$) is the heat transfer coefficient between the bottom shelf and the vial, T_{shelf} (K) is the shelf surface temperature, and T_b is the vial bottom temperature. As a remark, T_{shelf} is usually considered as the temperature of the heat-transfer fluid due to the high thermal conductivity of the metallic shelves (Scutellà et al., 2017a), and T_{shelf} is considered to have the same value for all the shelves in the freeze dryer. $K_{V,b}$ includes the contribution of each heat transfer mechanism from the bottom shelf to the serum vials in parallel according to the following equation (Pikal, 2000; von Graberg, 2011):

$$K_{V,b} = K_V^{cc} + K_{V,b}^{gc} + K_{V,b}^{rad} \qquad \text{Equation 2.2-13}$$

where $K_{V,b}^{cc}$ ($W.m^{-2}.K^{-1}$) is the heat transfer coefficient by contact conduction; $K_{V,b}^{gc}$ ($W.m^{-2}.K^{-1}$) is the heat transfer coefficient by conduction through the gas trapped between the bottom shelf and vial bottom surfaces; and $K_{V,b}^{rad}$ ($W.m^{-2}.K^{-1}$) is the heat transfer coefficient by radiation. Each term in $K_{V,b}$ can be modelled according to Equation 2.2-1, Equation 2.2-6 and Equation 2.2-9, arriving at the expression:

$$K_{V,b} = A_V^C \times k_V^{cc} + \frac{\alpha_V \Lambda_0 P_C}{1 + \alpha_V \Lambda_0 P_C l_{V,b}/\lambda_{gas}^{cont}} + 4F_{V,b}\sigma\bar{T}^3 \qquad \text{Equation 2.2-14}$$

where α_V (dimensionless) is the thermal accommodation coefficient between the bottom shelf and the vial bottom; $l_{V,b}$ (m) is the mean distance between the bottom shelf and the vial bottom; P_C (Pa) is the pressure inside the drying chamber, which is considered to be homogenous within the chamber; $F_{V,b}$ is the

visualisation factor from the vial bottom to the bottom shelf; and $\bar{T}$ is the average temperature between the shelf and the vial bottom.

Heat Transfer Coefficient between the Top Shelf and the Container

Similarly to $\dot{Q}_b$, $\dot{Q}_t$ can also be considered proportional to the temperature difference between the vial surface and the shelf surface, obtaining the following expression:

$$\dot{Q}_t = A_{V,t} \times K_{V,t} \times \left(T_{shelf} - T_t\right) \quad \text{Equation 2.2-15}$$

where $A_{V,t}$ (m^2) is the heat transfer area between the top shelf and the vial, $K_{V,b}$ ($W.m^{-2}.K^{-1}$) is the apparent heat transfer coefficient between the top shelf and the vial, and T_t (K) is the temperature at the vial top. T_t is usually considered equal to the bottom vial temperature (T_b) (Pisano et al., 2011; Scutellà et al., 2017a), under the assumption that the temperature difference within the vial ($T_b - T_t$) is negligible compared to the temperature difference between the vial and the shelf ($T_{shelf} - T_b$). $K_{V,t}$ considered the heat transfer mechanism from the top shelf to the serum vials in parallel, as follows:

$$K_{V,t} = K_{V,t}^{gc} + K_{V,t}^{rad} \quad \text{Equation 2.2-16}$$

where $K_{V,t}^{gc}$ ($W.m^{-2}.K^{-1}$) is the heat transfer coefficient by conduction through the gas between the top shelf and vial surfaces; and $K_{V,t}^{rad}$ ($W.m^{-2}.K^{-1}$) is the heat transfer coefficient by radiation. $K_{V,t}$ can be modelled based on Equation 2.2-6 and Equation 2.2-9 as follows:

$$K_{V,t} = \frac{\alpha_V \Lambda_0 P_C}{1 + \alpha_V \Lambda_0 P_C l_{V,t}/\lambda_{gas}^{cont}} + 4F_{V,t}\sigma\bar{T}^3 \quad \text{Equation 2.2-17}$$

where $l_{V,t}$ (m) is the mean distance between the top shelf and the vial, and $F_{V,t}$ is the visualisation factor from the vial to the top shelf. The first term of Equation 2.2-14 (representing $K_{V,t}^{gc}$) is commonly neglected (e.g. Kuu et al., 2006; Rambhatla and Pikal, 2003) compared to the heat transfer to the vial by other mechanisms (viz. $K_{V,t}^{rad}$, $K_{V,b}^{cc}$, $K_{V,b}^{gc}$, $K_{V,b}^{rad}$), presumably due to the great distance between the top shelf and the vial (l_t).

Apparent Heat Transfer Coefficient between the Shelves and the Container

Overall, the total heat flow reaching the vial ($\dot{Q}$) is commonly calculated using an apparent heat transfer coefficient between the shelves and the vials (K_V) (e.g. Assegehegn et al., 2019; Tang et al., 2006) as:

$$\dot{Q} = A_V \times K_V \times \left(T_{shelf} - T_b\right) \quad \text{Equation 2.2-18}$$

K_V is mechanistically modelled based on Equation 2.2-11, Equation 2.2-12, Equation 2.2-14, Equation 2.2-15, Equation 2.2-17, and Equation 2.2-18 as:

$$K_V = A_V^C \times k_V^{cc} + \frac{\alpha_V \Lambda_0 P_C}{1 + \alpha_V \Lambda_0 P_C l_{V,b}/\lambda_{gas}^{cont}} + 4\left(F_{V,b} + \frac{A_{V,t}}{A_V} F_{V,t}\right)\sigma\bar{T}^3 \quad \text{Equation 2.2-19}$$

Note that Equation 2.2-19 neglects the heat transfer coefficient by conduction through the gas between the top shelf and vial surfaces ($K_{V,t}^{gc}$, first term in Equation 2.2-17), as well as the difference between T_b and T_t. In practice, Equation 2.2-19 is usually simplified to a pressure-independent and a pressure-dependent term (e.g. Fissore et al., 2011; Pisano et al., 2011) as:

$$K_V = C_1 + \frac{C_2 P_C}{1 + C_3 P_C} \qquad \text{Equation 2.2-20}$$

where C_1 (W.m^{-2}.K^{-1}), C_2 (W.m^{-2}.K^{-1}.Pa^{-1}), and C_3 (Pa^{-1}) are:

$$C_1 = A_V^C \times k_V^{cc} + 4(F_{V,b} + \frac{A_{V,t}}{A_V} F_{V,t})\sigma \bar{T}^3$$

$$C_2 = \alpha_V \Lambda_0 P_C \qquad \text{Equation 2.2-21}$$

$$C_3 = \alpha_V \Lambda_0 P_C l_{V,b} / \lambda_{gas}^{cont}$$

The values of C_1, C_2, and C_3 are usually estimated from experimental data.

Based on the hypothesis used to build K_V, the estimated value of C_1 possibly includes other pressure-independent heat transfer coefficients by mechanisms; for example, the radiation and gas conduction from the chamber walls or door. Note that the heat transfer coefficient by gas conduction from the chamber walls or door is supposed independent of P_C since the distance between surfaces is considerably greater than the mean free path (Kn much smaller than 1, continuous regime). For example, considering a distance between the vial and the chamber wall or door ($l_{1,2}$ in Equation 2.2-7) of 10 cm and a thermal accommodation coefficient taken from Scutellà et al. (2017b) (α = 0.34), the heat transfer coefficient between the wall or door and the vial by gas conduction increases by less than 6% from P_C = 4 Pa to P_C = 15 Pa.

It is commonly supposed that C_1 (as well as C_2 and C_3) is independent of the operating conditions (T_{shelf} and P_C), even if according to Equation 2.2-10, $\bar{T}$ does depend on T_{shelf} (T_1 in Equation 2.2-10) and the vial temperature (T_2 in Equation 2.2-10). However, the validity of this supposition depends on the range of operating conditions. For example, assuming the vial is 20 °C hotter than T_{shelf} (Pikal, 2000), $\bar{T}^3$ increases 27% from T_{shelf} = -40 °C to T_{shelf} = -20 °C. The impact of such increase on K_V (Equation 2.2-19) may or may not be relevant depending on the value of the other terms.

2.2.2. Relevant Factors for the Heat Transfer during Primary Drying

The product temperature during primary drying depends not only on the operating conditions (i.e. shelf temperature and chamber pressure). Some other factors impact the heat transfer, ultimately causing differences between batches or among containers of the same batch.

2.2.2.1. Container Type

Several types of container can be employed to perform freeze-drying; Figure 2.2-2 shows a variety of containers found in the literature. Serum vials are the most common container used to freeze-dry vaccines at laboratory, pilot and industrial scale (Figure 2.2-2a) (Pikal, 1985; Rambhatla and Pikal, 2003; Sheehan and Liapis, 1998). However, syringes (Figure 2.2-2b) and ampoules (Figure 2.2-2c) are also used at various scales (Berny and Hennebert, 1991; Hottot et al., 2009a; Miyamoto-Shinohara et al., 2000). Some containers are strictly used for formulation research and development; such is the case of 96-well PCR-plates (Figure 2.2-2d), plastic 96-well plates (Figure 2.2-2e), and high-throughput vials inside aluminium well plates (Figure 2.2-2f). To the best of the author's knowledge, less than a handful of scientific works mention these containers strictly used for formulation research (e.g. Trnka et al., 2015; von Graberg, 2011).

The total heat flow reaching a container ($\dot{Q}$) is considered to be governed by the apparent heat transfer coefficient, K_V (Equation 2.2-18). As detailed in Equation 2.2-19, the geometry of the container impacts certain components of K_V (i.e. A_V^{cc}, $l_{V,b}$, $F_{V,b}$, $F_{V,t}$). Furthermore, the surface characteristics of the container and shelves (e.g. material, roughness) could also affect components of K_V (i.e. k_V^{cc}, α_V, $F_{V,b}$, $F_{V,t}$). Therefore, K_V should be determined for every container type and freeze dryer. As a remark, high-throughput vials are not directly placed on the shelf, so the expression of K_V as in Equation 2.2-19 does not have a physical meaning in their case. Regardless, von Graberg (2011) determined an apparent K_V between the high-throughput vial bottoms and the shelves at different chamber pressures. The results of von Graberg (2011) showed that Equation 2.2-20 was able to fit the data although it is not physically pertinent.

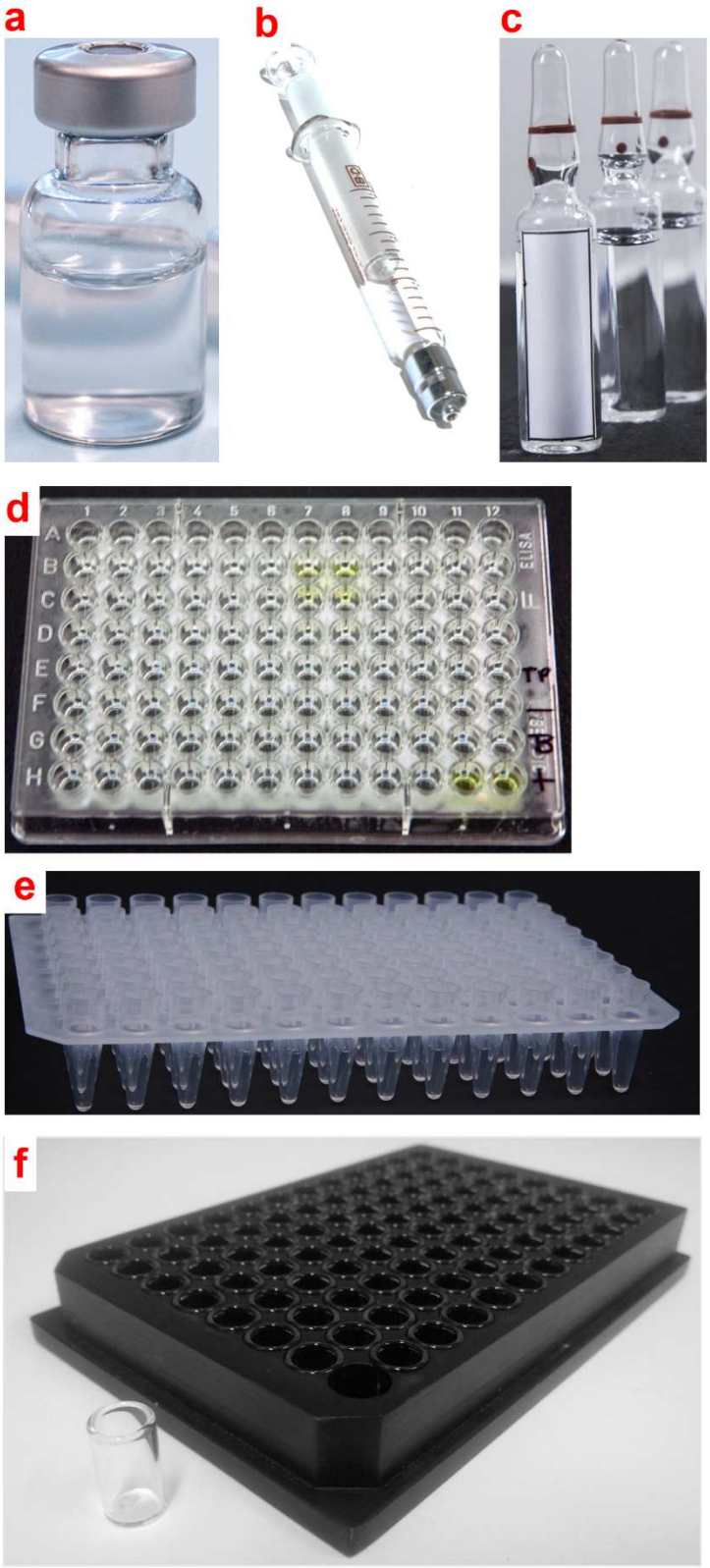

Figure 2.2-2 – Containers to perform freeze-drying. (a) Serum vial. (b) Syringe. (c) Ampoule. (d) 96-well PCR-plate. (e) Plastic 96-well plates. (f) 500-µL high-throughput vial in front of a 96-Well Freeze-Drying System manufactured by VirTis, consisting of an aluminium well plate carrying 96 high-throughput vials.

2.2.2.2. Container Geometry

Even if all the containers of a batch are of the same type and made of the same material, slight variations in the geometry could affect the heat received during primary drying. To the best of this author's knowledge, the only published research on this matter was carried using serum vials. The bottom shelf is considered to be the main heat transfer source, which is why the impact of the vial bottom geometry on K_V (and the total heat flow received by serum vials) has been the subject of more than one study (e.g. Brülls and Rasmuson, 2002; Pisano et al., 2011; Scutellà et al., 2017a).

Scutellà et al. (2017a) determined K_V for 210 serum vials at several chamber pressures (4 to 50 Pa) through gravimetric analysis during ice sublimation experiments. Then, Scutellà et al. (2017a) compared the experimental K_V distributions with modelled K_V distributions obtained using Equation 2.2-19 and experimental values of contact area (A_V^{cc}) and distance between surfaces ($l_{V,b}$), concluding that variations on A_V^{cc} are the main cause of K_V variations at chamber pressures lower than 30 Pa.

Other authors indicated that the impact of variations on $l_{V,b}$ was greater at increasing chamber pressures (e.g. Brülls and Rasmuson, 2002; Cannon and Shemeley, 2004). Indeed, at lower chamber pressures, the gas trapped tends to a free molecular regime, for which the distance between surfaces ($l_{V,b}$) does not impact the heat transfer. In contrast, at higher chamber pressures, the gas trapped tends to a continuous regime, for which the distance between surfaces impacts the heat transfer.

2.2.2.3. Presence of a Tray between the Shelf and the Container

Serum vials are arranged on a tray and framed by a rail before being charged on the freeze dryer. Once the vials are charged, the tray is removed in most cases, so the vials are placed directly on the shelf, and the rail is left to keep the vials in place during the drying cycle. However, in some freeze-drying protocols, the rail and the tray are left in the drying chamber, and the vials do not have direct contact with the shelf. Pisano et al. (2011) studied the impact of leaving the tray during freeze-drying, and determined the apparent heat transfer coefficient between the shelves and the vial bottom (K_V) with and without tray. Their work concluded that the tray represents a heat transfer resistance in series with K_V, as:

$$K_V = \left(\frac{1}{K_{shelf-tray}} + \frac{1}{K_{tray-vial}} \right)^{-1} \qquad \text{Equation 2.2-22}$$

where $K_{shelf-tray}$ (W.m^{-2}.K^{-1}) is the apparent heat transfer coefficient between the shelf and the tray, and $K_{tray-vial}$ (W.m^{-2}.K^{-1}) is the apparent heat transfer coefficient between the tray and the serum vial. Moreover, it was experimentally observed that placing a tray between the shelf and the vials reduced the heat transfer variations within the batch (Pisano et al., 2011).

2.2.2.4. Container Position: Edge Vial Effect

Several researchers pointed out that the position of the serum vials impacts the heat flow received during primary drying (e.g. Patel et al., 2010b; Pikal et al., 1984, 2016; Pisano et al., 2011; Rambhatla and Pikal, 2003; Schneid and Gieseler, 2008; Scutellà et al., 2017b; von Graberg, 2011; Wegiel et al., 2018). Figure 2.2-3 presents a common disposition of serum vials on the shelf surrounded by a containing rail. Vials situated at the borders of the shelf are commonly referred to as "edge vials" (red circles in Figure 2.2-3b), and vials surrounded by other vials are known as "central vials" (white circles in Figure 2.2-3b). Edge vials present higher heat flow rates during primary drying (hence higher product temperatures) than central vials, and this variation is known as "edge vial effect" or "edge effect" (Rambhatla and Pikal, 2003).

The standard explanation for the edge vial effect is that vials at the edge of the arrangement facing a rail, a chamber wall or a chamber door receive an "extra" heat contribution through their side faces. Traditionally, the edge vial effect is considered to be due to "extra" radiation received by edge vials from the chamber surfaces (Pikal et al., 1984; Pikal, 2000; Pikal et al., 2016a; Pisano et al., 2011; Rambhatla and Pikal, 2003; Schneid and Gieseler, 2008; Wegiel et al., 2018). However, Scutellà et al. (2017b) presented a 3D mathematical model of the heat transfer during ice sublimation, concluding that the main "extra" heat contribution from the chamber wall was transferred by gas conduction.

In practical situations, both radiation and conduction contribute to the edge vial effect, and their relative contribution is dependent on the exact configuration studied. According to the results obtained by Rambhatla and Pikal (2003), radiation shields of aluminium foil (placed on the chamber walls and door) reduced the difference in the sublimation rates between edge vials facing a chamber door and central vials by 55%, and reduced the difference between edge vials facing a chamber wall and central vials by 9%. Therefore, radiation shields were fairly effective for edge vials facing the chamber door, indicating that the edge effect for those vials has a considerable radiation contribution. However, for edge vials facing the chamber wall, the radiation shields had little impact, suggesting that gas conduction is the main mechanism behind the edge vial effect in this case, which is aligned with the results of Scutellà et al. (2017b). As a remark, radiation shields were intended to reduce radiation but may have also disturbed the conduction flow in an unknown (unstudied) way. It appears to be a disagreement between authors on how to define the edge vial effect: (i) either focusing on the influence of the chamber walls (e.g. Pisano et al., 2011; Scutellà et al., 2017b), or (ii) focusing on the influence of the chamber door (e.g. Rambhatla and Pikal, 2003; Wegiel et al., 2018). Therefore, it seems possible that different conclusions on which is the primary mechanism causing the effect could arise.

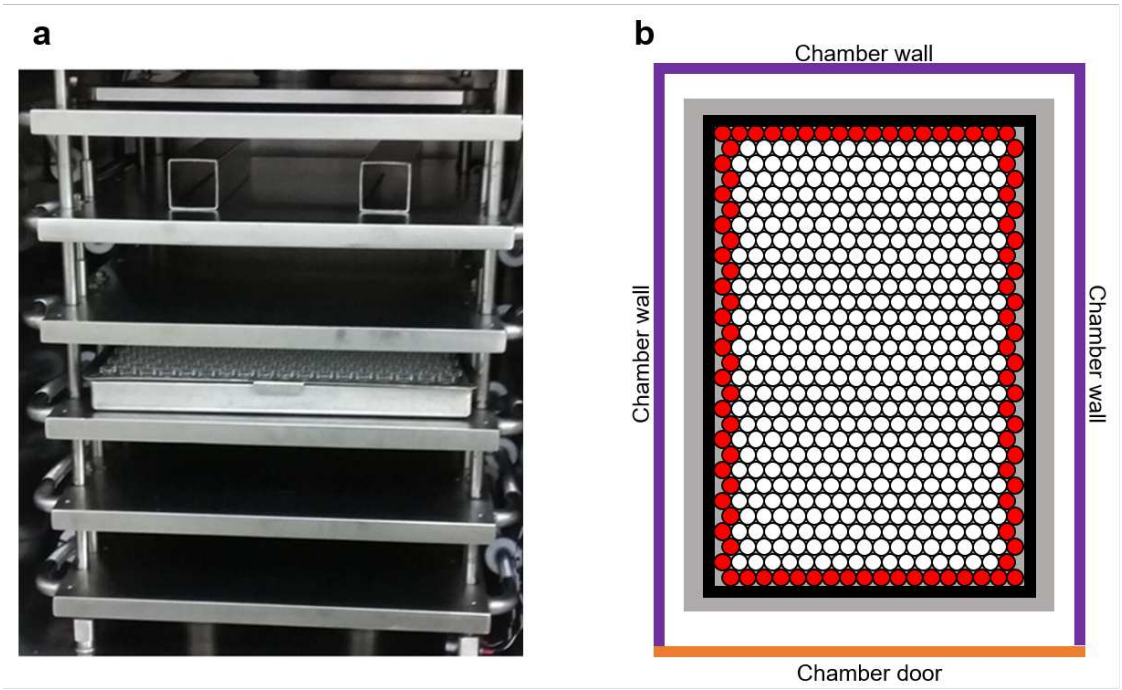

Figure 2.2-3 – Vials disposition on the shelf. (a) Lateral view of the shelves, vials and rail inside the chamber. (b) Schematic representation (not in scale) of the top view of the vials disposition on the shelf. The rail is represented as a black rectangle, edge vials are represented as red circles, and central vials are represented as white circles (adapted from Scutellà et al., 2017b).

2.2.3. Take-Home Message

The main four heat transfer mechanisms during primary drying were detailed in this section (i.e. contact conduction, solid conduction, gas conduction, and radiation). An apparent heat transfer coefficient between the shelf and the vial bottom (K_V*) was defined and mechanistically interpreted.*

Heat transfer variations among containers could entail differences in the product temperature within a batch or between batches during primary drying, and therefore cause quality heterogeneities. This Section 2.2 highlighted the main factors studied in the literature that cause such heat transfer variations: (i) the container type and geometry (i.e. shape, bottom curvatures, number of contact points, accommodation coefficients for gas conduction), (ii) the presence of a tray between the containers and the heating shelves, and (iii) the container position on the shelf.

2.3. Mass Transfer Modelling during Primary Drying

2.3.1. Mass Transfer Mechanisms

The sublimation mass flow during primary drying goes from the sublimation front (of each container) to the condenser. Figure 2.3-1 presents the most relevant mass transfer mechanisms within the gas phase during primary drying using serum vials, which are: (i) the mass flow through the dried product layer, (ii) the mass flow through the gap between the stopper and the vial neck, and (iii) the mass flow from the chamber to the condenser.

2.3.1.1. Mass Flow through the Dried Product Layer

The phase change at the sublimation front entails a pressure (P_{front}, Figure 2.3-1) higher than that of the vial's main gas volume (P_V, Figure 2.3-1). This pressure difference causes the circulation of vapour molecules from the sublimation front to the vial's main gas volume. As ice sublimates, the empty volume left behind by ice crystals become pores in the product layer. The gas diffusion through the pores in the dried product layer is responsible for the most significant pressure loss between the sublimation front and the condenser (Scutellà et al., 2018a).

The mass flow through the dried product is considered to occur under a free molecular regime due to the small distance between the dried product surfaces, i.e. pore size (lower than 0.2 mm; Oddone et al., 2016) and the low pressures in the matrix (the mean free path is 0.14 mm at 67 Pa; Pikal, 2000). Arguably, the most common approach in the freeze-drying community to model this mass transfer is that described by Pikal et al. (1983) based on the gas flow in capillaries. Another common approach was presented by Liapis and Litchfield (1979) based on the dusty-gas model (DGM), which considers the binary gas transport of the water vapour and the inert gas used to regulate the pressure in the chamber. The following paragraphs describe each approach used to model the mass transfer through the dried product layer.

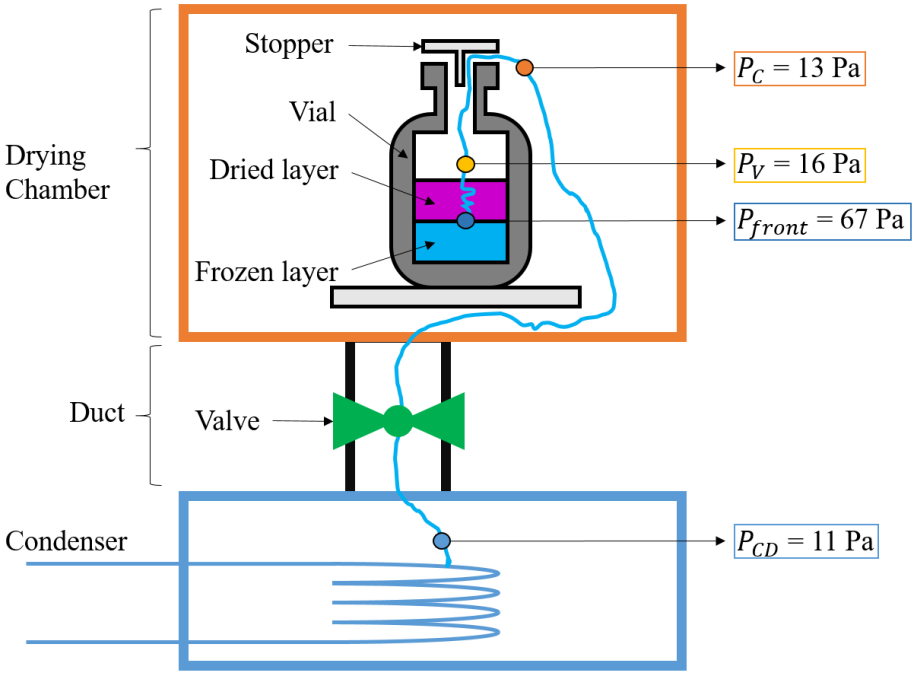

Figure 2.3-1 – Mass transfer in primary drying: schematic of resistances. Typical pressure values are given (adapted from Pikal, 1985). Note that the vapour-ice equilibrium pressure at the condenser temperature is lower than indicated, e.g. at -60 °C it would be 1.1 Pa.

Gas Flow in Capillaries

The shape of the pores does not follow a particular pattern and does not necessarily recall the shape of capillaries. Notwithstanding, Pikal et al. (1983) interpreted pores as a collection of capillaries due to the small diameter of the pores (e.g. smaller than 0.2 mm; Oddone et al., 2016) compared to the dry layer thickness (e.g. 10 mm, Scutellà et al., 2018a). In this vein, Pikal et al. (1983) presented an approach to determine the sublimation mass flow ($\dot{m}$, kg.s^{-1}) assuming: (i) pseudo-steady-state, (ii) one-directional flow, and (iii) the inner cross-sectional area of the container (A_{in}, m^2) as the mass transfer area. In this way, $\dot{m}$ could be considered proportional to the pressure loss through the dried product ($P_{front} - P_V$), as:

$$\dot{m} = \frac{A_{in}}{R_P} \times \left(P_{front} - P_V\right) \qquad (in\ capillaries) \qquad \text{Equation 2.3-1}$$

where P_{front} and P_V are expressed in Pa, and R_P (Pa.s.m^2.kg^{-1}) is the area-normalised product resistance to the mass transfer. Moreover, R_P is calculated based on kinetic theory of gases and assuming free molecular flow as (Pikal, 2000):

$$R_P = \sqrt{\frac{R\bar{T}}{W_{gas}}} \times l_d \times \frac{3\sqrt{\pi}}{4\sqrt{2}} \times \frac{\tau^2}{\phi r_{Pore}} \qquad (in\ capillaries) \qquad \text{Equation 2.3-2}$$

where τ (dimensionless) is the tortuosity, ϕ (dimensionless) is the porosity, r_{Pore} (m) is the average pore radius, $\bar{T}$ (K) is the average gas temperature, R (m^3.Pa.K^{-1}.mol^{-1}) is the ideal gas constant, W_{gas} (kg.mol^{-1}) is the molar mass of the gas, and l_d (m) is the dried product layer thickness.

Dusty-Gas Model

The pressure inside the drying chamber during primary drying is regulated using an inert gas (e.g. nitrogen, air). Some authors (e.g. Liapis and Litchfield, 1979; Mascarenhas et al., 1997; Nam and Song, 2005; Sheehan and Liapis, 1998) considered the inert gas in their mass transfer equations according to the dusty-gas model (DGM) proposed by Evans et al. (1962). The DGM describes the flow of two (or more) gases through a porous matrix, and it takes into account the contributions of diffusion and convection according to Darcy's Law (Darcy, 1856), as well as the Knudsen diffusion (Knudsen, 1909). According to the DGM, the mass flux rate of the vapour through the dried product ($\dot{M}_{H2O}$, kg.s^{-1}.m^{-2}) is calculated as:

$$\dot{M}_{H2O} = \frac{W_{H2O}}{RT}\left[\psi_{H20}\nabla P_{H2O} + \psi_B P_{H2O}\left(\nabla P_{H2O} + \nabla P_I\right)\right] \qquad \text{Equation 2.3-3}$$

where W_{H2O} (kg.mol^{-1}) is the molar mass of the water vapour, ψ_{H20} (m.s^{-1}) is the bulk diffusivity for the water vapour, ψ_B (m^4.N^{-1}.s^{-1}) is the self-diffusivity for both gases, P_{H2O} (Pa) is the partial pressure of the water vapour, and P_I (Pa) is the partial pressure of the inert gas.

Similarly, the mass flux rate of the inert gas through the dried product ($\dot{W}_I$, kg.s^{-1}.m^{-2}) is:

$$\dot{M}_I = \frac{W_I}{RT}[\psi_I \nabla P_I + \psi_B P_I(\nabla P_{H2O} + \nabla P_I)] \quad \text{Equation 2.3-4}$$

where W_I (kg.mol^{-1}) is the molar mass of the inert gas, and ψ_I (m.s^{-1}) is the bulk diffusivity for the inert gas.

It is possible to obtain Equation 2.3-1 for gas flow in capillaries (Pikal, 2000) based on Equation 2.3-3 for binary gas transport considering: (i) the partial pressure of the inert gas (P_I) in the porous layer is negligible compared to that of the vapour (P_{H2O}), (ii) the mass flow is one directional, (iii) A_{in} is the constant mass transfer cross area, (iv) $\bar{T}$ is the average gas temperature, and (v) steady-state. In this way, Equation 2.3-3 can be expressed as:

$$\dot{m} = A_{in} \times \dot{M}_{H2O} = A_{in} \times \left(\frac{W_{H2O}}{R\bar{T}} \times \frac{1}{l_d} \times \bar{D}_{H20}^{Kn}\right) \times (P_{sat} - P_V) \quad \text{Equation 2.3-5}$$

where $\bar{D}_{H20}^{Kn}$ is the Knudsen diffusivity for the vapour at $\bar{T}$. Note that in this case P_{sat} is equal to the pressure at the sublimation front (P_{front}). Equation 2.3-5 is commonly used in other fields of process engineering to describe diffusivity through porous media under a Knudsen regime (also knowns as the "Klinkenberg effect") (Carrigy et al., 2012; Cunningham and Williams, 1980; Kuila et al., 2012; Pant et al., 2012). Moreover, comparing Equation 2.3-1 and Equation 2.3-5, one can relate R_P to $\bar{D}_{H20}^{Kn}$ as:

$$R_P = \frac{R\bar{T}}{W_{H2O}} \times l_d \times \frac{1}{\bar{D}_{H20}^{Kn}} \quad \text{Equation 2.3-6}$$

2.3.1.2. Mass Flow through the Gap between the Stopper and the Vial Neck

Once the vapour escaped through the dried product, it reaches the free gas volume inside the vials at P_V. When vials do not have stoppers partially inserted into their necks, P_V is considered to be equal to the pressure inside the drying chamber (P_C, Figure 2.3-1). However, when stoppers are partially inserted into the vial necks, they entail a resistance to the mass transfer from the vial to the drying chamber and P_V greater than P_C. Similarly to Equation 2.3-1 for the mass flow through the dried product layer, the mass flow through the gap between the stopper and the vial neck ($\dot{m}$) is considered proportional to the pressure loss $(P_V - P_C)$ and inversely proportional to a mass transfer resistance (R_S, Pa.s.kg^{-1}) (Pikal, 1985):

$$\dot{m} = \frac{1}{R_S} \times (P_V - P_C) \quad \text{Equation 2.3-7}$$

Considering the total flow from the sublimation front to the condenser, several researchers pointed out that R_S does not play a significant role compared to R_P (Rambhatla et al., 2004; Scutellà et al., 2018a; X. C. Tang et al., 2006).

2.3.1.3. Mass Flow from the Drying Chamber to the Condenser

The molecules moving from the vial necks to the condenser may encounter several objects in their way (e.g. vials, shelves, chamber walls and door, ducts, valves). The mass flow in the drying chamber is commonly neglected, and the pressure inside the chamber is usually considered homogeneous (Pikal, 2000). However, the speed of the mass flow increases in the duct connecting the drying chamber and the condenser, because the duct is much narrower than the drying chamber (Petitti et al., 2013). The mass flow from the chamber to the condenser ($\dot{m}_{total}$, kg.s^{-1}) concerns all the containers in the drying chamber, and could be modelled (similarly to Equation 2.3-1 and Equation 2.3-7) as (Pikal, 2000):

$$\dot{m}_{total} = \frac{1}{R_{CD}} \times (P_C - P_{CD}) \qquad \text{Equation 2.3-8}$$

where R_{CD} (Pa.s.kg^{-1}) is the mass transfer resistance due to the duct between the drying chamber and the condenser, and P_{CD} (Pa) is the pressure at the condenser (Figure 2.3-1). Other more complex models than a constant R_{CD} were also used. For example, Trelea et al. (2015) considered a binary gas transport model (water vapour and inert gas), achieving a better prediction of the vapour pressure in the drying chamber compared to the predictions obtained with Equation 2.3-8.

Determining $\dot{m}_{total}$ is particularly important to avoid reaching a "choked flow" condition (Patel et al., 2010a). "Choked flow" occurs when the gas flow velocity through the duct reaches the speed of sound (Mach number = 1). In this case, an increase in the $\dot{m}_{total}$ would not be possible to be evacuated through the duct, causing an increase in the chamber pressure. When $\dot{m}_{total}$ is high enough to reach a "choked flow", the freeze dryer loses regulation of the chamber pressure. The "choked flow" condition depends on the geometry of the duct (and valves) connecting the chamber with the condenser. A deeper study of the impact of the duct geometry requires more complex models than Equation 2.3-8; for example, Alexeenko et al. (2009) studied the mass transfer through 2D mathematical modelling (computational fluid dynamics, CFD), focusing on how pipes in the duct could affect the mass flow.

2.3.1.4. Contribution of Desorption to the Mass Flow

Water removal by sublimation and desorption can occur in parallel during the primary drying step of freeze-drying. When ice crystals are removed by sublimation during primary drying, the sublimation front moves, leaving empty pores so the product phase in contact with the gas phase. While the gas inside the pore is saturated at the sublimation front (Scutellà et al., 2017a), it is not saturated in other regions where desorption can occur even if it is very slow at low temperatures encountered in primary drying (Pikal and Shah, 1990a). Different product regions in the same container or different containers in the same batch could be going through ice sublimation and water desorption at the same time. Overall the desorbed amount of water is four times less than the sublimed amount (Patel et al., 2010b). Moreover, with an Arrhenius equation for the temperature dependence of desorption and activation energy of ~29 $kJ.mol^{-1}$ (Trelea et al., 2016), the desorption is ~11 times slower at –25°C (typical shelf temperature during primary drying) than at +25 °C (typical shelf temperature during secondary drying). Therefore, most researches on primary drying neglect the contribution of the mass flow due to desorption (Konstantinidis et al., 2011; Liapis and Litchfield, 1979; Pikal, 1985; Scutellà et al., 2017a).

2.3.2. Relevant Factors for the Mass Transfer during Primary Drying

Operating conditions (i.e. shelf temperature and chamber pressure) are set to control the product temperature during primary drying. However, other factors impact the mass transfer and could affect the product temperature, causing quality heterogeneities within the batch or between batches. The limiting mass transfer mechanism during primary drying is that through the dried product layer, which is why this Section 2.3.2 will focus on R_P.

Ice crystals sublimate throughout primary drying, leaving empty pores in the dried product matrix. The pores sizes are identical to the ice crystals sizes obtained during freezing. Thus, the shape of the ice crystals impacts the structure of the dried product and R_p, so the freezing step will be addressed in the following discussion.

2.3.2.1. Formulation

Ice crystal growth depends on the physicochemical characteristics of the formulation (e.g. viscosity, freezing point) (Fan et al., 2019). Therefore, the size and shape distribution of ice crystals vary between formulations (ingredients and concentrations), and so do the pore size distributions and R_p values (Konstantinidis et al., 2011; Tang and Pikal, 2004). Moreover, the total concentration of all ingredients impacts the void volume or porosity, hence on R_p (Equation 2.3-2). For a same product, higher concentration values entail higher R_p values. Table 2.3-1 reports R_p values for common formulations found in the literature.

Table 2.3-1 – Area-normalised dried product resistances at a dried product layer thickness of 5 mm.

Product	R_P (kPa.s.m^2.kg^{-1}) for l_d = 5 mm	Nucleation		Container		Source
		T_n (°C)	Control	Filling depth (mm)	Inner diameter (mm)	
5% dextran aqueous solution	175	-2	Ice fog technique	7.5	29	Rambhatla et al. (2004)
	191	-7	Ice fog technique	7.5	29	Rambhatla et al. (2004)
3% mannitol, 2% sucrose aqueous solution	283	-2.4 to -4.1	Pressurization and depressurization	8.5	27	Konstantinidis et al. (2011)
5% mannitol aqueous solution	240	-2	Ice fog technique	7.5	29	Rambhatla et al. (2004)
	293	-7	Ice fog technique	7.5	29	Rambhatla et al. (2004)
	341	-11	Ice fog technique	7.5	29	Rambhatla et al. (2004)
	178	-2.3 to -3.7	Pressurization and depressurization	8.5	27	Konstantinidis et al. (2011)
	371	-8.0 to -15.9	Uncontrolled	8.5	27	Konstantinidis et al. (2011)

(Continued on the next page)

Continuation of Table 2.3-1.

Product	R_P (kPa.s.m^2.kg^{-1}) for l_d = 5 mm	Nucleation		Container		Source
		T_n (°C)	Control	Filling depth (mm)	Inner diameter (mm)	
5% sucrose aqueous solution	67	-1	Ice fog technique	7.5	29	Rambhatla et al. (2004)
	77	-6	Ice fog technique	7.5	29	Rambhatla et al. (2004)
	96	-11	Ice fog technique	7.5	29	Rambhatla et al. (2004)
	158	-10	Reduced pressure ice fog technique	7.5	18	Patel et al. (2009)
	149	-10	Reduced pressure ice fog technique	15	18	Patel et al. (2009)
	91	-2.4 to -3.7	Pressurization and depressurization	8.5	27	Konstantinidis et al. (2011)
	125	-7.2 to -16.6	Uncontrolled	8.5	27	Konstantinidis et al. (2011)
	92	-4	Nucleating agent (snomax 0.1 %)	10	15	Scutellà et al. (2018a)
10% sucrose aqueous solution	221	-10	Reduced pressure ice fog technique	7.5	18	Patel et al. (2009)
	202	-10	Reduced pressure ice fog technique	15	18	Patel et al. (2009)

2.3.2.2. Nucleation Temperature during Freezing

For a given formulation, the ice crystals size depends on the thermal history of the product during freezing. The nucleation temperature (T_n) has been traditionally linked to the ice crystal size (Fennema, 1973). Nucleation is a stochastic process, so T_n values differ among vials of the same batch or between batches, causing differences in the ice crystal sizes. In general, lower T_n values entail smaller ice crystals than higher T_n values (Geidobler and Winter, 2013; Nakagawa et al., 2006). This is why lower T_n values are related to product structures with smaller pores and greater R_p (Equation 2.3-2), and higher T_n values are related to greater pores and lower R_p (Searles et al., 2001a). Table 2.3-1 presents R_p values at different T_n.

Several methods have been developed to control nucleation and obtain consistent T_n values among containers (Assegehegn et al., 2019; Kasper and Friess, 2011; Morris and Acton, 2012; Nakagawa et al., 2006). Most of these methods induce nucleation by mechanically affecting the stability of the supercooled (or undercooled) solution and therefore generate nucleation sites simultaneously in all vials (e.g. ice fog freezing in Rowe, 1990; vacuum-induced surface freezing in Kramer et al., 2002; depressurization freezing in Otero and Sanz, 2000; gap freezing in Kuu, 2014). Mechanical methods have the disadvantage of requiring special equipment, which may not be compatible with all freeze dryers. Adding a nucleating agent to the formulation is a widely used technique to homogenize T_n among vials for research purposes, and it is compatible with all freeze dryers. Nucleating agents promote the crystallization by creating numerous nucleation sites, increasing the vial-averaged T_n value and reducing the vial-averaged R_P value. Nevertheless, nucleating agents may not be added to most real formulations such as vaccines, so the use of nucleating agents is for research purposes.

The cleanness of the container's surface also proved to have an impact on T_n. Particles on the container are potential nucleation sites; thus, cleaner surfaces present lower T_n values than those with particulate content (Searles et al., 2001b).

2.3.2.3. Annealing Step during Freezing

An annealing step can increase the size of the ice crystals obtained during freezing (Searles et al., 2001a; Shi et al., 2012). Annealing consists in maintaining the product at a temperature lower than the freezing point depression (point D in Figure 2.1-4) and higher than the glass transition temperature (points F and G in Figure 2.1-4a) (Searles, 2004). This step can be performed during the initial freezing of the product, after nucleation; however, it is most often performed after the initial freezing by increasing the shelf temperature, holding it, and decreasing it again (e.g. Abdelwahed et al., 2006; Lim et al., 2018). The ice crystals obtained after the first freezing melt at product temperatures higher than the glass transition temperature during the annealing step. Then, when the product temperature is lowered, water may crystallize as greater crystals than those obtained during the first freezing. This increase in the ice crystal size increases the pore size of the dried product layer and decreases R_P (Lu and Pikal, 2004).

2.3.2.4. Dried Product Layer Thickness

The dried product layer moves through the vial content during primary drying until all the ice crystals sublimate. Considering that the sublimation front remains flat and moves parallel to the vial bottom, the value of the dried product layer thickness (l_d, m) goes from 0 to the filling depth. Therefore, the length of the vapour's path from the sublimation front to the free gas volume inside the vial increases as primary drying proceeds. As l_d increases, vapour molecules may encounter more product structures on their way, so the resistance to the mass transfer (R_P) will also tend to increase.

According to Equation 2.3-2, R_p should be directly proportional to l_d. However, this mathematical relation between R_p and l_d may not be true due to two main factors: (i) variations in the pore size within the product, and (ii) non-flat sublimation fronts. Dried product structures are not necessarily homogenous, and the pore size may vary. Moreover, the shape of the sublimation front may not be flat and parallel to the vial bottom when the vial receives heat flows from the sides, and the curvature of the shape may vary during primary drying (Nam and Song, 2005; Sheehan and Liapis, 1998). Figure 2.3-2 shows the possible tendencies of R_p ploted as a function of l_d. The most common equation to relate R_p and l_d considering variations within the pore size distribution in a container is (Bosca et al., 2013; Konstantinidis et al., 2011; Rambhatla et al., 2004):

$$R_p = R_{p,0} + \frac{R_{p,1} \times l_d}{1 + R_{p,2} \times l_d} \qquad \text{Equation 2.3-9}$$

where $R_{p,0}$ (Pa.s.m^2.kg^{-1}), $R_{p,1}$ (Pa.s.m.kg^{-1}), and $R_{p,2}$ (m^{-1}) are coefficients related to the dried product structure. The value of $R_{p,0}$ embodies a possible "crust" on top of the product where the pore size is particularly smaller than in the rest of the dried product. $R_{p,1}$ represents the directly proportional relation between R_p and l_d theoretically expected (Equation 2.3-2). A positive $R_{p,2}$ (Figure 2.3-2a) could be explained by an increase in the pore size or an increase in the canalizations towards the bottom of the product. A negative $R_{p,2}$ (Figure 2.3-2b) could be explained by a decrease in the pore size or a decrease of the sublimation area towards the very end of primary drying, following the logic of a non-flat sublimation front. If $R_{p,2}$ is negligible ($R_{p,2}$ = 0 m^{-1}, Figure 2.3-2c), the pore size may be similar in all the product, except for a possible "crust" on top ($R_{p,0}$).

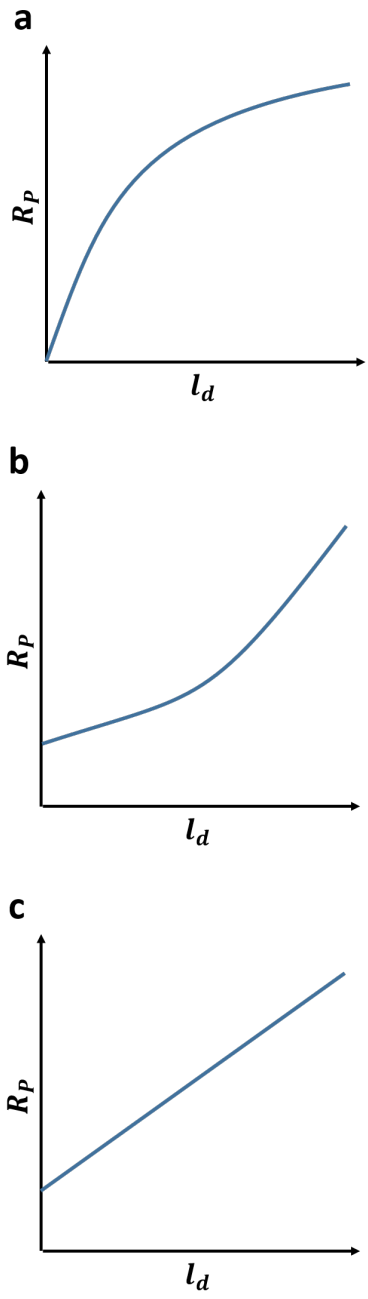

Figure 2.3-2 – Possible tendencies of the area normalised dried product resistance to mass transfer (R_P) vs the dried product layer thickness (l_d). (a) Representation of the tendency observed for a 5% sucrose solution or a 3% mannitol/2% sucrose solution frozen without controlling the nucleation temperature at approximately -3 °C (Konstantinidis et al., 2011). (b) Representation of the tendency observed for a 5% glycine solution (Gieseler et al., 2007). (c) Representation of the tendency observed for a 5% sucrose solution (Scutellà et al., 2018a).

2.3.2.5. Product Temperature Gradient during Freezing

The variations of the pore size distribution in the same vial are commonly attributed to the product temperature gradient in the product during freezing, which impacts the crystal growth (Arsiccio et al., 2018; Kurz and Fisher, 1989; Pisano and Capozzi, 2017). The temperature gradient could vary depending on each batch's freezing step (Hottot et al., 2007; Nakagawa et al., 2007) or the vial geometry (Rosa et al., 2016). The research on the freezing step of pharmaceutical freeze-drying consists almost exclusively of works using serum vials. Exceptionally, Hottot et al. (2009b) studied freezing in syringes (6 mm inner diameter, filling depth 7 mm) filled with a 5% sucrose aqueous solution. The morphology of the ice crystals obtained was studied through stereomicroscopy performed in a cold chamber, and these results were compared to those obtained using 3 mL serum vials. Unlike serum vials, ice crystals obtained in syringes presented a homogeneous size distribution. These results suggested an impact of the container on the freezing step, and ultimately on R_p.

2.3.2.6. Micro-Collapse

When the temperature of the product approaches the collapse temperature during primary drying, nanometric regions of the product can collapse and create tiny holes in the dried cake; this phenomenon is known as “micro-collapse” (Bosca et al., 2013; Kuu et al., 2011). Micro-collapse is not noticeable by visual inspection, but it can be observed at a microscopic scale. Overcashier et al. (1999) studied the structure of freeze-dried trehalose by Scanning Electron Microscopy (SEM), varying in the shelf temperature set during primary drying. The freeze-dried trehalose structure obtained at shelf temperature 10 °C presented more small holes (diameter smaller than 10 μm) than that obtained at shelf temperature -30 °C, suggesting that the greater product temperatures entailed by the higher shelf temperature caused a superior degree of micro-collapse. The small holes in the structure increase the pores' connectivity, reducing the dried product resistance to the mass transfer (Fissore and Pisano, 2015; Overcashier et al., 1999).

2.3.3. Take-Home Message

Throughout primary drying, the structure of the dried product matrix imposes a resistance to the mass transfer, which increases the pressure and temperature at the sublimation front. The greatest portion of the literature refers to the area-normalised product resistance to the mass transfer (R_P*) defined for the inner cross-sectional area of the container.* R_P *is considered independent of the operating conditions (i.e. shelf temperature and chamber pressure) in the absence of micro-collapse, but depends on the dried product matrix's characteristics (i.e. pore size, connectivity, and tortuosity), which in turn depend on the freezing conditions. This Section stressed five factors that could cause mass transfer variations: (i) the formulation, (ii) the nucleation temperature, (iii) an annealing step during freezing, (iv) the dried product layer thickness, and (v) micro-collapse.*

2.4. Coupled Heat and Mass Transfer Modelling of Primary Drying

2.4.1. Coupling Heat and Mass Transfer

According to the Quality by Design (QbD) approach, the dried cake's appearance is a Critical Quality Attribute (CQA) affected by the product temperature during primary drying, which is a Critical Process Parameter (CPP). Freeze dryers cannot regulate the product temperature directly; instead, the shelf temperature and chamber pressure are the two operating conditions that can be set.

Heat and mass transfer models of primary drying serve to relate the operating conditions with the product temperature. Several mathematical models have been developed consisting of the heat and mass transfer equations that govern the transfer mechanisms during primary drying. As different as most models might seem, they all share the same basic set of equations describing: (i) the heat transfer to the sublimation front, (ii) the mass transfer from the sublimation front to the condenser, and (iii) the coupling of heat and mass transfer at the sublimation front. The heat transfer to the sublimation front was described in Section 2.2.1, and the mass transfer from the sublimation front to the condenser was described in Section 2.3.1. The coupling of heat and mass transfer explains how the heat flow reaching the sublimation front ($\dot{Q}$, W) is related to the sublimation mass flow ($\dot{m}$, kg.s^{-1}). Under the hypothesis that all of the heat reaching the sublimation front is used for sublimation, $\dot{Q}$ and $\dot{m}$ are directly related in the simplest way as (Velardi and Barresi, 2008):

$$\dot{Q} = \Delta H \times \dot{m} \qquad \text{Equation 2.4-1}$$

where ΔH (J.kg^{-1}) is the latent heat of sublimation.

Mathematical models consider the solid phase (ice) and gas phase (vapour) in equilibrium at the sublimation front (e.g. Mascarenhas et al., 1997; Scutellà et al., 2017b; Trelea et al., 2007). This phase equilibrium serves to relate the saturation temperature (T_{sat}, K) with the saturated pressure (P_{sat}, Pa) at the sublimation front ($P_{front} = P_{sat}$) using the Clausius Clapeyron relation (Perry and Green, 2008):

$$T_{sat} = \frac{T_{triple}}{1 - \frac{RT_{triple}}{\widetilde{\Delta H_{sub}}} ln\left(\frac{P_{sat}}{P_{triple}}\right)} \qquad \text{Equation 2.4-2}$$

where T_{triple} (K) and P_{triple} (Pa) are the triple point temperature and pressure of the water respectively, R (J.K^{-1}.mol^{-1}) is the ideal gas constant, and $\widetilde{\Delta H_{sub}}$ (kJ.mol^{-1}) is the molar enthalpy of sublimation. Equation 2.4-2 links T_{sat} related to heat transfer with P_{sat} related to mass transfer and thus constitutes, together with Equation 2.4-1, the bridge between heat and mass transfer in primary drying.

2.4.2. Modelling Hypothesis

The mathematical resolution of the heat and mass transfer equations varies according to the author's hypothesis on the time dependency (i.e. transient-state or steady-state), the dimensions considered (i.e. 0D, 1D, 2D, or 3D), and the scale of the system considered (e.g. one container or all the containers in the freeze dryer). Depending on the simplifying hypothesis, the difficulty of the resolution (programming complexity) and calculation time varies greatly. Simplifications must be done considering the purpose of the model. An efficient or elegant model addresses the scientific question of interest while keeping calculations to the necessary minimum.

The author of this thesis grouped scientific questions on pharmaceutical freeze-drying according to the following topics:

(i) *Fundamental understanding*; aiming at developing, improving, and validating models to account for the product temperature, heat flows, and mass flows during primary drying.

(ii) *Process design*; revolving around the use of mathematical modelling to select the operating conditions during primary drying.

(iii) *Process variations*; focusing on how variations in the process (e.g. container type and geometry, container position, product freezing) could impact a CPP (e.g. product temperature).

(iv) *State estimation;* which refers to the use of mathematical modelling for in-line monitoring of CPP (e.g. product temperature) based on parameters that are easier to measure (e.g. mass flow).

Table 2.4-1 to Table 2.4-4 list works relevant for this thesis grouped according to their main research topic. Some scientific questions could involve more than one topic.

The following Sections 2.4.2.1 to 0 review common hypotheses used to address scientific questions similar to those of this thesis, focusing on how each hypothesis could be more or less useful to research on a particular topic.

*Table 2.4-1 – Mathematical models of primary drying for a **fundamental understanding of the process**. Adapted from Scutellà (2017), the table was updated for the present thesis.*

Source	Main innovation relevant for this thesis	Model		Container			Heat transfer from:			Mass transfer	Product
		D	Time dependency	Type	Fill depth (mm)	Inner diameter (mm)	bottom shelf	top shelf	chamber surfaces		
Liapis and Litchfield (1979)	Presented a transient model in 1D.	1D	Transient-state	Product slab on a holder	n.s.	n.s.	-	R	-	DGM	Not given
Liapis and Bruttini (1994)	Used a 1D transient model applied to a plate or tray.	1D	Transient-state	Plate or tray	20	n.s.	GC and R	n.s.	n.s.	DGM	Cloxacillin monosodium salt and skim milk
Mascarenhas et al. (1997)	Used a 2D transient model applied to a cylindrical geometry.	2D	Transient-state	Cylindrical geometry	3 and 6	n.s.	n.s.	n.s.	n.s.	DGM	Skim milk
Zhai et al. (2005)	Compared experimental and calculated heights of the sublimation front.	2D	Transient-state	Serum vial	18	20	GC	-	R	n.a.	Pure water
Nam and Song (2005)	Studied the shape of the sublimation front in various containers.	2D	Transient-state	Tray	20	n.s.	GC	R	-	DGM	Skim milk
				Cylindrical vial	20	10					
				Product without container	20	10, 20 and 30					

GC: gas conduction. R: radiation. DGM: dusty-gas model. "n.s.": not specified. "n.a.": not applicable.

"-": not considered.

*Table 2.4-2 – Mathematical models of primary drying for **process design**. Adapted from Scutellà (2017), the table was updated for the present thesis.*

Source	Main innovation relevant for this thesis	Model		Container			Heat transfer from:			Mass transfer	Product
		D	Time dependency	Type	Fill depth (mm)	Inner diameter (mm)	bottom shelf	top shelf	chamber surfaces		
Nail and Searles (2008)	Presented a design space.	0D	Steady-state	Serum vial	n.s.	n.s.	n.s.	n.s.	n.s.	n.s.	Not given
Koganti et al. (2011)	Presented a design space with operating conditions on the axis.	0D	Steady-state	Serum vial	n.s.	n.s.	CC, GC, and R	-	-	RP	Pfizer A
Scutellà et al. (2018b)	Presented a multi-vial model capable of predicting the percentage of accepted vials.	0D	Transient-state	Serum vial	10	15	CC, GC, and R	R	-	RP	5% w/w aqueous sucrose solution

CC: contact conduction. **GC**: gas conduction. **R**: radiation. **RP**: based on the area-normalised dried product resistance (R_P). "n.s.": not specified. "-": not considered.

*Table 2.4-3 – Mathematical models of primary drying for studying **process variations**. Adapted from Scutellà (2017), the table was updated for the present thesis.*

Source	Main innovation relevant for this thesis	Model		Container			Heat transfer from:			Mass transfer	Product
		D	Time dependency	Type	Fill depth (mm)	Inner diameter (mm)	bottom shelf	top shelf	chamber surfaces		
Pikal et al. (1984)	Studied geometric variations of the same container type.	0D	Steady-state	Serum vial	20	22, 27, 29, and 43	CC, GC, and R	R	-	RP	Pure water, dobutamine hydrochloride-mannitol solution, and KCl solution
Millman et al. (1985)	Studied the impact of the filled height on the speed of the moving sublimation front.	1D	Transient-state	Not given	3, 4,5, 6, 9, 12, and 15	n.s.	GC and R	GC and R	-	DGM	Skim milk
Sheehan and Liapis (1998)	Studied the impact of lateral heat contributions on the heat and mass transfer and the shape of the sublimation front.	2D	Transient-state	Serum vial	7, 12, and 22	10	GC	R	R	DGM	Skim milk
Brülls and Rasmuson (2002)	Studied the impact of the vial geometry (glass thickness and bottom curvature) and filled height on the heat transfer.	2D	Transient-state	Serum vial	21	24	GC and R	-	n.s.	n.a.	Pure water
Gan et al. (2005)	Studied the impact of using trays with sides on the heat transfer and the shape of the sublimation front.	2D	Transient-state	Serum vial	16	14	GC	R	R	DGM	Skim milk

(Continued on the next page)

CC: contact conduction. **GC**: gas conduction. **R**: radiation. **RP**: based on the area-normalised dried product resistance (R_P). **DGM**: dusty-gas model. "n.s.": not specified. "n.a.": not applicable. "-": not considered.

Continuation of Table 2.4-3.

Source	Main innovation relevant for this thesis	Model		Container			Heat transfer from:			Mass transfer	Product
		D	Time dependency	Type	Fill depth (mm)	Inner diameter (mm)	bottom shelf	top shelf	chamber surfaces		
von Graberg, (2011)	Studied the heat transfer resistance between the shelf and the high-throughput vial bottoms of different containers.	0D	Steady-state	96-Well PCR-plates	n.s.	5	CC, GC, and R	R	-	n.a.	Pure water
				High-throughput system	n.s.	5					
				Serum vial	0.2 and 0.5	14					
Pisano et al. (2011)	Considered the impact of a tray between the shelf and the serum vials on the heat transfer from the shelf below.	0D	Steady-state	Serum vial	n.s.	12, 15 and 22	CC, GC, and R	R	-	n.a.	Pure water
Scutellà et al. (2017a)	Studied the impact of the vial geometry (bottom curvature and contact area) on the heat transfer coefficient between the shelf and the vial bottom and on the product temperature.	0D	Steady-state	Serum vial	10	15	CC, GC, and R	R	-	RP	Pure water and 5% w/w aqueous sucrose solution
Scutellà et al. (2017b)	Studied the impact of the vial position using 3D modelling.	3D	Steady-state	Serum vial	9	15	CC, GC, and R	GC and R	GC and R	n.a.	Pure water

CC: contact conduction. **GC**: gas conduction. **R**: radiation. **RP**: based on the area-normalised dried product resistance (R_P). **DGM**: dusty-gas model.

"n.s.": not specified. "n.a.": not applicable. "-": not considered.

*Table 2.4-4 – Mathematical models of primary drying for **state estimation**. Adapted from Scutellà (2017), the table was updated for the present thesis.*

Source	Main innovation relevant for this thesis	Model		Container			Heat transfer from:			Mass transfer	Product
		D	Time dependency	Type	Fill depth (mm)	Inner diameter (mm)	bottom shelf	top shelf	chamber surfaces		
Chouvenc et al. (2004)	Used the Pressure Rise Analysis (PRA), a method to monitor the product temperature in-line.	0D	Transient-state	Tubing vial	10	14	CC, GC, and R	n.s.	R	RP	5% w/w aqueous mannitol solution
X. Tang et al. (2006)	Studied the factors that could cause systematic errors when using the Manometric Temperature Measurement (MTM) method to monitor the product temperature in-line.	0D	Transient-state	Serum vial	7	19	n.s.	n.s.	R	RP	5% w/v sucrose or 5% w/v glycine aqueous solutions
Velardi et al. (2008)	Used the Dynamic Parameters Estimation (DPE) method to monitor the product temperature in-line.	0D	Transient-state	Tubing vial	7.1	14.25	n.s.	n.s.	R	RP	10% w/w sucrose or 5% w/w bovine serum albumin aqueous solutions
					9.9	20.85					
Fissore et al. (2010)	Studied how the calculated product temperature is impacted by the mathematical model selected (i.e. MTM, PRA, DPE)	0D	Transient-state	Tubing vial	7.21	14.25	n.s.	n.s.	R	RP	10% w/w aqueous sucrose solution

CC: contact conduction. **GC**: gas conduction. **R**: radiation. **RP**: based on the area-normalised dried product resistance (R_P). "n.s.": not specified.

2.4.2.1. Transient-state vs Steady-state

The sublimation front moves through the product during the primary drying step of freeze-drying. The vapour's path through the dried product layer varies during primary drying, affecting the heat and mass transfer. Therefore, heat and mass transfer is, in essence, a transient process. Several authors reflected this transient-state in their models by considering time dependency in their equations (e.g. Brülls and Rasmuson, 2002; Liapis and Litchfield, 1979; Mascarenhas et al., 1997; Scutellà et al., 2018b).

Primary drying could last up to several days (Shukla, 2011); however, the characteristic times of the heat and mass transfer phenomena are considerably shorter (minutes or faster) (Lopez-Quiroga et al., 2012). For example, Table 2.4-5 presents the characteristic time of the typical heat and mass transfer phenomena that could take place during primary drying. At short time scales (minutes or less), primary drying could be considered as a succession of heat and mass transfer pseudo-equilibria. Several authors focused their research on particular moments of primary drying (e.g. beginning, an intermediate point, and end) and considered heat and mass transfer to be in a pseudo-steady-state or equilibrium (e.g. Pikal, 2000; Pisano et al., 2011; Scutellà et al., 2017a).

Transient-state and steady-state models exhibit practical advantages and disadvantages for researchers. On the one hand, transient-state models are better at identifying the most critical stages of the process, while steady-state models require previous knowledge of the system's behaviour to select the most interesting stages to be modelled. On the other hand, transient-state models are harder to solve than steady-state models, requiring more sophisticated calculation algorithms and more calculation time. Moreover, transient-state models offer results at different times (big data sets), so data treatment is more time-consuming than for steady-state models.

The selection of a transient-state or a steady-state model depends on the aim of our research. For the sake of an example, let us suppose we aimed at studying the impact of geometric variations of the serum vial bottom on the heat transfer from the shelf to the serum vial. Brülls and Rasmuson (2002) considered a transient-state model to evaluate the product temperature variations caused by using 2 serum vials with different bottom curvatures, and noticed that the maximal temperature difference was right after the beginning of primary drying. Hence, the work of Brülls and Rasmuson (2002) identified the critical stage when variations were greater. In contrast, Scutellà et al. (2017a) used a steady-state model to calculate the product temperature distribution at a certain stage of primary drying for 120 serum vials with different bottom curvatures. Scutellà et al. (2017a) obtained results that may have a greater statistical validity (more vials were sampled) than those of Brülls and Rasmuson (2002). However, previous knowledge of the system's behaviour is required to generalise the results of Scutellà et al. (2017a) during other stages of primary drying. While transient-state models were mostly used for the fundamental understanding of primary drying (Table 2.4-1), both transient-state and steady-state models were used for process design (Table 2.4-2) and the study of process variations (Table 2.4-3).

Table 2.4-5 – Characteristic times of the freeze-drying phenomena. (Adapted from Lopez-Quiroga et al., 2012)

Phenomena	Order of magnitude
Heat transfer in the dried product layer	Minutes
Heat transfer in the frozen product layer	Seconds
Heat transfer in the vapour phase	Milliseconds
Mass transfer in the vapour phase	Milliseconds

Transient-state models are particularly relevant for state estimation (Table 2.4-4). The most common methods used to estimate the product temperature in-line are the Manometric Temperature Measurement (MTM) (Milton et al., 1997; Pikal et al., 2005; Tang et al., 2005), the Pressure Rise Analysis (PRA) (Chouvenc et al., 2004), and the Dynamic Parameters Estimation (DPE) (Velardi et al., 2008). These methods require disturbing the system during a negligible period (usually less than a minute) by closing the valve connecting the drying chamber and the condenser; this causes an increase in the chamber pressure due to the sublimation mass flow that accumulates vapour in the chamber. Mathematical models are used to estimate the product temperature based on the pressure rise in the chamber, and must be solved in transient-state since the chamber pressure varies in time. Each method (MTM, PRA, DPE) differs in the algorithms used to treat the pressure rise signal. Overall, mathematical models applied for state estimation allow researchers to estimate the product temperature without using invasive methods, such as thermocouples or probes, that could bias the results.

2.4.2.2. Various Geometric Dimensions (1D to 3D) vs Lumped-Parameter (0D)

Heat and mass transfer models refer to the behaviour of real bodies in space (3D). However, solving heat and mass transfer equations in a 3D geometry is a labour-intensive task that involves complex calculation algorithms and even specific software. To the best of this author's knowledge, Scutellà et al. (2017b) is the only work that used 3D modelling to study the heat transfer during ice sublimation (vials contained water only, not a product).

3D geometries can be simplified into 2D or 1D geometries. Some authors (e.g. Mascarenhas et al., 1997; Sheehan and Liapis, 1998; Zhai et al., 2005) considered vials as cylindrical bodies of revolution, modelling the geometry of the vial and content using 2D (height and radius directions). Other authors (e.g. Liapis and Litchfield, 1979; Millman et al., 1985) neglected the heat contributions received at the side of the container, so the heat and mass transfer would be one-directional. Under this assumption, the heat and mass transfer in the container could be modelled using a 1D (vertical direction) model.

Non-dimensional models – also known as "0D" or "lumped-parameter" models – simplify the spatial distribution of the variables or parameters (e.g. temperatures, heat flux, mass flux) into discrete values that encompass the behaviour of one or several objects or regions of interest (e.g. vial bottom, shelf surface, sublimation front, among others) (Pikal, 2000; Pisano et al., 2011; Scutellà et al., 2017a; von Graberg, 2011). In this manner, equations are no longer solved "in space", and only the value of the discrete variables or parameters is calculated. For example, Velardi and Barresi (2008) presented a 0D heat and mass transfer model for primary drying considering two temperature values in the container: (i) the vial bottom temperature, and (ii) the temperature at the sublimation front.

Solving heat and mass transfer equations in 1D, 2D, and 3D geometries imply different numerical calculation methods. These methods discretise the geometry into a finite collection of points where equations are solved (Nam and Song, 2005). 0D models already contain spatially discrete parameters, so their "geometry" could be mathematically considered as a finite collection of one point. Calculation times increase with an increasing number of points required to discretize the geometry. The number of points tends to rise from 0D models to 1D, 2D and 3D, and calculation times increase following the same tendency.

2D and 3D models are mostly used to address scientific questions on fundamental understanding (Table 2.4-1) and process variations (Table 2.4-3) involving lateral flows reaching the container (Hottot et al., 2007; Zhai et al., 2005). 2D and 3D models entail long calculation times (e.g. one hour; Scutellà et al., 2017b); hence these models are commonly used to represent no more than a handful of different scenarios. For example, to explain how the heat from the chamber impact the heat and mass transfer during primary and secondary drying, Sheehan and Liapis (1998) used two 2D geometries: (i) a vial in the centre of the shelf surrounded by other vials, and (ii) a vial in the edge of the disposition facing a chamber surface.

The amount of data obtained with 0D models is less extensive than that of 1D, 2D and 3D models, simplifying the data treatment and the interpretation of the results. 0D models are particularly useful for addressing scientific questions that require comparing numerous conditions, such as the case of process design (Table 2.4-2) and the study of process variations (Table 2.4-3). For example, Pisano et al. (2013) used a 0D heat and mass transfer model to simultaneously study the impact of heat transfer variations among vials and the impact of the operating conditions. Moreover, fewer data simplifies the physical understanding of the system; thus, 0D models are commonly used for state estimation (Table 2.4-4).

2.4.2.3. Spatial Extension of the Model

The extension of a system of interest could go from a particular product region (e.g. a portion of the dried product layer and frozen layer) to the entire freeze dryer with all containers. The definition of the spatial limits of the system depends on the scientific question to be studied. The spatial extension of the model should be reduced as much as possible to simplify the model's equations and reduce calculation times. Finding a compromise between physical validity, mathematical complexity, and spatial extension is paramount to achieving an efficient model.

Assuming symmetry planes is an advantageous hypothesis to reduce the spatial extension of a model. For example, Scutellà et al. (2017b) studied how the serum vial position on the shelf impacts the heat transfer during ice sublimation. To do so, Scutellà et al. (2017b) presented a 3D geometry consisting of a fragment of the freeze dryer, four half-vials, and one quarter-vial. This fragment was considered representative of the drying chamber due to vertical symmetry planes between vials on the shelf, and horizontal symmetry planes between shelves. For a particular fragment of the system, a symmetry plane dividing two regions is mathematically analogous to neglecting the heat and mass exchange between regions. In this vein, several models were developed for vials in the centre of the shelf, neglecting the heat coming from other vials, therefore assuming symmetry planes between vials (e.g. Pikal, 2000; Pisano et al., 2011).

When a scientific question requires a wide spatial extension, the spatial complexity is usually compensated by considering 0D heat and mass transfer equations for individual containers (vials) to simplify calculations. For instance, most models related to process design (Table 2.4-2) or state estimation (Table 2.4-4) are spatially extended to include the drying chamber and condenser; therefore, equations for these models are commonly solved in 0D for the containers (vials) (Fissore et al., 2011; Giordano et al., 2011; Nail and Searles, 2008; Trelea et al., 2015; Velardi et al., 2008).

2.4.3. Design Space: a Widespread 0D Steady-State Model in view of Quality by Design

The QbD approach requires designing the process while considering the final product quality. In other words, the operating conditions need to be selected so the dried cake appearance will be acceptable; hence the product temperature during primary drying must remain lower than the collapse temperature. Process design requires comparing several combinations of operating conditions and the product temperature reached, which involves many simulations to be run. A 0D steady-state model is commonly used for process design purposes due to its fast calculation times and the reduced amount of data to be processed (Fissore et al., 2011; Giordano et al., 2011; Nail and Searles, 2008; Patel and Pikal, 2013). Solving the 0D steady-state model requires an iterative loop that makes it hard to directly see the connection between the operating conditions and the product temperature. A graphic solution of the 0D steady-state model was proposed by Nail and Searles (2008) to provide a visual understanding of the system's behaviour and simplify the selection of the operating conditions. This graphic solution is commonly referred to as the "design space" for primary drying.

The construction of the design space requires understanding the meaning of the equations composing the 0D steady-state model. Mathematically, the 0D steady-state model consists of a system of equations relating: (i) the two operating conditions (shelf temperature, T_{shelf}; and chamber pressure, P_C), (ii) the critical process parameter (CPP; product temperature, T_b), and (iii) a variable related to the optimization of the process duration (sublimation mass flow, $\dot{m}$). This system of equations has two degrees of freedom, meaning that, when setting the values of two, the values of the third degree is determined.

Design spaces express the solution of the 0D steady-state model through different graphic presentations – viz. the mathematical connection between four parameters: T_{shelf}, P_C, T_b, and $\dot{m}$. Figure 2.4-1 shows two examples of design space presentations. The axis of a design space embody the values of two parameters, while the other two parameters are represented as iso-parametric curves. For example, Nail and Searles (2008) (Figure 2.4-1a) proposed placing the values of P_C and $\dot{m}$ in the axis, and Pisano et al. (2013) (Figure 2.4-1b) placed the values of P_C and T_{shelf}. Design spaces present curves that relate the values in the axis by considering a third parameter (iso-parameter) as fixed. In this fashion, Nail and Searles (2008) plotted iso-T_{shelf} curves (green dashed curves in Figure 2.4-1a) by expressing $\dot{m}$ as a function of P_C and a fixing T_{shelf}, and iso-T_b curves (red dashed curves in Figure 2.4-1a) by fixing T_b. Similarly, Pisano et al. (2013) plotted iso-sublimation mass flow curves (expressed as $\dot{m}$ per vial inner cross-sectional area; grey dashed curve in Figure 2.4-1b) by expressing T_{shelf} as a function of P_C and a fixing $\dot{m}$, and a iso-T_b curve (red dashed curve in Figure 2.4-1b) by fixing or T_b. The value of the parameters in a design space are limited by: (i) the minimal T_{shelf} value for sublimation can occur, (ii) the minimal P_C value reached by the freeze dryer, (iii) the maximal $\dot{m}$ value that would not "choke" the flow in the duct between

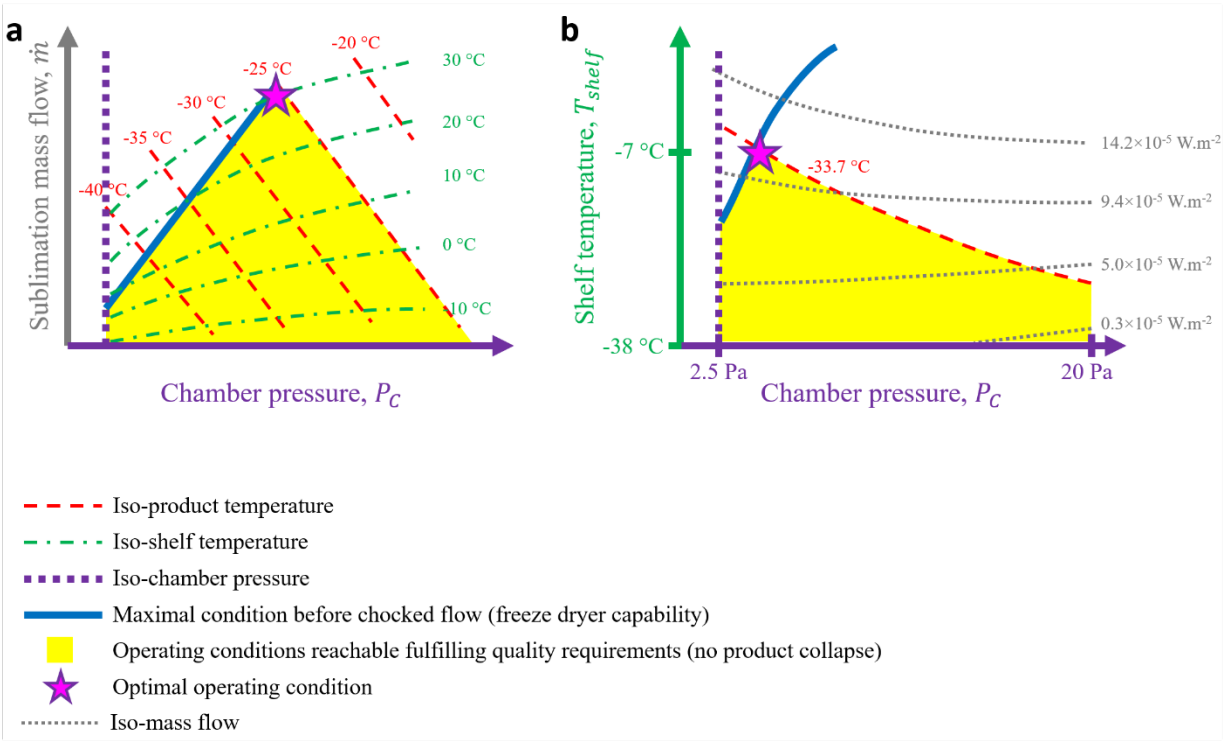

Figure 2.4-1 – (a) Design space adapted from Nail and Searles (2008). (b) Design space adapted from Pisano et al. (2013) for a mixture of sucrose and amino acids (total solid content 9% w/w).

the drying chamber and the condenser (so-called "freeze dryer capability"), and (iv) the maximal T_b value so the product does not collapse (T_c). Design spaces present an area (yellow areas in Figure 2.4-1) where all parameters are within the admissible limits. Ultimately, design spaces let visually identify the values of T_{shelf} and P_C (pink stars in Figure 2.4-1) that maximize $\dot{m}$ to accelerate the process, while maintaining T_b lower than T_c to obtain an elegant (non collapsed) dried cake. In other words, design spaces simplify the task of optimizing production while maintaining product quality.

One of the main shortcomings of design spaces is the difficulty to represent heat and mass transfer variations among vials. To address this difficulty, Mortier et al. (2016) introduced the uncertainty of heat and mass transfer coefficients, geometric parameters, and operating conditions. Their work offers a design space depending on the risk of failure acceptance levels. Another shortcoming of design spaces is their incapacity to represent different stages (or moments) during primary drying, since it is based on a steady-state model. Fissore et al. (2011) introduced a design space for primary drying that considers different dried product resistances (R_P), that could be interpreted as the time passage during primary drying, as the dried product layer forms and R_P increases.

Recently, other graphical tools similar to the designs space for primary drying have been used to simplify decision making in other research areas of freeze-drying. Pisano et al. (2012) presented a design space for secondary drying, optimising the operating conditions during this step. Arsiccio et al. (2018) built a design space to relate the shelf temperature during ice crystal growth, the holding time of this shelf temperature and the average ice crystal size; this design space could be particularly useful to design the freezing step.

2.4.4. Take-Home Message

Mechanistic modelling is the key to predicting the product temperature (T_p) and understanding how the operating conditions (i.e. shelf temperature and chamber pressure) and process variations (e.g. container type, geometry, or position) impact the final product quality. Models consist of heat and mass transfer equations. The resolution of these equations requires hypotheses on: (i) the time dependency of the parameters (i.e. transient-state, steady-state), (ii) the dimensions considered (from 0D to 3D), and (iii) the spatial extension of the model (e.g. just one vial, or the entire chamber and condenser). Efficient and elegant models are those whose hypotheses allow researchers to address the relevant scientific question while simplifying the equations and reducing calculation times.

3. Experimental Strategy

As previously established in Section 2, this thesis focused on the following scientific questions:

- Question 1: "*How could we identify the operating conditions that entail the same product temperature during primary drying in high-throughput systems and serum vials?"*
- Question 2: "*What are the main factors responsible for product quality variations during primary drying in high-throughput systems?*"

These scientific questions were addressed considering mathematical models of the heat and mass transfer during primary drying. Furthermore, models were developed, validated and analysed in the light of relevant bodies of acquired experimental data. The following Section 3.1 presents an overview of the modelling and experimental strategies followed to address Question 1, while Section 3.2 summarises the strategies to address Question 2.

3.1. Question 1: Translation of the Operating Conditions

The process design of the primary drying step of freeze-drying is commonly carried out using a lumped-variable (0D) steady-state heat and mass transfer model (Section 2.4, Table 2.4-2). This model allows one to easily relate the operating conditions (i.e. shelf temperature and chamber pressure) with the product temperature using an effective heat transfer coefficient between the shelf and the container (K_V) and an effective dried product resistance to the mass transfer (R_P). As it was previously discussed in the Literature Review, the container type could affect K_V (Section 2.2.2.1) and R_P (Section 2.3.2.5). Thus, the operating conditions must be modified ("translated") to obtain the same product temperature when using high-throughput or serum vials. To build the mathematical models for the translation, K_V and R_P for high-throughput vials were determined in this thesis, as represented in Figure 3.1-1.

K_V values in high-throughput systems were determined by gravimetric analysis during ice sublimation tests, considering 360 high-throughput vials with a maximal filling volume of 500 µL, and 360 high-throughput vials with a maximal filling volume of 1000 µL (upper blue rectangle in Figure 3.1-1). The gravimetric analysis method and data treatment to calculate K_V are detailed in Section 4.1.3 (Materials and methods). The effective K_V values were used to predict the product temperature using the 0D steady-state model originally developed for serum vials and considering a R_P value taken from the literature. Moreover, K_V values and product temperatures in high-throughput vials were compared with those previously determined for serum vials. Given the popularity of the design space approach and the use of response surfaces for process design, a graphic tool was proposed to simultaneously solve the 0D steady-state model for high-throughput and serum vials. The graphic tool connects the operating conditions that entail the same product temperature in both container types, and represents a proof of concept to scale-up high-throughput screening results to a serum vial production scale. The results of this investigation are reported in Section 4.1.3 (Results and discussion).

R_P values for a 5% (w/w) sucrose aqueous solution ("model" product) were determined by pressure rise tests using high-throughput systems and serum vials (lower red rectangle in Figure 3.1-1). A detailed description of the pressure rise test and the data treatment implemented is presented in Section 4.4.3 (Pressure rise test). Finally, the 0D steady-state model was validated by calculating the product temperature at the vial bottom (T_b) and comparing these results with the temperature registered during primary drying using thin thermocouples touching the vial bottom (red rectangle in Figure 3.1-1). The results for this validation are shown in Section 4.4.3 (Results and discussion).

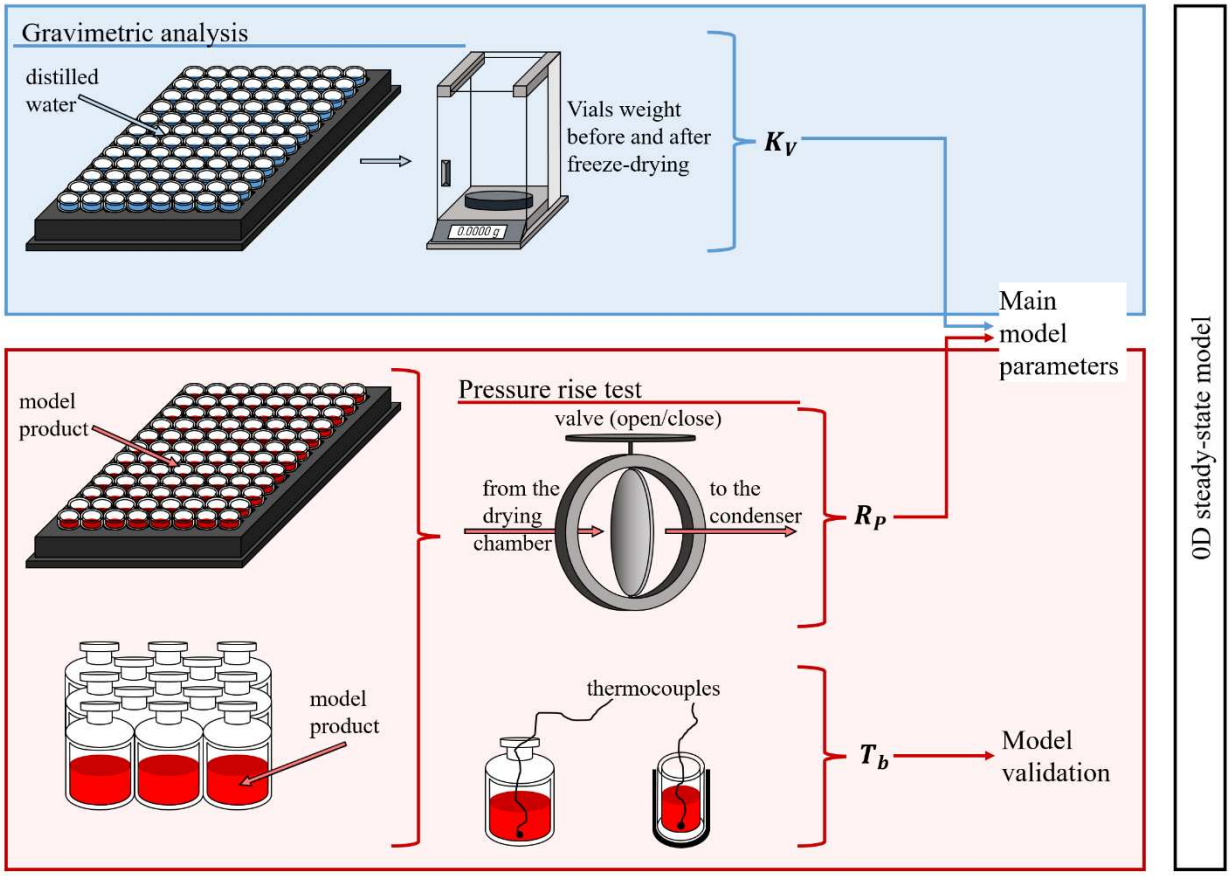

Figure 3.1-1 – Schematic of the experimental strategy to address Question 1: "How could we identify the operating conditions that entail the same product temperature during primary drying in high-throughput systems and serum vials?". These experiments served to develop a mathematical model to translate the operating conditions between high-throughput and serum vials, determining the most sensitive parameters (i.e. K_V and R_P) and obtaining data for validation. Experiments in the blue square are detailed in Section 4.1.3. Experiments in the red square are detailed in Section 4.4.3.

3.2. Question 2: Factors Responsible for Product Quality Variations

Based on the Literature Review (Sections 2.2.2 and 2.3.2), five factors were initially considered in this thesis to potentially cause variations in the heat and mass transfer between high-throughput vials: (i) the variability of the well plate bottom finish and well surfaces; (ii) the variability of the high-throughput vial bottom; (iii) the position of the vials in the well plate; (iv) the position of the well plate on the shelf; and (v) the variability of the nucleation temperature. Figure 3.2-1 presents the experimental strategies followed to investigate these five factors.

Regarding the impact of the well plate bottom and well surfaces on the heat transfer, two well plate types were considered in this thesis, each type presenting a different surface finish (brilliant black or matte black). The apparent heat transfer coefficient between the shelf and the well plate (K_{WP}) was determined for each well plate type by gravimetric analysis before and after ice sublimation tests using well plates without vials ("i" in Figure 3.2-1). Furthermore, the apparent heat transfer coefficient between the wells and the vials (K_{HV}) was calculated for each high-throughput vial size (500 or 1000 µL) and well plate type based on the effective K_V and K_{WP}. The heat transfer mechanisms responsible for the variations between well plate types were identified using mechanistic models of K_{WP} and K_{HV} – analogous to the mechanistic model of K_V in serum vials (Section 2.2.1.5). K_{WP} and K_{HV} are physically related to K_V, so K_{WP} was used to interpret how the variability of the well plate bottom affects K_V, while K_{HV} served to study how the variability of the well surfaces affects K_V. The detailed description of the materials and methods used, the theoretical framework, and the results are presented in Section 4.1.3.

The impact of the vial bottom on K_V is attributed in the literature to the vial bottom concavity (l_{HV}) and the contact area (A_{HV}^{cc}) (Section 2.2.2.2). l_{HV} of 192 vials was determined at high precision ("ii.1" in Figure 3.2-1). Moreover, A_{HV}^{cc} of 96 vials was determined by the imprint method ("ii.2" in Figure 3.2-1), consisting in measuring the area of the imprint left on a white paper when placing each vial bottom covered on a thin layer of black ink. K_V distributions were calculated based on mechanistic models of K_{WP} and K_{HV}, A_{HV}^{cc}, and l_{HV}. Calculated K_V distributions were compared to experimental K_V distributions to check if the variation on the vial bottom geometry could explain K_V variations. The results of this investigation are presented in Section 4.1.3.

3D mathematical modelling was employed to study how the position of high-throughput vials in the well plate could impact the heat flow received during primary drying. A 3D model for the heat transfer during ice sublimation (*distilled water model*) was proposed to calculate the heat flow rates received by eight representative vials inside a well plate in the centre of the shelf. This model was validated using experimental heat flows during ice sublimation tests ("iii" in Figure 3.2-1), and served to illustrate the initial

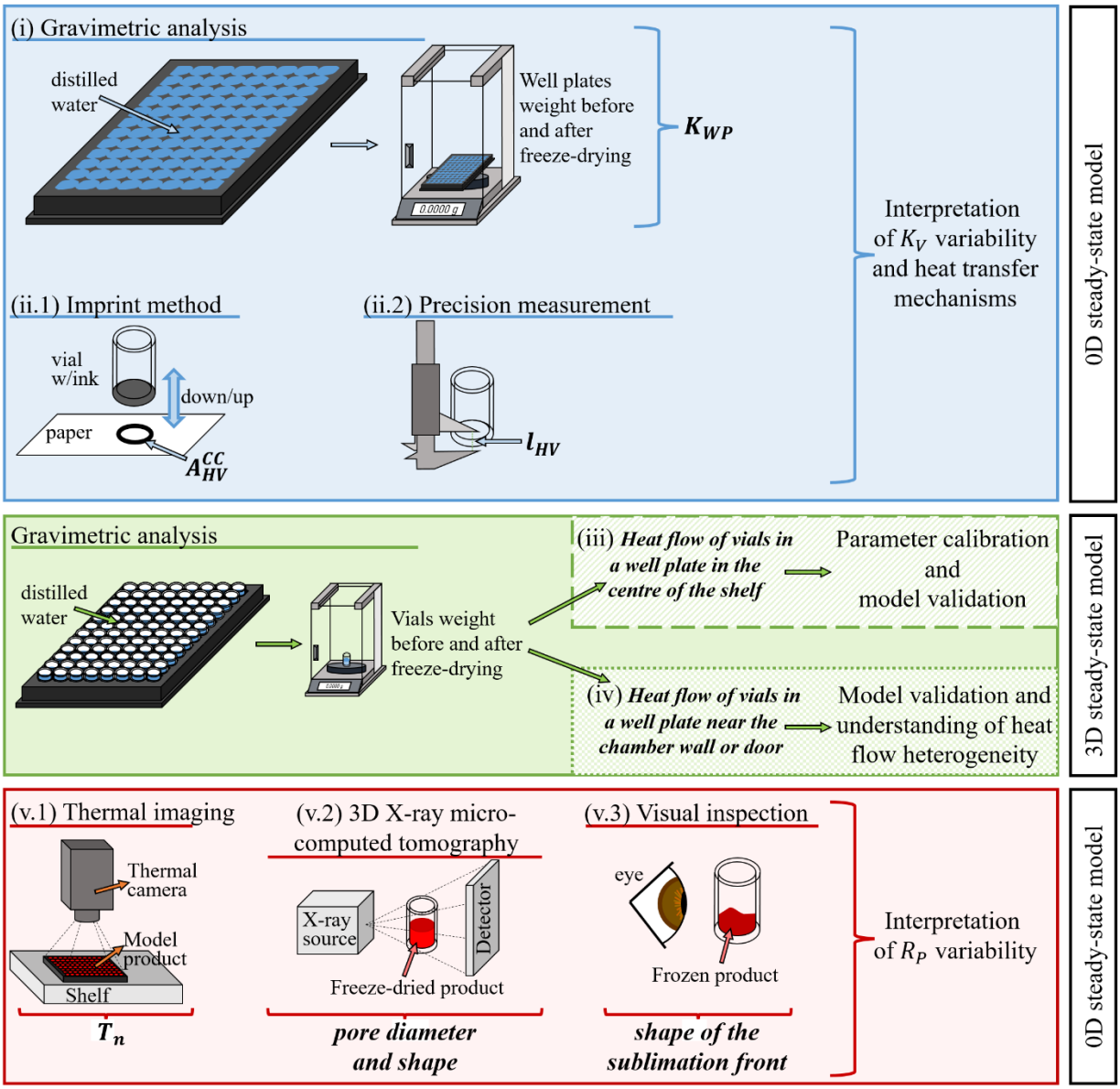

Figure 3.2-1 – Schematic of the experimental strategy to address Question 2: "What are the main factors responsible for product quality variations during primary drying in high-throughput systems?". These experiments study factors affecting the heat and mass transfer. Experiments in the blue square (i, ii.1, and ii.2) are detailed in Section 4.1.3. Experiments in the green square and the study of the heat flow of vials in a well plate in the centre of the shelf (iii) are detailed in Section 4.2.3. The study of the heat flow of vials in a well plate near the chamber wall or door (iv) is detailed in Section 4.3.3. Experiments in the red square (v.1, v.2, and v.3) are detailed in Section 4.4.3.

stage of primary drying, when there is no dried product resistance to the mass transfer. Moreover, the *distilled water model* was expanded to represent the heat and mass transfer during intermediate points of primary drying (*product model*) by considering a R_P value taken from the literature. The *distilled water* and *product models* were used to understand how the impact of the vial position in the well plate may vary from the beginning of primary drying (*distilled water model*) to an advanced point of primary drying (*product model*) and which are the mechanisms responsible for this variation. The complete description of the *models* and the results are detailed in Section 4.2.3.

The original *distilled water* and *product models* (Section 4.2.3) were modified to embody twelve representative vial positions in a well plate near the chamber wall or door. These modified models were used to study how the well plate position on the shelf could impact the heat transfer. The heat flows calculated using the modified *distilled water model* were validated using experimental heat flows determined during ice sublimation tests ("iv" in Figure 3.2-1). The impact of the well plate position on the shelf was studied in time by comparing the modified *distilled water model* (beginning of primary drying) and *product model* (advanced point of primary drying). The modified *models* and the results of this comparison are presented in Section 4.3.3.

The impact of the nucleating temperature (T_n) on R_P was evaluated by considering a 5% (w/w) sucrose aqueous solution ("model" product) with and without a nucleating agent. The nucleating temperature of 288 high-throughput vials and 264 serum vials filled with the model product with and without the nucleating agent was determined using a thermal camera during freezing ("v.1" in Figure 3.2-1). T_n values were correlated with the R_P values previously determined by a pressure rise test method (red rectangle in Figure 3.1-1). The relation between T_n and R_P was interpreted for each container type considering the pore size of the dried product and the shape of the sublimation front. The pore size of the dried product obtained in both containers was determined by 3D micro-computed tomography ("v.2" in Figure 3.2-1). Furthermore, the shape of the sublimation front was observed at different moments of primary drying ("v.3" in Figure 3.2-1), being considered an indicator of the mass transfer area. The materials and methods used, the theoretical framework, and the results of this research are presented in Section 4.4.3.

4. Results

4.1. Heat Transfer during Primary Drying Using High-Throughput Vial Systems

4.1.1. Context

Vaccines are freeze-dried in their final packaging container, which is typically cylindrical and made of glass. This container is known as “serum vial” and has a maximum filling volume of over 3000 µL (Pikal et al., 1984; Scutellà et al., 2017a; Zhai et al., 2005). The size of serum vials is advantageous for a correct reconstitution of the freeze-dried product and dosing the vaccines to the subjects. However, using smaller vials would be beneficial for research purposes since more vials could fit inside the freeze dryer; therefore, more formulations could be tested per freeze-drying cycle. In this vein, high-throughput systems consisting of small glass tubular vials (“high-throughput vials”, smaller than 1000 µL) inside an aluminium well plate were recently proposed to accelerate formulation screening (von Graberg, 2011).

Previous work proved that the vial geometry and the presence of an object (tray) between the shelf and the vial (Pisano et al., 2011) and the vial bottom geometry (Brülls and Rasmuson, 2002) could entail variations in the heat transfer to serum vials during the primary drying stage of freeze-drying, ultimately affecting the product quality. The product quality is expected to differ when using high-throughput or serum vials, given the differences in their geometry and the presence of a well plate in the case of high-throughput vials. To the best of this author’s knowledge, there is no published research on managing such change of container (high-throughput vials for research and serum vials for production) while maintaining the product quality. Furthermore, no published research was found on the impact of the high-throughput vial bottom geometry and the well plate characteristics.

4.1.2. Objectives

This Section 4.1 aimed at studying the heat transfer to high-throughput vials as a first step to understand how to obtain a product with the same quality when using serum vials (“translation” of the operating conditions). Moreover, this work delves into the impact of the high-throughput vial bottom geometry and the well plate’s surface characteristics to determine how these factors may entail deviations in the product quality.

4.1.3. Paper I

This article was published in the Journal of Pharmaceutical Sciences Volume 110, Issue 3, in March 2021, pages 1323-1336 (https://doi.org/10.1016/j.xphs.2020.11.029).

TITLE

"Heat transfer during freeze-drying using a high-throughput vial system in view of process scale-up to serum vials"

AUTHORS

Juan Patricio Buceta[1], Ioan CristianTrelea[1], Bernadette Scutellà[2], Erwan Bourlés[2], Fernanda Fonseca[1], and Stéphanie Passot[1]

[1] Université Paris-Saclay, INRAE, AgroParisTech, UMR SayFood, F-78850, Thiverval-Grignon, France

[2] GSK, Rixensart, Belgium

ACKNOWLEDGMENTS

The authors would like to thank Emanuele Tomba and Mohamed Belkacem (GSK) for reviewing this manuscript and Vincent Ronsse (technician) and Alain Philippart (operator) (GSK) for their help in data acquisition.

CONFLICTS OF INTEREST

Erwan Bourlés and Bernadette Scutellà are employees of the GSK group of companies. Juan Patricio Buceta participated in a post-graduate PhD programme at GSK. Stéphanie Passot, Fernanda Fonseca and Ioan Cristian Trelea report no financial conflicts of interest.

AUTHOR'S CONTRIBUTIONS

Juan Patricio Buceta, Stéphanie Passot, Bernadette Scutellà, Erwan Bourlés, Fernanda Fonseca and Ioan Cristian Trelea were involved in the conception and design of the study. Juan Patricio Buceta, Bernadette Scutellà and Erwan Bourlés acquired the data. Juan Patricio Buceta, Stéphanie Passot, Bernadette Scutellà, Erwan Bourlés, Fernanda Fonseca and Ioan Cristian Trelea analysed and interpreted the results. All authors were involved in drafting the manuscript or critically revising it for relevant intellectual content. All authors had full access to the data and approved the manuscript before it was submitted by the corresponding author.

CONTENTS OF PAPER I

ABSTRACT

Specific devices that combine 96-well plates and high-throughput vials were recently proposed to improve the efficiency of formulation screening. Such devices make it possible to increase the number of formulations tested while reducing the amount of active ingredients needed. The geometry of the product container influences the heat and mass transfer during freeze-drying, impacting product temperature (T_p) and therefore affecting the final product quality. Our study aimed at developing a tool to identify the operating conditions resulting in the same T_p when using high-throughput vials inside well plates and serum vials. Heat transfer coefficients between the shelf and the high-throughput vials (K_V) were measured using the gravimetric method at chamber pressures ranging from 4 to 65 Pa for a batch of 576 vials located at the centre of the well plates. K_V distributions were used to predict T_P distributions during primary drying of a 5% sucrose solution. T_p values were in average 6 °C higher using high-throughput vials instead of serum vials at chamber pressures lower than 12 Pa. This study provides a graphical solution for the management of process scale-up and scale-down between both types of product containers depending on their respective K_V and product resistance to mass transfer.

KEYWORDS

Freeze-drying; Lyophilization; Mathematical model(s); Mechanistic modeling; Vaccine(s).

INTRODUCTION

Freeze-drying is a dehydration method widely used in the pharmaceutical industry to preserve proteins, hormones, vaccines and bacteria, among others (Fonseca et al., 2015; Pikal, 1994; Pikal et al., 1991; Scutellà et al., 2017a). This method consists of three steps: freezing the product, removing the ice by sublimation (primary drying), and desorbing the bound water (secondary drying). Freeze-drying vaccines extends their shelf life during storage and transportation, and is the recommended procedure for formulations that are not stable enough in liquid form. Because of the rapid growth of the biopharmaceutical industry, it is necessary to find ways to accelerate the development phase of new products. Novel devices combining 96-well plates and small glass tubular containers – known as high-throughput vials – could speed-up the formulation development step by increasing the number of formulations tested per freeze-drying cycle, while limiting the amount of active ingredients. The final product containers used for commercial distribution are usually serum vials, which have a vial bottom area three times greater than high-throughput vials, and are directly placed on the freeze dryer shelf usually contained by a bottomless tray.

The US Food and Drug Administration (FDA) now requires that product quality be integrated into process design. This initiative is known as Quality by Design (QbD). Constructing a "design space" is a key step in the QbD initiative. A design space is defined as the "multidimensional combination and interaction of input variables (e.g., material attributes) and process parameters that have been demonstrated to provide assurance of quality" (US Food and Drug Administration, 2009). When considering the primary drying step of the freeze-drying process, the design space is a graphical solution of the heat and mass transfer equations, capable of predicting the product temperature and sublimation rate at a given time during the process. The design space is built taking account of the product container used at the production scale. Changing the product container during the formulation development step implies a change in the heat and mass transfer properties (Pikal et al., 1984; Pisano et al., 2011) and, consequently, the design space. The design spaces using high-throughput and serum vials must be connected in order to "translate" the results of high-throughput formulation screening to a pilot or industrial scale. This strategy enables researchers to accelerate the development of new products, particularly when the container used at industrial scale is defined and known before the formulation development step – 3 mL serum vials in our case of study. In this work, the connection between design spaces will be done considering the predicted product temperature for each vial geometry. Product temperature is a crucial process parameter that affects product appearance; and that could subsequently result in unacceptable values of residual moisture content and reconstitution time, as well as a loss of product potency. If the product exceeds a critical temperature known as the collapse temperature, it will not present the desired appearance and will therefore not be accepted on the basis of quality standards. We will use the term "scale-up" to refer to the "translation" of the operating conditions that use high-throughput vials to the operating conditions that use serum vials at the same product

temperature. Similarly, we will use the term "scale-down" for the "translation" of the operating conditions from serum to high-throughput vials.

Little research has been conducted on the heat transfer during primary drying using high-throughput vials in well plates: Patel and Pikal (2011) and von Graberg (2011) estimated a global heat transfer coefficient between the shelf and the high-throughput vial bottom (K_V), and Trnka et al. (2015) measured the temperature of plastic well plates and compared it to that of serum vials for only one set of operating conditions. In our study, we applied the approach of Scutellà et al. (2017a) for investigating heat transfer in serum vials to the high-throughput vial system. Our objective was to propose a graphical solution for interconnecting the design space of both types of product containers. Only vials located in the centre of the well plate and surrounded by other vials were considered. Different types of well plates and high-throughput vials were investigated. The global heat transfer coefficient between the shelf and the high-throughput vial bottom (K_V) was experimentally determined and was described as the contribution of two heat transfer coefficients: one between the shelf and the well plate, and one between the well plate and the vial. K_V heterogeneity was also quantified and explained by the contact area between the high-throughput vial bottom and the well plate. K_V values were used to predict the product temperature during primary drying of an aqueous sucrose solution (5% w/w). Our data on high-throughput vials were systematically compared to the data obtained with serum vials by Scutellà et al. (2017a). Finally, a graphical method was presented to scale-up and scale-down the operating conditions of the process when changing the product container.

MATERIALS AND METHODS

High-throughput vial system

The *96-Well Freeze-Drying System* manufactured by VirTis (SP Scientific, Stone Ridge, New York, USA) consisting of aluminium well plates and glass tubular vials, and referred to below as high-throughput vials, was used in our study. Figure 4.1-1a presents the two types of well plates used, which differ in their surface finish: (*i)* brilliant black (A-type well plate), and (*ii)* matte black (B-type well plate). A-type well plate bottom surfaces have circular marks due to the way they are manufactured, whereas B-type well plate bottom surfaces do not present such marks (Figure 4.1-1c). Furthermore, Figure 4.1-1b shows the two high-throughput vial sizes used that differ only in height, which, therefore, present a maximal filling volume of either 500-µL or 1000-µL. Figure 4.1-1b also shows a 3-mL serum vial, the traditional container used for vaccine freeze-drying (Brülls and Rasmuson, 2002; Pikal et al., 1984; Pisano et al., 2011; Scutellà et al., 2017a) for comparison. Seven A-type well plates, five B-type well plates, and 576 high-throughput vials of each size were used for the study.

A robotic tube handler (model XL9; BioMicrolab, Concord, CA, USA) shown in Figure 4.1-1d was used to weigh the high-throughput vials. The tube handler consisted of a mechanical arm and an analytical scale (± 0.0001 g). Vials were manually placed in a custom-made plate designed to fit on the loading area of the robot. The mechanical arm took the vials one by one, placed them on the analytical scale, and returned them to the custom-made plate.

Freeze dryer

A laboratory-scale freeze dryer (Epsilon 2-25D, Martin Christ Gefriertrocknungsanlagen GmbH, Osterode am Harz, Germany) was used in this study. The freeze dryer had seven shelves measuring 0.27 m^2 each, a distance between shelves of 57 mm, a drying chamber volume of 0.38 m^3, a duct between the chamber and the condenser closed by a mushroom valve, and a capacitance manometer to monitor the pressure inside the chamber. Tempris wireless temperature probes (iQ-mobil solution GmbH, Holzkirchen, Germany) were used to register the ice temperature.

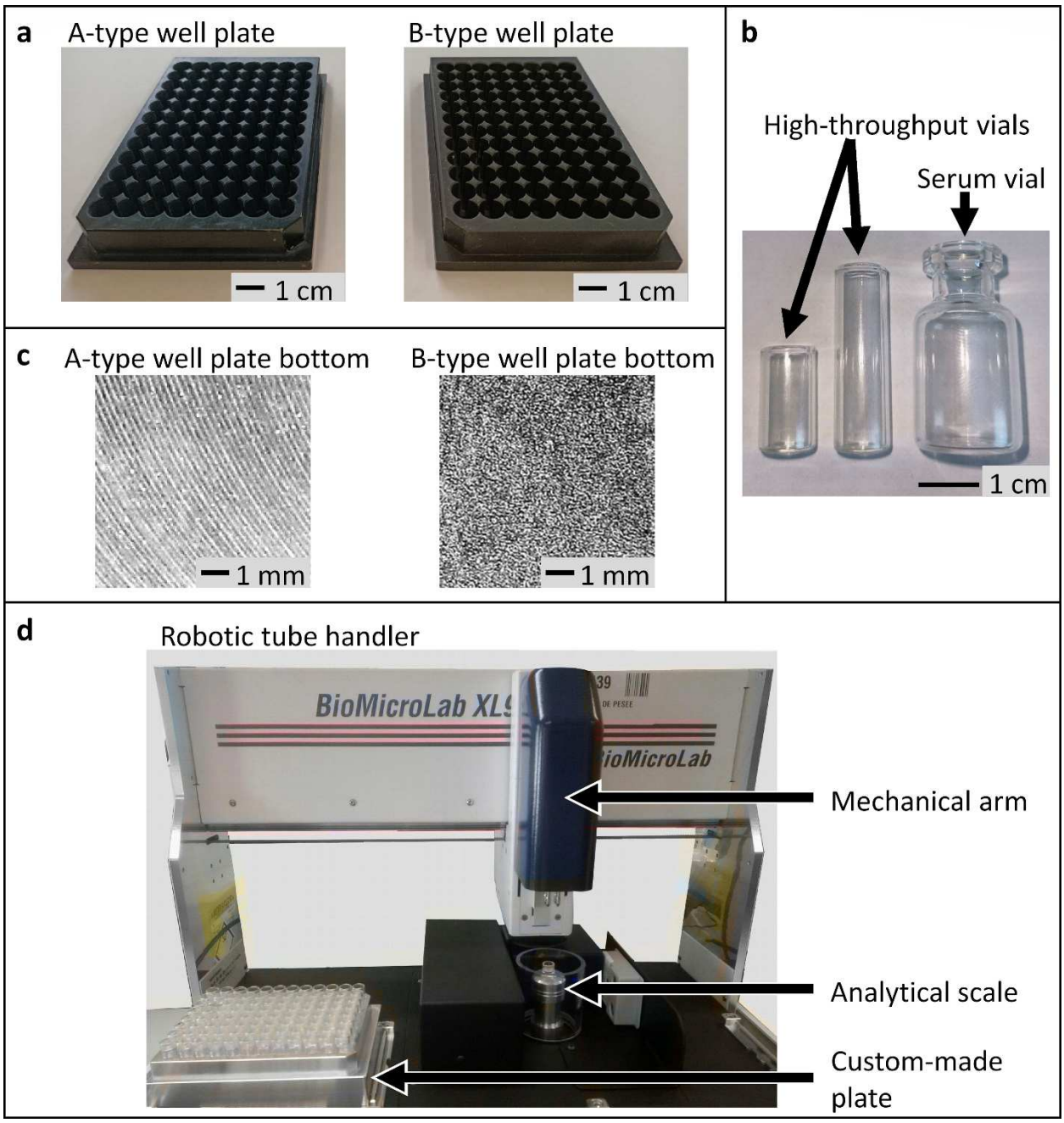

Figure 4.1-1 – 96-Well Freeze-Drying System manufactured by VirTis composed of (a) well plates and (c) high-throughput glass vials; (b) close-ups of the well plate bottom surfaces; (d) the robotic tube handler specifically developed for weighing the high-throughput glass vials.

Ice sublimation experiments

Ice sublimation experiments were performed using well plates with and without high-throughput vials inside. The procedure previously described by Scutellà et al. (2017a) for serum vials was applied with some modifications. Stoppers were not inserted into the vial necks.

The 1000-µL vials were filled with 600 µL of distilled water. Three A-type well plates and three B-type well plates, each filled with 96 1000-µL vials, were placed on the middle shelf of the freeze dryer according to the arrangement shown in Figure 4.1-2a. During each experiment, the same vial was placed in the same well of the same well plate, and the same well plate was placed in the same position on the shelf. Well plates were quickly loaded onto the pre-cooled shelf at -50 °C. Relative air humidity was limited by a dry air laminar flow in front of the freeze dryer door, reducing condensation on the shelves. A freezing step of 2 hours was carried out to ensure complete water solidification. The sublimation step began after the freezing step by decreasing the chamber pressure and increasing the shelf temperature at a rate of 1 °C.min^{-1}. Experiments were carried out at 4, 6, 12, 25, and 65 Pa with a shelf fluid inlet temperature (shelf temperature) of -15 °C. Sublimation lasted long enough to remove approximately 20% of the initial ice mass. Tempris probes were inserted into three vials located in the centre of A-type well plates.

During experiments with 500-µL vials, well plates were arranged as shown in Figure 4.1-2b, and Tempris probes were not used since they could not be properly placed in the vials. Four A-type well plates and two B-type well plates were each charged with 96 500-µL vials filled with 400 µL of distilled water. During experiments without vials, well plates were arranged as in Figure 4.1-2a, and one Tempris probe was placed in a well in the centre of each well plate. Well plates were filled with 60 mL of distilled water.

The time-averaged sublimation mass flow was gravimetrically measured for each vial, $\dot{m}_{HV}$, kg.s^{-1} (experiments with vials), and for each well plate, $\dot{m}_{WP}$, kg.s^{-1} (experiments without vials). $\dot{m}_{HV}$ and $\dot{m}_{WP}$ were calculated as the mass loss divided by the time the sublimation lasted. Vials of 500 µL and 1000 µL were individually weighed before and after the experiment using a robotic tube handler. The mass loss during waiting and weighing times was quantified and shown to be negligible (< 0.5% of the initial ice mass). Well plates were weighed on a precision scale (± 0.001 g; Mettler Toledo, Zaventem, 142 Belgium). Sublimation time was considered to begin when the shelf fluid inlet temperature was greater than the ice-vapour equilibrium temperature at the chamber pressure.

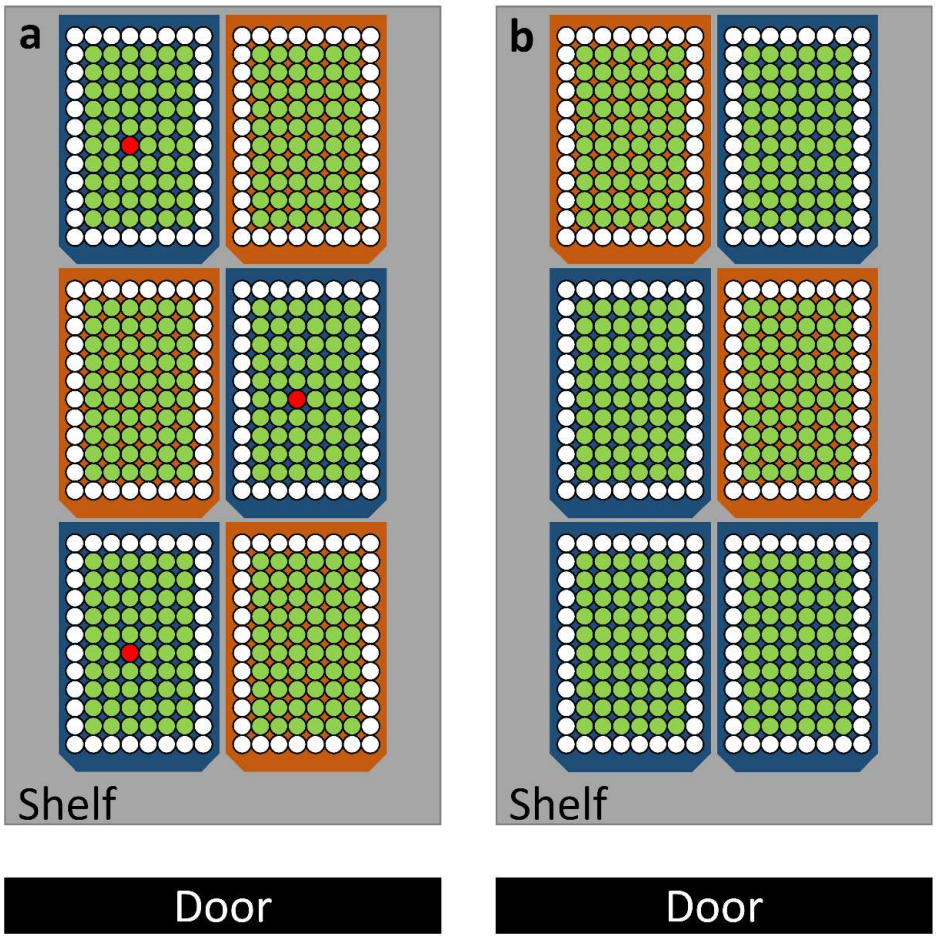

Figure 4.1-2 – Arrangement of the well plates on the freeze dryer shelf for tests with (a) 1000-µL vials, and (b) 500-µL vials; tests without vials were performed using the same well plate arrangement as (a). View of the shelf from the top not in scale. Well plate positions with A-type well plates are in blue, and B-type well plate positions are in orange. Circles represent vial positions, green circles represent positions considered for K_V and K_{HV} treatment, white circles represent positions on the edge of the well plate not considered in this work, and red circles represent vial positions with temperature probes during tests with 1000-µL vials.

Measurement of dimensions and emissivity of well plates and high-throughput vials

The dimensions of 96 vials of each size (500-µL and 1000-µL), and one well plate were measured by Precis&Mans (Le Mans, Pays de la Loire, France). The following geometrical parameters were determined with a precision of 0.01 mm: (i) inner and outer bottom diameters of the vial; (ii) maximum and minimum vial bottom concavity; (iii) length and width of the well plate; and (iv) diameter and depth of the wells. These values were used to calculate additional dimensions: (i) inner and outer bottom areas of the vial; and (ii) well plate bottom area.

Emissivity measurements of the well plate surfaces and the high-throughput vials were carried out by Themacs Ingénierie (Champs sur Marne, France) using a Fourier Transform Infrared Spectrometer Frontier (PerkinElmer, Waltham, MA, USA). The emissivity of well plates and vials varied less than 0.02 between -40 °C and -10 °C; for our purposes, the emissivity values were considered to be constant and equal to the temperature-averaged values.

Furthermore, the imprint method proposed by Kuu et al. (2009) was used to evaluate the vial bottom-well plate contact area (A_{HV}^{cc}) of 96 vials. This method consisted of placing the vials on an inkpad and then on a piece of white paper. The ink marks left on the paper were scanned and pixels with ink were counted using a code especially developed for this task using MATLAB R2017a (The MathWorks, Inc, Natick, MA, USA). Finally, the number of pixels per mm^2 was established using a figure of known area treated by the same procedure. The measured dimensions and surface emissivity values are given in Table 4.1-1.

Characterisation of the bottom surface of the well plate in contact with the freeze dryer shelf

The surface of A-type and B-type well plates in contact with the shelf was characterised by detailed inspection through high-definition photography. Two A-type and two B-type well plates were placed in a light-controlled cabin and were photographed using a Reflex Canon EOS camera (Canon France, Paris, France). The image of each well plate bottom surface contained 4892 × 3294 pixels. Pictures were treated using Adobe Photoshop (Adobe Inc., San José, CA, USA), original images were enlarged four times, and contrast was increased by 75% to enhance the shades created by the surface marks as presented in Figure 4.1-1c.

Numerical calculations and statistical analysis

Calculations were performed using MATLAB R2017a. The system of equations described in the Section *Theory and data analysis* (of this Paper I) was solved by an iterative code especially developed for this study, and the convergence criterion was the relative tolerance of the heat flow value (0.1%). Parameter estimations were performed using the *nlinfit* function of the Statistics and Machine Learning Toolbox, chi-square goodness-of-fit tests were performed using the *chi2gof* function, and artificial standard distributions consisting of 1000 elements were created using the *normrnd* function.

Table 4.1-1 – Well plate, vial dimensions, properties and physical properties.

Symbol	Significance	Value	Standard deviation	Units	Source
Well plate (A-type and B-type)					
A_{WP}	Bottom area of the well plate	1.08×10^{-2}	-	m^2	Calculated
d_{well}	Diameter of the wells	9.2655×10^{-3}	0.0056×10^{-3}	m	Measured
h_{well}	Depth of the wells	1.5245×10^{-2}	-	m	Measured
L_{WP}	Well plate length	1.2712×10^{-1}	-	m	Measured
W_{WP}	Well plate width	8.519×10^{-2}	-	m	Measured
ε_{WP}	Emissivity of the well plate	0.87	-	Dimensionless	Measured
High-throughput vial					
A_{HV}	Outer bottom area of the vial	6.103×10^{-5}	0.039×10^{-5}	m²	Calculated
A_{in}^{HV}	Inner bottom area of the vial	4.081×10^{-5}	0.032×10^{-5}	m²	Calculated
A_{HV}^{cc}	Vial-well plate contact area	1.93×10^{-5}	0.71×10^{-5}	m^2	Measured
d_{VE}	Outer bottom diameter of the vial	8.815×10^{-3}	0.028×10^{-3}	m	Measured
d_{VI}	Inner bottom diameter of the vial	7.208×10^{-3}	0.028×10^{-3}	m	Measured
$h_{HV,500}$	500-µL vial height	1.569×10^{-2}	0.0066×10^{-2}	m	Measured
$h_{HV,1000}$	1000-µL vial height	2.906×10^{-2}	0.0083×10^{-2}	m	Measured
l_{HV}^{max}	Maximum bottom concavity	9.0×10^{-5}	1.9×10^{-5}	m	Measured
l_{HV}^{min}	Minimum bottom concavity	4.4×10^{-5}	2.3×10^{-5}	m	Measured
ε_{HV}	Emissivity of the vial	0.85	-	Dimensionless	Measured
Serum vial					
A_V^{ser}	Outer bottom area of the vial	2.07×10^{-4}	0.37×10^{-4}	m²	(Scutellà et al., 2017a)
A_i^{ser}	Inner bottom area of the vial	1.78×10^{-4}	0.29×10^{-4}	m²	(Scutellà et al., 2017a)
A_{ser}^{cc}	Vial-shelf contact area	1.67×10^{-5}	0.40×10^{-5}	m²	(Scutellà et al., 2017a)
l_V^{ser}	Mean bottom curvature depth	1.23×10^{-4}	0.34×10^{-4}	m	(Scutellà et al., 2017a)
k_{ser}^{cc}	Empirical constant for serum vial-shelf contact conduction	2.20×10^{5}	0.27×10^{5}	$W.m^{-4}.K^{-1}$	(Scutellà et al., 2017a)
ε_V	Emissivity of the vial	0.78	-	Dimensionless	(Scutellà et al., 2017a)
Other parameters					
F_{HV}	Visualisation factor at the bottom of the vial (Equation 4.1-21]	0.75	-	Dimensionless	Calculated
F_{WP}	Visualisation factor at the bottom of the well plate (Equation 4.1-21)	0.18	-	Dimensionless	Calculated

Continuation of Table 4.1-1.

Symbol	Significance	Value	Standard deviation	Units	Source
Other parameters					
l_f	Initial ice thickness				
	In 500-µL vial	9.8×10^{-3}	-	mm	Calculated
	In 1000-µL vial	1.5×10^{-2}	-	mm	Calculated
P_{triple}	Triple point pressure of water	611.66	-	Pa	(Wagner et al., 1994)
R	Ideal gas constant	8.3144	-	$J.K^{-1}.mol^{-1}$	Perry and Green, 2008)
R_P	Area-normalized product resistance	1.248×10^{5}	-	$Pa.s.m^2.kg^{-1}$	(Konstantinidis et al., 2011)
T_{triple}	Triple point temperature of water	273.16	-	K	(Perry and Green, 2008)
ΔH_{sub}	Mass latent heat of sublimation of ice	2.763×10^{6}	-	$J.kg^{-1}$	(Scutellà et al., 2017a)
$\widetilde{\Delta H_{sub}}$	Molar latent heat of sublimation of ice	5.1059×10^{4}	-	$J.mol^{-1}$	(Murphy and Koop, 2005)
ε_{shelf}	Emissivity of the shelf	0.18	-	Dimensionless	Measured
λ_{gas}^{cont}	Thermal conductivity of the water vapour at atmospheric pressure	0.025	-	$W.m^{-1}.K^{-1}$	(Haynes, 2014)
λ_{ice}	Thermal conductivity of the ice	2.23	-	$W.m^{-1}.K^{-1}$	(Scutellà et al., 2017a)
Λ_0	Free molecular flow heat conductivity	1.99	-	$W.m^{-2}.K^{-1}.Pa^{-1}$	(Pikal, 2000)
σ	Stefan-Boltzmann constant	5.67×10^{8}		$W.m^{-2}.K^{-4}$	(Perry and Green, 2008)

THEORY AND DATA ANALYSIS

Evaluation of the heat transfer coefficients based on experimental data

By analogy with the work on serum vials (Pikal, 2000; Pikal et al., 1984; Pisano et al., 2011; Scutellà et al., 2017a), an apparent heat transfer coefficient between the shelf and the high-throughput vial bottom (K_V, W.m^{-2}.K^{-1}) was calculated using the equation:

$$K_V = \frac{\dot{Q}_{HV}}{A_{HV}\left(T_{shelf} - T_b\right)} = \frac{\dot{m}_{HV}\Delta H_{sub}}{A_{HV}\left(T_{shelf} - T_b\right)} \qquad \text{Equation 4.1-1}$$

where $\dot{Q}_{HV}$ (W) is the heat flow received by the vial, A_{HV} (m^2) is the outer bottom area of the vial, T_{shelf} (K) is the average temperature between the inlet and outlet shelf fluid temperatures, Bu, ΔH_{sub} (J.kg^{-1}) is the latent heat of sublimation, and $\dot{m}_{HV}$ is the sublimation mass flow (kg.s^{-1}). Since it was not possible to insert temperature probes in all vials to monitor the product temperature at the bottom of the vial, T_b was theoretically calculated for each vial as follows:

$$T_b = T_{sat} + \frac{\dot{Q}_{HV} l_f}{\lambda_f A_{in}} \qquad \text{Equation 4.1-2}$$

where λ_f (W.m^{-1}.K^{-1}) is the thermal conductivity of the ice, l_f (m) is the average between the initial and final ice thickness calculated based on the mass loss, A_{in} (m^2) is the inner bottom area of the vial, and T_{sat} (K) is the ice-vapour equilibrium temperature. T_{sat} was obtained using the Clausius Clapeyron relation (Perry and Green, 2008):

$$T_{sat} = \frac{T_{triple}}{1 - \frac{RT_{triple}}{\widetilde{\Delta H_{sub}}} ln\left(\frac{P_{sat}}{P_{triple}}\right)} \qquad \text{Equation 4.1-3}$$

where T_{triple} (273.16 K) is the triple point temperature of water, P_{triple} (611.66 Pa) is the triple point pressure of water, R (8.3144 J.K^{-1}.mol^{-1}) is the ideal gas constant, $\widetilde{\Delta H_{sub}}$ (5.1059×10^4 J.mol^{-1}) is the molar latent heat of sublimation, and P_{sat} (Pa) is the pressure at the ice sublimation front (ice-vapour interface). P_{sat} was assumed to be equal to the chamber pressure (P_C) during ice sublimation experiments, considering that: (*i)* the chamber was saturated with vapour; and (*ii)* the pressure loss between the ice sublimation front and the chamber was negligible since no stoppers were inserted into the vial necks. The calculated T_b were compared to the product temperature value registered by the Tempris probes in three 1000-µL vials, a good agreement (< 0.8 °C difference) was observed between experimental data and calculated values.

Due to the presence of the well plate between the shelf and the high-throughput vial, this apparent heat transfer coefficient K_V can be considered as a combination of two heat transfer coefficients: (*i)* a coefficient between the shelf and the well plate K_{WP}; and (*ii)* a coefficient between the well plate and the bottom of the vial K_{HV}.

K_{WP} was obtained using the data from the experiments performed without vials inside the well plates:

$$K_{WP} = \frac{\dot{Q}_{WP}}{A_{WP}\left(T_{shelf} - T_{WP}\right)} = \frac{\dot{m}_{WP}\Delta H_{sub}}{A_{WP}\left(T_{shelf} - T_{WP}\right)} \qquad \text{Equation 4.1-4}$$

where $\dot{Q}_{WP}$ (W) is the heat flow received by the well plate, A_{WP} (m^2) is the bottom area of the well plate, T_{WP} (K) is the product temperature at the bottom of the wells, and $\dot{m}_{WP}$ ($kg.s^{-1}$) is the sublimation mass flow of each well plate. T_{WP} was considered to be homogeneous for each well plate due to the high thermal conductivity of the aluminium compared to that of the surrounding gas (more than 9000 times greater) (Perry and Green, 2008). Similarly to the estimation of the vial bottom temperature (T_b) during tests with vials, T_{WP} was theoretically calculated for each well plate during tests without vials as follows:

$$T_{WP} = T_{sat} + \frac{\dot{Q}_{WP} l_f}{\lambda_f A_{WP}} \qquad \text{Equation 4.1-5}$$

The calculated T_{WP} were in agreement (< 0.9 °C difference) with the values recorded by the Tempris probes inside the well plates.

The heat transfer coefficient between the well plate and the high-throughput vial bottom K_{HV} can be expressed according to the following equation:

$$K_{HV} = \frac{\dot{Q}_{HV}}{A_{HV}\left(T_{WP} - T_b\right)} = \frac{\dot{m}_{HV}\Delta H_{sub}}{A_{HV}\left(T_{WP} - T_b\right)} \qquad \text{Equation 4.1-6}$$

Since T_{WP} was not monitored during the experiments with vials, we applied the following approach to determine the heat transfer coefficient K_{HV}: if we assume that the heat flows received individually by the 96 high-throughput vials in the well plate came only from the well plate, the heat flow received by the well plate and the vials are directly related:

$$\dot{Q}_{WP} = \sum_{i=1}^{96} \dot{Q}_{HV} \qquad \text{Equation 4.1-7}$$

The value of T_{WP} was estimated using Equation 4.1-4 and Equation 4.1-7 as:

$$T_{WP} = T_{shelf} - \frac{\sum_{i=1}^{96} \dot{Q}_{HV}}{A_{WP} K_{WP}} \qquad \text{Equation 4.1-8}$$

The 1000-µL vials protruded from the well plate and were more exposed to heat flow contributions from the freeze dryer. The assumption that the heat flows received by the vials came only from the well plate was presumably more realistic for the 500-µL vials than for the 1000-µL vials; therefore, T_{WP} values during tests with 1000-µL vials were considered to be the same as during the test with the 500-µL vials in the same well plate type.

K_V, K_{WP}, and K_{HV} can be related in a simple way under the hypothesis that all high-throughput vials and all the wells in a well plate had the same geometry and that all vials had the same heat transfer coefficients. In this way, heat flows can be expressed using the following equations:

$$96\dot{Q}_{HV} = \dot{Q}_{WP} \qquad \text{Equation 4.1-9}$$

$$96\dot{Q}_{HV} = 96 A_{HV} K_{HV} (T_{WP} - T_b) \qquad \text{Equation 4.1-10}$$

$$\dot{Q}_{WP} = A_{WP}K_{WP}\left(T_{shelf} - T_{WP}\right) \quad \text{Equation 4.1-11}$$

$$96\dot{Q}_{HV} = 96A_{HV}K_V\left(T_{shelf} - T_b\right) \quad \text{Equation 4.1-12}$$

From Equation 4.1-9 to Equation 4.1-11, we obtain:

$$\dot{Q}_{HV}\left(\frac{1}{A_{HV}K_{HV}} + \frac{96}{A_{WP}K_{WP}}\right) = T_{shelf} - T_b \quad \text{Equation 4.1-13}$$

Equation 4.1-12 and Equation 4.1-13 give:

$$\dot{Q}_{HV}\left(\frac{1}{A_{HV}K_V}\right) = T_{shelf} - T_b \quad \text{Equation 4.1-14}$$

Finally, the apparent heat transfer coefficient between the shelf and the high-throughput vial bottom can be expressed as:

$$\frac{1}{K_V} = \frac{1}{K_{HV}} + \frac{96A_{HV}}{A_{WP}K_{WP}} \quad \text{Equation 4.1-15}$$

Theoretical description of the heat transfer coefficients K_{WP} and K_{HV}

The heat transfer coefficients K_{WP} between the shelf and the well plate and K_{HV} between the well plate and the high-throughput vial can be described as the sum of the contribution of three heat transfer mechanisms:

$$K_{WP} = K_{WP}^{cc} + K_{WP}^{rad} + K_{WP}^{gc} \quad \text{Equation 4.1-16}$$

$$K_{HV} = K_{HV}^{cc} + K_{HV}^{rad} + K_{HV}^{gc} \quad \text{Equation 4.1-17}$$

where K_{WP}^{cc} and K_{HV}^{cc} represent the thermal conctact conduction between the shelf and the well plate, and between the well plate and the vial, respectively; similarly, K_{WP}^{rad} and K_{HV}^{rad} represent the thermal radiation; and K_{WP}^{gc} and K_{HV}^{gc} account for the thermal conduction through the gas entrapped in the bottom curvature of the well plate and the vial, respectively.

Heat transfer coefficient by thermal contact conduction K_{WP}^{cc} and K_{HV}^{cc}

Most authors (Pikal et al., 1984; Pisano et al., 2011; Scutellà et al., 2017a; von Graberg, 2011) considered contact conduction as a constant value independent of the operating conditions. Therefore, K_{WP}^{cc} and K_{HV}^{cc}, were considered as temperature- and pressure-independent. Scutellà et al. (2017a) assumed that the contact conduction between the shelf and serum vials was proportional to the vial-shelf contact area. Analogously, the contact conduction coefficient between the well plate and the high-throughput vials K_{HV}^{cc} was considered to be proportional to the contact area between the vial bottom and the well plate (A_{HV}^{cc}):

$$K_{HV}^{cc} = k_{HV}^{cc}A_{HV}^{cc} \quad \text{Equation 4.1-18}$$

where k_{HV}^{cc} ($W.m^{-4}.K^{-1}$) is an empirical constant of proportionality.

Heat transfer coefficient by thermal radiation K_{WP}^{rad} and K_{HV}^{rad}

K_{WP}^{rad} *and* K_{HV}^{rad} were calculated according to the Stefan-Boltzmann formula for grey diffuse surfaces:

$$K_{WP}^{rad} = \sigma F_{WP}\left(T_{shelf} + T_{WP}\right)\left(T_{shelf}^2 + T_{WP}^2\right) \quad \text{Equation 4.1-19}$$

$$K_{HV}^{rad} = \sigma F_{HV}(T_{WP} + T_b)\left(T_{WP}^2 + T_b^2\right) \quad \text{Equation 4.1-20}$$

where σ is the Stephan-Boltzmann constant (W.m^{-2}.K^{-4}), and the view factors F_{WP} and F_{HV} were calculated as for two parallel surfaces (Perry and Green, 2008):

$$F_{WP} = \frac{1}{\frac{1-\varepsilon_{shelf}}{\varepsilon_{shelf}} + \frac{1-\varepsilon_{WP}}{\varepsilon_{WP}} + 1} \quad \text{Equation 4.1-21}$$

$$F_{HV} = \frac{1}{\frac{1-\varepsilon_{WP}}{\varepsilon_{WP}} + \frac{1-\varepsilon_{HV}}{\varepsilon_{HV}} + 1} \quad \text{Equation 4.1-22}$$

where ε_{shelf}, ε_{WP}, and ε_{HV} are the emissivity values of the shelf, the well plate and the high-throughput vial, respectively.

Heat transfer coefficient by thermal conduction through the gas K_{WP}^{gc} and K_{HV}^{gc}

Three gas conduction regimes occur within the usual chamber pressure range during sublimation (< 15 Pa): free molecular, transition and continuous regimes. Pikal (2000) modelled the heat transfer coefficient for conduction through the gas trapped between two parallel surfaces assuming the transition regime as:

$$K_{WP}^{gc} = \frac{\alpha_{WP}\Lambda_o P_C}{1 + \frac{l_{WP}}{\lambda_{gas}^{cont}}\alpha_{WP}\Lambda_o P_C} \quad \text{Equation 4.1-23}$$

$$K_{HV}^{gc} = \frac{\alpha_{HV}\Lambda_o P_C}{1 + \frac{l_{HV}}{\lambda_{gas}^{cont}}\alpha_{HV}\Lambda_o P_C} \quad \text{Equation 4.1-24}$$

where α_{WP} and α_{HV} are the thermal accommodation coefficients related to the quality of momentum exchange between the gas molecules and the solid surfaces (shelf and well plate, and well plate and vial, respectively), Λ_0 (W.m^{-2}.K^{-1}.Pa^{-1}) is the heat transfer coefficient of the gas at 0 °C in a free molecular regime, P_C (Pa) is the chamber pressure, l_{WP} and l_{HV} are the average distances between the solid surfaces, and λ_{gas}^{cont} (W.m^{-1}.K^{-1}) is the thermal conductivity of the water vapour in a continuous regime. l_{HV} was considered to be the average between the maximum and minimum vial bottom concavity.

Theoretical description of the heat transfer coefficient K_V

The heat transfer coefficient between the shelf and the high-throughput vial bottom K_V corresponds to an apparent heat transfer coefficient. Consequently, its representation as the sum of the three heat transfer contributions described above has no real physical meaning due to the presence of the well plate. However, for sake of comparison with the large existing body of literature, the following equation was used to represent the evolution of the coefficient K_V with the chamber pressure by analogy with serum vials (Pikal, 2000; Pikal et al., 1984; Pisano et al., 2011; Scutellà et al., 2017a; von Graberg, 2011):

$$K_V = K_V^{cc} + K_V^{rad} + \frac{\alpha_V \Lambda_o P_c}{1 + \frac{l_V}{\lambda_{gas}^{cont}} \alpha_V \Lambda_o P_c} \qquad \text{Equation 4.1-25}$$

where, K_V^{cc} and K_V^{rad} were considered to be constants.

Calculation of K_V distributions based on high-throughput vial geometry

The impact of the vial bottom-well plate contact area A_{HV}^{cc} on the global heat transfer coefficient K_V was evaluated for both well plate types (A-type and B-type) and both vial sizes (500-µL and 1000-µL vials) at chamber pressures of 4, 6, 12, 25, and 65 Pa. A chi-square goodness-of-fit test was performed with the A_{HV}^{cc} values from the imprint tests, indicating that the data came from a normal distribution at a 0.05 significance level. K_V distributions based on vial geometry were obtained using the mean value and standard deviation of A_{HV}^{cc} and Equation 4.1-15 to Equation 4.1-17.

Calculation of K_V distributions in serum vials

K_V distributions in high-throughput vials were compared to K_V distributions in serum vials calculated based on the work of Scutellà et al. (2017a) – considering serum vials placed in the centre of the shelf. K_V distributions in serum vials were obtained using Equation 4.1-25 and injecting two normal distributions: (*i)* one normal distribution of the distance between the shelf and the serum vial (l_V^{ser}); and (*ii)* one normal distribution of the serum vial-shelf contact area (A_{ser}^{cc}) in:

$$K_{V,ser}^{cc} = A_{ser}^{cc} k_{ser}^{cc} \qquad \text{Equation 4.1-26}$$

where k_{ser}^{cc} is an empirical constant for contact conduction between the shelf and serum vials. Normal distributions were created based on the mean value and standard deviations of l_V^{ser} and A_{ser}^{cc} in Table 4.1-1.

Simulation of the product temperature distribution using K_V distributions

Product temperature distributions were calculated using the approach proposed by Scutellà et al. (2017a) based on K_V distribution. For high-throughput vials, K_V values were the experimental distribution of the *96-Well Freeze-Drying Systems*. For serum vials, K_V values were the distribution obtained as described in *Calculation of K_V distributions in serum vials*. Product temperatures were calculated for a 5% sucrose solution considering a shelf temperature of -15 °C and five chamber pressures (4, 6, 12, 25, and 65 Pa). The

mass flow ($\dot{m}$) during sublimation was related to the pressure difference between the chamber (P_C) and the ice sublimation front (P_{sat}) as (Pikal et al., 1984):

$$\dot{m} = \frac{A_{in}(P_{sat} - P_C)}{R_P} \qquad \text{Equation 4.1-27}$$

where R_P (Pa.s.m^2.kg^{-1}) is the area-normalized product resistance, and A_{in} (m^2) is the inner bottom area of the vial. The R_P value was taken from literature (Konstantinidis et al., 2011) for a dried layer of 5% sucrose with a thickness of 0.5 cm, as reported in Table 4.1-1. To simulate the product temperature distribution, the non-linear system composed of Equation 4.1-1 to Equation 4.1-3 and Equation 4.1-27 was solved for each K_V value, considering the temperature at the bottom of the vial (T_b) as the product temperature (T_p).

RESULTS AND DISCUSSION

Effect of the well plate type and vial size on the apparent heat transfer coefficient between the shelf and the high-throughput vial bottom K_V

The values of the apparent heat transfer coefficient K_V were calculated for 576 500-µL vials and 573 1000-µL vials at a shelf temperature of -15 °C for five chamber pressures (from 4 to 65 Pa). High-throughput vials located at the edge of the well plates (white circles in Figure 4.1-2) presented greater K_V values than those located in the centre (green circles in Figure 4.1-2); increasing up to 10% for 500-µL vials and 25% for 1000-µL vials at a chamber pressure of 4 Pa; consequently, they were not considered in this study.

Figure 4.1-3a and Figure 4.1-3b display the evolution of the average K_V value with the chamber pressure for the 500-µL and 1000-µL vials, respectively. The data concerning the two well plate types (A-type presenting a brilliant surface finish, and B-type presenting a matte surface finish) are reported on each figure, as well as the K_V evolution with the chamber pressure for serum vials in the centre of the shelf obtained by Scutellà et al. (2017a). The experimental data obtained using high-throughput vials and serum vials (Scutellà et al., 2017a) were acquired using the same freeze dryer (Epsilon 2-25D, Martin Christ). Regardless of the well plate type and vial sizes (500-µL and 1000-µL), K_V of high-throughput vials were more than twice as great as K_V of serum vials at chamber pressures lower than 25 Pa. Therefore, the heat transfer per vial cross-section was more efficient in high-throughput vials placed in well plates than in serum vials placed directly on the shelf. Von Graberg (2011) measured K_V of 500-µL vials using the *96 Well Freeze-Drying System* manufactured by VirTis, and the values are included in Figure 4.1-3a. Results obtained by Von Graberg (2011) are within the range of our K_V values considering both well plate types. Coefficients of Equation 4.1-25 were estimated using experimental data, and their values are presented in Table 4.1-2.

The average K_V values were greater for B-type well plates (orange symbol in Figure 4.1-3) than for A-type (blue symbol in Figure 4.1-3). At a chamber pressure of 4 Pa, the K_V difference between well plate types appeared to be quite narrow (lower than 12%), and then increased with increasing chamber pressure to reach 34% for 500-µL vials and 24% for 1000-µL vials at 65 Pa.

Furthermore, when considering chamber pressures lower than 25 Pa, K_V values of 1000-µL vials were an average of 21% greater than K_V values of 500-µL vials. Since the two vial sizes differed only by vial height, this reported K_V difference could be ascribed to an extra heat contribution received by the top portion of 1000-µL vials protruding from the well plate. This possible extra heat contribution is reflected in the unphysical α_V values for 1000-µL vials (Table 4.1-2); these estimated values were greater than the highest theoretical accommodation coefficient between two surfaces (≈ 1; Pikal, 2000), whereas 500-µL vials presented α_V values below 0.9.

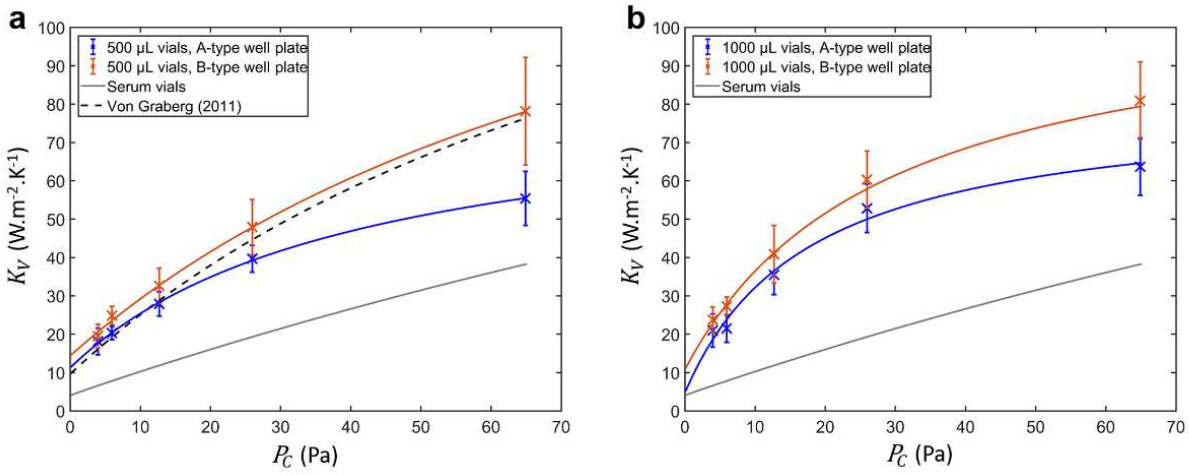

Figure 4.1-3 – Apparent heat transfer coefficients between the shelf and the vial bottom (K_V) vs. chamber pressure (P_C) for: (a) 500-µL vials, and (b) 1000-µL vials. The curves correspond to the values calculated with Equation 4.1-25. Error bars represent standard deviations. K_V for serum vials are based on Scutellà et al. (2017a) represented in grey. K_V estimated by von Graberg (2011) are represented as a dotted black line; values were readjusted to have the same heat transfer area (A_{HV}) considered in our study.

Table 4.1-2 – Heat transfer model coefficients evaluated by fitting Equation 4.1-25 to K_V data obtained in 500-µL and 1000-µL high-throughput vials in A-type and B-type well plates, as well as coefficients for serum vials taken from Scutellà et al. (2017a).

	$K_V^{cc} + K_V^{rad}$ (W m^{-2} K^{-1})	α_V	l_V (m)
A-type – 500-µL	11.23 ± 0.40	0.884 ± 0.036	(3.460 ± 0.067) ×10^{-4}
A-type – 1000-µL	4.7 ± 1.2	2.15 ± 0.17	(3.375 ± 0.044) ×10^{-4}
B-type – 500-µL	14.34 ± 0.92	0.822 ± 0.062	(1.57 ± 0.14) ×10^{-4}
B-type – 1000-µL	10.77 ± 0.87	1.742 ± 0.092	(2.532 ± 0.040) ×10^{-4}
Serum vials (Scutellà et al., 2017a)	4.22 ± 0.45	0.335 ± 0.013	(1.23 ± 0.34) ×10^{-4}

Mean values ± standard errors. $K_V^{cc} + K_V^{rad}$ is the pressure-independent contribution to heat transfer by contact conduction and radiation, α_V is the effective thermal accommodation coefficient, and l_V is the effective distance between surfaces for the gas conduction contribution.

Since there was no direct contact between the shelf and high-throughput vials, the coefficients of Equation 4.1-25 reported in Table 4.1-2 do not have a physical meaning. To better understand the role of the well plate and the vial on the heat transfer mechanisms, we broke down the apparent heat transfer coefficient K_V in two heat transfer phenomena in series: (*i)* from the shelf to the well plate; and (*ii)* from the well plate to the vial.

Effect of chamber pressure on the heat transfer coefficients between the shelf and the well plate ($\mathbf{K_{WP}}$) and between the well plate and the vial ($\mathbf{K_{HV}}$)

K_{WP} values were calculated using the data of the sublimation experiments carried out without vials inside the well plates and Equation 4.1-3 to Equation 4.1-5, while K_{HV} were calculated using the data of the sublimation experiments with vials and Equation 4.1-2, Equation 4.1-3, Equation 4.1-6, and Equation 4.1-8. Only the K_{HV} of vials located in the centre of the well plates (represented as green circles in Figure 4.1-2) were considered. Figure 4.1-4a shows the evolution of K_{WP} values with the chamber pressure for both well plate types (A-type and B-type), and Figure 4.1-4b presents the evolution of K_{HV} for both well plate types and vial sizes (500-µL and 1000-µL). K_{WP} values varied with chamber pressure, increasing five times from 4 to 65 Pa, whereas K_{HV} values appeared to be quite constant with the chamber pressure. Table 4.1-3 presents the values of the coefficients presented in Equation 4.1-16, Equation 4.1-17, Equation 4.1-23, and Equation 4.1-24 fitted with the K_{WP} and K_{HV} data. The absence of significant pressure dependence of K_{HV} resulted in numerical difficulties to estimate the parameter α_{HV}, therefore causing the significant variation of this parameter for each combination of well plate type and vial size.

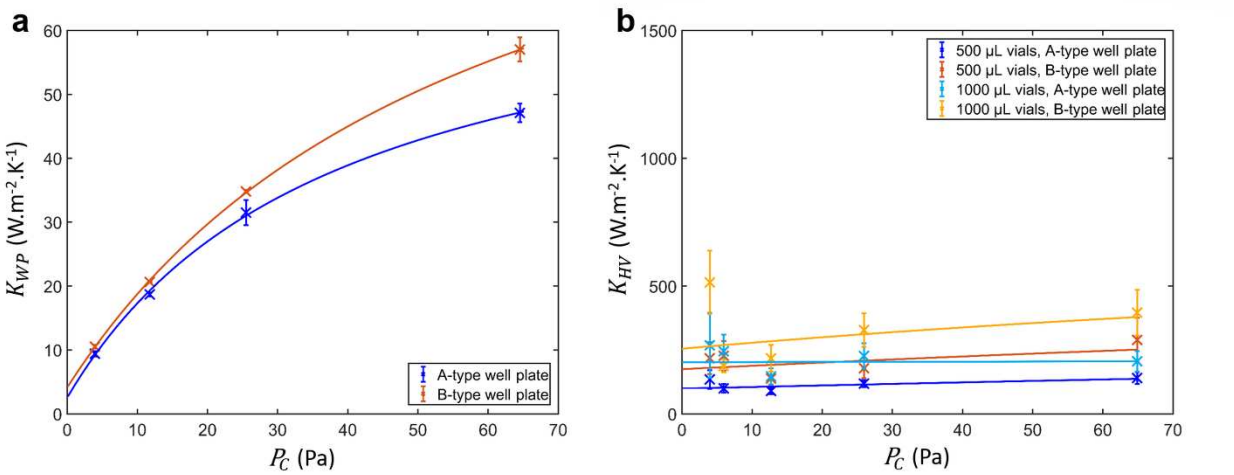

Figure 4.1-4 – Heat transfer coefficients (a) between the shelf and well plate bottom (K_{WP}), and (b) between the well plate and vial bottom (K_{HV}), vs. chamber pressure (P_C). The curves correspond to the values calculated with Equation 4.1-16, Equation 4.1-17, and Equation 4.1-19 to Equation 4.1-24. Error bars represent standard deviations.

Table 4.1-3 – Heat transfer model coefficients calculated or fitted using Equation 4.1-16, Equation 4.1-17, and Equation 4.1-19 to Equation 4.1-24 to K_{WP} and K_{HV} data obtained in 500-µL and 1000-µL high-throughput vials in A-type and B-type well plates.

	K^{rad} (W.m^{-2}.K^{-1})	K^{cc} (W.m^{-2}.K^{-1})	α	l (m)
K_{WP}				
A-type	0.601 ± 0.038	2.91 ± 0.93	0.813 ± 0.074	(3.28 ± 0.16) ×10^{-4}
B-type	0.601 ± 0.038	3.58 ± 0.60	0.848 ± 0.043	(2.405 ± 0.087) ×10^{-4}
K_{HV}				
A-type – 500-µL	2.20 ± 0.29	96.4 ± 1.0	0.32 ± 0.019	(6.7 ± 0.7) ×10^{-5}
A-type – 1000-µL	2.20 ± 0.29	200.0 ± 3.6	0.024 ± 0.058	(6.7 ± 0.7) ×10^{-5}
B-type – 500-µL	2.20 ± 0.29	172.4 ± 4.7	0.686 ± 0.094	(6.7 ± 0.7) ×10^{-5}
B-type – 1000-µL	2.20 ± 0.29	252.5 ± 8.4	1.23 ± 0.20	(6.7 ± 0.7) ×10^{-5}

Mean values ± standard errors. K_{WP} and K_{HV} are the heat transfer coefficients between the shelf and the well plate bottom, and the well plate bottom and the vial bottom, respectively. K^{rad} is the contribution to K_{WP} or K_{HV} due to heat transfer by the calculated radiation, K^{cc} is the fitted contribution to K_{WP} or K_{HV} due to heat transfer by contact conduction, α is the fitted thermal accommodation coefficient for gas conduction in K_{WP} or K_{HV}, and l is the effective distance between the shelf and well plate surfaces or between the well plate and the vial.

The contributions of the heat transfer mechanisms to the heat transfer coefficients K_{WP} and K_{HV} were calculated using Equation 4.1-16, Equation 4.1-17, and Equation 4.1-19 to Equation 4.1-24, and the fitted coefficients are reported in Table 4.1-3. Figure 4.1-5 shows the relative contribution of contact conduction (K_{WP}^{cc} and K_{HV}^{cc}), conduction through the gas (K_{WP}^{gc} and K_{HV}^{gc}), and radiation (K_{WP}^{rad} and K_{HV}^{rad}) to K_{WP} (Figure 4.1-5a) and K_{HV} (Figure 4.1-5b). Gas conduction (K_{WP}^{gc}) was the greatest contributor to K_{WP}, increasing from 62% at 4 Pa to 93% at 65 Pa (average between well plate types); contact conduction (K_{HV}^{cc}) was the greatest contributor to K_{HV}, representing 96% at 4 Pa and 73% at 65 Pa (average between well plate types and vial sizes).

The contribution to heat transfer by radiation was very low (< 7%), regardless of the heat transfer coefficient (K_{WP} and K_{HV}) and the chamber pressure, whereas the radiation contribution represents around 20 to 30% of K_V for serum vials at chamber pressures below 10 Pa (Scutellà et al., 2017a).

Several authors reported the importance of the vial bottom curvature on heat transfer between the shelf and the bottom of the serum vials (Brülls and Rasmuson, 2002; Pisano et al., 2011; Scutellà et al., 2017a). When considering high throughput vials, the vial bottom curvature is small enough to consider the divisor in Equation 4.1-24 equal to 1 ($l_{HV} \ll \frac{\lambda_{gas}^{cont}}{\alpha_{HV} \Lambda_o P_C}$), so l_{HV} did not have an impact on K_{HV}. This explains the quasi linear pressure dependence of K_{HV} (Figure 4.1-4b). The only gas layer thickness involved in the gas conduction that impacted K_V was the apparent distance between the bottom shelf and the well plate bottom (l_{WP}) through its effect on K_{WP}.

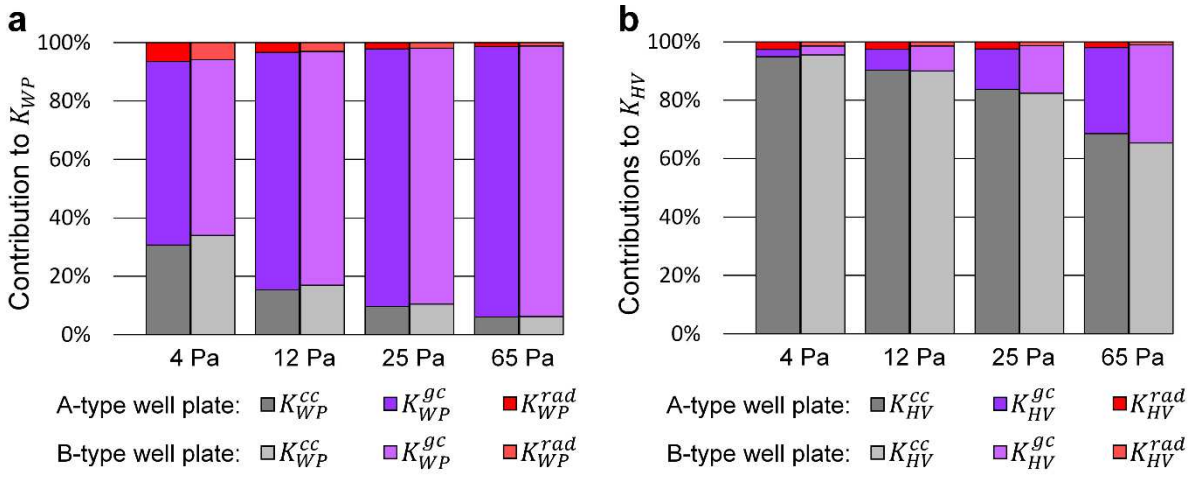

Figure 4.1-5 – Relative contributions of the heat transfer coefficients by contact conduction (K_{WP}^{cc}, K_{HV}^{cc}), conduction through the gas (K_{WP}^{gc}, K_{HV}^{gc}), and radiation (K_{WP}^{rad}, K_{HV}^{rad}) as percentages of the total heat transfer coefficients: (a) between shelf and wall plate (K_{WP}), and (b) between wall plate and vial (K_{HV}). K_{HV} values for 500-µL vials.

Regarding the effect of the well plate type on K_{WP}, A-type well plates exhibited lower K_{WP} values than B-type well plates, in particular for chamber pressure higher than 25 Pa. The effect of the well plate type on K_{WP} could be ascribed to the circular marks on the bottom surface of A-type well plates (Figure 4.1-1b); these marks could reduce the number of contact points with the shelf, which explains the lower K_{WP}^{cc} value observed in Table 4.1-3 compared to that of B-type well plates. Furthermore, these surface deformations (observed as marks) could leave more space for trapped gas between the shelf and the well plate, which is in agreement with the higher l_{WP} values for A-type well plates than for B-type well plates.

In Figure 4.1-4b, we observe that 1000-µL vials exhibited higher K_{HV} values than 500-µL (by approximately 50%), which was not initially expected since both vial sizes have similar bottom geometry and differ only in height. As was previously observed for K_V data, 1000-µL vials may have received extra heat via the portion of vials that protruded from the well plate. Furthermore, K_{HV} values of 500-µL vials in B-type well plates were more than 44% greater than those in A-type well plates, which could be ascribed to a higher contribution of heat transfer by contact conduction (K_{HV}^{cc}) and, therefore, to a better contact between the bottom of the wells and the vials. The internal surface of the well bottoms in A-type well plates also presented noticeable manufacturing marks. Therefore, the number of contact points between the wells and the vials might have varied among well plate types, impacting K_{HV}^{cc}.

Equation 4.1-15 made it possible to calculate the heat transfer resistance induced by the well plate $\{[K_{WP}A_{WP} \,/\, (nA_{HV})]^{-1}\}$ and by the vial $[(K_{HV})^{-1}]$. The dominant resistance to the heat transfer was between the shelf and the well plate, representing more than 70% of the total heat transfer resistance for chamber pressures lower than 12 Pa. This explains the clear pressure dependence of K_V (Figure 4.1-3), following a trend similar to that of K_{WP} (Figure 4.1-4a).

The values of the heat transfer resistances $[K_{WP}A_{WP} \,/\, (nA_{HV})]^{-1}$ and $(K_{HV})^{-1}$ were considerably lower than $(K_V)^{-1}$ for serum vials determined by Scutellà et al. (2017a), 3 times and 20 times lower, respectively (at chamber pressures lower than 12 Pa). The low values of $[K_{WP}A_{WP} \,/\, (nA_{HV})]^{-1}$ were due to the high quality of momentum exchange between the gas molecules and the well plate surface; as previously mentioned, the thermal accommodation coefficients between the shelf and the well plate (> 0.8, Table 4.1-3) were greater than that between the shelf and serum vials (≈ 0.33; Scutellà et al., 2017a). Furthermore, the low values of $(K_{HV})^{-1}$ were due to the flatness of the high-throughput vial bottoms, which increased the contact area (A^{cc}, Table 4.1-1) and the heat transfer by contact conduction; A_{HV}^{cc} represents 32% of the outer bottom area of high-throughput vials, while A_{ser}^{cc} is only 8% of the outer bottom area of serum vials. Finally, the low $[K_{WP}A_{WP} \,/\, (nA_{HV})]^{-1}$ and $(K_{HV})^{-1}$ explain why the high-throughput system was more effective to transfer the heat from the shelf to the vials than placing serum vials on the shelf.

Impact of vial geometry on the K_V distribution and predicted product temperature distribution

Figure 4.1-6 shows the distributions of the experimental K_V values of high-throughput vials in positions represented as green circles in Figure 4.1-2 (vials in the centre of the well plate), as well as the K_V distributions of serum vials placed in the centre of the shelf calculated from the results obtained by Scutellà et al. (2017a). Regardless of the well plate type (A-type or B-type) and vial size (500-µL or 1000-µL), we observed a significant variability in the K_V values, and the standard deviation (SD) increased with pressure from approximately 4 to 10 $W.m^{-2}.K^{-1}$. The K_V distribution of high-throughput vials appeared considerably wider than that of serum vials, with a coefficient of variation for high-throughput vials of approximately 14%, compared to 4-8% for serum vials (Scutellà et al., 2017a). The measurement uncertainty of K_V was estimated to be approximately 1%, and could therefore not explain the K_V variability observed.

By following the approach proposed by Scutellà et al. (2017a), we investigated the impact of vial geometry, in particular the contact area between the vial and the well plate on K_V variability. As mentioned before, l_{HV} values were too low to have an impact on K_{HV} ($l_{HV} \ll \frac{\lambda_{gas}^{cont}}{\alpha_{HV}\Lambda_o P_C}$), so its impact on K_V was not considered in this study. K_{HV}^{cc} can be expressed as a function of an empirical constant k_{HV}^{cc} and the vial bottom-well plate contact area A_{HV}^{cc} (Equation 4.1-18). A normal distribution of A_{HV}^{cc} values was created based on the mean value and standard deviation estimated by the imprint test. The simulated K_V distributions obtained using the A_{HV}^{cc} normal distribution and Equation 4.1-15, Equation 4.1-17, and Equation 4.1-18 are plotted as red lines in Figure 4.1-6. These simulated distributions were similar to the experimental distributions. As a result, A_{HV}^{cc} variability could potentially explain the heterogeneities of the heat flows received by vials in the centre of the same well plate. Similarly, Scutellà et al. (2017a) revealed the importance of the contact area on the variability of K_V of serum vials at chamber pressures lower than 15 Pa.

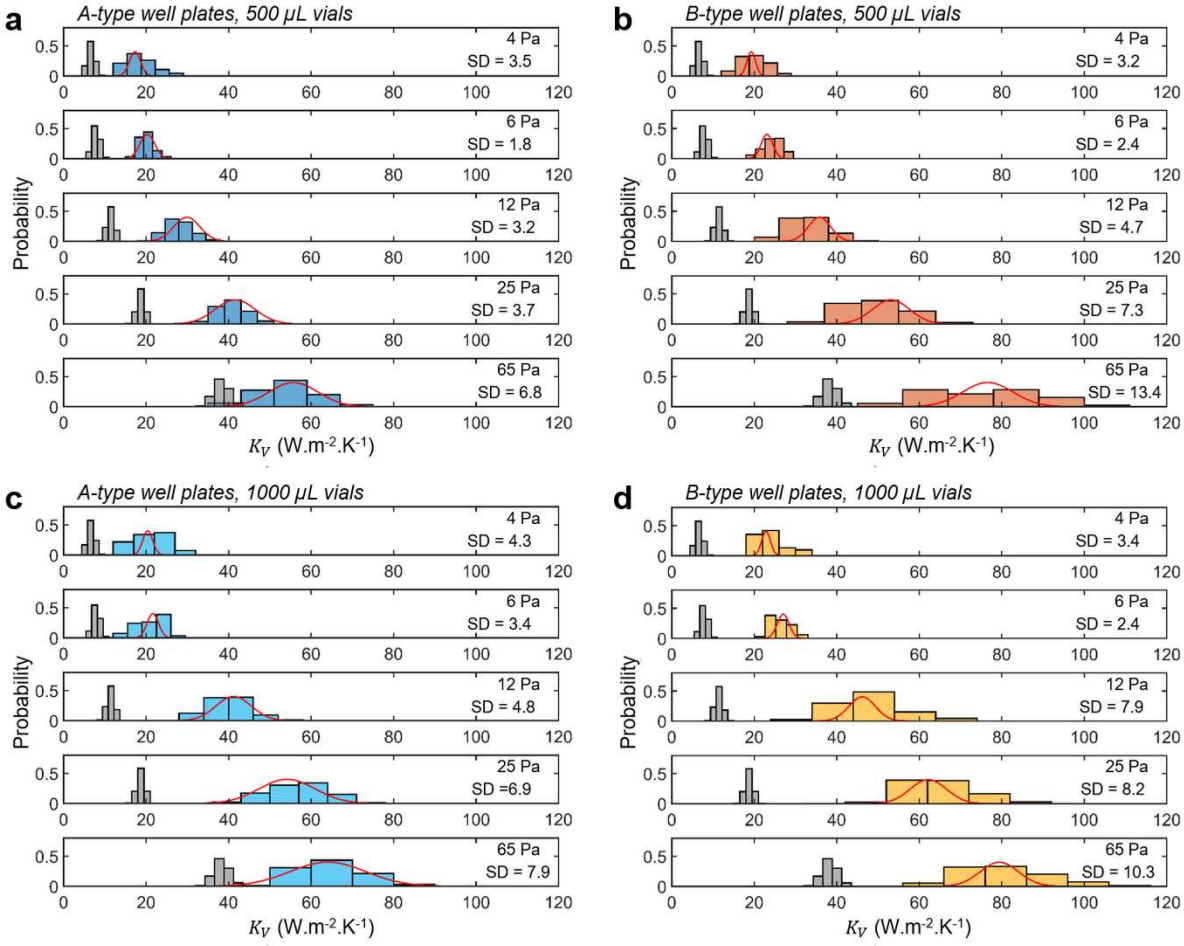

Figure 4.1-6 – Distributions of the heat transfer coefficient between the shelf and the vial (K_V) and their respective standard deviations (SD) for both well plate types and vial sizes. Distributions in grey are taken from Scutellà et al. (2017a) for serum vials. Red lines are the calculated K_V based on vial geometry variation (contact area) distributions. Results using: (a) 500-µL vials inside A-type well plates, (b) 500-µL vials inside B-type well plates, (c) 1000-µL vials inside A-type well plates, and (d) 1000-µL vials inside B-type well plates.

Product temperature (T_p) is a key process parameter governing product quality, in particular the visual aspect of the dried cake. Vial-to-vial variability of the heat and mass transfer during primary drying could result in T_p heterogeneities within the vial batch and, thus, in potential product quality variations. Figure 4.1-7 shows the T_p distributions based on the experimental K_V distributions of high-throughput vials and artificial K_V distributions of serum vials at different chamber pressures, considering a constant product resistance (1.248×10^5 Pa.s.m^2.kg^{-1}, Table 4.1-1) and a shelf temperature of -15 °C. Greater K_V values are associated with higher T_p values. As expected from K_V results, T_p increased with chamber pressure for all vial geometries, and T_p were greater for high-throughput vials than for serum vials. However, the temperature gap between both vial geometries decreased with chamber pressure from 6.5 °C at 4 Pa to 2.0 °C at 65 Pa. The variability of T_p using high-throughput vials was estimated to be approximately 2.6 °C at 12 Pa and 3.3 °C at 4 Pa, considering +/- 3 times the standard deviation reported in Figure 4.1-7 that includes 99.7% of the vials. Therefore, a temperature safety margin of 3 °C is recommended when designing freeze-drying cycles using high-throughput vials placed in the centre of a well plate, regardless of the well plate type and vial size. This margin is in agreement with the recommendations of Nail and Searles (2008) when using a design space. However, it is greater than the 2 °C proposed by Scutellà et al. (2017a) for serum vials because of the greater K_V standard deviations of high-throughput vials.

T_p values for each well plate type and vial size (500-µL and 1000-µL) differed due to the differences observed in K_V. When considering chamber pressures below 12 Pa, T_p values using 1000-µL vials were 1.6 °C higher than those using 500-µL (average increase considering both well plate types), and T_p values using B-type well plates were 1.1 °C higher than values using A-type well plates (average increase considering both high-throughput vial sizes). Therefore, the vial size and well plate type should be taken into account during freeze-drying experiments using high-throughput vial systems.

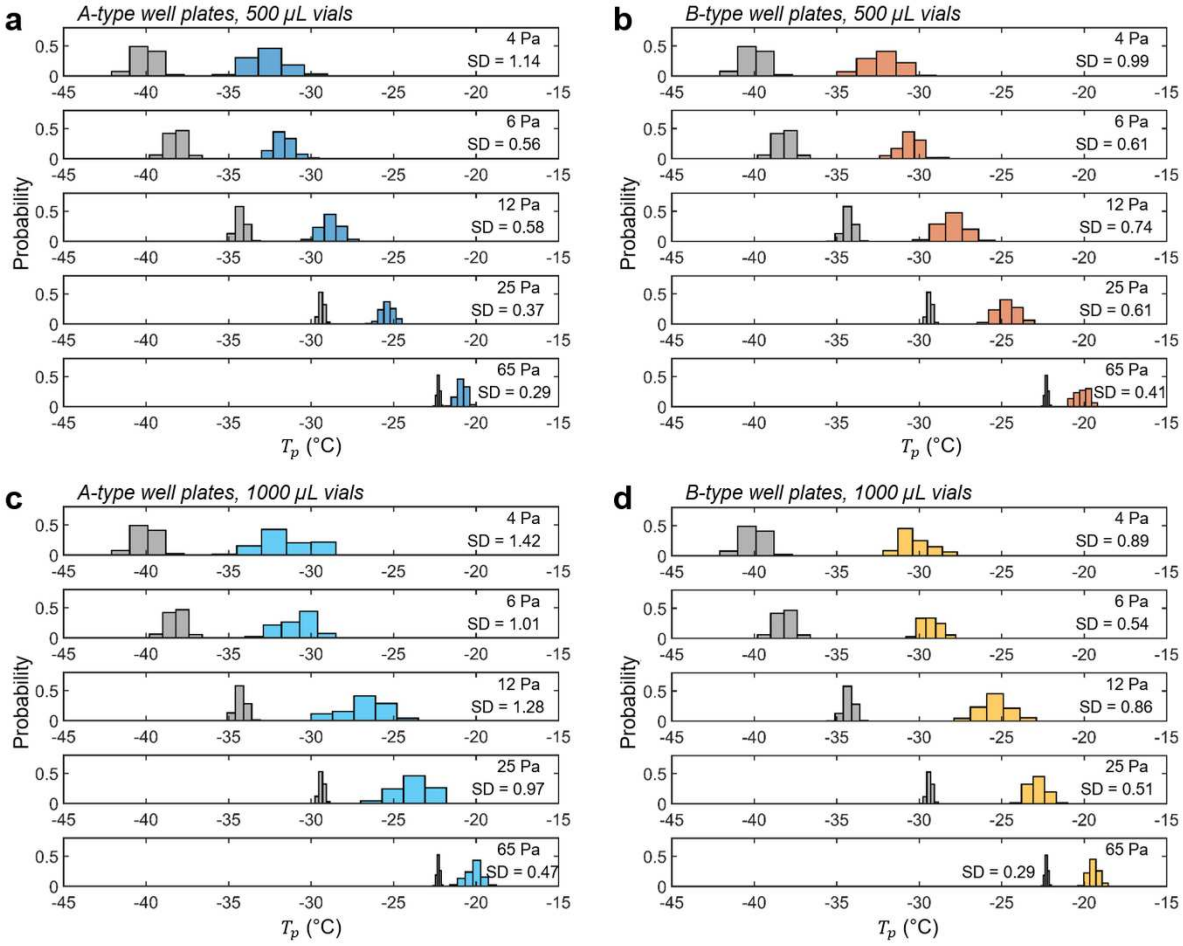

Figure 4.1-7 – Product temperature (T_P) distributions and standard deviations (SD) at shelf temperature (15 °C) obtained from the heat transfer coefficient between the shelf and the vial (K_V) for both well plate types and vial sizes. Distributions in grey are based on K_V taken from Scutellà et al. (2017a) for serum vials. Results using: (a) 500-µL vials inside A-type well plates, (b) 500-µL vials inside B-type well plates, (c) 1000-µL vials inside A-type well plates, and (d) 1000-µL vials inside B-type well plates.

Process scale-up from high-throughput to serum vials and vice versa

High-throughput vial systems are increasingly used to accelerate the formulation development stage since they require less active ingredients, and more formulations could be tested per freeze-drying cycle. Once a pool of formulations is pre-selected based on their aptitude to preserve the active ingredient, the final formulation is usually selected based on the physical properties: the collapse temperature and the glass transition temperature of the maximally freeze-concentrated phase (Pikal and Shah, 1990a). After selecting a given formulation using high-throughput vials, it is necessary to define the operating conditions during freeze-drying in the container used at industrial scales – in serum vials, for example. Conversely, it could be necessary to "translate" operating conditions of cycles developed using serum vials to cycles using high-throughput vials. The criterion for the "translation" between containers will be to maintain the same product thermal history during the process, in particular the same product temperature during sublimation. The strategies we propose to operate process scale-up from high-throughput to serum vials and scale-down from serum to high-throughput vials are analogous and consist of two steps: (*i)* creating a "design space" (Nail and Searles, 2008) to identify the optimal operating conditions using the departure vial geometry; and (*ii)* constructing a graphical solution to define the design space of the final vial geometry considering the operating condition selected for the departure vial geometry.

Figure 4.1-8a shows the design space for freeze-drying a 5% sucrose solution using high-throughput 500-µL vials in an A-type well plate; analogous figures are obtained applying the same approach to other high-throughput vial sizes and well plate types. Design spaces link the operating conditions during primary drying (i.e., shelf temperature and chamber pressure) with the predicted sublimation mass flows ($\dot{m}$) and the product temperature (T_p), serving as a graphical solution of Equation 4.1-1 to Equation 4.1-3, Equation 4.1-25, and Equation 4.1-27. The grey area in Figure 4.1-8a represents the operating conditions that involve a T_p lower than the maximum allowed product temperature. In this case, it was considered the collapse temperature of a 5% sucrose solution (-32 °C; Greco et al., 2013) minus the temperature safety margin defined in the previous section of this study (3 °C) for high-throughput vials in the centre of the well plate. This grey area represents the "safe" combinations of operating conditions that ensure a high quality freeze-dried product. It is possible to optimize the freeze-drying process by selecting an operating condition leading to the highest sublimation rate. For example, in Figure 4.1-8a, we have chosen the black square frame as the combination of operating conditions (a shelf temperature of -25 °C and a chamber pressure of 5 Pa) that allow the maximisation of the sublimation rate in high-throughput vials (y-axis), at a T_p of -36 °C.

Figure 4.1-8b presents the graphical method we built to identify the operating conditions using serum vials at the same product temperature reached during previous tests using high-throughput vials (scale-up). The graph links the shelf temperature (T_{shelf}^{ser}) and chamber pressure (P_C^{ser}) using serum vials to iso-T_p curves represented as linear colour maps obtained by solving Equation 4.1-1 to Equation 4.1-3, Equation 4.1-25, and Equation 4.1-27 applied to serum vials. This system of equations used to model the

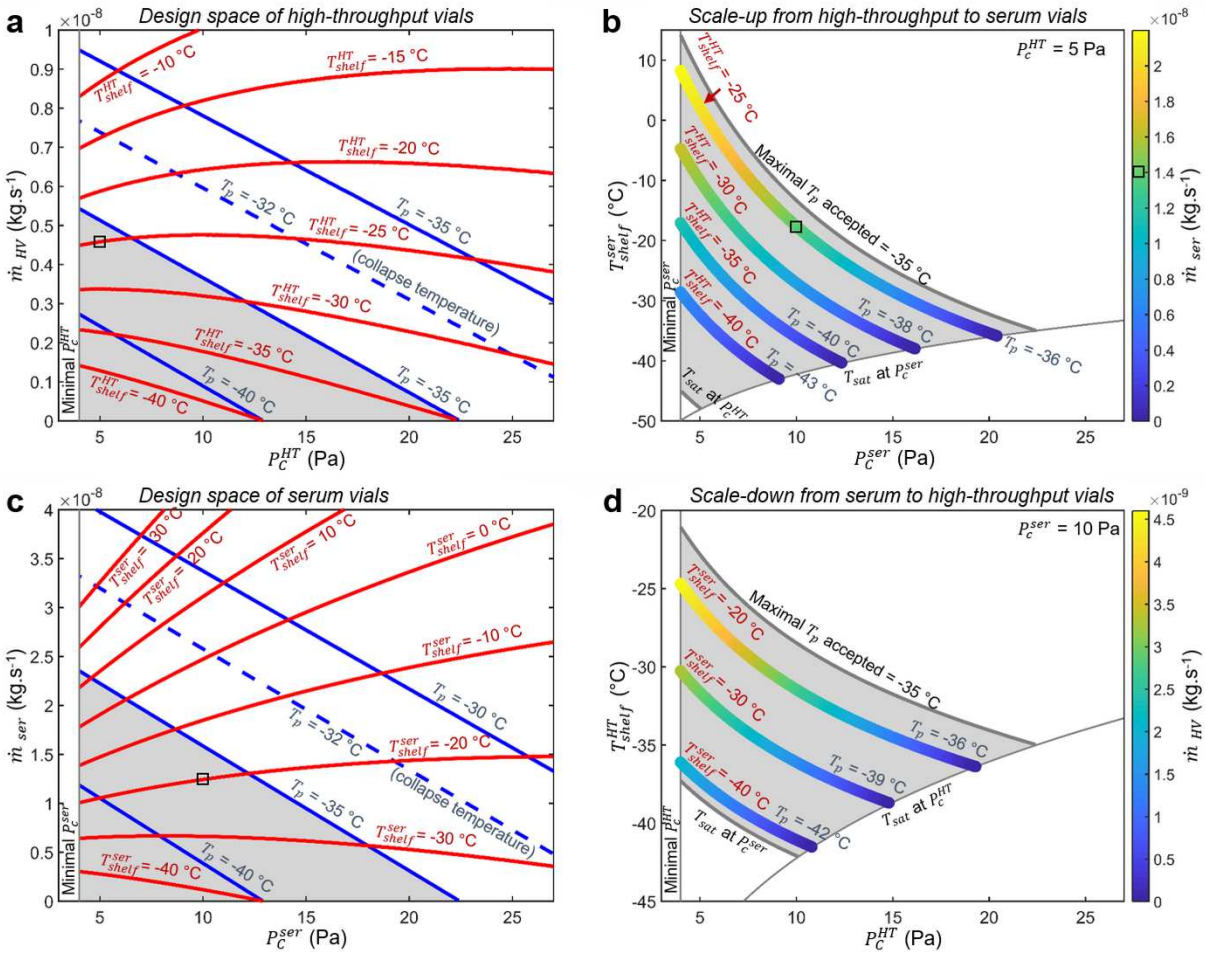

Figure 4.1-8 – Primary drying design spaces of a 5% sucrose solution calculated for: (a) high-throughput vials and (c) serum vials; and graphic solution to operate process change from: (b) high-throughput to serum vials, and (d) from serum to high-throughput vials. P_C^{HT}, T_{shelf}^{HT}, and $\dot{m}_{HV}$ are the chamber pressure, shelf temperature and sublimation mass flow rate during primary drying performed with high-throughput vials, respectively. P_C^{ser}, T_{shelf}^{ser}, and $\dot{m}_{ser}$ are the chamber pressure, shelf temperature and sublimation mass flow rate during primary drying performed with serum vials, respectively. T_{sat} is the ice-vapour equilibrium temperature. T_p is the product temperature, and the maximal T_p considered was -35 °C. Blue lines in (a) a and (c) represent iso-T_p curves and red lines iso-T_{shelf} curves. The grey area in the four graphs represents the safe zone of the process where T_p is lower than -35 °C. Linear colour maps in (b) and (d) represent iso-T_p curves. Calculations were performed considering the global heat transfer coefficient between the shelf and the vial bottom for 500-µL vials in A-type well plates.

heat and mass transfer for each vial geometry has two degrees of freedom; hence, we only need to fix two inputs to define the system. Interesting inputs to fix from a practical point of view could be: the chamber pressure, the shelf temperature, T_p, or $\dot{m}$. Figure 4.1-8b was designed for the chamber pressure value previously selected by process optimisation in high-throughput vials using Figure 4.1-8a (P_C^{HT} = 5 Pa); consequently, iso-T_p curves are associated with only one shelf temperature condition when considering high-throughput vials (T_{shelf}^{HT}). For our example, all the different combinations of T_{shelf}^{ser} and P_C^{ser} represented in the iso-T_p= -36 °C (T_{shelf}^{HT} = -25 °C) correspond to the operating conditions using high-throughput vials represented as a black square frame in Figure 4.1-8a. It is then possible to select the optimal combination of operating conditions to maximise the sublimation rate using serum vials (colour scale in Figure 4.1-8b) by moving towards lower P_C^{ser} values in the iso-T_p curve (yellow part of the iso-T_p= -36 °C curve). Nevertheless, working at low chamber pressures could involve a greater edge effect between serum vials (Pisano et al., 2011; Scutellà et al., 2017b) and/or require a finer control of the chamber pressure to avoid process deviations. We selected a chamber pressure (P_C^{ser}) of 10 Pa (moderate value), corresponding to a shelf temperature (T_{shelf}^{ser}) of -18 °C represented as the black square frame in Figure 4.1-8b, obtaining a mass flow rate in serum vials of 1.4×10^{-8} kg.s^{-1}. The grey area in Figure 4.1-8b represents the operating conditions that are safe to apply using serum vials and "translatable" between geometries. The limits of the grey area are: the maximal T_p accepted at the top edge, the minimal pressure using serum vials at the left edge, the zero mass flow conditions using serum vials at the right edge (T_{sat} at P_C^{ser}), and the zero mass flow condition using high-throughput vials at the bottom edge (T_{sat} at P_C^{HT}).

Figure 4.1-8c and Figure 4.1-8d illustrate the procedure applied when "translating" operating conditions from serum to high-throughput vials (scale-down). When using serum vials, the operating conditions represented by the black square frame in Figure 4.1-8c were selected: shelf temperature of -20 °C and chamber pressure of 10 Pa. Analogously to Figure 4.1-8b, the grey area in Figure 4.1-8d represents the safe area of operating conditions that could be applied with high-throughput and serum vials.

CONCLUSIONS

There is a growing demand from some pharmaceutical companies to consider the steps of formulation screening, process optimization, and scale-up in an integrated way. For this reason, the primary packaging of the final product is increasingly often defined in advance before starting the formulation development. The use of a high-throughput vial system to screen formulations during freeze-drying could accelerate the development of new pharmaceutical products. Additionally, identifying the operating conditions that entail the same product temperature when using the final production container (serum vials for instance) would lead researchers to develop representative processes at pilot or industrial scale. This identification will require forecasting heat transfer parameters and heterogeneities in both geometries. We established that the surface finish of the well plate and the height of the vials influence the heat transfer. Variations between well plate types were due to the conduction within the gas trapped between the shelf and the well plate, as well as the contact conduction at pressures lower than 12 Pa. Variations in the heat flow received by high-throughput vials in the centre of a well plate could be explained by the contact conduction between the well plate and the vial. The variability in the heat flow resulted in the identification of a product temperature safety margin of 3 °C for choosing the operating conditions to be applied during primary drying using a design space approach.

The heat transfer coefficients between the shelf and the vial bottoms (K_V) were approximately three times greater in high-throughput vials than in serum vials at chamber pressures lower than 12 Pa; consequently, the predicted product temperatures were in average 8 °C higher using high-throughput vials than serum vials at a shelf temperature of -15 °C and chamber pressures lower than 12 Pa. A novel diagram representing the operating conditions at the same product temperature in high-throughput vials and serum vials is proposed. This diagram presents a range of operating conditions that are possible to scale-up or scale-down.

Further research should be conducted on the impact of the vial position in the well plate on the heat flow received.

4.1.4. Take-Home Message

For the pressure range used for vaccine production (lower than 12 Pa), the heat transfer coefficients between the shelf and the vial bottoms (K_V) were approximately 3 times greater in high-throughput vials than in serum vials. Therefore, considering the same dried product resistance to mass transfer (R_P), the predicted product temperatures were approximately 8 °C higher using high-throughput vials than serum vials. An original diagram was proposed to "translate" the operating conditions (i.e. shelf temperature and chamber pressure) between high-throughput and serum vials to obtain the same product temperature.

At chamber pressures lower than 12 Pa, the heat transfer variations between well plates were due to the heat transfer by conduction within the gas trapped between the surfaces and by contact conduction. The heat transfer variations between vials in the centre of the well plate were due to the heat transfer by contact conduction.

This Section 4.1 considered the heat transfer from the shelves to high-throughput vials in the centre of the well plate, surrounded by other vials. Vials at the edge of the well plate, may receive higher total heat flows due to heat contributions from the chamber surfaces (e.g. chamber wall). In this regard, the following Section 4.2 studies the heat transfer variations among high-throughput vials due to their position inside the well plate.

4.2. How the High-Throughput Vial Position in the Well Plate Impacts the Heat Transfer

4.2.1. Context

The freeze dryer's shelves are considered the main heat source in the drying chamber during the primary drying step of freeze-drying. However, the chamber surfaces (e.g. walls) are commonly warmer than the shelves and may contribute to the total heat flow received by the vials (Pikal et al., 2016a; Wegiel et al., 2018). Those vials at the edge of the arrangement on the shelf (edge vials) are more directly exposed to the chamber surfaces, and therefore may receive a greater heat flow contribution from these surfaces than the vials in the centre of the arrangement (central vials). The increase in the total heat flow received from central vials compared to edge vials is commonly referred to as the "edge vial effect" (Rambhatla and Pikal, 2003). Such an effect causes higher product temperatures in the edge vials than in the central vials. When the process is carried out so that the product temperature is close to the collapse temperature, the edge vial effect could entail heterogeneities in the final product quality within the batch.

Previous authors studied the edge vial effect using serum vials during the primary drying step of freeze-drying (e.g. Pisano et al., 2011; Scutellà et al., 2017b). However, to the best of this author's knowledge, no work has been published on how the high-throughput vial position impacts the heat flow received. The edge vial effect is commonly studied based on the results obtained during sublimation in vials filled with water (only). In this way, vials do not contain a dried product layer, so the mass transfer from the sublimation front to the chamber is not considered, and the heat transfer is "decoupled" from the mass transfer. As useful as these results of "decoupled" heat transfer experiments may be for determining heat transfer coefficients, such results do not represent the actual (coupled) heat and mass transfer during primary drying, and need to be completed by the consideration of the mass transfer in the dry product layer.

4.2.2. Objectives

The present Section 4.2 studies how the high-throughput vial position in the well plate – with respect to a chamber wall – affects the heat transfer during primary drying. To do so, 3D steady-state mechanistic models are proposed to represent different stages of primary drying. Mathematical modelling would allow us to go beyond the results of sublimation tests in high-throughput vials filled with water (only), and predict how heat transfer variations may evolve during primary drying, as a dried product layer forms.

4.2.3. Paper II

This article was published in the journal Applied Thermal Engineering Volume 207, in May 2022 (10.1016/j.applthermaleng.2022.118099).

TITLE

"Use of 3D mathematical modelling to understand the heat transfer mechanisms during freeze-drying using high-throughput vials"

AUTHORS

Juan Patricio Buceta[1], Stéphanie Passot[1], Bernadette Scutellà[2], Erwan Bourlés[2], Fernanda Fonseca[1], and Ioan Cristian Trelea[1]

[1] Université Paris-Saclay, INRAE, AgroParisTech, UMR SayFood, F-78850, Thiverval-Grignon, France

[2] GSK, Rixensart, Belgium

CONFLICTS OF INTEREST

Erwan Bourlés and Bernadette Scutellà are employees of the GSK group of companies. Juan Patricio Buceta participated in a post-graduate PhD programme at GSK. Stéphanie Passot, Fernanda Fonseca and Ioan Cristian Trelea report no financial conflicts of interest.

AUTHOR'S CONTRIBUTIONS

Juan Patricio Buceta, Stéphanie Passot, Bernadette Scutellà, Erwan Bourlés, Fernanda Fonseca and Ioan Cristian Trelea were involved in the conception and design of the study. Juan Patricio Buceta, Bernadette Scutellà and Erwan Bourlés acquired the data. Juan Patricio Buceta, Stéphanie Passot, Bernadette Scutellà, Erwan Bourlés, Fernanda Fonseca and Ioan Cristian Trelea analysed and interpreted the results. All authors were involved in drafting the manuscript or critically revising it for relevant intellectual content. All authors had full access to the data and approved the manuscript before it was submitted by the corresponding author.

CONTENTS OF PAPER II

ABSTRACT

Screening potential vaccine formulations during freeze-drying is a time-consuming task. High-throughput systems, consisting of small vials inside aluminium well plates, can accelerate formulation selection. However, heat transfer variations among vials due to the edge effect can entail deviations in the final product quality and bias results. This work investigates how the vial position in the well plate impacts the heat flow received during the primary drying step of freeze-drying. Two 3D steady-state models were proposed and compared to evaluate the effect of time passing. One model, called the *distilled water model*, represents vials containing only a frozen layer at the beginning of primary drying. A second model, called the *product model*, represents vials containing frozen and dried product layers after drying has progressed (up to half of the product dried). Heat transfer models were validated using heat flows determined by gravimetric analysis during sublimation tests (shelf temperatures -40 and -15 °C, chamber pressures from 4 to 65 Pa). At the beginning of primary drying, the *distilled water model* indicated that vials facing a chamber wall received heat flows up to 25% greater than those in the centre of the well plate. As sublimation progressed (*product model*), the dried product layer resistance to mass transfer tended to counterbalance the impact of the chamber wall.

KEYWORDS

Lyophilisation; Vaccines; 3D modelling; Well plate; Edge effect; Vial heat transfer coefficient; Inter-vial heterogeneity; Product resistance.

INTRODUCTION

Freeze-drying or lyophilisation is a drying process that consists of three stages: (i) freezing the product solution, (ii) removing the frozen solvent (usually water) by sublimation (primary drying), and (iii) removing the unfrozen solvent by desorption (secondary drying). The low temperatures reached by the product make freeze-drying suitable to preserve thermolabile products like vaccines and proteins, among others (Bourlés et al., 2019; Passot et al., 2012b; Pikal et al., 1992).

The increasing demand for new vaccines pushes researchers to accelerate the development stage of formulations. The use of high- throughput vials systems consisting of aluminium 96-well plates and small tubular vials (maximal volume 1000 µL; Buceta et al., 2021; von Graberg, 2011) can improve the time efficiency during formulation screening for product development. High-throughput vial systems permit the placement of over twice the amount of containers on the shelf than serum vials (traditional container) (Buceta et al., 2021; Scutellà et al., 2017a) while also requiring fewer quantities of the active ingredient for the same number of tested formulations. Changing the container during the formulation development step implies modifications in the heat and mass transfer properties compared to the primary packaging used at the production scale (serum vials) (Pisano et al., 2011; Scutellà et al., 2017a). A graphical solution has been recently developed to manage the process scale-up and scale-down between both types of product containers (high-throughput vials used for formulation development and serum vials for production) (Buceta et al., 2021). This previous work showed that the heat transfer coefficients between the shelf and the vial bottoms (commonly denoted as K_V) were almost three times greater in high throughput vials than in serum vials in the usual range of conditions used in pharmaceutical freeze-drying (Buceta et al., 2021).

The product temperature is a critical quality parameter (Fissore et al., 2011; Patel et al., 2017; Vanbillemont et al., 2020) and should remain lower than a specific value during primary drying – known as collapse temperature – to preserve the product structure obtained by freezing and attain an acceptable final product appearance (Pikal and Shah, 1990a). Moreover, obtaining a freeze-dried product with a low moisture content (generally below 3%), a rapid reconstitution time, and no potency reduction, depends greatly on avoiding product collapse during primary drying. Several factors can affect the heat and mass transfer balance and the resulting product temperature; for example, the operating conditions (i.e. shelf temperature and chamber pressure) (Nail and Searles, 2008; Velardi and Barresi, 2008), the geometry of the containers (usually vials), (Brülls and Rasmuson, 2002; Scutellà et al., 2017a), and their location on the shelf (Rambhatla and Pikal, 2003; Sheehan and Liapis, 1998).

Previous experimental data suggest that the heat flow contribution from the chamber walls may not be negligible for serum vials located at the edge of the vials' arrangement on the shelf (e.g. Pikal et al., 2016, 1984; Pisano et al., 2011; Rambhatla and Pikal, 2003; Schneid and Gieseler, 2008; Wegiel et al., 2018). Many authors represented these "extra" heat flow contributions as a higher value of the heat transfer coefficient between the shelf and the vial (K_V) for vials at the edge compared to those in the centre (e.g.

Pikal et al., 2016, 1984; Pisano et al., 2011; Rambhatla and Pikal, 2003; Schneid and Gieseler, 2008; Wegiel et al., 2018), and estimated the product temperature using lumped-parameter models (0D models) for different vial positions (Giordano et al., 2011; Koganti et al., 2011), with the assumption that shelves are the only heat sources in the system (Pikal, 2000). However, the theoretical groud behind the modification of K_V to account for the heat transfer from these extra sources (e.g. chamber walls and door) may be questioned since their temperatures are different from those of the shelves (K_V was defined for the temperature difference between the vials and the shelf). Recently, a 3D steady-state model of the heat transfer during the sublimation step highlighted conduction through low-pressure water vapour as the dominant heat transfer mechanism to serum vials, also explaining the extra heat transfer to serum vials at the edge compared to central ones (Scutellà et al., 2017b). 3D modelling serves thus to avoid the shortcut of using K_V, detailing heat transfer mechanisms for each heat source (e.g. shelves, chamber walls) and their relative importance. However, the previous 3D model (Scutellà et al., 2017b) did not consider the resistance to mass transfer through the dried product layer when a pharmaceutical formulation was processed. Therefore, such a 3D model could not predict how the heat flow rate variation between vial positions would evolve throughout primary drying.

A similar edge effect is expected between high-throughput vials in a well plate, where high-throughput vials near a well plate edge may receive greater heat flows than those in the centre (surrounded by other vials). However, no research has been carried out on this matter to the best of our knowledge.

The main novelty of this paper was the extension of the 3D model previously developed for serum vials (Scutellà et al., 2017b) to represent the heat transfer mechanisms between the well plate and the high-throughput vials, as well as to include the mass transfer through the dried product layer and its coupling to the heat transfer. The present work thus aimed at better understanding the contribution of individual heat transfer mechanisms in high-throughput systems, the edge effect, and the impact of the product resistance associated with the progress of primary drying. We have considered primary drying as a succession of heat and mass transfer equilibria (Nail and Searles, 2008; Pikal et al., 1984), and studied the time effect using steady-state models representing different positions of the sublimation front. Based on the work of Scutellà et al. (2017b), two 3D steady-state models for heat and mass transfer during primary drying in high-throughput vials were thus proposed to consider the progress of time: (i) the *distilled water model*, and (ii) the *product model*. The *distilled water model* represented the beginning of primary drying when there is no dried product in the vials (only ice). The *product model* represented two stages during primary drying with two different thicknesses of a dried product layer (0.1 and 5 mm). Finally, a sensitivity analysis was performed with the *product model*, which indicated the parameters that should be measured carefully for a better estimation of the heat flows received by the vials.

EXPERIMENTAL DATA

Materials

Ice sublimation experiments were performed using the *96-Well Freeze-Drying System* manufactured by VirTis (SP Scientific, Stone Ridge, New York, USA), comprising aluminium well plates with a black matte finish and tubular glass vials (non-siliconised), as shown in Figure 4.2-1a. Two vial sizes were employed, both presenting the same diameter but differing in height, and consequently, in the maximal filled volume: (i) 500-µL (Figure 4.2-1a, left), and (ii) 1000-µL (Figure 4.2-1a, right). Figure 4.2-1b presents a picture of the vials and well plates inside a freeze dryer. Experiments were performed in an Epsilon 2-25D pilot scale freeze dryer (Martin Christ Gefriertrocknungsanlagen GmbH, Osterode am Harz, Germany). The freeze dryer had a drying chamber with a total volume of 0.38 m^3, and a capacitive manometer monitored the chamber pressure. Inside the chamber, there were seven shelves of 0.27 m^2 each; the distance between shelves was 57 mm.

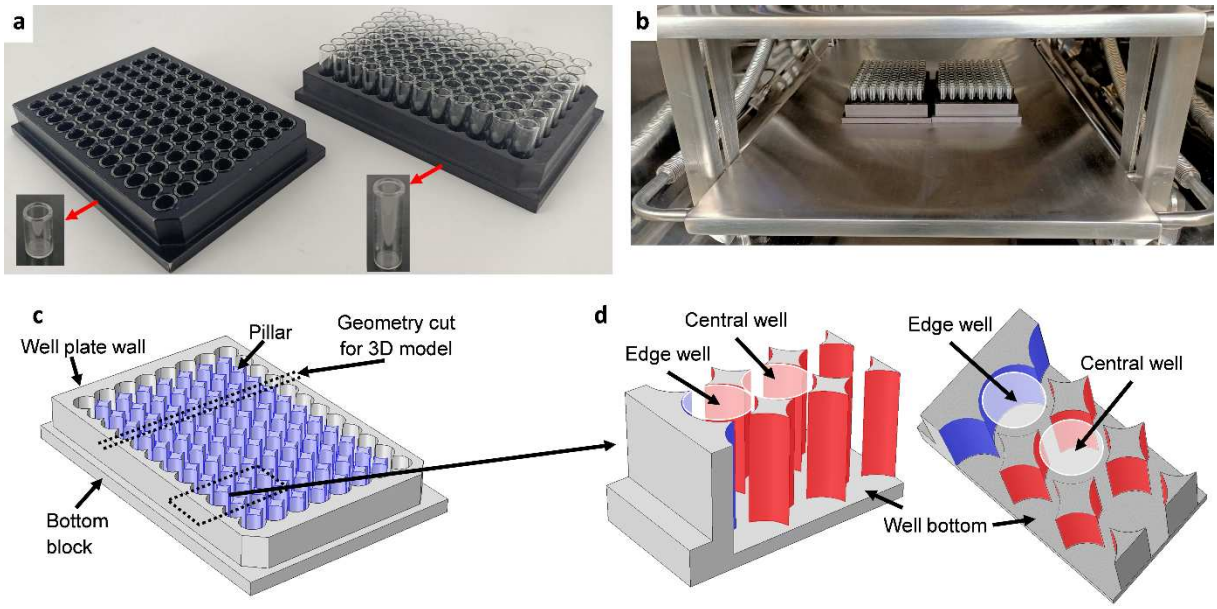

Figure 4.2-1 – Vials and well plate geometry. (a) Well plates filled with 500-µL vials (left) and 1000-µL vials (right). (b) Well plates and vials inside a freeze-dryer. (c) Well plate geometry with pillars coloured purple. (d) Geometry details with different view angles. Red surfaces are the pillar surfaces facing the vial. Blue surfaces are the well plate wall surfaces facing the vial.

Methods

Experimental heat flow rates received by vials were measured through gravimetric analysis, as detailed in Buceta et al. (2021). 500-µL vials were filled with 400 µL of distilled water, and 1000-µL vials were filled with 600 µL of distilled water. No stoppers were placed on the vial necks. Tempris wireless temperature probes (iQ-mobil solution GmbH, Holzkirchen, Germany) were used to register the ice temperature in six 1000-µL vials. Two well plates containing vials of the same size were loaded on the centre of the shelf pre-cooled at -50 °C. The freezing step lasted for 2 hours, then the sublimation step started by decreasing the pressure inside the chamber and increasing the shelf temperature at 1 °C.min^{-1} up to the set point. The inlet temperature of the heat-transfer fluid circulating inside the shelves was set to either -40 or -15 °C during sublimation. Furthermore, the shelf temperature was considered equal to the average between the inlet and the outlet temperature of the heat-transfer fluid due to the great conductivity of the metallic shelves. At a shelf temperature of -40 °C, the chamber pressure was set to 4 Pa, and at -15 °C, the chamber pressures tested were 4, 6, 12, 25, and 65 Pa. The sublimation step lasted until approximately 20% of each vial's initial ice content was removed, then this step was ended by rapidly breaking the vacuum inside the drying chamber. Vials were weighed before and after ice sublimation experiments using a robotic tube handler model XL9 manufactured by BioMicroLab (Concord, California, USA) with an analytical scale (± 1×10^{-7} kg). Time-averaged heat flows throughout the experiment ($\dot{Q}_{exp}$) were calculated for each vial as (Pisano et al., 2011; Scutellà et al., 2017a):

$$\dot{Q}_{exp} = \frac{m_{initial} - m_{final}}{\Delta t} \Delta H_{sub} \qquad \text{Equation 4.2-1}$$

The significance of all symbols is given in the Nomenclature. The sublimation was considered to start when the shelf temperature was higher than the ice-vapour equilibrium temperature at the chamber pressure, and finish when the vacuum was broken.

The temperature of the chamber walls was measured using Tempris wireless temperature probes (iQ-mobil solution GmbH, Holzkirchen, Germany) fixed using heat conductive tape during ice sublimation experiments at a chamber pressure of 4 Pa and a shelf temperature of -40 and -15 °C.

HEAT AND MASS TRANSFER MODEL

Well plate geometry

High-throughput vials were positioned inside aluminium well plates to keep them in place during freeze-drying, as shown in Figure 4.2-1a and Figure 4.2-1b. Figure 4.2-1c presents a 3D reconstruction of a well plate, indicating the main components: (i) the bottom block, (ii) the well plate wall, and (iii) the pillars. The geometry is not the same for all wells of the well plate; two types of well positions were distinguished: (i) well positions next to a well plate wall hereinafter referred to as edge wells (Figure 4.2-1d); (ii) well positions non-contiguous to a well plate wall hereinafter referred to as central wells (Figure 4.2-1d). Edge wells have four surfaces facing the vials: a bottom surface (Figure 4.2-1d), two lateral surfaces belonging to the two metallic pillars around (Figure 4.2-1d, red surfaces), and one lateral surface belonging to the well plate wall (Figure 4.2-1d, blue surface). Central wells have five surfaces facing the vials: a well bottom surface (Figure 4.2-1d), and four lateral surfaces belonging to the four metallic pillars around (Figure 4.2-1d, red surfaces).

Due to the dimensions and geometry of the system, it is not possible for the vials to touch either four pillars (in the case of central vials) or two pillars and the well plate wall (in the case of edge vials) simultaneously. Therefore, for all vials and well positions, physical contact was only considered between: (i) the vial side and only two pillars referred to as “physical contact” pillars, and (ii) the vial bottom and the well bottom. Note that the differences between edge and central wells did not imply that edge wells and vials had more physical contact than central wells and vials; thus, all well and vial positions were assumed to have the same physical contact.

Model geometry

3D models represented ice sublimation using 500-µL or 1000-µL vials inside the well plate filled with either distilled water or a "model" product (5% w/w sucrose aqueous solution). Figure 4.2-2a shows the geometry used for 500-µL vials as an example, the geometry for 1000µL vials is similar (with higher vial and content heights). Each geometry represented: (i) a portion of the drying chamber wall, (ii) a fragment of the top and bottom shelves; (iii) eight half-vials (two edge half-vials and six central half-vials), all filled with either an ice layer or presenting a dried product layer and a frozen product layer (Figure 4.2-2b); (iv) the section of the well plate where the vials were placed, including four physical contact pillars (red arrow in Figure 4.2-2a) and three non-physical contact pillars, so each half-vial "rested" on one physical contact pillar.

Edge vials and edge wells in the geometry were further subdivided according to the well plate position on the shelf (Figure 4.2-2): (i) edge positions facing a chamber wall were referred to as outer edge positions, and (ii) edge positions facing another well plate were referred to as inner edge positions.

Different 3D geometries were built depending on the vial size and content. The model considering all vials filled with an ice layer (only) is referred to as the *distilled water model*, and the model considering all vials presenting a dried product layer and a frozen product layer is referred to as the *product model*. In the *distilled water model*, the vial content was only an ice cylinder (Scutellà et al., 2017b) with a volume equal to 90% of the initial ice volume used in the sublimation experiments. This represents an "average" situation during the laboratory experiments between the beginning of the ice sublimation (0% of the ice mass was removed) and the end (approximately 20% of the ice mass removed). In the *product model*, the vial content was a cylinder of frozen product with a cylinder of dried product on top; the total volume of both cylinders was considered equal to the initial ice volume used in the sublimation experiments. All dimensions relevant to the 3D model geometry are reported in Table 4.2-1.

When considering the dynamics of the primary drying step, the *distilled water model* can be associated with the beginning of this step, where the dried layer is not yet present. In contrast, the *product model* represents an intermediate moment during primary drying, after the appearance and progress of a sublimation front (ice-vapour interface) that moves from the top to the bottom of the vial content, leaving a dried product layer above the remaining frozen product layer (Figure 4.2-2b).

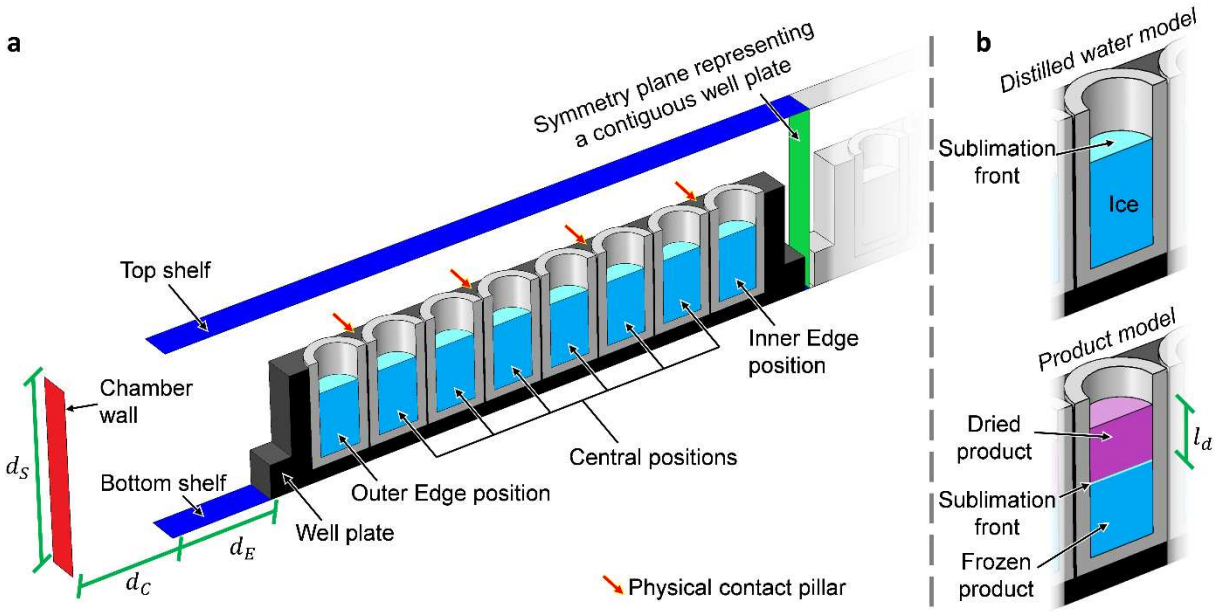

Figure 4.2-2 – Model geometry (not in scale) for 500-µL vials in well plates. (a) Overall view, with only the vials closer to the chamber wall represented for clarity. (b) Detail of the vial and its content for distilled water and product models. d_S is the vertical distance separating shelves, d_C is the distance between the shelf and the chamber wall, d_E is the distance between the edge of the shelf and the well plate, and l_d is the dried product layer thickness.

Table 4.2-1 – Relevant physical constants, geometric dimensions, and other model parameters from the literature.

Parameter	Value	Units	Source
Physical constants			
d_{gas}	2.8×10^{-10}	m	(D'Arrigo, 1978)
k	1.38×10^{-23}	$J.K^{-1}$	(Perry and Green, 2008)
P_t	612	Pa	(Perry and Green, 2008)
R	8.3144	$J.K^{-1}.mol^{-1}$	(Perry and Green, 2008)
T_t	273.16	K	(Perry and Green, 2008)
α	0.87	Dimensionless	(Pikal, 2000)
ΔH_{sub}	2.763×10^{6}	$J.kg^{-1}$	(Scutellà et al., 2017a)
$\widetilde{\Delta H_{sub}}$	5.11×10^{4}	$J.mol^{-1}$	(Murphy and Koop, 2005)
ε_d	0.95	Dimensionless	(Emteborg et al., 2014)
ε_{ice}	0.98	Dimensionless	(Heldman and Moraru, 2010)
ε_{shelf}	0.18	Dimensionless	(Buceta et al., 2021)
ε_{vial}	0.85	Dimensionless	(Buceta et al., 2021)
ε_{wall}	0.13	Dimensionless	(Buceta et al., 2021)
ε_{wp}	0.87	Dimensionless	(Buceta et al., 2021)
Λ_0	1.99	$W.m^{-2}.K^{-1}.Pa^{-1}$	(Pikal, 2000)
σ	5.67×10^{-8}	$W.m^{-2}.K^{-4}$	(Perry and Green, 2008)
λ_{gas}^{cont}	0.025	$W.m^{-1}.K^{-1}$	(Haynes, 2014)
λ_{ice}	2.23	$W.m^{-1}.K^{-1}$	(M. S. van Dusen, 1929)
λ_d	0.043	$W.m^{-1}.K^{-1}$	5% of the sucrose thermal conductivity (Renaud et al., 1992; Smith et al., 2013)
Geometric dimensions			
d_C	1.08×10^{-1}	m	Measured
d_E	1.40×10^{-1}	m	Measured
d_S	5.7×10^{-2}	m	Measured
d_{VE}	8.82×10^{-3}	m	(Buceta et al., 2021)
d_{VI}	7.20×10^{-3}	m	(Buceta et al., 2021)
h_{well}	1.525×10^{-2}	m	(Buceta et al., 2021)
l_d	1×10^{-4} or 5×10^{-3}	m	Consideration for this work
l_{HV}^{B}	6.7×10^{-5}	m	(Buceta et al., 2021)
l_{HV}^{S}	2.3×10^{-4}	m	(Buceta et al., 2021)
V_i	392 (for 500-µL vials) 589 (for 1000-µL vials)	µL	90% of the initial ice volume

Continuation of Table 4.2-1.

Parameter	Value	Units	Source
Geometric dimensions			
V_p	436 (for 500-µL vials)	µL	Initial frozen volume
	654 (for 1000-µL vials)		
Other model parameters			
l_{fp}	1.0×10^{-3}	m	Calculated using Equation 4.2-5
R_P	0.119×10^{5}	$Pa.s.m^2.kg^{-1}$	(Konstantinidis et al., 2011)
	1.248×10^{5}		
T_{wall}	0.1 (for T_{shelf} = -15 °C)	°C	Measured
	5.1 (for T_{shelf} = -40 °C)		

Distilled water model

The *distilled water model* was developed and validated based on the laboratory ice sublimation experiments described in Section *Methods* (of this Paper II). The heat transfer mechanisms considered in this work are schematised in Figure 4.2-3. Figure 4.2-3a and Figure 4.2-3b refer to the heat transfers between surfaces and within bodies at a macroscopic scale, while Figure 4.2-3c represents the heat transfers between surfaces at a microscopic scale. The heat transfer mechanisms of the model were:

(i) *Conduction through solids*, concerning the well plate, vials, and ice (yellow arrows in Figure 4.2-3a and Figure 4.2-3b).

(ii) *Contact conduction between solids*, including the contact between the bottom shelf and the well plate bottom, the wells (bottom and physical contact pillars) and the vials (red triangles in Figure 4.2-3c), and the vials and the ice (red dashes in Figure 4.2-3c).

(iii) *Conduction through the gas* (green arrows in Figure 4.2-3a and Figure 4.2-3c); the thermal conductivity of gases in vacuum conditions depends on the gas regime, according to the ratio between the average distance a gas molecule travels between collisions with other molecules (mean free path) and the separation between surfaces.

(iv) *Radiation* emitted and received by the wall, both shelves, the well plate, the vials, and the ice (orange "lightning" arrows in Figure 4.2-3a and Figure 4.2-3c).

Heat transfer by convection was considered negligible, as previously proved by other authors in similar operating conditions (Mascarenhas et al., 1997; Pikal et al., 2016a; Sheehan and Liapis, 1998). To support this assumption, the Rayleigh number (Ra) near the vials was estimated to be between 300 and 1300 depending on the operating conditions, which is lower than the critical value required for a significant contribution of heat transfer by convection ($Ra > 1700$; Heitz and Westwater, 1971; Perry and Green, 2008).

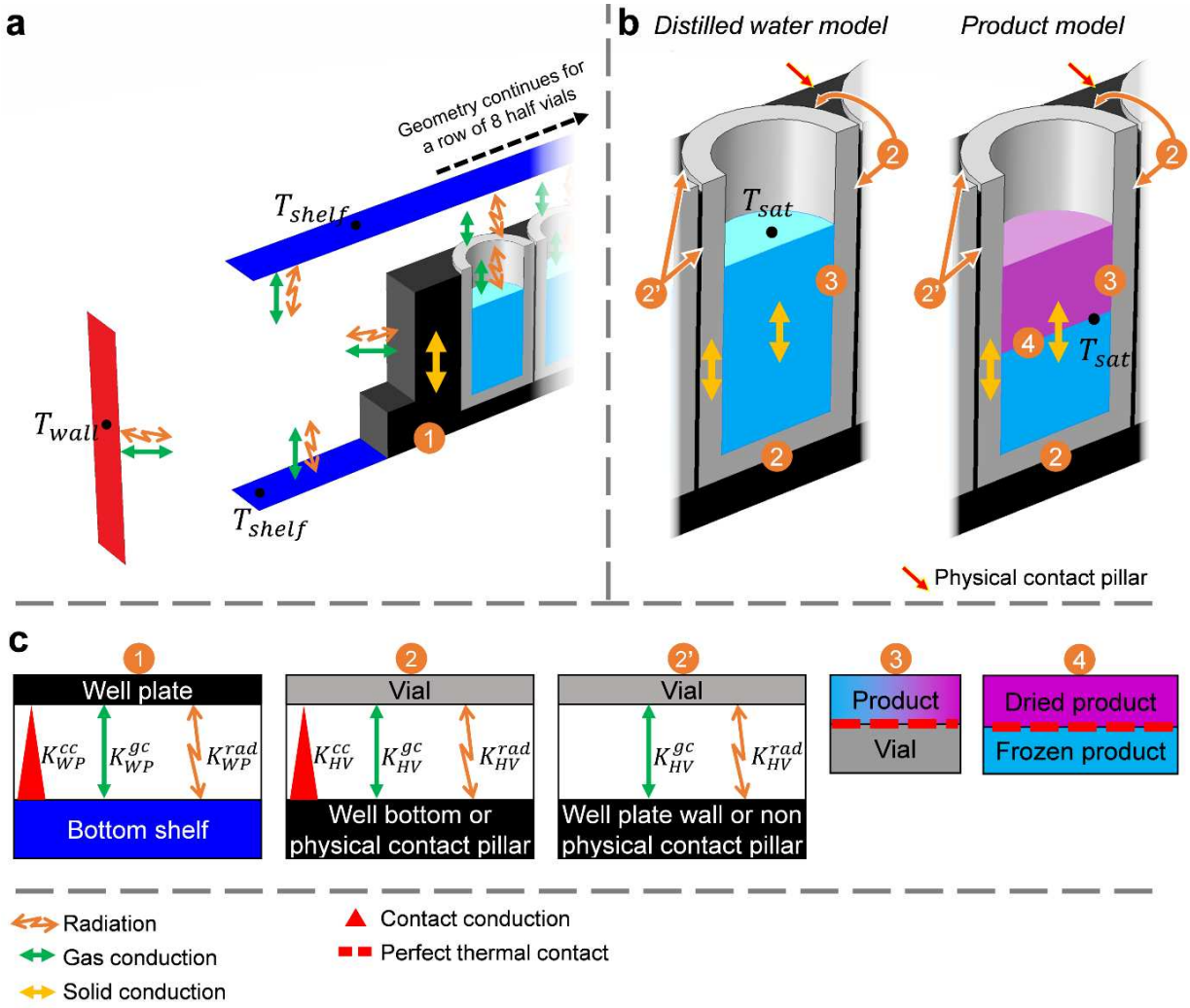

Figure 4.2-3 – Schematic representation (not in scale) of the main heat transfer mechanisms and fixed temperatures in the analysed system. (a) Overall view, only the vials closer to the chamber wall are represented for clarity. (b) Details of the mechanisms within the vial and its content for the distilled water and product models. (c) Heat transfer mechanisms at a microscopic scale. K_{WP} and K_{HV} are detailed according to the individual heat transfer mechanism involved: K^{cc} by contact conduction, K^{gc} by conduction through the gas trapped between the surfaces, K^{rad} by radiation.

Conduction through solids

At a microscopic scale, thermal conduction within a body is the mechanism by which heat is transferred due to collisions between the body particles (Perry and Green, 2008). At a macroscopic scale, the conductive heat flux (q^c, W.m^{-2}) within the solids (well plate, vials, and ice) were calculated using Fourier's law:

$$q^c = \lambda \nabla T \qquad \text{Equation 4.2-2}$$

Conductivity values are reported in Table 4.2-1.

Contact conduction between solids

Heat transfer by contact conduction occurs between solids directly touching each other and depends on the macroscopic (apparent) contact area and the microscopic state of the surface, such as roughness. The contact conduction heat flux between the bottom shelf and the well plate bottom (q_{WP}^{cc}, W.m^{-2}), symbolised by a red triangle in Figure 4.2-3c, was calculated as:

$$q_{WP}^{cc} = K_{WP}^{cc}\left(T_{shelf} - T_{WP}\right) \qquad \text{Equation 4.2-3}$$

Similarly, the contact conduction heat flux (q_{HV}^{cc}) between the well bottoms and the vial bottoms, and between the physical contact pillars and the vial sides, symbolised by red triangles in Figure 4.2-3c, were calculated as:

$$q_{HV}^{cc} = K_{HV}^{cc}(T_{WP} - T_{vial}) \qquad \text{Equation 4.2-4}$$

K_{WP}^{cc} and K_{HV}^{cc} were estimated based on experimental data as detailed in the Section *Parameter estimation* (of this Paper II), and values are reported in Table 4.2-2. The heat transfer mechanism between the vials and the ice, symbolised by a red dashed line in the orange dot 3 of Figure 4.2-3c, was considered perfect contact conduction (zero resistance to the heat transfer). Hence, the local temperature of the vial and the ice was the same at their contact surface.

Table 4.2-2 – Values of parameters estimated based on measured heat flow data for 500-µL vials at a shelf temperature of -15 °C and chamber pressures of 4, 12, and 65 Pa.

Parameter	Mean value in this work	95 % Confidence interval		Units
		This work	(Buceta et al., 2021)*	
Heat transfer from the bottom shelf to the well plate bottom				
K_{WP}^{cc}	5.1	1.6 – 8.6	2.4 – 4.8	$W.m^{-2}.K^{-1}$
α_{WP}	0.95	0.60 – 1.00**	0.764 – 0.932	Dimensionless
l_{WP}	4.20×10^{-4}	2.46×10^{-4} – 5.29×10^{-4}	2.23×10^{-4} – 2.58×10^{-4}	m
Heat transfer from the wells to the vials				
K_{HV}^{cc}	20.1	12.1 – 28.1	59.7 – 66.5	$W.m^{-2}.K^{-1}$
α_{HV}	0.33	0.29 – 0.37	0.184 – 0.319	Dimensionless

** Values reported for 500-µL vials in a "B-type well plate", which refers to a well plate type described in* Buceta et al. (2021).

*** Upper bound truncated to the maximum possible physical value.*

Conduction through the gas

The heat transfer by conduction through the gas phase in the system was divided as: (i) gas conduction within the chamber, concerning the largest gas volume in the chamber, symbolised by green arrows in Figure 4.2-3a; or (ii) conduction through the gas trapped between adjacent surfaces (i.e. between the bottom shelf and the well plate bottom, and between the wells and the vials), symbolised by green arrows in Figure 4.2-3c.

Gas conduction within the chamber

All the gas in the freeze dryer chamber was assumed to be water vapour (Pikal, 2000). Heat transfer by conduction through the gas within the chamber (Figure 4.2-3a) was considered under a continuous regime with a boundary layer of free molecular regime next to all the solids in the chamber (i.e. wall, shelves, well plate, vials, and ice; Figure 4.2-3a). Scutellà et al. (2017b) fixed the boundary layer thickness as a value relatively small compared to the serum vial geometry. Similarly, in our work, the boundary layer thickness was selected as the mean free path (l_{fp}, 1 mm) calculated at 10 Pa (usual chamber pressure value used in pharmaceutical freeze-drying) and -15 °C (= 258.15 K, usual shelf temperature value) as (Hoffman et al., 1997):

$$l_{fp} = \frac{\kappa \times 258.15\ [K]}{\sqrt{2}\pi {d_{gas}}^2 \times 10\ [Pa]} \qquad \text{Equation 4.2-5}$$

Fourier's law (Equation 4.2-2) was used to model the conductive heat flux within the gas, and the thermal conductivity depended on the gas regime. Outside of the boundary layer (gas portion farther than a mean free path from the solids), the gas was considered under a continuous regime and the thermal conductivity (λ_{gas}^{cont}) was that of water vapour at atmospheric pressure (Scutellà et al., 2017b). Inside the boundary layer (gas portion closer than a mean free path from the solids), the gas was considered under a free molecular regime, and the thermal conductivity (λ_{gas}^{fm}) was calculated as (Scutellà et al., 2017b):

$$\lambda_{gas}^{fm} = \alpha \Lambda_0 P_C l_{fp} \qquad \text{Equation 4.2-6}$$

Relevant constant values are reported in Table 4.2-1.

Conduction through the gas trapped between adjacent surfaces

The heat flux by conduction through the trapped gas between the bottom shelf and the well plate bottom (q_{WP}^{gc}, W.m^{-2}), symbolised by a green arrow in the orange dot 1 of Figure 4.2-3c, was expressed as:

$$q_{WP}^{gc} = K_{WP}^{gc}\left(T_{shelf} - T_{WP}\right) \qquad \text{Equation 4.2-7}$$

Similarly, the heat flux by conduction through the trapped gas between the wells and the vials (q_{HV}^{gc}), symbolised by a green arrow in Figure 4.2-3c, was:

$$q_{HV}^{gc} = K_{HV}^{gc}(T_{WP} - T_{vial}) \qquad \text{Equation 4.2-8}$$

The heat transfer by conduction through gas trapped between adjacent surfaces is traditionally assumed under a transition regime between free molecular and continuous regimes (Pikal, 2000, 1985; Pisano et al., 2011; Scutellà et al., 2017a). K_{WP}^{gc} was thus calculated as (Pikal, 2000):

$$K_{WP}^{gc} = \frac{\alpha_{WP}\Lambda_o P_C}{1 + \frac{l_{WP}}{\lambda_{gas}^{cont}}\alpha_{WP}\Lambda_o P_C} \qquad \text{Equation 4.2-9}$$

Likewise, K_{HV}^{gc} was calculated as:

$$K_{HV}^{gc} = \frac{\alpha_{HV}\Lambda_o P_C}{1 + \frac{l_{HV}}{\lambda_{gas}^{cont}}\alpha_{HV}\Lambda_o P_C} \qquad \text{Equation 4.2-10}$$

The average distance between the well and the vial bottom (l_{HV}^{B}) was considered as the average vial bottom concavity, and l_{HV} between the well's pillars and the vial sides (l_{HV}^{S}) was considered as the difference between the well radius and the outer radius of the vial. Parameters α_{WP}, α_{HV}, and l_{WP} were estimated using experimental data, and values are reported in Table 4.2-2. The parameter values and physical constants taken from the literature are gathered in Table 4.2-1.

Radiation

Heat transfer by radiation refers to the transmission of heat as waves through a transparent or translucent medium (in this case, the gas phase). Solid surfaces of the chamber wall, shelves, well plate, vials, and ice were considered diffuse grey-bodies with constant emissivity values (ε). The gas was modelled as transparent to radiation ($\varepsilon = 0$).

The heat transfer by radiation was divided as: (i) radiation between distant surfaces, concerning all surfaces of the geometry in contact with the gas within the chamber, symbolised by orange "lightning" arrows in Figure 4.2-3a; or (ii) radiation between adjacent surfaces (i.e. between the bottom shelf and the well plate bottom, and between the wells and the vials), symbolised by orange "lightning" arrows in Figure 4.2-3c.

Radiation between distant surfaces

In the case of radiation between distant surfaces (Figure 4.2-3a), the heat flow transmitted by radiation from a surface 1 to a surface 2 ($Q_{1\to2}^{rad}$, W) was calculated as (van Eck et al., 2016):

$$Q_{1\to2}^{rad} = A_1 F_{1\to2}(J_1 - J_2) \qquad \text{Equation 4.2-11}$$

The radiative heat flux of each surface was calculated as:

$$J = \omega G + \varepsilon\sigma T^4 \qquad \text{Equation 4.2-12}$$

In this way, the irradiation received by each surface (G) depends on the radiative heat fluxes (J) of the other surfaces and the system's geometry.

Radiation between adjacent surfaces

The heat flux by radiation between the bottom shelf and the well plate bottom (q_{WP}^{rad}, W.m^{-2}), symbolised by orange "lightning" arrows in Figure 4.2-3c, was calculated using the Stefan-Boltzmann's law for two parallel diffuse grey-body surfaces of equal areas (Scutellà et al., 2017a):

$$q_{WP}^{rad} = K_{WP}^{rad}\left(T_{shelf} - T_{WP}\right) \qquad \text{Equation 4.2-13}$$

The heat transfer coefficient by radiation between the bottom shelf and the well plate bottom (K_{WP}^{rad}) was calculated as (Perry and Green, 2008):

$$K_{WP}^{rad} = \sigma \frac{1}{\frac{1-\varepsilon_{shelf}}{\varepsilon_{shelf}} + \frac{1-\varepsilon_{WP}}{\varepsilon_{WP}} + 1}\left(T_{shelf} + T_{WP}\right)\left(T_{shelf}^2 + T_{WP}^2\right) \qquad \text{Equation 4.2-14}$$

Likewise, the radiation flux between the wells and the vials (q_{HV}^{rad}, W.m^{-2}), symbolised by orange arrows in orange dots 2 and 2' of Figure 4.2-3c, was calculated according to Stefan-Boltzmann's law as:

$$q_{HV}^{rad} = K_{HV}^{rad}(T_{WP} - T_{vial}) \qquad \text{Equation 4.2-15}$$

The heat transfer coefficient by radiation between the wells and the vials (K_{HV}^{rad}) was calculated as:

$$K_{HV}^{rad} = \sigma \frac{1}{\frac{1-\varepsilon_{WP}}{\varepsilon_{WP}} + \frac{1-\varepsilon_{vial}}{\varepsilon_{vial}} + 1} (T_{WP} + T_{vial})\left(T_{WP}^2 + T_{vial}^2\right) \qquad \text{Equation 4.2-16}$$

Constant values are given in Table 4.2-1.

.

Ice-vapour equilibrium

The temperature at the sublimation front (T_{sat}, K) was set as the ice-vapour equilibrium temperature calculated using the Clausius Clapeyron relation (Perry and Green, 2008):

$$T_{sat} = \frac{T_t}{1 - \frac{RT_t}{\widetilde{\Delta H_{sub}}} ln\left(\frac{P_{sat}}{P_t}\right)} \qquad \text{Equation 4.2-17}$$

For the *distilled water model*, P_{sat} was assumed equal to P_C based on the hypothesis that the chamber is saturated with water vapour and neglecting the vapour pressure loss between the sublimation front and the chamber.

Product model

When considering partially dried product inside the vials (as opposed to vials filled with only ice), a porous dried product layer builds up above the ice sublimation interface (Figure 4.2-2b and Figure 4.2-3). The heat and mass transfer model with a "model" product (5% sucrose aqueous solution), referred to as the *product model*, was developed by extending the *distilled water model*.

Heat transfer

The heat transfer equations of the *product model* were the same as for the *distilled water model* apart from the following modifications.

(i) *Conduction through solids:* heat transfer inside the dried product layer was also considered and represented using Equation 4.2-2.

(ii) *Conduction between solids:* the heat transfer mechanism between the frozen layer and the dried product layer (Figure 4.2-3c, orange dot 4) was considered to be perfect contact conduction (zero resistance to the heat transfer) since the product forms a continuous body, so the local temperature of the frozen and dried product layers was the same (equal to T_{sat}) at their junction.

(iii) *Conduction through the gas within the chamber* and *radiation between distant surfaces* concerned the top dried product layer surface (instead of the top ice surface considered in the *distilled water model*).

The physical properties of the frozen product were considered the same as ice (Scutellà et al., 2017a). The emissivity value of the dried product (ε_d) was considered as 0.95 (Emteborg et al., 2014). Moreover, the thermal conductivity of the dried product (λ_d, W.m^{-1}.K^{-1}) used in Equation 4.2-2 was defined, according to Smith et al. (2013), as the thermal conductivity of sucrose (0.85 W.m^{-1}.K^{-1} for a 50% aqueous sucrose gel (Renaud et al., 1992)) multiplied by the sucrose mass fraction of the initial solution (0.85 W.m^{-1}.K^{-1} × 5% = 0.043 W.m^{-1}.K^{-1}).

Mass transfer

Mass transfer is involved in the heat transfer calculation through the ice-vapour equilibrium temperature (T_{sat}). T_{sat} was calculated with Equation 4.2-17, but the pressure at the sublimation front (P_{sat}, Pa) was modified considering the vapour pressure loss within the dried product layer. In the *product model* P_{sat} was no longer equal to P_C, instead P_{sat} was calculated assuming the mass flow through the porous layer was in Knudsen regime as (Fissore et al., 2011; Scutellà et al., 2018c):

$$P_{sat} = P_C + \frac{\dot{m}\, R_P}{\frac{\pi}{4} {d_{VI}}^2} \qquad \text{Equation 4.2-18}$$

where $\frac{\pi}{4} {d_{VI}}^2$ is the inner cross-section area of the vial. The Knudsen regime in the dried product layer was confirmed by estimating the mean free path at the sublimation front l_{fp} = 0.3 mm considering a product temperature equal to the maximal allowable value (T_{sat} = -32 °C, P_{sat} = 31 Pa) and an upper bound for the

pore diameter taken from the literature (0.2 mm (Oddone et al., 2016)). Two R_P values were taken from the literature (Konstantinidis et al., 2011) for a dried product layer thickness (l_d) of 0.1 and 5 mm as reported in Table 4.2-1. For l_d = 0.1 mm, the *product model* represents a stage of primary drying when 0.9 % of the product was dried in 500-µL vials or 0.6% of the product was dried in 1000-µL vials (% of dried product = $[l_d \times \frac{\pi}{4} {d_{VI}}^2 / V_p] \times 100\%$; Table 4.2-1). Moreover, for l_d = 5 mm, the *product model* represents a stage when 47% of the product was dried in 500-µL vials or 31% of the product was dried in 1000-µL vials (% of dried product = $[l_d \times \frac{\pi}{4} {d_{VI}}^2 / V_p] \times 100\%$; Table 4.2-1). The mass flux was related to the total heat flux at the sublimation front ($\dot{Q}$) (for the total vial, twice the value for the half-vial) via the following Equation:

$$\dot{m} = \frac{\dot{Q}}{\Delta H_{sub}} \qquad \text{Equation 4.2-19}$$

COMSOL IMPLEMENTATION

COMSOL Multiphysics 5.3a (COMSOL, Inc, Burlington, USA) is a simulation software used to solve partial differential equations. Heat transfer was simulated using the "Heat Transfer with Surface-to-Surface Radiation" module, and equations were solved using the geometric multigrid solver. This section details how COMSOL was used to simulate the heat transfer during ice sublimation in high-throughput vials inside well plates.

Imposed temperatures

The sublimation front was considered a flat ice-vapour interface at the top of the frozen layer contained in each vial. Moreover, the freeze dryer chamber was supposed saturated with water vapour (Pikal, 2000, 1985; Pisano et al., 2011; Scutellà et al., 2017b). Three surface temperatures were imposed in our system (Figure 4.2-3): (i) T_{sat}, calculated using Equation 4.2-17; (ii) T_{shelf}, which was considered as the average between the inlet and the outlet temperature of the heat-transfer fluid circulating inside the shelves; (iii) the wall temperature (T_{wall}), which was measured during the experiments (Section *Methods* of this Paper II).

Definition of the heat transfer areas between adjacent surfaces

Minimal gaps between adjacent solid bodies observed in real objects were simplified in our models' geometry, so adjacent solids shared the same surface where heat transfer coefficients were applied. The well plate bottom in the geometry was flat and shared its surface with the bottom shelf below. Heat transfer from the bottom shelf to the well plate bottom (Figure 4.2-3c, orange dot 1) occurred through their shared area, where the K_{WP}^{cc}, K_{WP}^{gc}, and K_{WP}^{rad} were applied (in parallel, $K_{WP}^{cc} + K_{WP}^{gc} + K_{WP}^{rad}$). The well diameter was considered equal to the external vial diameter, so the well sides shared surfaces with the vial sides; moreover, the vial bottoms were deemed to be flat and sharing surface with the well bottoms. Heat transfer from the wells to the vials (Figure 4.2-3c, orange dots 2 and 2') occurred through their shared areas, where K_{HV}^{cc}, K_{HV}^{gc}, and K_{HV}^{rad} were applied as illustrated in Appendix 4.2-A (in parallel, $K_{HV}^{cc} + K_{HV}^{gc} + K_{HV}^{rad}$ or $K_{HV}^{gc} + K_{HV}^{rad}$).

Calculation of the heat flows

Calculations were performed with the Heat Transfer Surface-to-Surface Radiation physics interface of COMSOL by the finite-element method using a relative tolerance of 10^{-5} as a convergence criterion. The Surface-to-Surface Radiation feature was used to calculate the view factors between surfaces by the hemi-cube method, taking into account the shadowing effect as previously done by Scutellà et al. (2017b). For the *product model*, the consideration of a dried product layer implied an iterative calculation; for a given R_P, T_{sat} depends on P_{sat} hence on $\dot{Q}$ (Equation 4.2-17 to Equation 4.2-19). This iteration was performed using the LiveLink interface connecting MATLAB R2017a (The MathWorks, Inc, Natick, Massachusetts, USA) and COMSOL. The following iteration path was followed to solve the heat and mass transfer equations:

a) solving the 3D heat transfer model with an initial guess of T_{sat} values in each vial (using COMSOL), obtaining first-iterated $\dot{Q}$ values at the sublimation front for each vial;
b) calculating the new T_{sat} values using Equation 4.2-17 to Equation 4.2-19 (using MATLAB), based on the first-iterated $\dot{Q}$ values;
c) solving the 3D heat transfer model with the new T_{sat} values (using COMSOL), obtaining the second-iterated $\dot{Q}$ values at the sublimation front for each vial;
d) comparing first-iterated and second-iterated $\dot{Q}$ values (using MATLAB);
e) repeating steps b) to d) until the difference between iterated $\dot{Q}$ values was smaller than 0.1%.

Parameter estimation

Five model parameters, relevant to heat transfer between adjacent solid surfaces, had to be estimated based on measured heat flows in selected conditions: K_{WP}^{cc}, K_{HV}^{cc}, α_{WP}, α_{HV}, and l_{WP}. Parameters were estimated using the experimental heat flows received by 500-µL vials at shelf temperature -15 °C and chamber pressures 4, 12, and 65 Pa. The estimation was performed by calculating the heat flows using the 3D model in COMSOL and tuning the parameters using a code containing the *nlinfit* function of the Statistics and Machine Learning Toolbox provided by MATLAB to match measured heat flows in a least-square sense. The LiveLink interface connected COMSOL and MATLAB. The final values of the parameters are presented in Table 4.2-2.

Sensitivity analysis

Investigating how variations in the parameters impact the model results is critical to identify sensitive parameters that require special effort for determination or control, in contrast to those parameters for which rough estimations are sufficient for practical purposes. The Morris' method (Morris, 1991) was used to classify the twenty model parameters listed in Table 4.2-3 according to their impact on $\dot{Q}$ received by the central vials calculated using the *product model*. The range of each parameter was discretised in six uniformly distributed levels. Ten combinations of the twenty parameters and two operating conditions – hereinafter referred to as "domain samples" – were considered in this work. Domain samples were selected using the Latin hyper-cube sampling method, ensuring each parameter's level is selected once. The relative impact of the jth parameter in the ith domain sample (dimensionless sensitivity, ${E_j}^{(i)}$) was calculated as:

$${E_j}^{(i)} = \frac{\dot{Q}\left({x_1}^{(i)}, \dots, {x_j}^{(i)} + \Delta_j, \dots, {x_{22}}^{(i)}\right) - \dot{Q}\left({x_1}^{(i)}, \dots, {x_{22}}^{(i)}\right)}{\Delta_j} \times \frac{\Gamma_j}{\dot{Q}({x_1}^{(i)}, \dots, {x_{22}}^{(i)})} \quad \text{Equation 4.2-20}$$

where ${x_j}^{(i)}$ is the value of the jth parameter in the ith domain sample, Γ_j is the range of the jth input, and Δ_j is the increment of the jth input. Input ranges and increments are given in Table 4.2-3, and Δ_j was considered as 10% of the range.

The limits of the value ranges (Table 4.2-3) were established for each input according to different criteria: (i) for the emissivity values, limits were the extreme values taken from the literature or measured using an emissometer EM-2 by Themacs Ingénierie (Champs sur Marne, France); (ii) for the geometric dimensions of the vials, limits were taken from extreme values measured by Precis&Mans (Le Mans, Pays de la Loire, France) using 96 vials of each size (500-µL and 1000-µL) and one well plate for the work presented in Buceta et al. (2021); (iii) for the geometric dimensions of the shelves and chamber wall, and for the surface temperature of the chamber wall, limits were taken from extreme values measured in this work; (iv) for the estimated parameters, the range was the 95% confidence interval; and (v) for the dried product resistance to the mass transfer, limits were the extreme values taken from the literature for a dried product layer thickness of 5 mm. Values of the parameters that depend on the dried product layer (i.e. ε_d, λ_d) were not found in the literature on freeze-drying. Therefore, the range of ε_d went from 0 to 1 (minimal to maximal physically possible emissivity values). Moreover, the lower limit of the λ_d range was 0 $W.m^{-1}.K^{-1}$, and the upper limit was considered as ten times the value initially considered.

Table 4.2-3 – Ranges of the model inputs values considered for the sensitivity analysis.

Input	Range	Units
Physical constants		
ε_d	0 – 1	Dimensionless
ε_{shelf}	0.17* – 0.42*	Dimensionless
ε_{vial}	0.78(Scutellà et al., 2017a) – 0.94(Perry and Green, 2008)	Dimensionless
ε_{wall}	0.13* – 0.42*	Dimensionless
ε_{wp}	0.82(Perry and Green, 2008) – 1.00	Dimensionless
λ_d	0 – 0.43	$W.m^{-1}.K^{-1}$
Geometric dimensions		
d_C	$(9.6 – 12.0)\times10^{-2}$	m
d_E	$(1.10 – 1.4)\times10^{-1}$	m
d_S	$(5.0 – 6.6)\times10^{-2}$	m
d_{VI}	$(7.14 – 7.25)\times10^{-3}$	m
l_{HV}^B	$(4.4 – 9.0)\times10^{-5}$	m
l_{HV}^S	$(4.2 – 4.8)\times10^{-4}$	m
V_i	349 – 436	µL
	523 – 654	
V_p	392 – 479	µL
	587 – 717	
Estimated parameters		
K_{HV}^{cc}	12.1 – 28.1	$W.m^{-2}.K^{-1}$
K_{WP}^{cc}	1.6 – 8.6	$W.m^{-2}.K^{-1}$
l_{WP}	$(2.46 – 5.94)\times10^{-4}$	m
α_{HV}	0.287 – 0.373	Dimensionless
α_{WP}	0.597 – 1.303	Dimensionless
Other model parameters		
R_P	(1(Fissore and Pisano, 2015) – 5(Scutellà et al., 2018c))$\times10^5$	$Pa.s.m^2.kg^{-1}$
T_{wall}	0 – 15	°C
Operating Conditions		
P_C	4 – 15	Pa
T_{shelf}	-40 – 0	°C

** Measured using an emissometer EM-2 by Themacs Ingénierie (Champs sur Marne, France).*

RESULTS AND DISCUSSION

Mesh convergence

The accuracy of the models' numerical solution depends on the resolution considered to discretise the system of equations within the geometry (meshing). Therefore, a convergence study was performed considering two meshes suggested by COMSOL (Table 4.2-4). The "coarse" meshes (for 500-µL and 1000-µL vials), with approximately 47% fewer elements and degrees of freedom than "normal" meshes, calculated heat flows that differed from "normal" meshes in less than 0.2% and were obtained in approximately 72% less time (average calculation time for all operating conditions). Given the experimental variability of the data (the average coefficient of variation was 11%), "coarse" meshes were considered robust enough for the study of both vial sizes (500-µL and 1000-µL vials) and were used throughout this work.

Table 4.2-4 – Convergence test.

Mesh	Number of degrees of freedom	Number of elements	Average calculation time for all operating conditions (min)	Maximum absolute difference in heat flow, relative to the "Normal" mesh (%)
500-µL vials				
Normal	212000	91000	29	*not applicable*
Coarse	107000	43000	7	0.2
1000-µL vials				
Normal	245000	106000	20	*not applicable*
Coarse	137000	56000	6	0.2

Parameter estimation and model validation against experimental heat flows

Heat flows received by 500-µL vials under three operating conditions (Figure 4.2-4b, the nine striped bars) were used for model parameter estimation. The rest of the experimental data (Figure 4.2-4b and Figure 4.2-4c, the twenty-seven white bars) were used for model validation.

Table 4.2-2 reports the values of the five parameters estimated (i.e. K_{WP}^{cc}, K_{HV}^{cc}, α_{WP}, α_{HV}, l_{WP}), which are related to the heat transfer between adjacent surfaces. Parameters' values were compared to those of previous work (Buceta et al., 2021) where the same five parameters were estimated using a 0D model in steady-state considering the following simplifying hypothesis: (H1) all the heat flow received by the well plate came from the shelf below (bottom shelf, Figure 4.2-2), and (H2) all the heat flow received by central vials arrived from the well plate. To compare parameters' values of different works, the heat transfer areas considered for the heat transfer between adjacent surfaces should be the same. Therefore, the 95% confidence intervals of K_{HV}^{cc} and α_{HV} of 500-µL vials in "B-type well plates" (as referred in Buceta et al., 2021) were multiplied by the heat transfer area of that work (outer cross-section area of the vial) and divided by the heat transfer areas of our work; the final values are reported in Table 4.2-2. The 95% confidence intervals of K_{WP}^{cc}, α_{WP}, and l_{WP} estimated in the previous and present work overlapped, suggesting that H1 was accurate enough to determine the coefficients involved in the heat transfer between the bottom shelf and the well plate. However, the confidence intervals of K_{HV}^{cc} did not overlap, suggesting that H2 was not valid and perhaps a considerable part of the heat received by the vials came from other hot surfaces in the chamber (e.g. top shelf).

The validation of the 3D model consisted of comparing the calculated heat flows received by the vials to the heat flows obtained through gravimetric analysis during ice sublimation experiments. The values of the heat flows were grouped according to the vial position inside de well plate (Figure 4.2-4a): (i) central vials (CV), (ii) inner edge vials (IEV), and (iii) outer edge vials (OEV). Figure 4.2-4b and 4c show the calculated heat flow rates (blue, grey and red bars) plotted next to the experimental values (white bars). The values of the heat flow received by the six central vials in each model geometry were averaged since the coefficient of variation was less than 2% among central vials. Differences between calculated and experimental heat flow rates used for parameter estimation were on average 2.2% of the experimental values, and 3.6% in the case of validation conditions; in all cases, differences were smaller than the experimental coefficient of variation (approximately 11%).

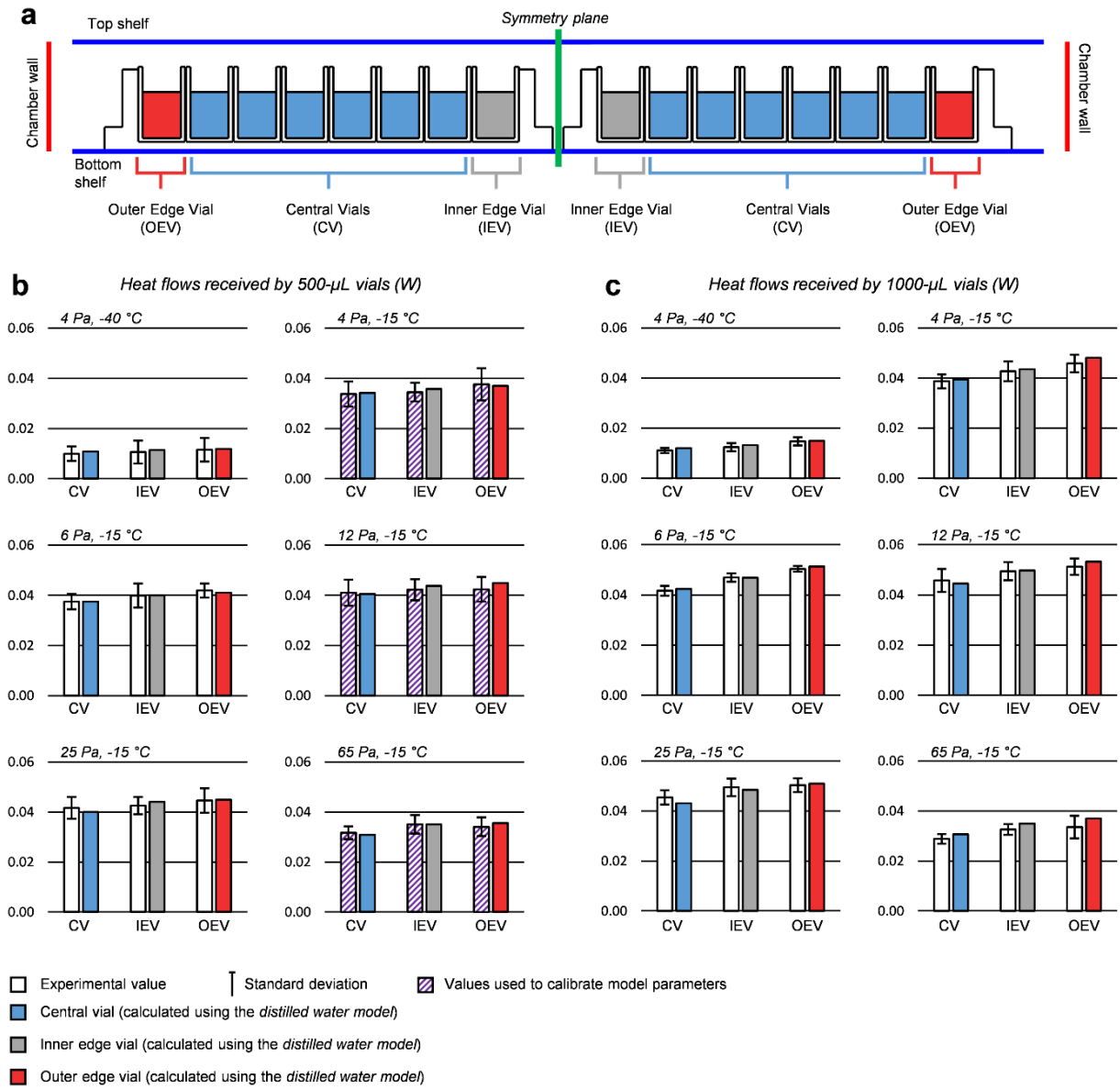

Figure 4.2-4 – (a) Vial positions in the well plate on the shelf (not in scale): central vials (CV, average flow of the six central vials in the geometry) in blue, inner edge vials (IEV) in grey, and outer edge vials (OEV) in red. (b) Comparison of experimental and simulated heat flows received by 500-µL vials. (c) Comparison of experimental and simulated heat flows received by 1000-µL vials. Several combinations of shelf temperatures (-40 °C and -15 °C) and chamber pressures (4, 6, 12, 25, and 65 Pa) were tested. Error bars in experimental data represent standard deviations.

The agreement between the predicted and experimental heat flows was statistically tested by calculating the coefficient of determination (R^2). Figure 4.2-5 shows the predicted versus observed heat flows for all vial positions inside de well plate (i.e. CV, IEV, OEV). Data was close to the 1:1 line, and R^2 values were over 0.98, both results put forward the simulations' goodness. Thus, the model generalisation ability was considered adequate, and heat transfer simulations in new operating conditions (i.e. shelf temperature and chamber pressure) within the considered experimental range were thought reliable.

Additionally, the calculated temperature at the vial bottom was compared with the temperature values measured using the Tempris thermal probes, obtaining a good agreement (< 0.8 °C difference).

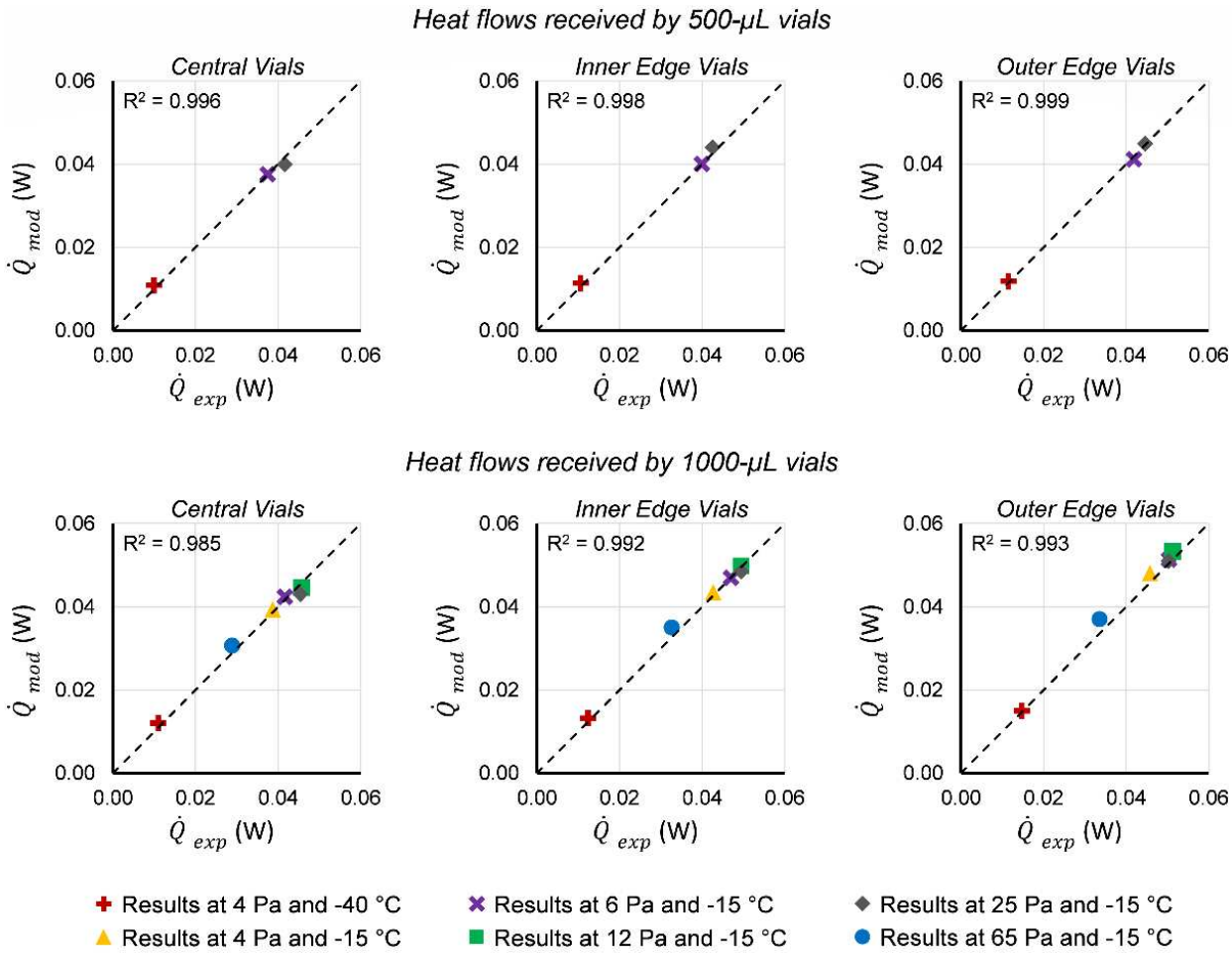

Figure 4.2-5 – $\dot{Q}_{exp}$ vs $\dot{Q}_{mod}$. The 1:1 dotted line represents perfect agreement between predicted and observed values. The values of the coefficient of determination (R^2) are reported in each graph.

Heat flow variations between different vial positions in the distilled water model

The impact of the vial position on the heat flow received by the vials during primary drying, commonly known as the "edge effect", has been previously studied by several authors using serum vials filled with water (e.g. Pikal et al., 2016; Pisano et al., 2011; Rambhatla and Pikal, 2003; Scutellà et al., 2017b). Scutellà et al. (2017b) observed that heat flows received by serum vials (filled with water) located at the periphery of the shelf increased by 47% compared to the heat flows received by serum vials in the centre of the arrangement (at shelf temperature 0 °C and chamber pressure 4 Pa); furthermore, Rambhatla and Pikal (2003; Figure 3 therein) reported an increase of 40% (at shelf temperature -25 °C and chamber pressure 13 Pa). In the case of high-throughput vials, a similar effect of the vial position in the well plate may be initially speculated; however, there is no published research or work to this date investigating this hypothesis.

Figure 4.2-6 shows the relative increase in the heat flow reaching high-throughput vials in the edge of the well plate ($\dot{Q}_E$) compared to those in the centre ($\dot{Q}_C$), expressed as the ratio of the heat flow rates ($\dot{Q}_E/\dot{Q}_C$). Two edge vials configurations were investigated: (i) edge vials facing the chamber wall (Outer Edge Vials, results in red in Figure 4.2-6), and (ii) edge vials facing another well plate (Inner Edge Vials, results in grey in Figure 4.2-6). Moreover, two vial sizes were considered: (i) 500-µL vials (striped bars) and (ii) 1000-µL vials (filled bars). Simulations were run at a chamber pressure of 4, 6 and 12 Pa and shelf temperatures of -40 °C and -15 °C. Considering outer edge vials, 500-µL vials exhibited a heat flow rate approximately 11% (= [$\dot{Q}_E$ / $\dot{Q}_C$ – 1] × 100%) greater than central vials, while reaching up to 25% (= [$\dot{Q}_E$ / $\dot{Q}_C$ – 1] × 100%) for 1000-µL vials (worst case 4 Pa and -40 °C). However, when considering inner edge vials, the heat flow increase compared to central vials was lower than 11% (= [$\dot{Q}_E$ / $\dot{Q}_C$ – 1] × 100%), regardless of the vial's size.

Placing a 1000-µL vial in an outer edge position instead of a central position had the most critical impact on the heat flow received (19% to 25%; = [$\dot{Q}_E$ / $\dot{Q}_C$ – 1] × 100%). This impact seemed to increase with lower shelf temperatures and lower chamber pressures, as previously noted between serum vial positions on the shelf (Rambhatla and Pikal, 2003; Scutellà et al., 2017b). However, for 500-µL vials and 1000-µL inner edge vials, the impact of the high-throughput vial position in the well plate could be considered negligible compared to that of serum vials (over four times lower; Rambhatla and Pikal, 2003; Scutellà et al., 2017b).

The use of 500-µL vials would be recommended to avoid heat transfer variations between vial positions in the well plate. However, screening tests may frequently require sampled volumes over 500 µL; hence, 1000-µL vials may be the only alternative. The results for 1000-µL vials should be considered as a worst-case situation.

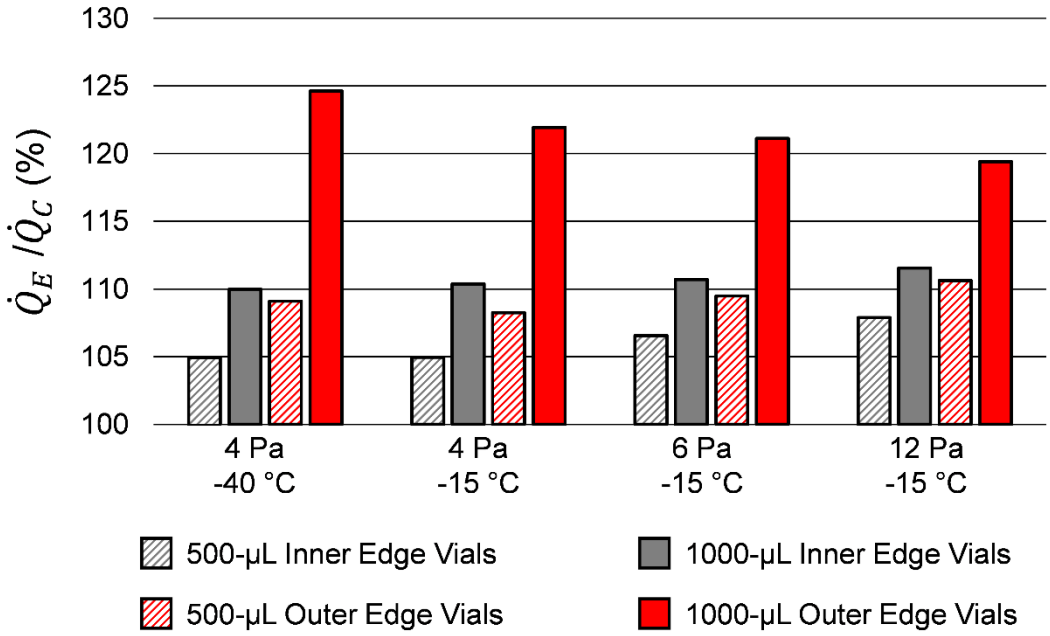

Figure 4.2-6 – Ratio (%) of $\dot{Q}_E$ to $\dot{Q}_C$ (= [$\dot{Q}_E$ / $\dot{Q}_C$] × 100%). Results were obtained using the distilled water model at different shelf temperatures (-40 and -15 °C) and chamber pressures (4, 6 and 12 Pa). Vial positions refer to those shown in Figure 4.2-2.

Temperature profile and heat flux distribution in the distilled water model

The temperature profiles and the heat fluxes in the drying chamber were simulated using 3D modelling. As an example, Figure 4.2-7 shows the results obtained at shelf temperature -15 °C and chamber pressure 4 Pa using the *distilled water model*. The temperature profiles are represented as colour maps, and heat fluxes are represented as arrows whose lengths indicate their module on a logarithmic scale to accentuate the visualisation of the smaller fluxes. Two vial sizes were considered: 500-µL vials (Figure 4.2-7a) and 1000-µL vials (Figure 4.2-7b). For each vial size, the geometry presented an outer edge vial, an inner edge vial, and six central vials. Comparing 500-µL and 1000-µL vials, 1000-µL edge vials received extra heat fluxes through the vial area protruding from the well plate, which explains why placing a vial in an edge position was more critical for the heat flow received in the case of 1000-µL vials than 500-µL vials. These extra heat fluxes came mostly from the top shelf and chamber wall in the case of 1000-µL outer edge vials, and from the top shelf in the case of 1000-µL inner edge vials.

The difference between the maximal and minimal temperature in the well plate was less than 0.16 °C. Hence, the well plate temperature could be considered homogenous compared to the rest of the system's temperature variations, e.g. 4.4 °C between the vials and the well plate and 24.7 °C between the well plate and the shelf at chamber pressure 4 Pa and shelf temperature -15 °C. Such low variation within the well plate temperature was due to the aluminium's high conductivity (Buceta et al., 2021; Perry and Green, 2008). The temperature difference within the ice/frozen layer was less than 2.0 °C due to the relatively high thermal conductivity of the ice compared to the vapour in the vial headspace and the chamber (> 80 times greater). The highest temperature in the ice/frozen layer occurred at the bottom of the content and the lowest temperature (T_{sat}) was observed at the ice sublimation front, as noted in previous modelling studies (Scutellà et al., 2017b; Sheehan and Liapis, 1998). Remarkably, the heat flux in the ice/frozen layer was essentially one-directional, coming from the bottom to the top (following the temperature gradient direction) despite lateral heat transfer to the vial sides from the metallic pillars and well plate walls.

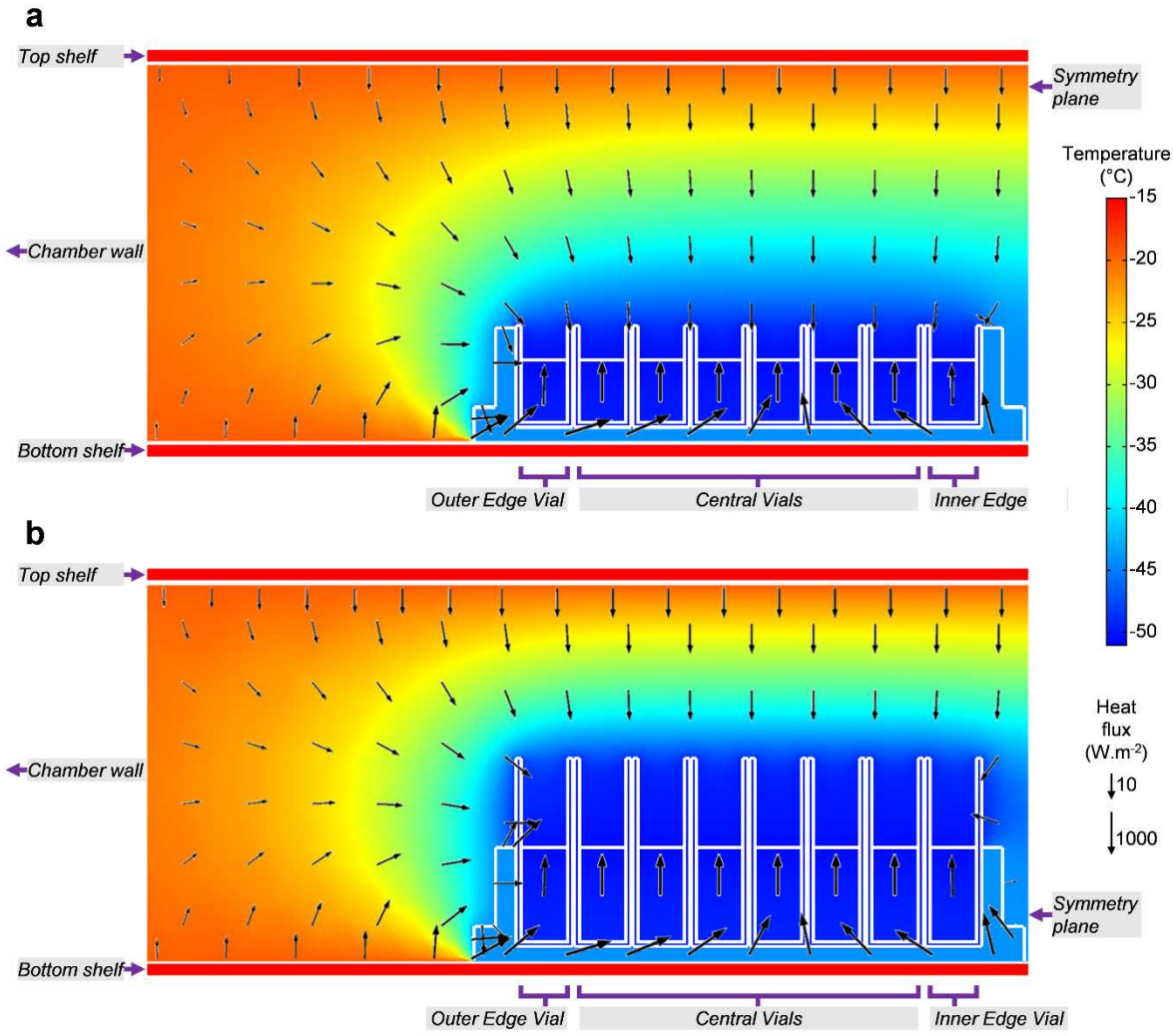

Figure 4.2-7 – Temperature profiles and heat fluxes obtained with the distilled water model for (a) 500-µL vials and (b) 1000-µL vials. Temperatures are represented as colour maps. Heat fluxes through the loose gas, vials and frozen product layers are represented as arrows whose lengths indicate their module on a logarithmic scale. Calculations were performed at a shelf temperature of -15 °C and a chamber pressure of 4 Pa.

Relative importance of individual heat transfer mechanisms in the distilled water model

According to the *distilled water model*, 1000-µL vials in outer edge positions received higher heat flows than in central positions (Figure 4.2-6), while this tendency was less pronounced when using 500-µL vials. To identify which heat transfer mechanisms were responsible for these observations, Figure 4.2-8a presents the heat flow contributions of each mechanism received by 500-µL and 1000-µL vials (respectively) calculated using the *distilled water model* at chamber pressure 4 Pa and shelf temperature -15 °C. Most of the heat flow received by the vials came from the well (over 50% of the total heat flow; e.g. 0.028 W out of the total 0.048 W received by the outer edge 1000-µL vial in Figure 4.2-8a), primarily by contact conduction (over 39% of the total heat flow; e.g. 0.019 W out of the total 0.048 W received by the outer edge 1000-µL vial in Figure 4.2-8a).

Regarding vial sizes, the heat contribution of radiation from distant surfaces in central vials increased from 500-µL vials to 1000-µL vials (e.g. from 0.0022 W for 500-µL vials to 0.0064 W for 1000-µL vials in Figure 4.2-8a), and so did the conduction through the gas within the chamber (e.g. from 0.0044 W for 500-µL vials to 0.0065 W for 1000-µL vials in Figure 4.2-8a). Comparing 1000-µL edge vials to central vials (Figure 4.2-8a), the greater heat flow received by the inner edge vial (up to 11%, = $[\dot{Q}_E/\dot{Q}_C] \times 100\%$) was due to conduction through the gas within the chamber, and the even greater heat flow received by the outer edge vial (up to 25%, = $[\dot{Q}_E/\dot{Q}_C - 1] \times 100\%$) also had a contribution of radiation from distant surfaces. These results put forward that the impact of the vial position was due to the heat flow contributions received through the vial surface protruding from the well plate. 500-µL vials protrude less than 0.1 cm from the well-plate, while 1000-µL vials protrude around 1 cm (half of the total vial height). Thus, the greater height of 1000-µL vials, compared to 500µ-L vials, exposed them more to radiation and gas conduction from the chamber. At the same time, the well plate considerably protected the 500-µL vials from such heat flow contributions, consequently limiting the edge effect.

In the case of serum vials, most authors attribute the edge effect to the heat transfer by radiation from the chamber surfaces (Pikal et al., 1984; Pikal, 2000; Pikal et al., 2016a; Pisano et al., 2011; Rambhatla and Pikal, 2003; Schneid and Gieseler, 2008; Wegiel et al., 2018), while Scutellà et al. (2017b) concluded through 3D mathematical modelling that the main "extra" heat contribution from the chamber wall was transferred by gas conduction to the serum vials. In the case of high-throughput vials, radiation and gas conduction from distant surfaces had similar contributions in the *distilled water model***.**

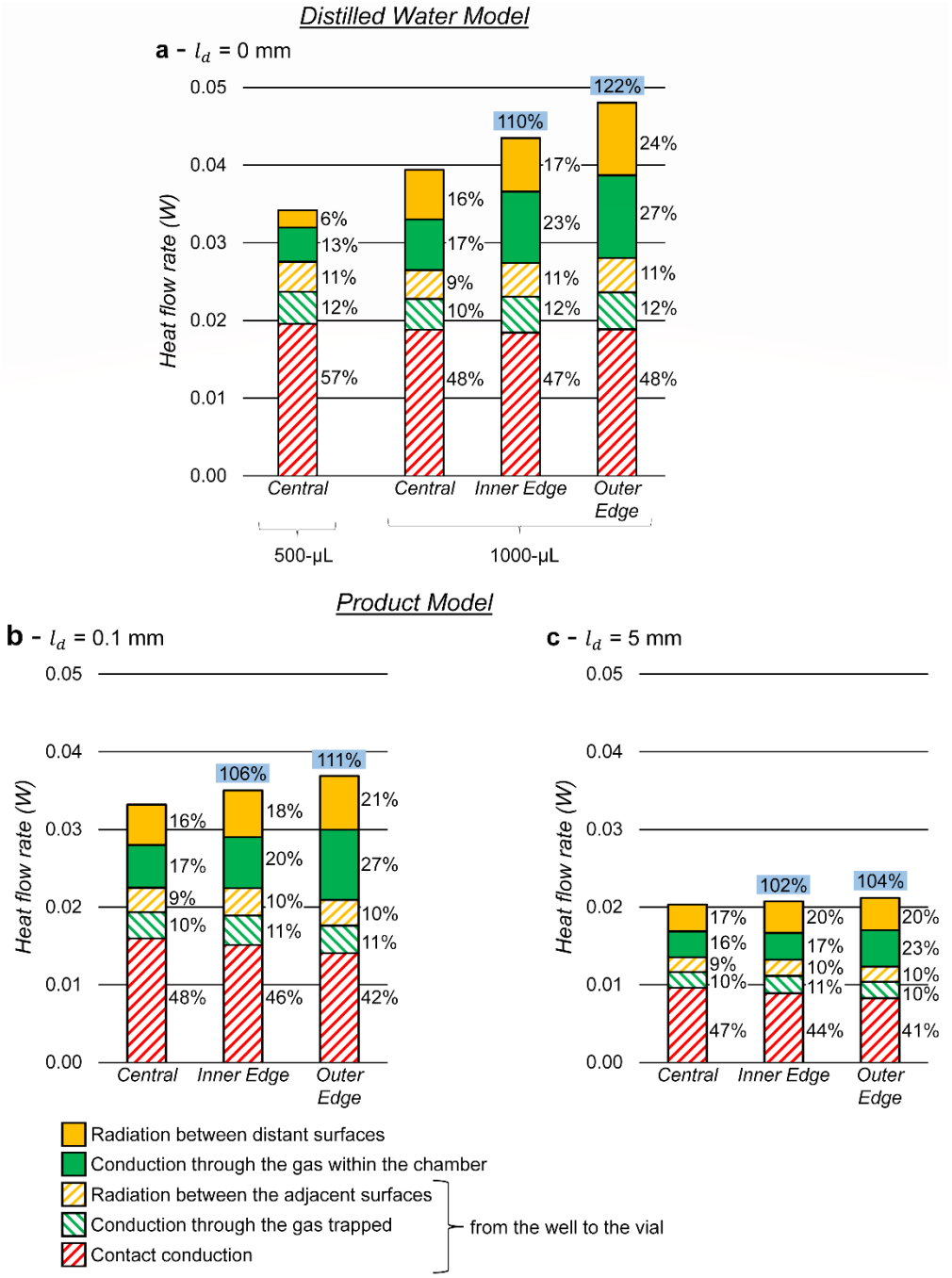

Figure 4.2-8 – Heat flow rates and their relative contributions to the total heat flow received by the vials using (a) the distilled water model for 500-µL vials and 1000-µL vials; and using the product model for 1000-µL vials considering a dried layer thickness (l_d) of (b) 0.1 mm and (c) 5 mm. Blue squares report the ratio (%) of $\dot{Q}_E$ to $\dot{Q}_C$ (= [$\dot{Q}_E$ / $\dot{Q}_C$] × 100%). Relative contribution (%) of each mechanism with respect to $\dot{Q}_C$ (= [heat flow contribution / $\dot{Q}_C$] × 100%) are reported next to the corresponding bar. Calculations were performed at a shelf temperature of -15 °C and a chamber pressure of 4 Pa. Central, Inner Edge, and Outer Edge refer to vial positions detailed in Figure 4.2-2.

The *distilled water model* could be considered as a representation of the beginning of primary drying when there is no dried product layer (hence no dried product resistance, R_P = 0). As drying continues, a dried product layer forms and progresses from the top of the frozen layer and increases P_{sat} and T_{sat} at the sublimation front, therefore affecting the heat received by the product. The following Section (*Heat flow variations between different vial positions in the product model*) will study how a dried product layer's presence could affect the heat transfer by using the *product model*. Moreover, we could interpret the variation in the heat flow received by different vial positions "in time" during primary drying by comparing the *distilled water model* results (representing the beginning of primary drying) and the *product model* results (representing an advanced moment during primary drying).

Heat flow variations between different vial positions in the product model

By considering the resistance to the mass transfer imposed by a dried product layer, the *product model* gives an insight into how the heat flow variations among vial positions observed in the *distilled water model* will evolve as ice sublimation progresses during primary drying. Figure 4.2-8b and Figure 4.2-8c present the heat flows received by 1000-µL vials calculated using the *product model* at chamber pressure 4 Pa and shelf temperature -15 °C. Two R_P values corresponding to different l_d were considered in this work, one representing an early stage of primary drying (Figure 4.2-8b, l_d = 0.1 mm, R_P = 0.119×10^5 Pa.s.m^2.kg^{-1}), and another representing a more advanced stage (Figure 4.2-8c, l_d = 5 mm, R_P = 1.248×10^5 Pa.s.m^2.kg^{-1}).

As expected, heat flows received by the vials decreased when R_P increased. For example, the heat flow received by central vials decreased by 50% (= [$\dot{Q}_C$ in the *product model* / $\dot{Q}_C$ in the *distilled water model*] × 100%) compared to the *product model* at l_d = 5 mm (Figure 4.2-8a vs Figure 4.2-8c). This occurred because R_P increased P_{sat} and hence T_{sat}, which reduced the temperature difference between the sublimation front of all the vials and the hot surfaces (i.e. shelves and chamber wall), and ultimately the total heat flow to the vials.

Variations in the heat flows received by vials in different positions were smaller in the *product model* than in the *distilled water model* and decreased when R_P increased. As it was previously mentioned in Section *Heat flow variations between different vial positions in the distilled water model* (of this Paper II), outer edge vials presented heat flows up to 25% (= [$\dot{Q}_E$ / $\dot{Q}_C$ – 1] × 100%) greater than central vials in the distilled water model (Figure 4.2-6, 1000-µL vials). In the *product model*, however, such increase in the heat flow from central to outer edge vials was 11% (= [$\dot{Q}_E$ / $\dot{Q}_C$ – 1] × 100%) at l_d = 0.1 mm (blue square in Figure 4.2-8b) and only 4% (= [$\dot{Q}_E$ / $\dot{Q}_C$ – 1] × 100%) at l_d = 5 mm (blue square in Figure 4.2-8c). Thus, the edge effect is expected to diminish throughout primary drying as R_P increases, which is a beneficial practical outcome.

The heat flow from the top shelf and the chamber door (red, yellow, and green plain bars in Figure 4.2-8) increased from central to edge vials in the *distilled water* and *product models*, being the main cause of the heat flow variations between vial positions. In the *distilled water model*, T_{sat} only depends on the chamber pressure so all vials were essentially at the same temperature. In the *product model*, however, T_{sat} increased with the total heat flow received (as described above and in Section *Calculation of the heat flows* of this Paper II), so the edge vials were slightly warmer (< 1 °C) than the central vials, as further discussed in the following Section *Temperature profile in the product model*.

Temperature profile in the product model

Figure 4.2-9 shows the temperature profiles of an outer edge vial and a central vial considering different dry layer thicknesses (l_d values). Product temperature profiles in the outer edge and central vials are similar at the beginning of primary drying (Figure 4.2-9a, l_d = 0 mm) when the temperature at the sublimation front (-51.5°C) is determined by the chamber pressure alone. In contrast, the introduction of a dried product layer entailed a higher product temperature in outer edge vials (-44.3°C at the sublimation front) compared to central vials (-45.0°C) (Figure 4.2-9b, l_d = 0.1 mm) due to the coupling between heat and mass transfer: a higher heat flow near the edge induced a higher mass flow through the porous layer (Equation 4.2-19), which resulted in a higher pressure at the sublimation front (Equation 4.2-18) and hence in a higher temperature at this surface (Equation 4.2-17). As primary drying continued (Figure 4.2-9c, l_d = 5 mm) and R_P increased, the overall vial temperature increased, e.g. by about 10 °C from figure Figure 4.2-9b to Figure 4.2-9c. Thus, heat flows to the vials decreased (Figure 4.2-8b vs Figure 4.2-8c) because they depend on the temperature difference between the hot surfaces (mainly shelves) and the vials. This difference between shelf and vial temperatures was larger for the "colder" central vials than for the "warmer" edge vials. As a result, in the *product model*, the larger heat flow received from the shelves by the "colder" central vials partly compensated the extra heat flow received from the walls by the edge vials, explaining the reduction of the edge effect as l_d increased. Ultimately, the temperature difference between edge and central vials diminished (0.4 °C in Figure 4.2-9b vs 0.2 °C in Figure 4.2-9c), which is a favourable consequence for product homogeneity.

Figure 4.2-9 also indicates that the temperature differences within the dried product layer were always less than 1.1 °C. Most lumped-variable (0D) models do not consider heat conduction through the dry layer and calculate the product temperature at the sublimation front (lowest temperature in the dried product layer). Consequently, an additional safety margin should be considered for process design based on T_{sat} to avoid collapse in any part of the dried product layer.

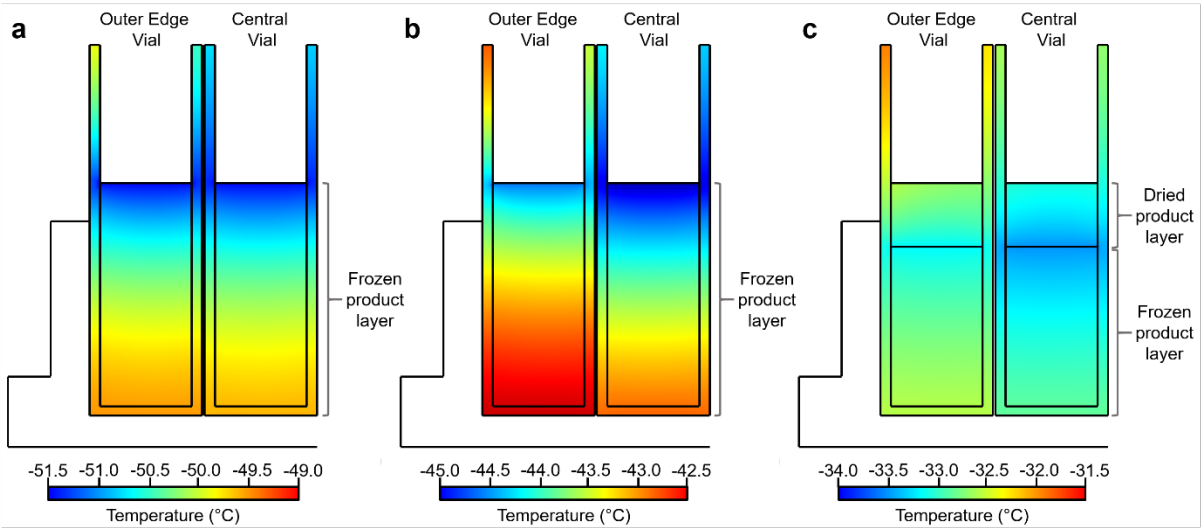

Figure 4.2-9 – Temperature profiles for 1000-µL outer edge and central vials for a filling height of 16 mm, obtained with (a) the distilled water model (l_d = 0 mm), (b) the product model considering l_d = 0.1 mm, and (c) the product model considering l_d = 5 mm. Temperatures are represented as colour maps; note the same temperature span (2.5°C) in each case. Calculations were performed at a shelf temperature of -15 °C and a chamber pressure of 4 Pa.

Sensitivity analysis

A sensitivity analysis was performed to identify the model parameters (inputs) that should be more precisely determined when calculating heat flows received by the vials ($\dot{Q}$) using the *product model*. The relative impacts of the variation of each parameter on the calculated heat flow received by all vial positions (i.e. central, inner edge, outer edge) and vial sizes (i.e. 500-µL and 1000-µL) were similar. Figure 4.2-10 presents the average values and standard deviations of E_j for central 1000-µL vials. Positive E_j values refer to an increase in the heat flow when increasing the parameter value, while negative values denote a decrease. The most sensitive parameters were: (i) α_{WP}, (ii) K_{WP}^{cc}, and (iii) R_P. α_{WP} and K_{WP}^{cc} are related to the well plate bottom surface, their high sensitivity indicates the key role of the heat transfer between the bottom shelf and the well plate bottom (limiting resistance) on the total heat transfer to the sublimation front (Buceta et al., 2021). The importance of K_{WP}^{cc} is in agreement with previous research using serum vials, which highlighted the impact of the contact conduction between the shelf and the serum vial bottom (Brülls and Rasmuson, 2002; Kuu and Nail, 2009; Pisano et al., 2011; Scutellà et al., 2017a). However, while α_{WP} was found as a sensitive parameter, to the best of our knowledge, well plate-to-well plate variation has not been studied in the literature. Manufacturing glass serum vials appears to entail lower vial-to-vial variations in the surface finish compared to the well-plate-to-well-plate variations caused by the aluminium turning technique observed in this study. The high impact of R_P highlighted the importance of the mass transfer during primary drying. The negative value of the R_P sensitivity (Figure 4.2-10) indicates that an increase of R_P tends to reduce the heat transfer to the vial. Similar results were obtained when performing the sensitivity analysis with l_d values in a lower range (0 to 0.1 mm; data not shown).

On another note, many heat and mass transfer models for the primary drying do not take into account heat transfer parameters depending on the dried product layer (i.e. ε_d, λ_d) (e.g. Mortier et al., 2016; Pikal, 1985; Scutellà et al., 2017a). The sensitivity of ε_d and λ_d were over 20 times lower than that of the most sensitive parameter (α_{WP}), confirming that much experimental effort does not need to be put in their determination and rough estimations are sufficient.

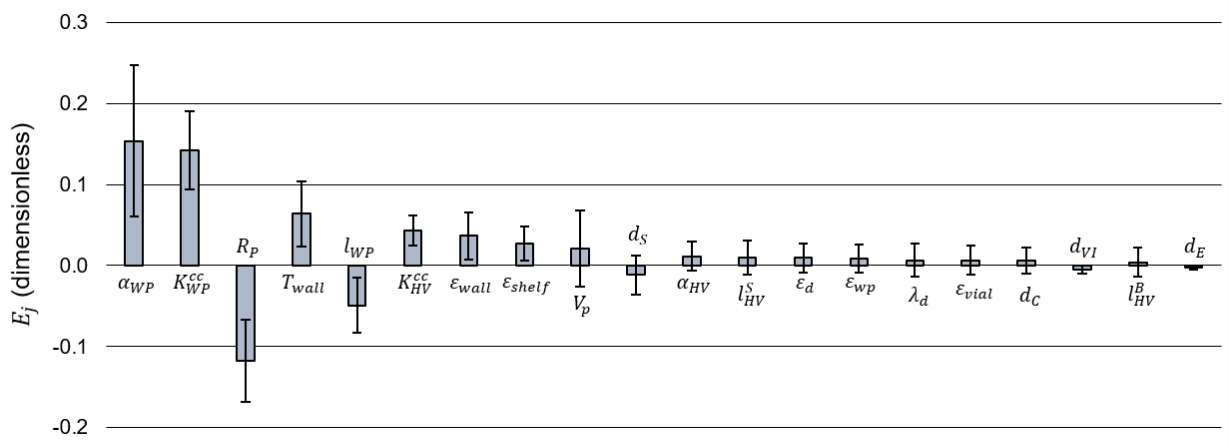

Figure 4.2-10 – E_j values of the parameters reported in Table 4.2-3, calculated using Equation 4.2-20. Grey bars represent the average values for the domain samples, and error bars represent the standard deviations within the "domain samples".

CONCLUSIONS

This work studied heat transfer mechanisms and the edge effect in a high-throughput and well plate system (i.e. heat flow increase in vials facing the chamber wall) using 3D modelling. Two 3D steady-state models were developed and compared: one representing the beginning of primary drying with only frozen water, and another one representing intermediate stages of primary drying (for a sucrose aqueous solution) by including the formation and progress of a dried product layer.

The edge effect was only significant in vials protruding from the well plate (1000-µL vials) and at the very beginning of primary drying. The edge effect is thus expected to diminish throughout primary drying as the dried product layer thickness increases. Our work suggested that heat transfer variations due to the vial position in the well plate are caused by the heat flow contributions from the chamber wall and top shelf by radiation and conduction through the gas within the chamber. Interestingly, compared to freeze-drying in serum vials, the presence of a metallic well plate significantly reduce the impact of the vial position (over 50%, = 100% × $[\dot{Q}_E \,/\, \dot{Q}_C]$ in high-throughput vials / $[\dot{Q}_E \,/\, \dot{Q}_C]$ in serum vials) in all studied situations by improving the heat transfer from the bottom shelf and redistributing a portion of the extra heat flow from the chamber wall to the high-throughput vials (i.e. central and edge).

Based on the models presented in this work, further model development could help to understand the impact of the well plate position on the shelf.

APPENDIX 4.2-A

The geometry between the adjacent surfaces of the wells and the vials was modified to simplify the COMSOL model. Figure 4.2-11a is a 3D reconstruction of a real well plate with pillars between the wells. Furthermore, Figure 4.2-11b presents the 3D geometry of a simplified well plate without pillars, assuming that wells are not connected and have a diameter equal to the external vial diameter.

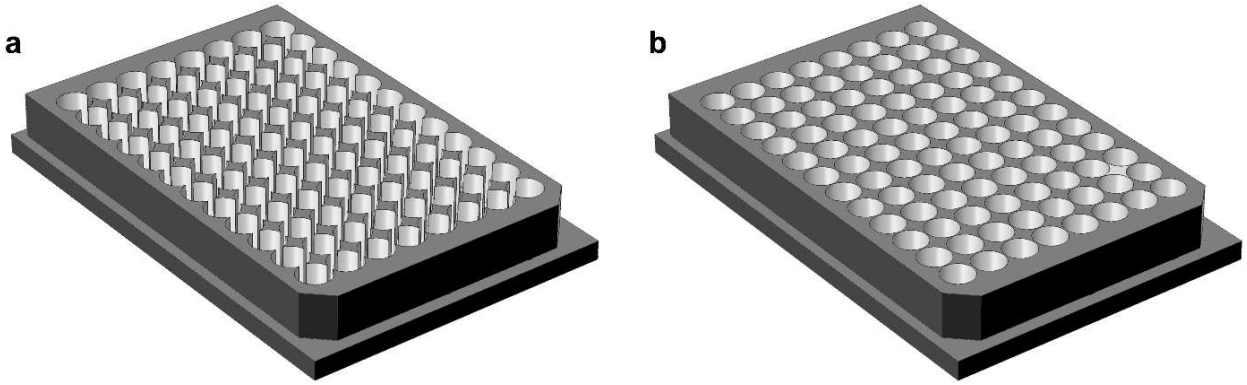

Figure 4.2-11 – 3D reconstruction of a well plate. (a) Geometry of a "real" well plate with pillars. (b) Geometry of a simplified well plate without pillars, assuming the well diameter equal to the external vial diameter.

Figure 4.2-12a shows the cut of the well plate initially aimed at being represented in the model geometry. Figure 4.2-12b presents the modified well plate geometry obtained by considering the well diameter equal to the external vial diameter, so the well sides share surfaces with the vial sides. Figure 4.2-12c details the physical meaning of each portion of the surface shared between the wells and the vials. The shared surface include: (i) a bottom portion where the well bottom faces the vial bottom; (ii) a lateral portion where the physical contact pillar faces the vial, (iii) a lateral portion where the other pillar (in the case of a central well) or the well plate wall (in the case of an edge well) faces the vial side, and (iv) a lateral portion where the vial faces an adjacent vial. The lateral surfaces shared between the wells and the vials were divided into eight equal parts where different coefficients were applied according to Figure 4.2-12c. K_{HV}^{gc} and K_{HV}^{rad} were applied in surface portions corresponding to wells facing vials (continuous orange surfaces and orange striped surfaces in Figure 4.2-12c). K_{HV}^{cc} was applied in surface portions corresponding to a well bottom and a physical contact pillar facing a vial (continuous orange surfaces in Figure 4.2-12c). The heat transfer through the lateral surfaces between vials (green surfaces in Figure 4.2-12c) was considered negligible compared to the transfer from the well plate, which corresponds to assuming a symmetry condition between vials.

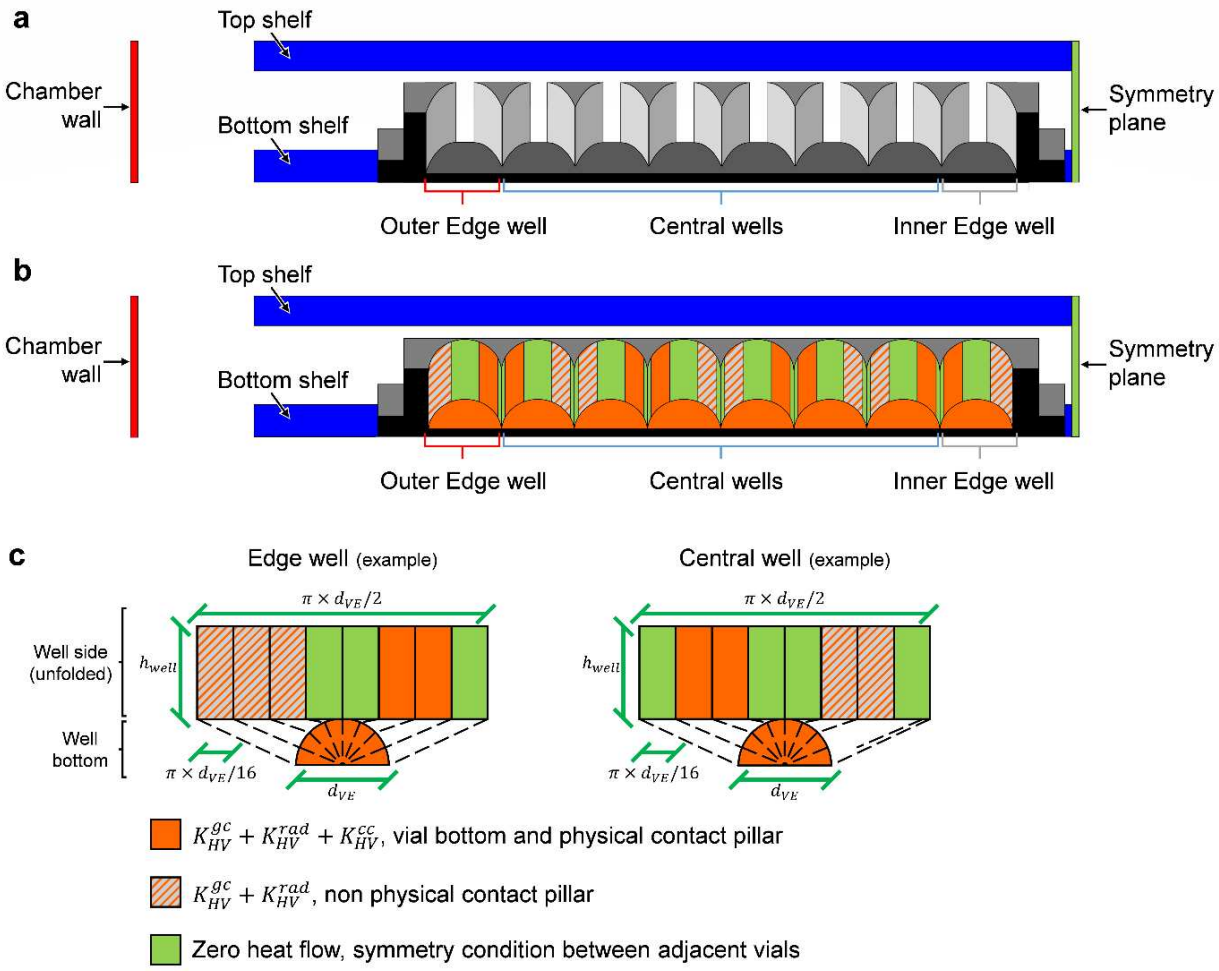

Figure 4.2-12 – Schematic representation (not in scale) of the heat transfer area and coefficients between the wells and the vials (not in scale). (a) View from top of the well plate cut considered in the geometry (vials are not shown). (b) View from top of the well plate cut considered in the geometry when assuming the wells and the vials share the same surface equal to the external vial diameter (vials are not shown). (c) Surface shared by the wells and the vials where heat transfer coefficients were applied. Geometric dimensions refer to Table 4.2-1. K_{HV} are detailed according to the heat transfer mechanism involved: K^{cc} by contact conduction, K^{gc} is by conduction through the gas trapped between the surfaces, K^{rad} by radiation.

4.2.4. Take-Home Message

A comprehensive 3D physical model for heat transfer was build and validated for high-throughput systems for the first time. Thanks to the model, heat transfer mechanisms were investigated in the considered system in great detail. As a practical outcome of the study, the edge vial effect within a well plate caused by a chamber wall should only be considered at the beginning of primary drying when using vials protruding from the well plate (1000-µL vials). In this condition, heat flows received by vials at the edge of the well plate were over 19% greater than the rest. As primary drying continues, the dried product resistance to mass transfer increases the product temperature while reducing the edge vial effect. Consequently, the heat transfer variations due to the vial position can be neglected during the most critical part of primary drying, when the product temperature is the highest.

To complement the study on the impact of the vial position in the well plate developed in this Section 4.2, the following Section 4.3 addresses how the well plate position in the shelf impacts the heat flow received by the vials.

4.3. How the Well Plate Position on the Shelf Impacts the Heat Transfer

4.3.1. Context

Numerous investigations have been carried out on how the serum vial position on the shelf affects the heat transfer during primary drying (e.g. Pisano et al., 2011; Rambhatla and Pikal, 2003; Scutellà et al., 2017a). The previous Section 4.3 studied how the high-throughput vial position in the well plates could affect the heat transfer. However, the well plates in Section 4.2 were placed in the centre of the shelf, so the impact of the well plate position was not considered.

4.3.2. Objectives

Section 4.3 investigates how placing a well plate near a chamber wall or door could increase the heat transfer to the vials. The 3D steady-state mechanistic models proposed in Section 4.3 are modified to represent different well plate positions in the shelf. In this way, the variations on the heat flow received by vials in different well plate positions are evaluated in time by comparing models for different stages of primary drying.

4.3.3. Paper III

This draft has not been submitted to a scientific journal.

PROVISIONAL TITLE

"3D mathematical modelling to understand the impact of the well plate position on the shelf during freeze-drying using high-throughput vials"

CONTENTS OF PAPER III

ABSTRACT

High-throughput systems consisting of small (500 or 1000 µL) vials inside 96-well plates were recently considered to accelerate the screening of potential vaccine formulations during freeze-drying. However, heat transfer variations between vials due to their position on the freeze dryer's shelf could cause deviations in the final product quality and bias the screening results. This work used 3D modelling to understand how the well plate position on the shelf impacts the heat transfer during ice sublimation in vials filled with distilled water or a "model" product (5% sucrose solution). For vials filled with distilled water, placing a well plate near the chamber door increased the heat flow received up to 33% compared to a well plate in the middle of the shelf. In the presence of a dried product layer formed during primary drying, placing a well plate near the door could increase the heat flow by up to 42% and raise the product temperature by 2 °C. Therefore, variations between well plates may evolve during primary drying, as the dried product layer thickness and associated resistance to mass transfer increase. Comparing 3D and 0D modelling results, a safety margin on the product temperature near the chamber door of 2 °C is suggested for 0D models due to their simplifying assumptions.

KEYWORDS

Freeze-drying; Lyophilization; Mathematical model(s); 3D modelling; Vaccine(s).

INTRODUCTION

Freeze-drying is widely used in the pharmaceutical industry to stabilise vaccines and facilitate their storage and transportation (Adams, 2007; Izutsu, 2018; Wiggan et al., 2011). The freeze-drying process consists of three steps: (i) freezing, (ii) primary drying, and (iii) secondary drying. During the freezing step, approximately 80% of the initial water content is turned into ice crystals (Pikal, 2000), which are then removed by sublimation during primary drying in vacuum conditions (less than 15 Pa). Most of the bound water in the cryoconcentrated phase remaining after primary drying is finally removed by desorption during secondary drying. The product's structure during primary drying is still fragile due to the remaining adsorbed (or absorbed) water, and could collapse if heated above a specific critical temperature known as collapse temperature (Pikal and Shah, 1990a). Product collapse could cause a loss of potency, an unacceptably high final moisture content, and an excessively long reconstitution time. Thus, the product appearance is an important criterion to accept or refuse candidate formulations during the development of new vaccines (World Health Organization, 2011). Screening formulations to evaluate which one is less prone to collapse or degradation during primary drying is very time-consuming, and recently, high-throughput systems were proposed to accelerate this labour (Buceta et al., 2021; von Graberg, 2011). Each high-throughput system consists of an aluminium 96-well plate containing (96) small tubular vials – known as high-throughput vials – with a maximal filling volume of 500 or 1000 µL. The smaller size of the high-throughput vials compared to the "traditional" serum vials (over 3000 µL; Brülls and Rasmuson, 2002; Pikal et al., 2016; Scutellà et al., 2017a) allows to fit more containers on the freeze dryer and hence to test more formulations per freeze-drying cycle. Moreover, the high-throughput vial disposition in the well plate is compatible with many robots used to prepare and fill formulations, and simplifies the transport and storage of the vials.

The product temperature is a critical process parameter for the dried product appearance (Patel et al., 2017; Pikal and Shah, 1990a). During freeze-drying, vials are placed on the shelves inside the drying chamber of the freeze dryer. Two main operating conditions can be set to control the product temperature: the temperature of the shelves and the pressure inside the drying chamber. However, many other factors can impact the product temperature, remarkably, the vial position on the shelf (Pikal et al., 1984; Rambhatla and Pikal, 2003; Schneid and Gieseler, 2008; Scutellà et al., 2017b; Wegiel et al., 2018). Vial positions near the chamber wall or door usually receive greater heat flows than those in the centre of the shelf, causing variations in the product quality within the freeze-dried batch. In the case of high-throughput vials, which are used for screening formulations, these variations could lead to biased results and the selection of sub-optimal formulations.

Previous work carried out by our team focused on how the vial position in the well plate could affect the heat flow received during ice sublimation (Section 4.2). That work developed a 3D mechanistic model for heat transfer during ice sublimation using high-throughput vials (*distilled water model*), which

was then extended to a heat and mass transfer model for ice sublimation coupled to mass transfer through a dried product layer (*product model*). The *distilled water model* represented a situation similar to the beginning of primary drying (no dried product resistance to mass transfer; Konstantinidis et al., 2011), while the *product model* represented a typical moment during primary drying (5 mm of a dried product layer). Following the approach of Section 4.2.3, the present work will focus on how the well plate position on the shelf impacts the heat flow received by the vials. The geometry of the *distilled water* and *product models* described in Section 4.2.3 was modified to represent a well plate near the chamber wall or door. The new *distilled water model* was validated using experimental data obtained by gravimetric analysis during ice sublimation experiments. Finally, comparing the heat flows calculated using all the *distilled water* and *product models* introduced the notion of drying progress, so we could simulate how the impact of the well plate position would evolve (in time) during primary drying.

MATERIALS AND METHODS

Containers

The *96-Well Freeze-Drying System* manufactured by VirTis (SP Scientific, Stone Ridge, NY, USA) consisting of aluminium well plates and tubular glass vials – hereinafter referred to as high-throughput vials – was used in our research. Two well plate types were used (Buceta et al., 2021):

(i) A-type exhibiting a brilliant black surface finish and circular marks due to the way they were manufactured, and

(ii) B-type exhibiting a matte black surface finish and no visible marks.

Furthermore, two high-throughput vial sizes were used, which only differed in height, presenting a maximal filling volume of 500 µL or 1000 µL (Section 4.2.3).

Ice sublimation experiments

Several ice sublimation experiments were performed as described in Buceta et al. (2021), using a pilot scale freeze dryer Epsilon 2-25D (Martin Christ Gefriertrocknungsanlagen GmbH, Osterode am Harz, Germany). Each experiment required 768 vials in 8 well plates. During experiments with 500-µL vials, these were filled with 400 µL of distilled water; while during experiments with 1000-µL vials, these were filled with 600 µL of distilled water. Well plates were placed on the freeze dryer's shelf (pre-cooled at -50 °C) according to Figure 4.3-1. Relative air humidity was limited during loading by a dry air laminar flow in front of the freeze dryer door, reducing condensation on the shelves. Once well plates were loaded, a freezing step of 2 hours at -50 °C was performed to ensure all the water solidified. After the freezing step, the pressure inside the drying chamber was decreased until the set value for primary drying, and the shelf temperature was increased to the setpoint (at 1 °C.min^{-1}). The sublimation step thus started when the shelf temperature exceeded the ice-vapour equilibrium temperature at the chamber pressure. The inlet temperature of the heat-transfer fluid circulating inside the shelves (referred to as shelf temperature for short) was set during sublimation to either -40 or -15 °C. At shelf temperature -40 °C, the chamber pressure was set to 4 Pa; and at -15 °C, the chamber pressure was set to either 4, 12, 25, and 65 Pa. Ice sublimation experiments ended after sublimation of approximately 20% of the ice by quickly breaking the vacuum inside the chamber.

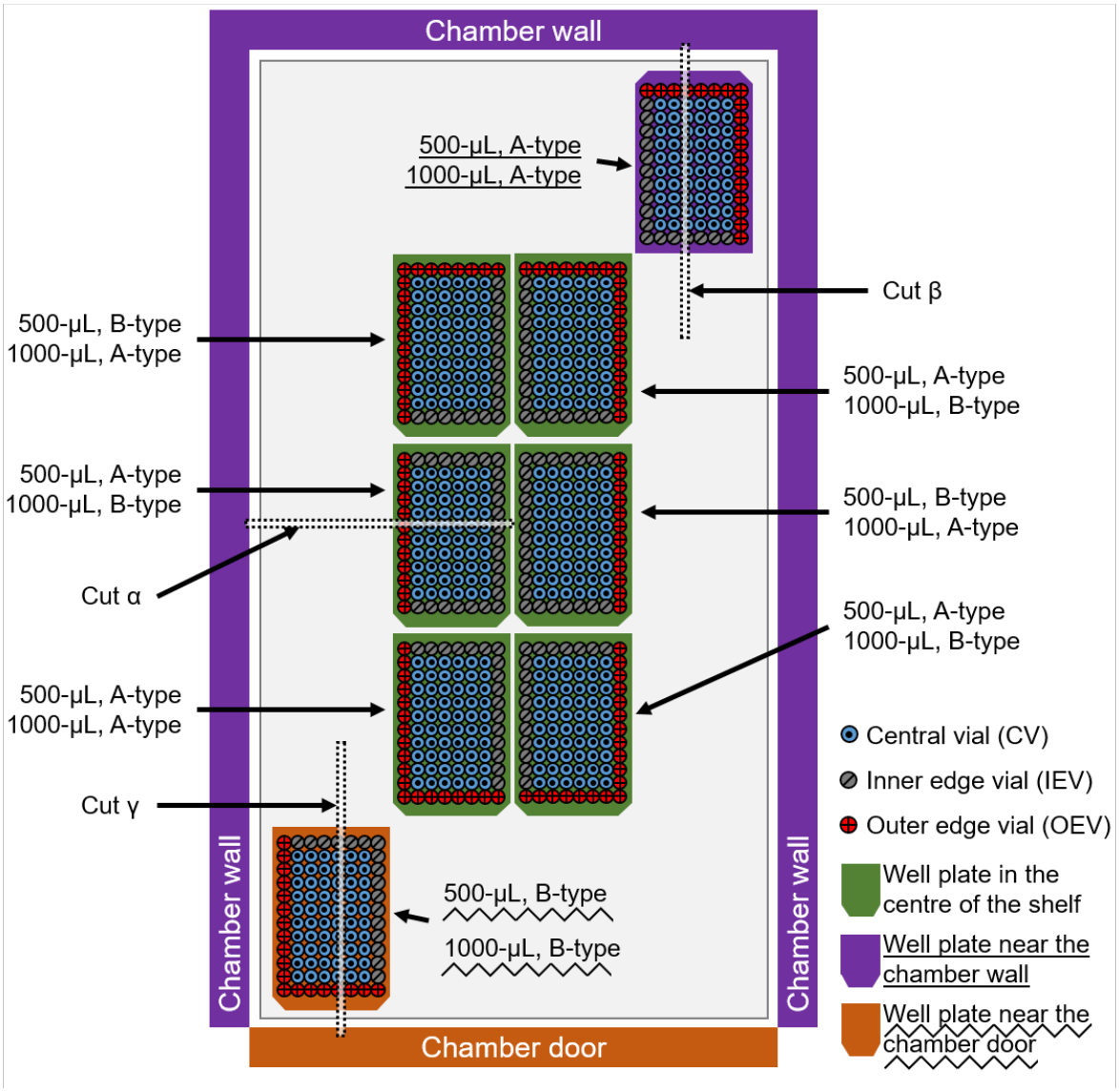

Figure 4.3-1 – Arrangement of the well plates on the freeze dryer shelf for tests (not in scale, view from the top). Dotted rectangles (cuts α, β, and γ) denote sections of the system represented in the 3D models.

Sublimation mass flow rates were gravimetrically measured. All vials in the well plate were weighed before ($m_{initial}$, kg) and after (m_{final}, kg) the ice sublimation experiments using a robotic tube handler model XL9 manufactured by BioMicroLab (Concord, California, USA) with an analytical scale (± 0.0001 g). Time-averaged heat flows ($\dot{Q}_{exp}$, W) were calculated for each vial as (Scutellà et al., 2017a):

$$\dot{Q}_{exp} = \frac{m_{initial} - m_{final}}{\Delta t} \Delta H_{sub} \qquad \text{Equation 4.3-1}$$

where Δt (s) is the duration of the ice sublimation experiment and ΔH_{sub} (2.763×10^6 J.kg^{-1}) is the latent heat of sublimation of water.

Determination of the surface emissivity and temperature of the chamber door

The surface emissivity of the door was measured by Themacs Ingénierie (Champs-sur-Marne, France) using the emissometer EM-2 (Monchau et al., 2013). Moreover, the surface temperature of the door was measured during ice sublimation experiments at chamber pressure 4 Pa and shelf temperature -40 and -15 °C using Tempris wireless temperature probes (iQ-mobil solution GmbH, Holwkirchen, Germany) secured with heat conductive tape.

MATHEMATICAL MODELLING

There are several possible loading configurations on the shelf of the freeze dryer when using high-throughput vials inside well plates. Figure 4.3-1 presents the three well plate positions that have been considered in this work:

(i) in the centre of the shelf (Figure 4.3-1, green well plates);

(ii) near the chamber wall (Figure 4.3-1, purple well plate); and

(iii) near the chamber door (Figure 4.3-1, orange well plate).

Moreover, high-throughput vials can be grouped depending on their position inside the well plate and with respect to the chamber:

(i) vial positions next to a well plate edge and facing the closest chamber surface (wall or door) hereinafter referred to as "outer edge vials" (Figure 4.3-1, red circles with black crosses);

(ii) vial positions next to a well plate edge facing another well plate or a distant chamber surface (wall or door) hereinafter referred to as "inner edge vials" (Figure 4.3-1, grey circles with a black diagonal line); and

(iii) vial positions surrounded by other vials, hereinafter referred to as "central vials" (Figure 4.3-1, blue circles with a black dot inside).

3D model for a well plate situated in the centre of the shelf

The 3D mathematical models for ice sublimation with vials filled with distilled water (*distilled water model*) and vials filled with a sucrose solution (*product model*) fully described in Section 4.2.3 were used to calculate the heat flow rates received by high-throughput vials inside a well plate in the centre of the shelf. In the *distilled water model*, vials were considered filled with frozen distilled water; and in the *product model*, vials were considered filled with a frozen 5% w/w sucrose solution (product) (same volume as during ice sublimation tests).

The geometries of the 3D models represented a portion of the drying chamber indicated as a "cut α" in Figure 4.3-1, and were created using the software COMSOL Multiphysics 5.3a (COMSOL, Inc, Burlington, USA). As an example, Figure 4.3-2a shows the 3D geometry for the 500-µL vials, consisting of a portion of the chamber wall, the shelves, the well plate, and eight vials with their content. Moreover, Figure 4.3-2c details the two contents considered (i.e. only ice, or frozen product with a dried product layer of 5 mm). The geometry for the 1000-µL vials was similar to that of 500-µL vials, only varying the vial height and filled depth. Relevant dimensions of the geometry are reported in Table 4.3-1.

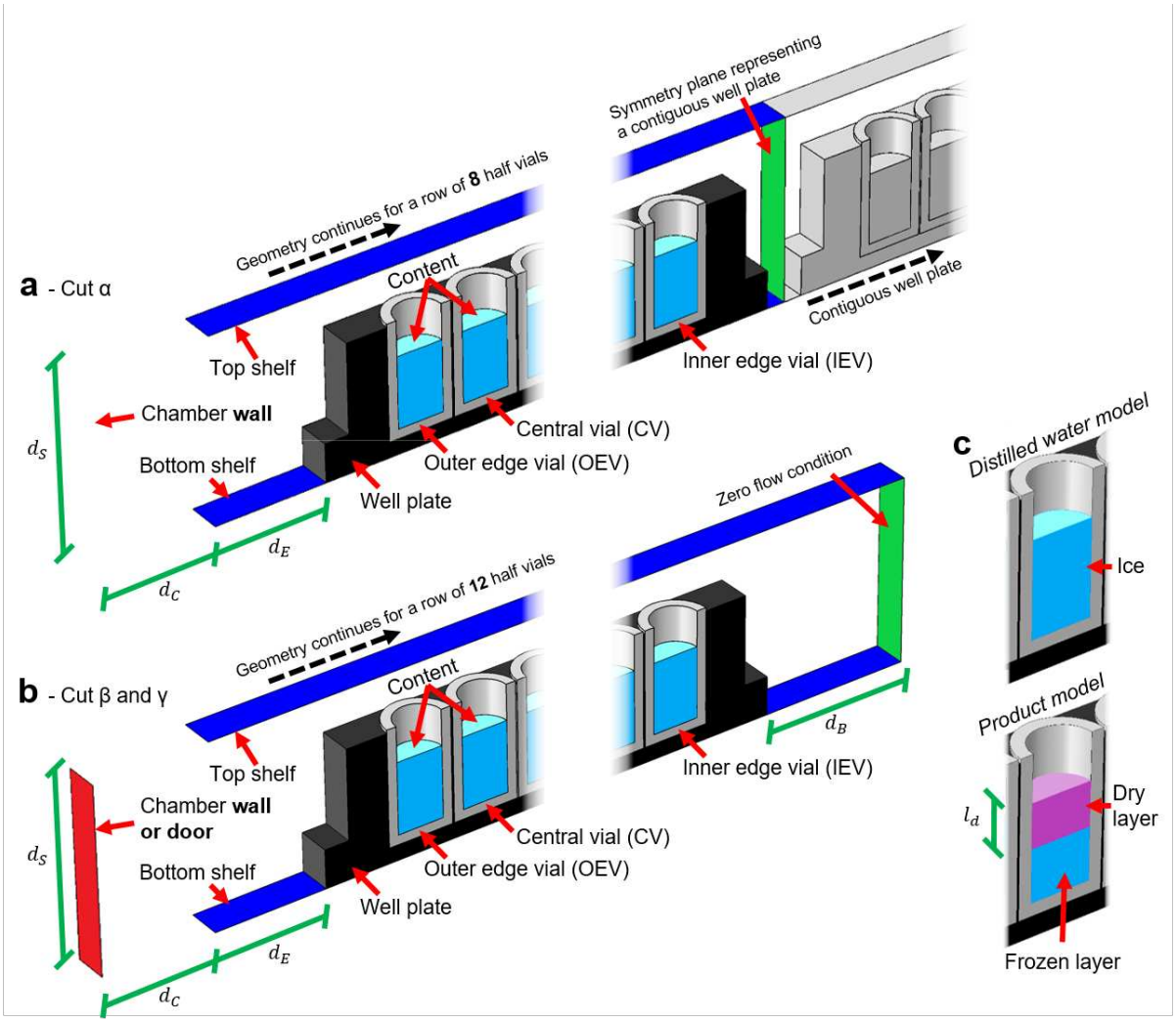

Figure 4.3-2 – Model geometry (not in scale) for 500-µL vials in well plates (a) in the centre of the shelf (cut α in Figure 4.3-1), and (b) near the chamber door or wall (cut β or γ in Figure 4.3-1). Overall view, with only the vials closer to the edge represented for clarity. (c) Detail of the vial and its content for the distilled water model and product model.

Table 4.3-1 – Relevant 3D model dimensions, fixed temperatures, surface emissivity values, and physical characteristics of the dried product.

Parameter	Description	Value	Units	Source
d_B	Distance between the well plate and the vertical symmetry plane	90	mm	Parametric analysis in this work
d_C	Distance between the shelf and the chamber wall	108	mm	Section 4.2.3
	Distance between the shelf and the chamber door	128	mm	Measured
d_E	Distance between the edge of the shelf and the well plate in the centre of the shelf	140	mm	Section 4.2.3
	Distance between the edge of the shelf and the well plate near the chamber wall or door	10	mm	Measured
d_S	Vertical separation between shelves	57	mm	(Buceta et al., 2021)
d_{VE}	Outer diameter of the vial	8.82	mm	(Buceta et al., 2021)
d_{VI}	Inner diameter of the vial	7.20	mm	(Buceta et al., 2021)
$h_{HV,500}$	500-µL vial height	15.7	mm	(Buceta et al., 2021)
$h_{HV,1000}$	1000-µL vial height	29.1	mm	(Buceta et al., 2021)
h_{well}	Depth of the wells	15.2	mm	(Buceta et al., 2021)
l_d	Dried product layer thickness	5	mm	Consideration for this work
R_P	Area normalised product resistance	1.248×10^5	$Pa.s.m^2.kg^{-1}$	(Konstantinidis et al., 2011)
T_{wall}	Surface temperature of the chamber wall when shelf temperature is set to -40 °C	0.1	°C	Section 4.2.3
	Surface temperature of the chamber wall when shelf temperature is set to -15 °C	5.1		
T_{door}	Surface temperature of the chamber door when shelf temperature is set to -40 °C	0.2	°C	Measured
	Surface temperature of the chamber door when shelf temperature is set to -15 °C	11.0		
ε_d	Emissivity of the dried product layer	0.95	Dimensionless	(Emteborg et al., 2014)
ε_{door}	Emissivity of the chamber door	0.88	Dimensionless	Measured

Continuation of Table 4.3-1.

Parameter	Description	Value	Units	Source
ε_{ice}	Emissivity of the ice	0.98	Dimensionless	(Heldman and Moraru, 2010)
ε_{shelf}	Emissivity of the shelf	0.18	Dimensionless	Section 4.2.3
ε_{vial}	Emissivity of the vial	0.85	Dimensionless	Section 4.2.3
ε_{wall}	Emissivity of the chamber wall	0.13	Dimensionless	Section 4.2.3
ε_{wp}	Emissivity of the well plate	0.87	Dimensionless	Section 4.2.3
λ_d	Thermal conductivity of the dried product layer	0.043	$W.m^{-1}.K^{-1}$	5 % of the sucrose thermal conductivity (Krokida et al., 2001)

The heat transfer mechanisms considered in the models were previously described in Section 4.2.3 and are briefly recalled hereafter:

(i) Contact conduction. Two contact conduction coefficients were defined: one between the bottom shelf and the well plate bottom (K_{WP}^{cc}, W.m^{-2}.K^{-1}), and one between the wells and the vials (K_{HV}^{cc}, W.m^{-2}.K^{-1}). A perfect thermal contact was considered between the vials and the content (neglecting thermal resistance).

(ii) Conduction through the solids. The conduction within the well plate, vials, and content was modelled using the Fourier equation, which relates the heat fluxes and the local temperature gradients considering the geometric dimensions of the objects and their thermal conductivity (λ, W.m^{-1}.K^{-1}).

(iii) Conduction through the gas. The conduction through the water vapour in the chamber was modelled using the Fourier equation considering a boundary layer (Knudsen layer) next to all solids (i.e. the chamber wall, shelves, well plate, vials and content). Moreover, two thermal accommodation coefficients related to the quality of momentum exchange between the gas molecules and adjacent surfaces were defined: one between the bottom shelf and the well plate bottom (α_{WP}, dimensionless), and one between the wells and the vials (α_{HV}, dimensionless).

(iv) Radiation. The radiation fluxes in the chamber were modelled by the radiosity method, and depended on the geometric dimensions of the surfaces, their disposition in the geometry, and their surface emissivity value (ε, dimensionless).

Heat transfer equations of the mentioned mechanisms were solved using COMSOL. Relevant model parameters are reported in Table 4.3-1, and calibrated parameters are reported separately in Table 4.3-2.

The *distilled water model* and *product model* neglected the mass transfer within the chamber, assuming the chamber filled with water vapour and the chamber pressure uniform and equal to the specified setpoint. The *product model* considered the mass transfer within the dried product layer, however, which was modelled considering the area-normalised dried product resistance (R_P, Pa.s.m^2.kg^{-1}, Table 4.3-1). The mass transfer equation was solved in MATLAB R2017a (The MathWorks, Inc, Natick, Massachusetts, USA), and results obtained with COMSOL and MATLAB were connected through the LiveLink interface.

Table 4.3-2 – Mean values and standard errors (SE) of the parameters calibrated based on measured heat flow data for 500-µL vials in A-type well plates in the centre of the shelf at a shelf temperature of -15 °C and chamber pressures of 4, 12, and 65 Pa. Values for B-type well plates were previously determined in Section 4.2.3 and are recalled for comparison.

Parameter	Description	Value for A-type well plate (mean ± SE)	Value for B-type well plate (mean ± SE)*	Units
K_{HV}^{cc}	Contact conduction heat transfer coefficient between the wells and the vials.	16.5 ± 2.5	20.1 ± 4.1	$W.m^{-2}.K^{-1}$
K_{WP}^{cc}	Contact conduction heat transfer coefficient between the bottom shelf and the well plate bottom.	4.2 ± 1.4	5.1 ± 1.8	$W.m^{-2}.K^{-1}$
l_{WP}	Average gas layer thickness between the shelf and the well plate bottom.	523 ± 24	420 ± 89	µm
α_{HV}	Accommodation coefficients for conduction through the trapped gas between the wells and the vials.	0.241 ± 0.018	0.330 ± 0.022	Dimensionless
α_{WP}	Accommodation coefficients for conduction through the trapped gas between the bottom shelf and the well plate bottom.	0.84 ± 0.16	0.95 ± 0.18	Dimensionless

*Taken from Section 4.2.3.

3D model for a well plate situated near the chamber wall or door

The models for central well plates were modified as follows to represent heat and mass transfer near the chamber walls and door (Figure 4.3-2b):

(i) The number of vials in the row was changed from 8 to 12. As shown in Figure 4.3-1, a row of 8 vials was considered for the model of well plates in the centre of the shelf (cut α); however, a row of 12 vials was considered to face the chamber door and back wall (cuts β and γ).

(ii) The distance between the chamber door and the shelf (d_C, Figure 4.3-2), and the shelf and the well plate (d_E, Figure 4.3-2) were changed accordingly.

(iii) The distance between the well plate and the zero flow condition plane (d_B, Figure 4.3-2) was set to 90 mm, which was found long enough to fully develop the gas's temperature profile near the inner edge vials. The heat flow received by the inner edge vials varied by less than 0.1% when increasing d_B to 180 mm (double the length).

(iv) In the particular case of a well plate near the chamber door, the chamber wall's surface emissivity and temperature were changed to those of the chamber door.

The values of the changed model parameters are also reported in Table 4.3-1.

Use of the experimental heat flows for parameter calibration and model validation

For each well plate type (i.e. A-type and B-type), five model parameters related to microscopic contact between solids and to the gas entrapped therein had to be calibrated:

(i) the contact conduction contributions between adjacent solids (K_{WP}^{cc}, K_{HV}^{cc}),

(ii) the accommodation coefficients for conduction through the trapped gas (α_{WP}, α_{HV}), and

(iii) the average gas layer thickness between the shelf and the well plate bottom (l_{WP}).

Parameters for B-type well plates were taken from Section 4.2.3. Parameters for A-type well-plates were calibrated following the same approach described in Section 4.2.3, considering the 3D model for a well plate situated in the centre of the shelf, and using $\dot{Q}_{exp}$ values of 500-µL vials inside well plates in the centre of the shelf under nine conditions (3 operating conditions: shelf temperature -40 °C and chamber pressures 4, 12, and 65 Pa; and 3 vial positions: central, inner edge and outer edge). The validation of the 3D heat transfer models consisted in comparing the heat flows calculated using the *distilled water model* with $\dot{Q}_{exp}$ for the remaining twenty-one conditions (Section 4.2.3, Appendix 4.2-A).

RESULTS AND DISCUSSION

Parameter calibration and validation of the 3D models

Model parameters related to microscopic contact between solids and conduction through the gas entrapped therein were calibrated for A-type well plates. Table 4.3-2 presents the values of said parameters as well as the parameter values for B-type well plates previously determined in Section 4.2.3. The contact conduction contributions between the bottom shelf and the well plate bottom (K_{WP}^{cc}) and between wells and vials (K_{HV}^{cc}) were lower for A-type than B-type well plates. The surfaces of A-type well plates presented circular manufacturing marks that made them have fewer contact points, reducing the heat transfer by contact conduction (i.e. K_{WP}^{cc} and K_{HV}^{cc}). Furthermore, the accommodation coefficients for conduction through the trapped gas (α_{WP}, α_{HV}) were also lower for A-type well plates; which was expected since polished surfaces as those of A-type well plates typically present lower accommodation coefficients than matte (unpolished) surfaces like those of B-type well plates (Pikal, 2000). Finally, the average gas layer thickness between the shelf and the well plate bottom (l_{WP}) was greater for A-type well plates than B-type; this could be related to the circular manufacturing marks of the well plate bottom and the overall wavier visual aspect of the surface of B-type well plates.

Calculated and experimental heat flows received by the vials during ice sublimation were compared to validate the 3D heat transfer models (*distilled water models*); results are presented in Appendix 4.3-A and Appendix 4.3-B. The agreement between measurements and model predictions was found satisfactory. Deviations between measured and predicted heat flows in cases not used for calibration were on average 5% (Appendix 4.3-A), and the coefficients of determination (R^2) were higher than 0.96 (Appendix 4.3-B). For reference, deviations for conditions used for parameter calibration were on average 4%. Deviations were similar or lower than the experimental coefficients of variation (approximately 11%); therefore, the models' simulations in new conditions within the considered experimental range were deemed trustworthy.

Heat and mass transfer variations between well plate positions

The impact of the container position on the shelf was previously studied by several authors for serum vials during ice sublimation (e.g. Pikal et al., 2016; Pisano et al., 2011; Rambhatla and Pikal, 2003). While Section 4.2.3 studied the impact of the high-throughput vial position in the well plate, to the best of the authors' knowledge, there is no published research so far addressing the impact of the well plate position on the shelf.

Figure 4.3-3 presents the ratios of the average heat flows received by vials in well plates near the chamber wall or door to vials inside well plates in the centre of the shelf ($\dot{Q}_{WD}/\dot{Q}_C$), obtained using the *distilled water model* and the *product model* at chamber pressure 4 Pa and shelf temperatures -40 and -15 °C. Similar results were obtained at all chamber pressures lower than 12 Pa, of pharmaceutical interest. The value of R_P increases during primary drying (Pikal, 2000); hence the results obtained with the *distilled water model* are a representation of the very beginning of primary drying (no dry layer, R_P=0 Pa.s.m^2.kg^{-1}, Konstantinidis et al., 2011), and results obtained with the *product model* represent an intermediate point of primary drying.

According to the *distilled water model* (Figure 4.3-3, stripped purple bars), the impact of placing a well plate near the chamber wall was not noticeable at -15°C but only at -40 °C, when $\dot{Q}_{WD}/\dot{Q}_C$ reached between 115 and 120%. Scutellà et al. (2017b) reported that the ratio of the heat flow received by serum vials filled with distilled water near the chamber wall to serum vials in the centre of the arrangement could go from 147% to 190%. Thus the impact of the well plate position on the shelf seemed considerably lower than that of serum vials. The impact of the chamber door, however, was significant for all conditions according to the *distilled water model*, when $\dot{Q}_{WD}/\dot{Q}_C$ reached between 120 and 133% (Figure 4.3-3, stripped orange bars).

Compared to the *distilled water model*, the dried product layer considered in the *product model* altered the impact of the well plate position on the heat flow received by the vials (Figure 4.3-3, plain bars). This occurred because, in the *distilled water model*, the temperature at the sublimation front only depended on the chamber pressure and was the same for all well plate positions; however, in the *product model*, the temperature at the sublimation front depended on the total heat flow reaching the vial (Section 4.2.3). Interestingly, in the *product model*, the dependence of the vial temperature on the heat flow increased or decreased $\dot{Q}_{WD}/\dot{Q}_C$ with respect to the *distilled water model*, depending on the operating conditions (shelf temperature and chamber pressure) and vial size (500-µL or 1000-µL). From a practical point of view, the worst cases are when $\dot{Q}_{WD}/\dot{Q}_C$ increases from the *distilled water model* to the *product model*, because this implies that variations among well plate positions would increase during the process. These worst cases were observed for well plates near the chamber door at shelf temperature -40 °C for 500-µL and 1000-µL vials, and at -15 °C for 1000-µL vials.

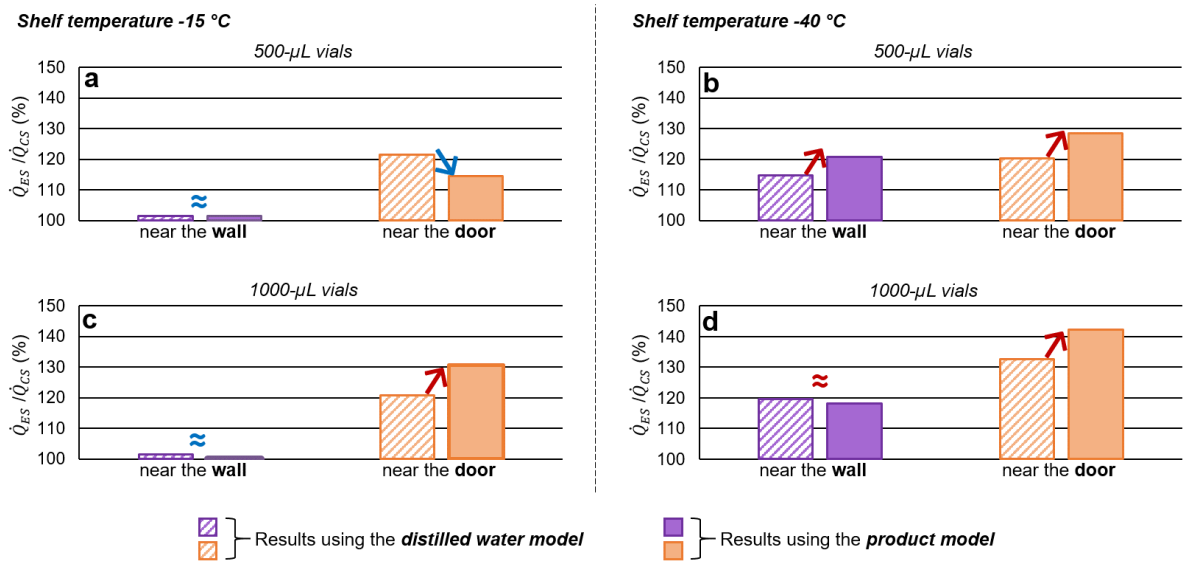

Figure 4.3-3 – Ratio of the average heat flows received by vials in well plates near the chamber wall or door ($\dot{Q}_{WD}$) to those in centre of the shelf ($\dot{Q}_C$) at a chamber pressure of 4 Pa. (a) Results for 500-µL vials at shelf temperature -15 °C. (b) Results for 500-µL vials at shelf temperature -40 °C. (c) Results for 1000-µL vials at shelf temperature -15 °C. (d) Results for 1000-µL vials at shelf temperature -40 °C. The red arrows pointing upwards represent an increase in the variation in the product model compared to the distilled water model. The blue arrows pointing downwards represent a reduction. The approximate symbol (≈) represents a similar variation in the distilled water and product models.

The following is a detailed analysis of how the dried product layer could increase or decrease the variation on the heat flow received by different well plate positions, as described in Figure 4.3-4. The dried product layer had different impacts on $\dot{Q}_{WD}/\dot{Q}_C$ because the dried product resistance to mass transfer (R_P) had two opposite outcomes in parallel:

(i) On one hand, R_P increased T_{sat} (for all well plate positions) compared to the *distilled water model*, which raised the vial and well plate temperatures and reduced the heat flow from the bottom shelf. Thus, the heat from the chamber wall or door had a relatively greater contribution to the total heat flow received by the vials in the *product model*. This outcome was predominant in cases presenting a red arrow pointing upwards in Figure 4.3-3, intensifying the impact of the well plate position compared to the *distilled water model*. For these cases, we expect an increase (positive feedback, Figure 4.3-4) in the variation of the heat flows received by vials in different well plate positions during primary drying.

(ii) On the other hand, R_P implied that T_{sat} was greater in well plates that received greater heat flows. Therefore, in the *product model*, the temperature difference between the well plate and the bottom shelf was lower for well plates near the chamber wall or door compared to well plates in the centre of the shelf, penalising the heat transfer to well plates near the chamber wall or door. This outcome was predominant in the case presenting a blue arrow pointing downwards in Figure 4.3-3. For this case, we expect a reduction (negative feedback, Figure 4.3-4) in the variation of the heat flow received by vials in different well plate positions during primary drying.

Both of these phenomena exist simultaneously, and either may become dominant depending on the studied situation: shelf temperature, chamber pressure, proximity to the chamber wall or door, vial size, among others.

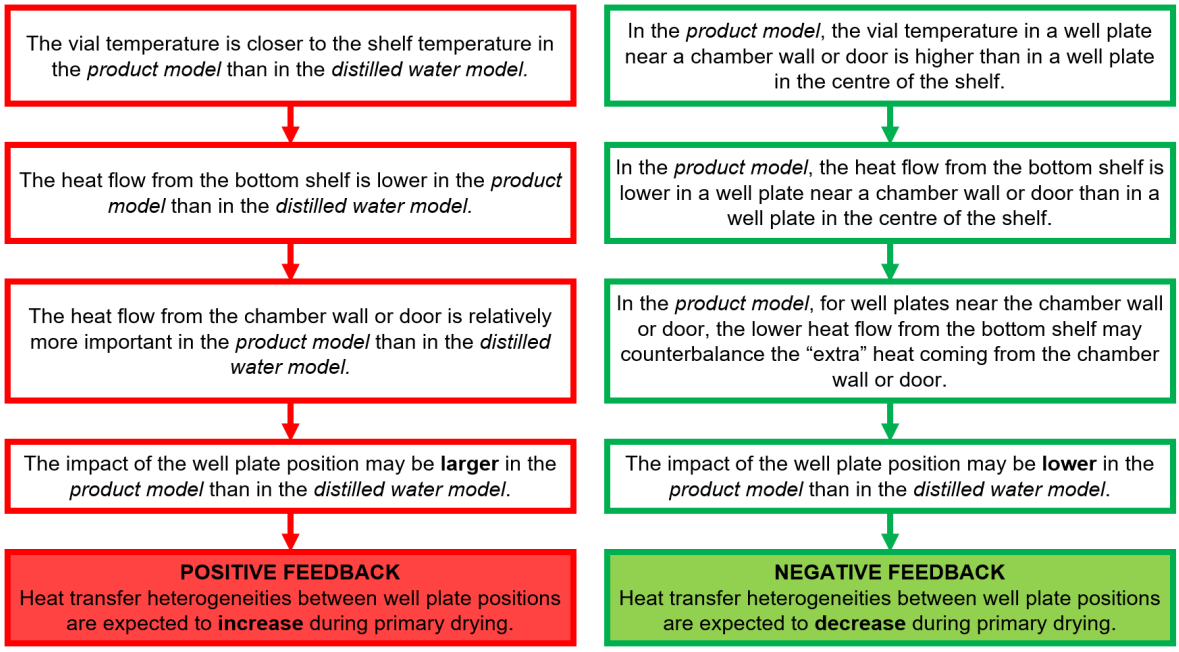

Figure 4.3-4 – Causes of negative and positive feedback on the variation between heat flows received by the vials due to their position.

Heat transfer to the metallic well plates

3D mathematical modelling is a powerful tool to identify the mechanisms behind the total heat flow received by the objects (e.g. vials, well plates) in the drying chamber. Figure 4.3-5a and Figure 4.3-5b present the total heat flows received by the well plate (not the vials) calculated using the *distilled water model* for 1000-µL vials (similar results were obtained for 500-µL vials). The heat flow contributions arriving at the well plate bottom from the bottom shelf by radiation, gas conduction, and contact conduction represented together over 86% of the total heat flow reaching the well plate (= heat flow arriving at the well plate bottom / total heat flow arriving at the well plate × 100%). Previous work by Buceta et al. (2021) showed that the global heat transfer coefficient between the shelf and the well plate is more than two times greater than between the shelf and serum vials, enlightening the high efficiency of the heat transfer between the shelf and the metallic well plate bottom. This efficiency made the extra heat flow contribution forn the chamber wall or door less important in comparison, helping to reduce the impact of the well plate position compared to the case of serum vials.

Figure 4.3-5c and Figure 4.3-5d show the same results calculated using the product model. The total heat flows were over 2 to 4 times lower in the *product model* than the *distilled water model* (Figure 4.3-5a and Figure 4.3-5b). This occurred because the product resistance to mass transfer (R_P) increased the pressure and temperature at the sublimation front, and therefore the temperature of the high-throughput system. Consequently, the temperature difference between the well plate and the hot surfaces in the drying chamber (i.e. shelves, chamber wall and door) diminished in the *product model*, and so did the heat flow received by the well plate. According to the *product model*, at shelf temperature -15 °C, the heat flow reaching a well plate by radiation between distant surfaces and conduction through the gas within the chamber remained low (less than 8% of the total heat flow arriving at the well plate; Figure 4.3-5c). However, the relative radiation contribution from the chamber (wall or door) drastically increased at shelf temperature -40 °C near the chamber wall and door (up to 65% of the total heat flow arriving at the well plate, Figure 4.3-5d), when the heat flow contribution from the bottom shelf was particularly low (less than 30% of the total heat flow arriving at the well plate, Figure 4.3-5d). At shelf temperature -40 °C and near a chamber wall or door, the heat flow arriving at the high-throughput system by radiation from the chamber (mainly) raised the well plate temperature very close to the shelf temperature (up to -40.9 °C), so the shelf was almost too cold to heat the well plate. These results highlight the importance of 3D modelling to predict heat transfer variations near the chamber wall or door at low shelf temperatures, when the shelf is not the main heat source, and simpler models may fail to account for the observed phenomena. Moreover, results obtained with the *product model* illustrated the additional complexity introduced by coupled heat and mass transfer compared to the *distilled water model*, for which the temperature of the vials depends primarily on the chamber pressure.

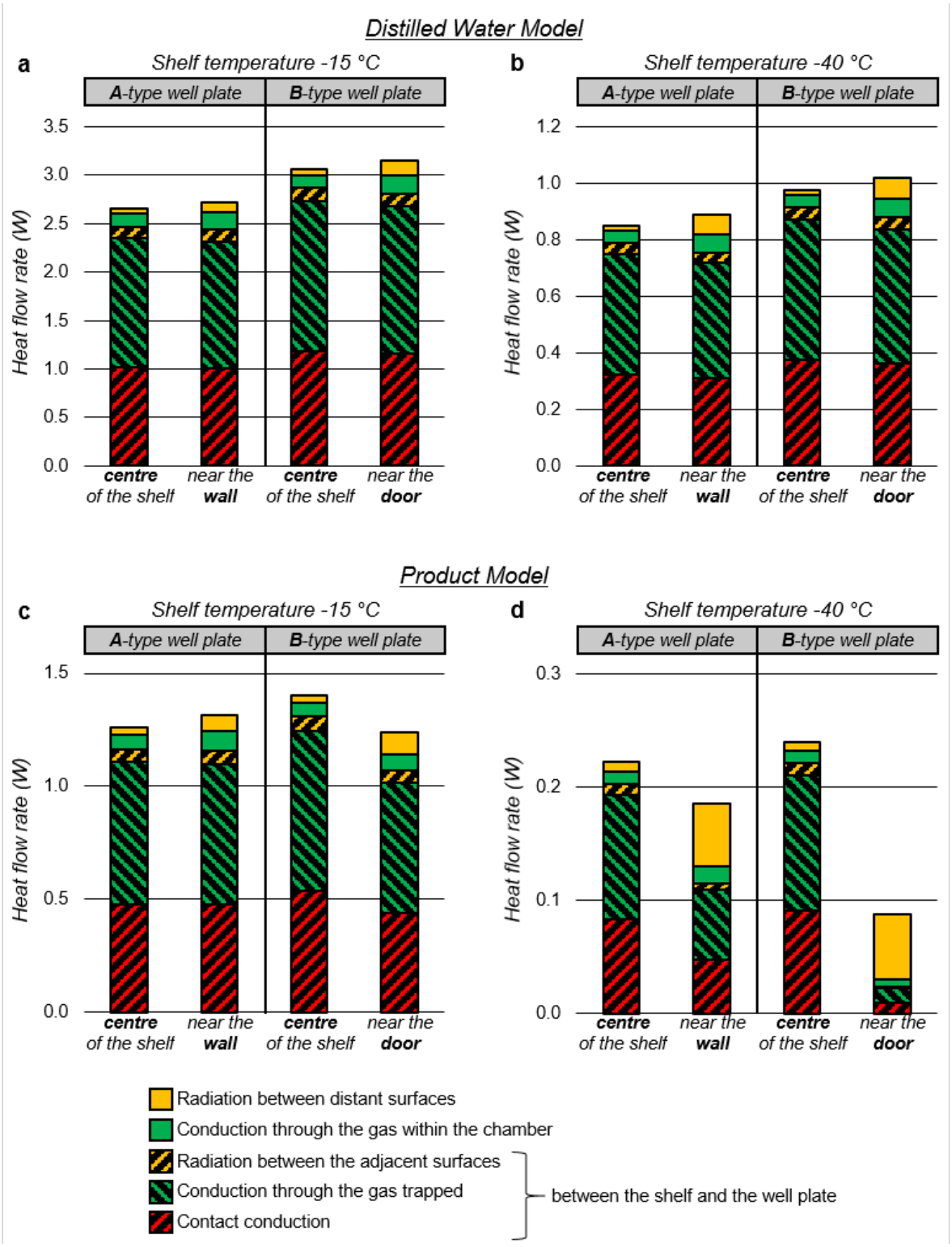

Figure 4.3-5 – Calculated heat flow rates received by the well plates (not the vials) containing 1000-µL vials at chamber pressure 4 Pa using: (a) the distilled water model at shelf temperature -15 °C, (b) the distilled water model at shelf temperature -40 °C, (c) the product model at shelf temperature -15 °C, (d) the product model at shelf temperature -40 °C. Well plates positions in the "centre of the shelf", "near the (chamber) wall", or "near the (chamber) door" are shown in Figure 4.3-1.

Heat transfer to the vials

Figure 4.3-6a shows the contributions of each heat transfer mechanism to the total heat flow received by the vials calculated using the *distilled water model* at chamber pressure 4 Pa and shelf temperature -15 °C. Heat flows arriving from the wells (sum of radiation, gas conduction, and contact conduction) were the main contributors to the heat flows reaching central vials, representing over 56% of the total. Radiation between distant surfaces (mostly from the chamber door) explained the increase in the heat flow received by vials in the well plates near the chamber door. To study what happens when sublimating at lower shelf temperatures, Figure 4.3-6b displays the contributions of each heat transfer mechanism calculated using the *distilled water model* at -40 °C. In this case, the impact of placing the well plate near the chamber wall was noticeable since the heat flow contribution from the wells was lower in comparison with the extra heat transfer from the wall by radiation and conduction through the gas within the chamber.

Similarly, placing the well plate near the chamber door had an even greater relative impact than at -15 °C. The chamber door's surface emissivity was almost seven times greater than that of the chamber wall (Table 4.3-1), which explains the greater impact of radiation on the well plate near the chamber door compared to near the chamber wall. Similar conclusions were obtained for 500-µL vials (data not shown).

Results for the *product model* are given in Figure 4.3-6c and Figure 4.3-6d. As previously observed in Section 4.2.3, the presence of the dried product layer tended to reduce the heat flows due to the increase of the pressure and temperature at the sublimation front. Regarding the impact of the vial position in the well plate, the presence of the dry layer reduced the variation of the heat flow received by vials in different positions in the well plate (heat flow received by 1000-µL outer edge vials / heat flow received by 1000-µL central vials × 100% ≈ 104% in the *product model*, and ≈ 129% in the *distilled water model*), as previously noted in Section 4.2.3. Concerning the impact of the well plate position on the shelf, the heat flow arriving at the vials by radiation between distant surfaces near the chamber wall and door was relatively greater in the *product model* than in the *distilled water model*. Hence, according to the *product model*, radiation is expected to play a greater role in the impact of the well plate position as primary drying progresses.

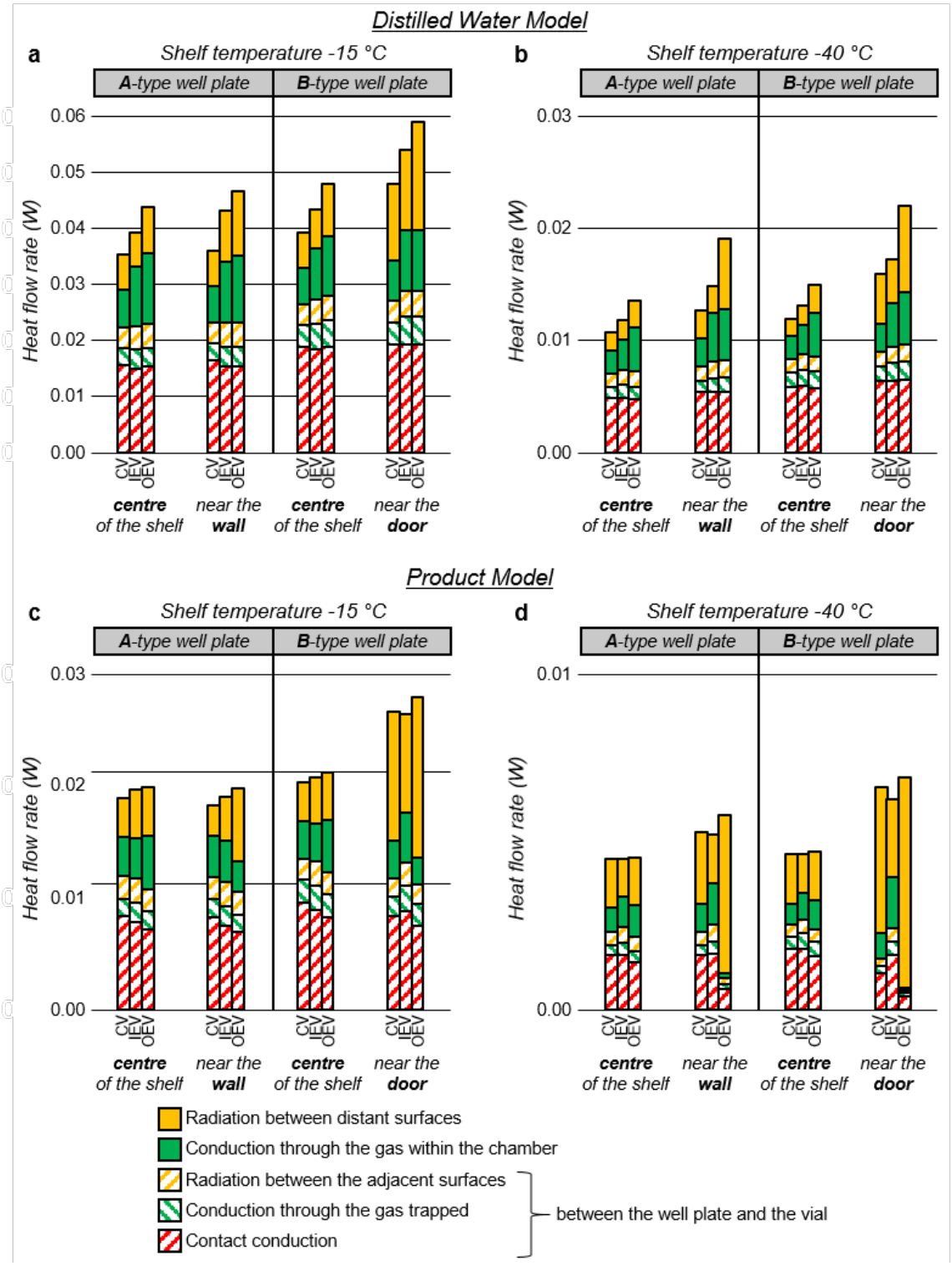

Figure 4.3-6 – Calculated heat flow rates received by 1000-µL vials at chamber pressure 4 Pa using: (a) the distilled water model at shelf temperature -15 °C, (b) the distilled water model at shelf temperature -40 °C, (c) the product model at shelf temperature -15 °C, (d) the product model at shelf temperature -40 °C. Well plates positions in the "centre of the shelf", "near the (chamber) wall", or "near the (chamber) door" are referred to Figure 4.3-1. "C" are values for central vials, "IE" are values for inner edge vials, and "OE" are values for outer edge vials, also referred to Figure 4.3-1.

Heat fluxes in the drying chamber

To understand the impact of the distance from the well plate to the edge of the shelf (d_E, Figure 4.3-2) on the heat transfer, we compared the heat fluxes by radiation and conduction ($\dot{q}$, W.m^{-2}) for different well plate positions. Figure 4.3-7 shows the $\dot{q}$ lines of flux (coloured lines) and their module (colour logarithmic scale) calculated using the *distilled water model* for 1000-µL vials; similar results were obtained for 500-µL vials. For the well plate in the centre of the shelf, d_E was long enough to "cushion" the impact of the heat fluxes from the chamber wall; this could be observed in Figure 4.3-7 (cut α) as most of the $\dot{q}$ lines of flux from the chamber wall go to the shelves and not the well plate and vials. For the well plate near the chamber wall,-most of the $\dot{q}$ lines of flux from the chamber wall in Figure 4.3-7 (cut β) went to the high-throughput system (well plate and vials).

These observations on the $\dot{q}$ lines of flux can also be mechanistically explained. A longer d_E reduces the view factor from the chamber wall or door to the vials and well plate, diminishing the heat transfer by radiation. Moreover, a longer d_E also lets space for the gas to cool from the edge of the shelf to the centre, reducing the heat transfer by gas conduction.

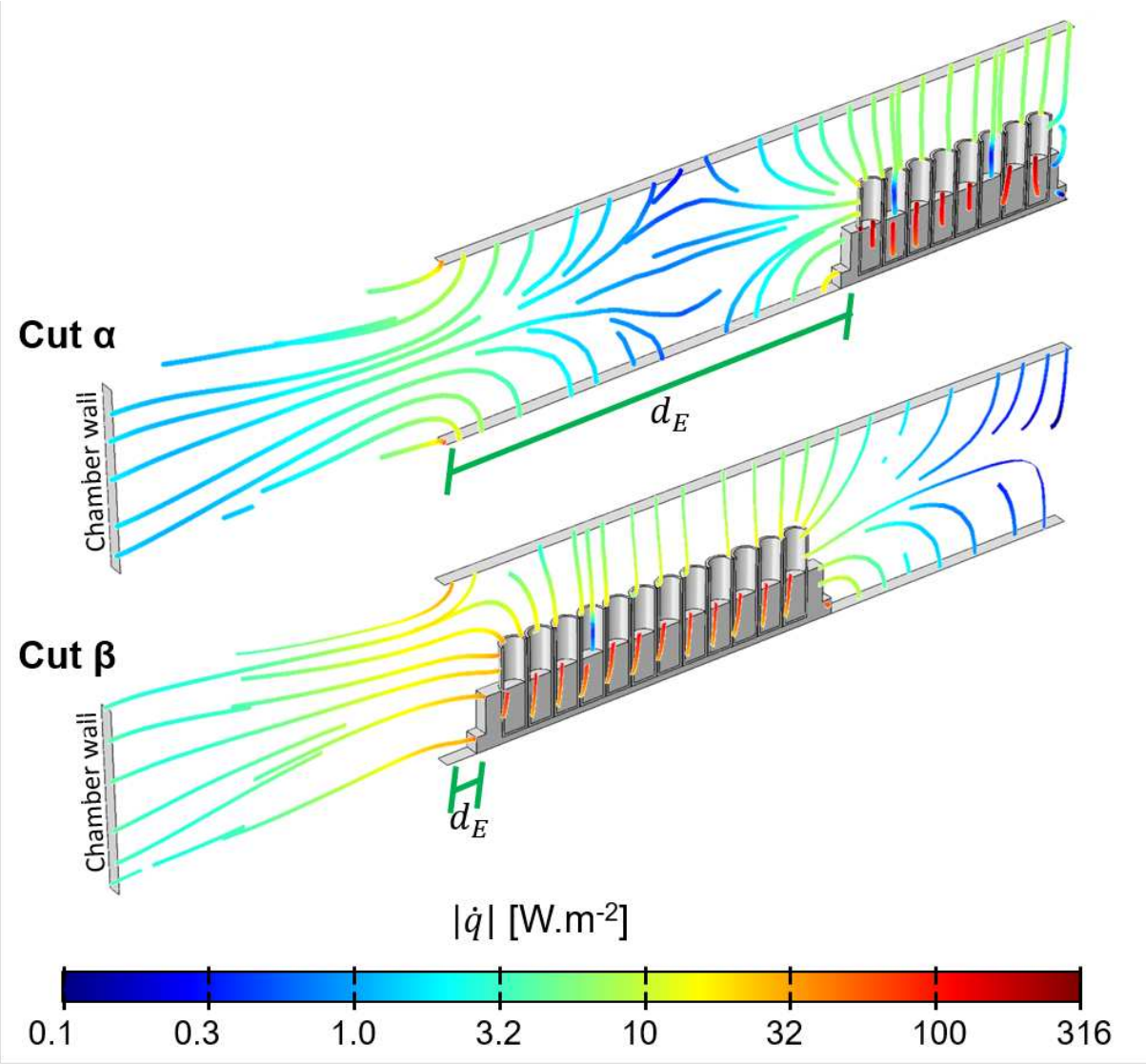

Figure 4.3-7 – Total heat fluxes by radiation and conduction ($\dot{q}$, W.m^{-2}) calculated using the distilled water model for 1000-µL vials at chamber pressure 4 Pa and shelf temperature -40 °C. $\dot{q}$ lines of flux are represented as coloured lines where the colours represent the modules of $\dot{q}$ expressed in a logarithmic scale. $\dot{q}$ within well plates are not shown. Cuts α and β refer to Figure 4.3-1.

Product temperatures

The temperature of the product during primary drying could affect the appearance and the dried product's structure. Therefore, variations in product temperature among vials must be foreseen during process design to ensure the final product quality. Product temperature of central, inner edge, and outer edge vials varied by less than 0.6 °C within the same well plate, at shelf temperatures -40 and -15 °C and chamber pressures lower than 12 Pa, for both 500-µL and 1000-µL vials. Figure 4.3-8 presents the product temperature increase due to the well plate type and position on the shelf. The well plate type induced a variation in the product temperature between 0.3 and 0.7 °C. Placing a well plate near the chamber wall increased the product temperature close to 1 °C at shelf temperature -40 °C, and had a negligible effect at shelf temperature -15 °C. Furthermore, placing a well plate near the chamber door increased the product temperature between 1 and 2 °C compared to the centre of the shelf.

Comparing our 3D *product models* with other models from the literature, it appears that at 4 Pa and -40 °C, less accurate results could be obtained using the classic simplified 0D model based on a global heat transfer coefficient between the shelf and the vials (commonly known as K_V; Buceta et al., 2021; Pikal, 2000; Pisano et al., 2011; Scutellà et al., 2017a; Velardi and Barresi, 2008; von Graberg, 2011). This is mainly because the 0D model assumes that all the heat flow comes from the bottom shelf. For the sake of example, consider the 0D model as described in Buceta et al. (2021) with a global heat transfer coefficient determined based on the heat flows calculated with the *distilled water model*. In this case, the calculated product temperature for central vials in a well plate near the chamber door could be up to 2.2 °C lower than calculated by 3D modelling. Additional safety margins of 2 °C on the product temperature are thus advised when using simplified 0D models.

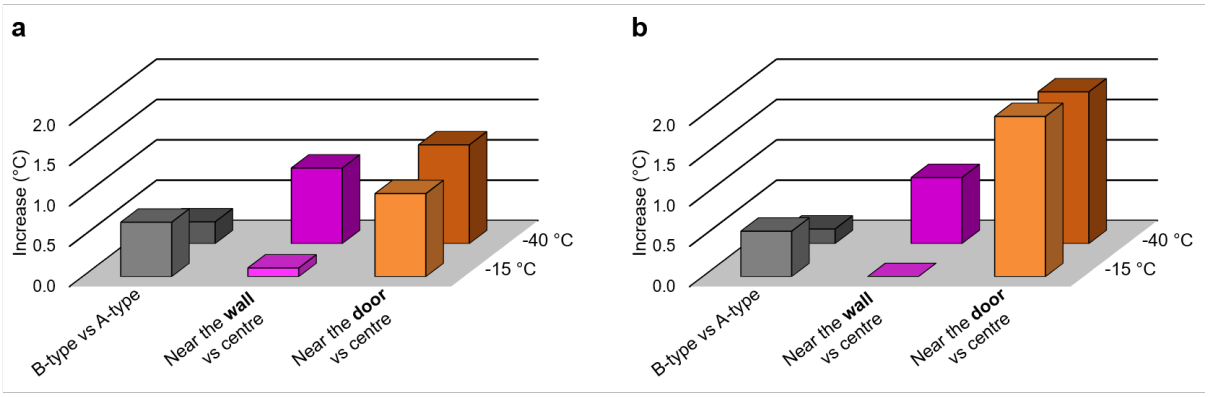

Figure 4.3-8 – Product temperature increase due to: (i) a B-type well plate instead of an A-type well plate (both in the centre of the shelf), (ii) placing the A-type well plate near the chamber wall instead of the centre of the shelf, (iii) placing the B-type well plate near the chamber door instead of the centre of the shelf. Results at chamber pressure 4 Pa.

CONCLUSIONS

Throughout this work, 3D models previously developed during this thesis for primary drying using a high-throughput system were expanded to represent a broader range of situations. 3D models accounted for the relative contributions of various heat transfer mechanisms and shed light on the causes of heat transfer variations among different well plate positions on the freeze dryer's shelf relative to the walls and door.

Heat flows received by high-throughput vials were calculated when placing well plates in different positions on the shelf (centre of the shelf, near the chamber wall or door). Results obtained using models for vials filled with distilled water (*distilled water model*) represented the beginning of primary drying. In contrast, results obtained with the model considering the mass transfer through a dried product layer (*product model*) represented a later stage of primary drying. The increase in the heat flow received by vials in a well plate near a chamber wall was significant at shelf temperature -40 °C ($\dot{Q}_{WD}/\dot{Q}_C \times 100\% > 115\%$) but not at -15°C. Moreover, the increase in the heat flow received by vials in a well plate near a chamber door was significant at both shelf temperatures -40 °C and -15°C ($\dot{Q}_{WD}/\dot{Q}_C \times 100\% > 114\%$). The impact of the well plate position may increase ($\dot{Q}_{WD}/\dot{Q}_C \times 100\%$ up to 142%) as the dried product resistance to mass transfer increases during primary drying from 0 to 1.248×10^5 Pa.s.m^2.kg^{-1} (comparing *distilled water model* and *product model*).

While radiation and gas conduction from the chamber wall or door were the main mechanisms causing variations among well plate positions at the beginning of primary drying (*distilled water model*), radiation from the chamber wall or door played the most important role as primary drying evolved (*product model*). This variation of the relative contributions of the heat transfer mechanisms was not traditionally considered by 0D models based on heat transfer coefficients between the shelf and the vial. Therefore, a safety margin for the product temperature of about +2 °C is recommended when using simplified 0D models for well plates near the chamber door.

APPENDIX 4.3-A

Validation of the 3D models.

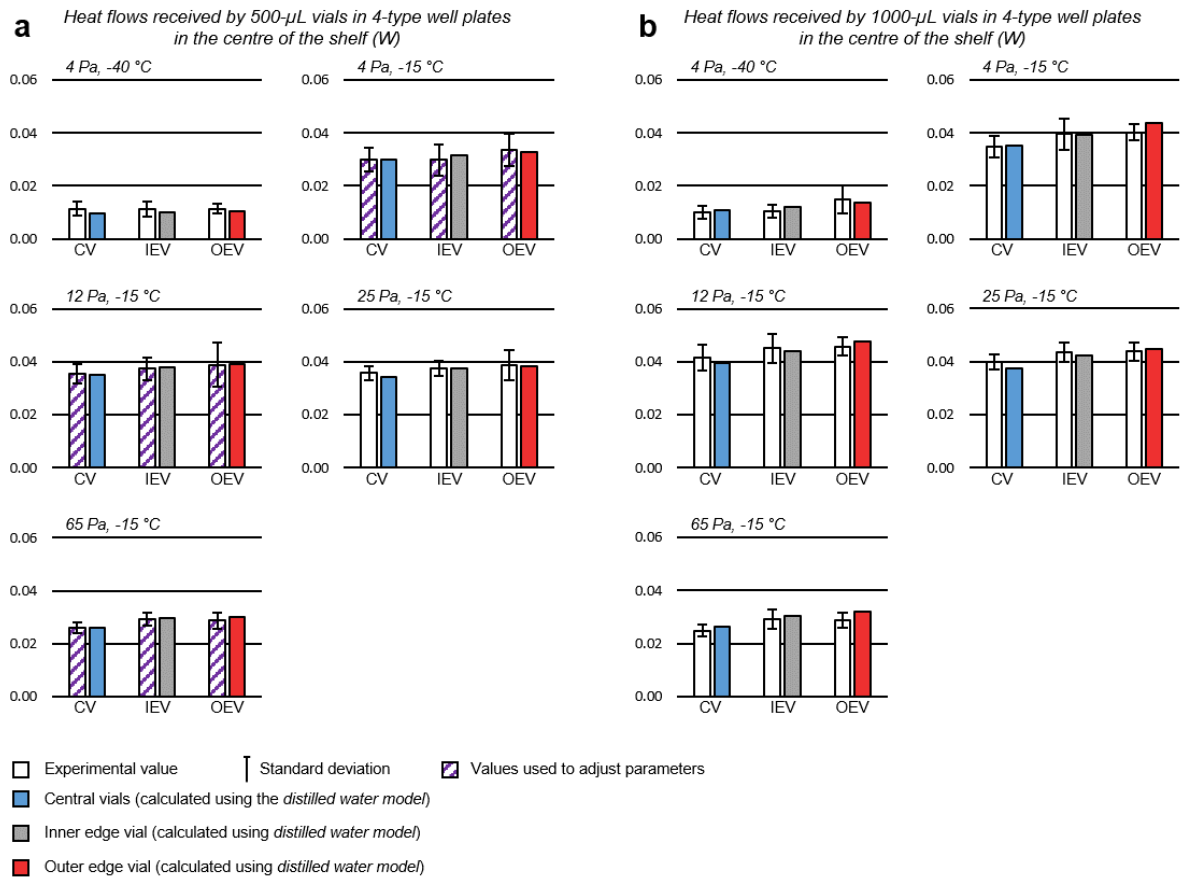

*Figure 4.3-9 – Comparison of experimental and simulated heat flows received by (a) 500-µL vials and (b) 1000-µL vials in an **A-type well plate in the centre of the shelf**. Several combinations of shelf temperatures (-40 °C and -15 °C) and chamber pressures (4, 12, 25, and 65 Pa) were tested. Error bars in experimental data represent standard deviations. "C" are values for central vials (positions in blue in Figure 4.3-1), "IE" are values for inner edge vials (positions in grey in Figure 4.3-1), and "OE" are values for outer edge vials (positions in red in Figure 4.3-1).*

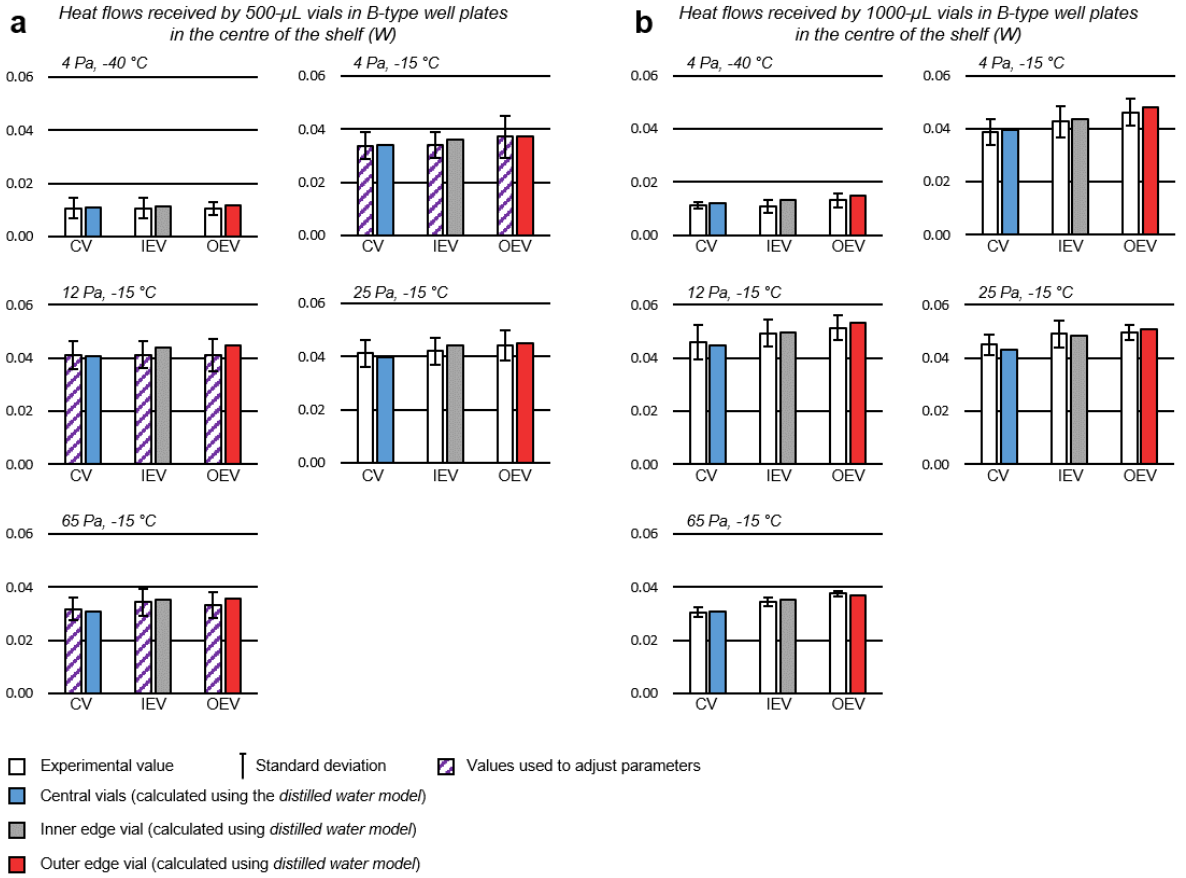

*Figure 4.3-10 – Comparison of experimental and simulated heat flows received by (a) 500-µL vials and (b) 1000-µL vials in a **B-type well plate in the centre of the shelf**. Several combinations of shelf temperatures (-40 °C and -15 °C) and chamber pressures (4, 12, 25, and 65 Pa) were tested. Error bars in experimental data represent standard deviations. "C" are values for central vials (positions in blue in Figure 4.3-1), "IE" are values for inner edge vials (positions in grey in Figure 4.3-1), and "OE" are values for outer edge vials (positions in red in Figure 4.3-1).*

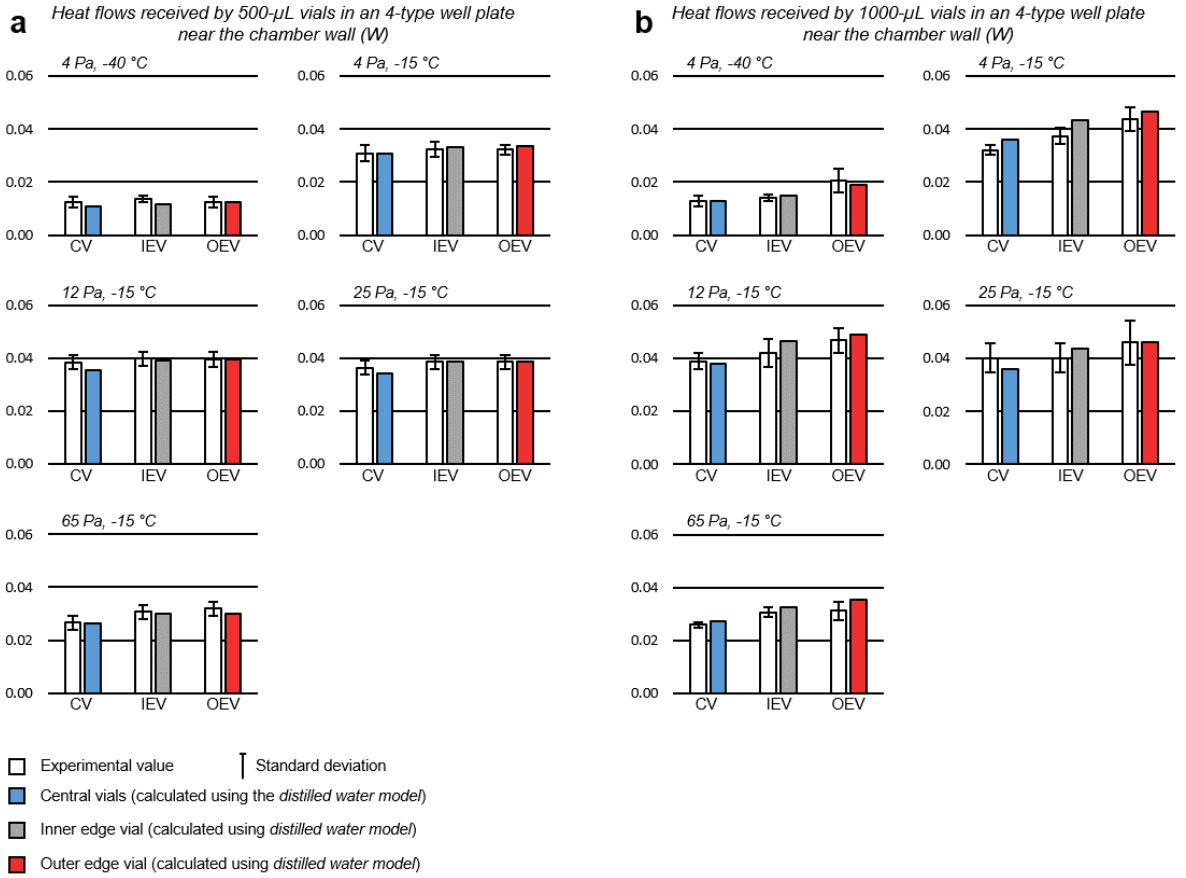

*Figure 4.3-11 – Comparison of experimental and simulated heat flows received by (a) 500-µL vials and (b) 1000-µL vials in an **A-type well plate near the chamber wall**. Several combinations of shelf temperatures (-40 °C and -15 °C) and chamber pressures (4, 12, 25, and 65 Pa) were tested. Error bars in experimental data represent standard deviations. "C" are values for central vials (positions in blue in Figure 4.3-1), "IE" are values for inner edge vials (positions in grey in Figure 4.3-1), and "OE" are values for outer edge vials (positions in red in Figure 4.3-1).*

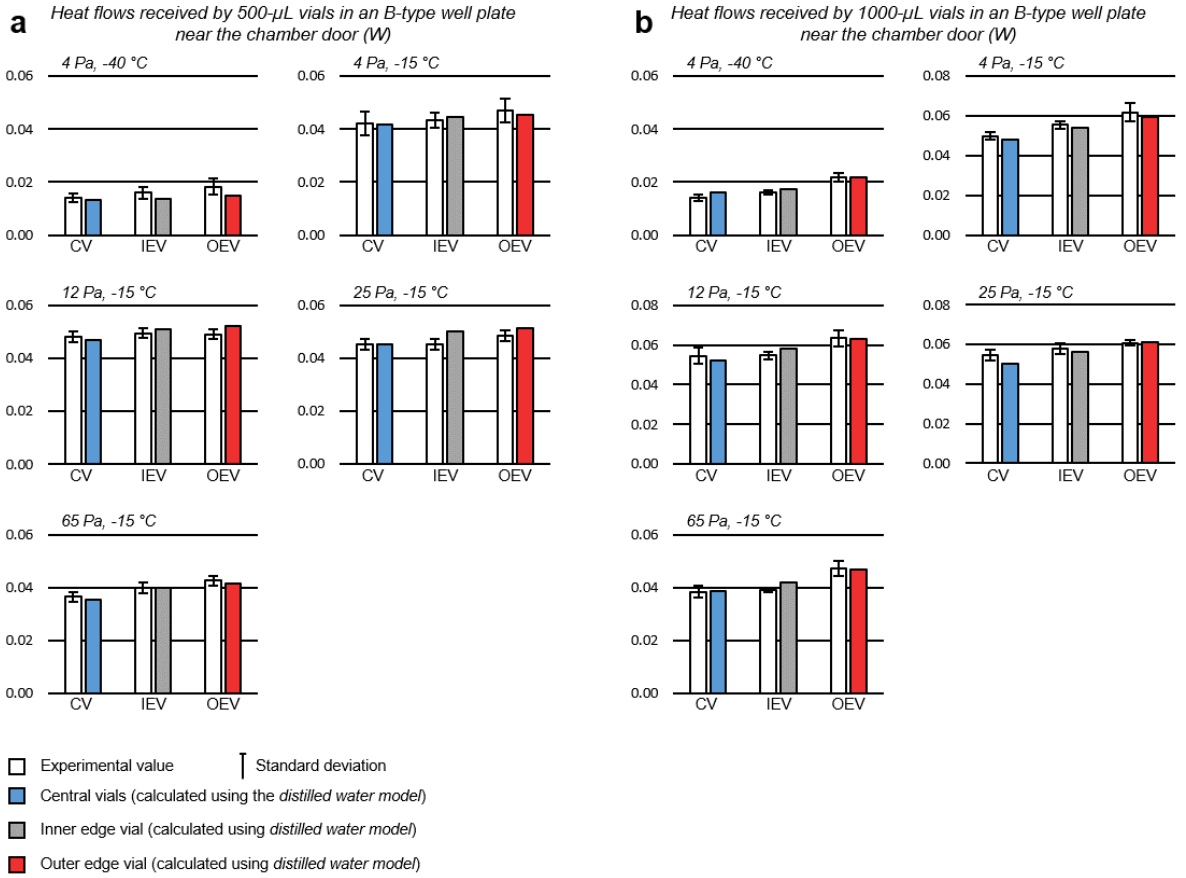

*Figure 4.3-12 – Comparison of experimental and simulated heat flows received by (a) 500-µL vials and (b) 1000-µL vials in a **B-type well plate near the chamber door**. Several combinations of shelf temperatures (-40 °C and -15 °C) and chamber pressures (4, 12, 25, and 65 Pa) were tested. Error bars in experimental data represent standard deviations. "C" are values for central vials (positions in blue in Figure 4.3-1), "IE" are values for inner edge vials (positions in grey in Figure 4.3-1), and "OE" are values for outer edge vials (positions in red in Figure 4.3-1).*

APPENDIX 4.3-B

Comparison of mean heat flows of the 3D models.

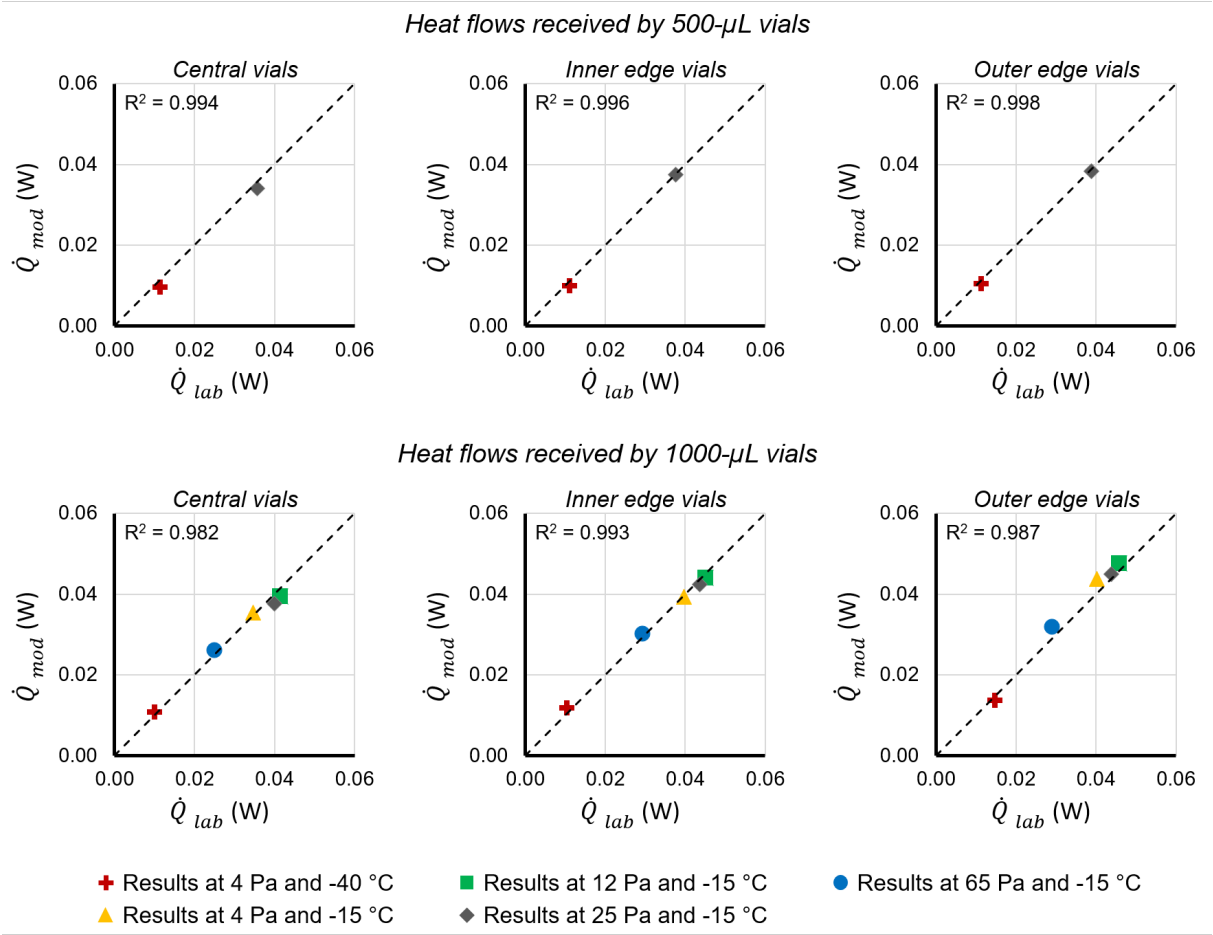

*Figure 4.3-13 – Comparison of mean experimental ($\dot{Q}_{lab}$) and simulated ($\dot{Q}_{mod}$) heat flows received by 500-µL vials and 1000-µL vials in an **A-type well plate in the centre of the shelf**. Several combinations of shelf temperatures (-40 °C and -15 °C) and chamber pressures (4, 12, 25, and 65 Pa) were tested. Central vials, inner edge vials, and outer edge vials refer to positions in Figure 4.3-1. The values of the coefficient of determination (R2) are reported in the figure.*

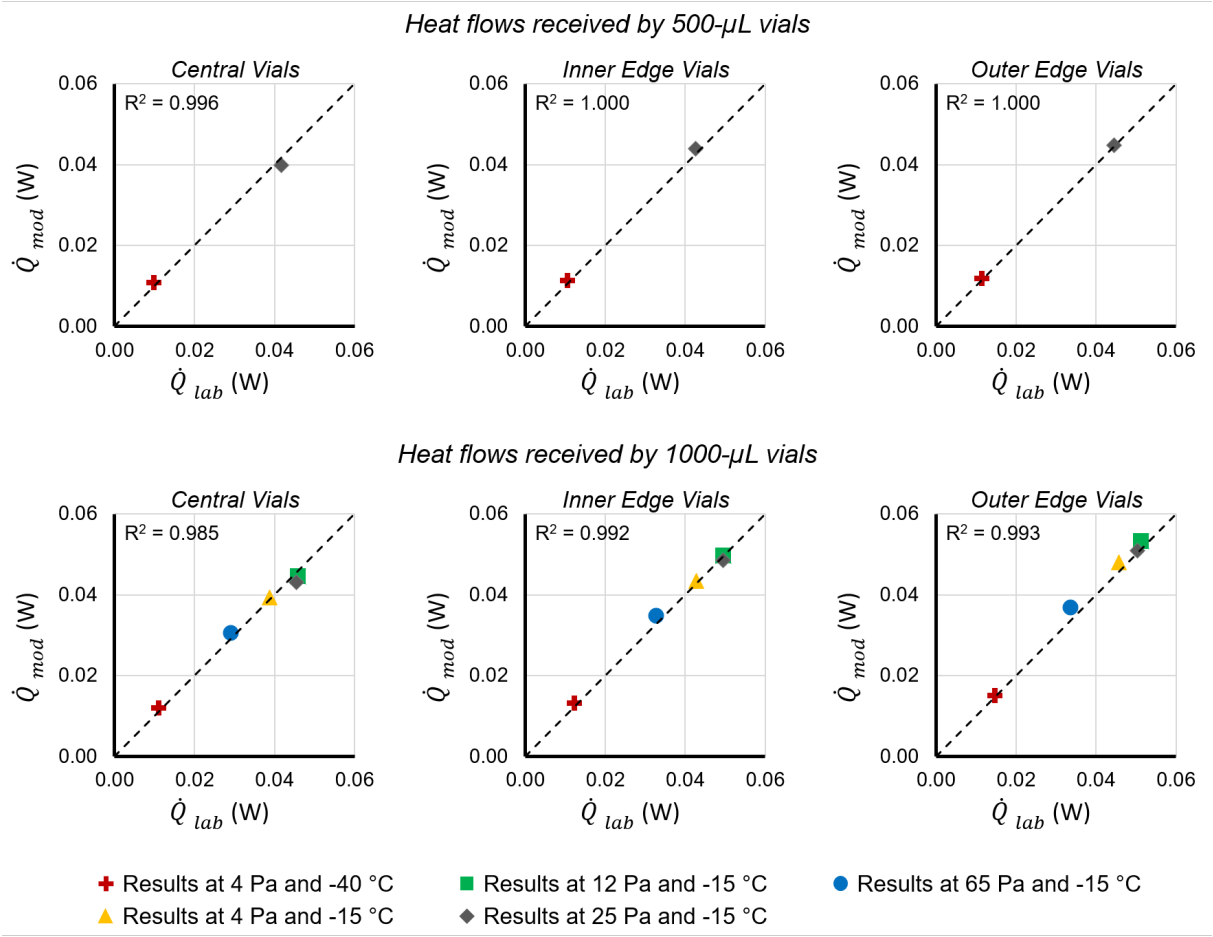

*Figure 4.3-14 – Comparison of mean experimental ($\dot{Q}_{lab}$) and simulated ($\dot{Q}_{mod}$) heat flows received by 500-µL vials and 1000-µL vials in a **B-type well plate in the centre of the shelf**. Several combinations of shelf temperatures (-40 °C and -15 °C) and chamber pressures (4, 12, 25, and 65 Pa) were tested. Central vials, inner edge vials, and outer edge vials refer to positions in Figure 4.3-1. The values of the coefficient of determination (R2) are reported in the figure.*

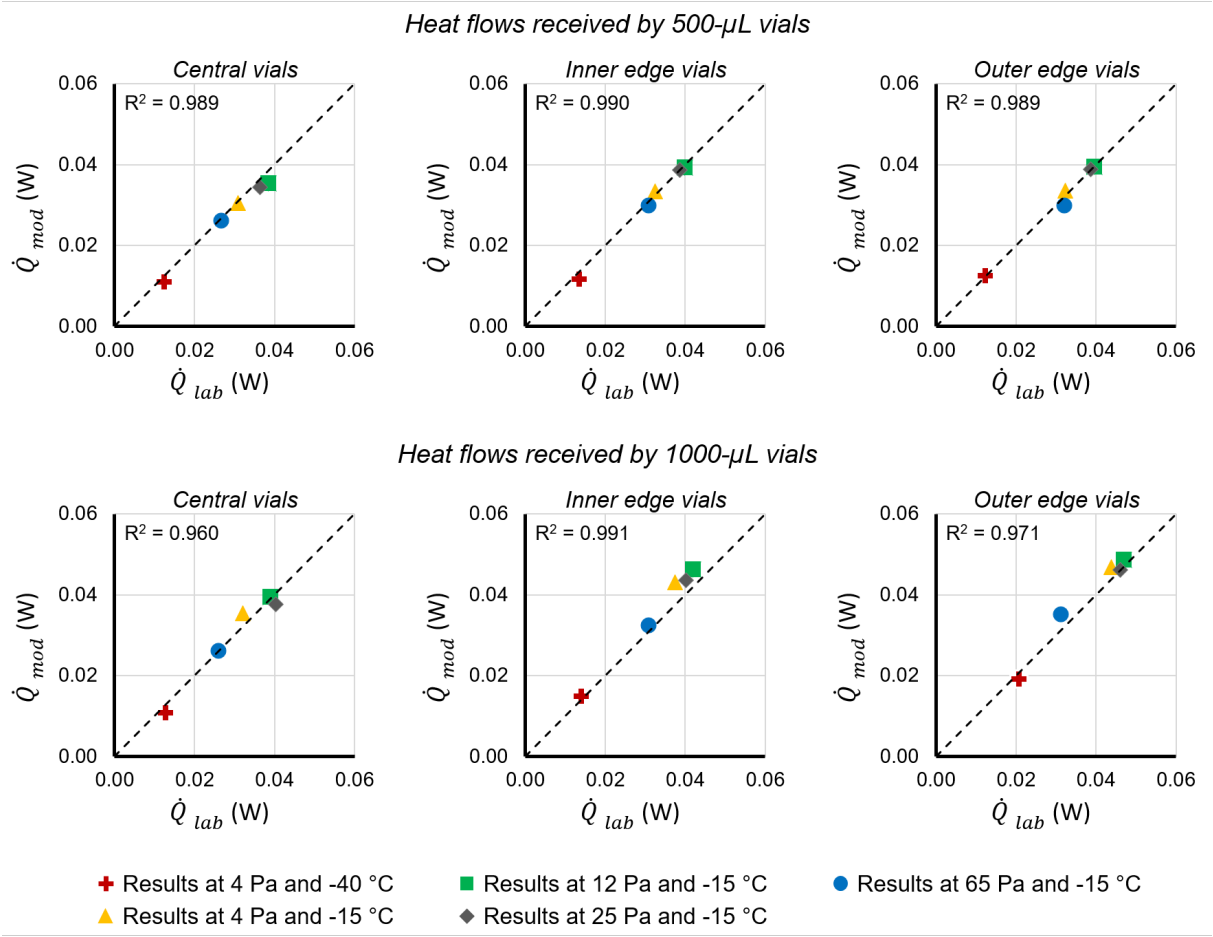

*Figure 4.3-15 – Comparison of mean experimental ($\dot{Q}_{lab}$) and simulated ($\dot{Q}_{mod}$) heat flows received by 500-µL vials and 1000-µL vials in an **A-type well plate near the chamber wall**. Several combinations of shelf temperatures (-40 °C and -15 °C) and chamber pressures (4, 12, 25, and 65 Pa) were tested. Central vials, inner edge vials, and outer edge vials refer to positions in Figure 4.3-1. The values of the coefficient of determination (R2) are reported in the figure.*

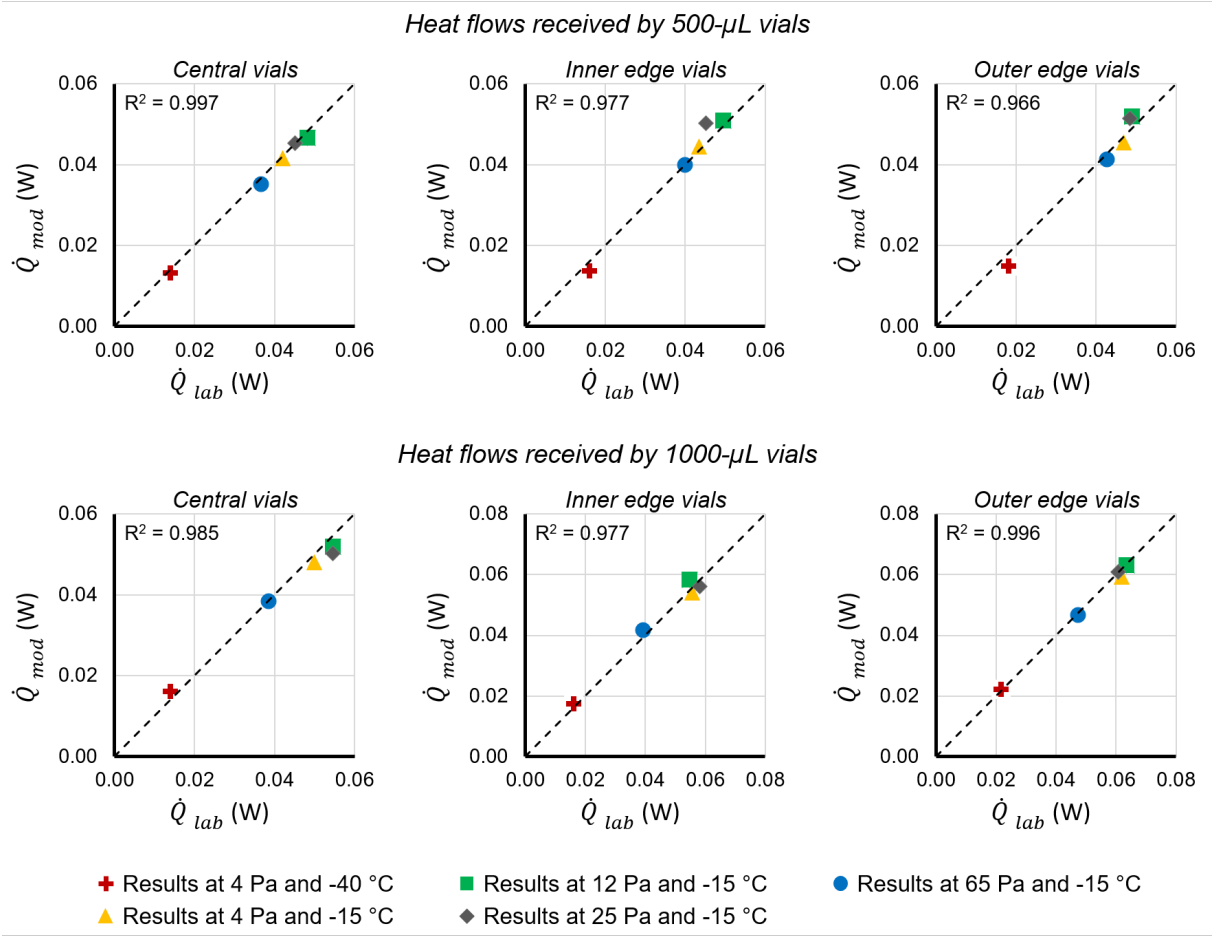

*Figure 4.3-16 – Comparison of mean experimental ($\dot{Q}_{lab}$) and simulated ($\dot{Q}_{mod}$) heat flows received by 500-µL vials and 1000-µL vials in a **B-type well plate near the chamber door**. Several combinations of shelf temperatures (-40 °C and -15 °C) and chamber pressures (4, 12, 25, and 65 Pa) were tested. Central vials, inner edge vials, and outer edge vials refer to positions in Figure 4.3-1. The values of the coefficient of determination (R2) are reported in the figure.*

4.3.4. Take-Home Message

The previously developed 3D heat and mass transfer model for high-throughput systems (Section 4.2, Paper II) was used to investigate the impact of the well plate type and position on the shelf on the heat flows and product temperature in primary drying. Placing a well plate near the chamber door increased the heat flow received by the vials compared to a well plate in the centre of the shelf (over 14%) at the beginning of primary drying. As the process continues, 3D modelling suggested the impact of placing a well plate near the chamber door becomes greater (up to 42%) at low shelf temperatures (e.g. -40 °C) or when using tall vials (1000-µL vials). A similar tendency was observed when placing a well plate with 500-µL vials near a chamber wall at low shelf temperature (e.g. -40 °C). Therefore, for the mentioned conditions, the "traditional" approach to study heat transfer variations during ice sublimation tests using vials filled with water (only) may lead to underestimating the impact of the well plate position during primary drying with a product.

The previous Sections 4.1, 4.2, and 4.3 investigated the heat transfer to high-throughput vials during the primary drying step of freeze-drying. In particular, the heat transfer to high-throughput vials was compared to that to serum vials (Section 4.1), and several factors involved in the heat transfer were addressed, such as the vial geometry (Section 4.1) and the position with respect to the chamber surfaces (Sections 4.2 and 4.3). Analogously, the following Section 4.2.3 focuses on the mass transfer when using high-throughput vials, comparing it to the mass transfer using serum vials, and studying a relevant factor involved in the mass transfer (the nucleation temperature).

4.4. Mass Transfer during Primary Drying in High-Throughput Vial Systems

4.4.1. Context

During the primary drying step of freeze-drying, the product temperature depends on the heat transfer to the vial and the mass transfer from the sublimation front to the condenser. As primary drying occurs, a dried product layer is formed in the vials, affecting the mass transfer. The mass transfer through the dried product layer has been previously modelled for serum vials and trays (e.g. Konstantinidis et al., 2011; Liapis and Bruttini, 1994). However, to the best of this author's knowledge, no published research addressed the mass transfer in high-throughput vials.

The geometry of the pores in the dried product layer affects the mass transfer (Pikal, 2000). Furthermore, pores are reminiscent of the ice crystals obtained during the freezing step. The ice crystal size distribution is related to the temperature at which the first ice nuclei form in the container (nucleation temperature) (Geidobler and Winter, 2013; Nakagawa et al., 2006). Therefore, the nucleation temperature is ultimately related to the pore size distribution and the area-normalised dried product resistance to mass transfer (R_P) (Searles et al., 2001a).

Previous research using 2D transient-state models showed that the shape of the sublimation front varies depending on the container type (Nam and Song, 2005; Sheehan and Liapis, 1998). In particular, sublimation fronts are utterly curved when lateral heat flows reaching the container are important and rather flat when lateral heat flows are negligible. Therefore, it is suspected that even if the pore size is the same in different containers, the shape of the sublimation front may impact the area-normalised dried product resistance to mass transfer (normalised by the inner section of the container).

4.4.2. Objectives

The mass transfer during primary drying is addressed in this Section 4.4. The impact of the container type (i.e. high-throughput or serum vials) and the nucleation temperature on the area-normalised dried product resistance is interpreted based on the pores in the dried product structure and the shape of the sublimation front.

4.4.3. Paper IV

This draft has not been submitted to a scientific journal.

PROVISIONAL TITLE

"Comparing freeze-drying in high-throughput and serum vials: mass transfer, dried product resistance, nucleation temperature, pore diameter, and sublimation front shape"

ACKNOWLEDGMENTS

We would like to thank Hayat Benkhelifa (AgroParisTech) for her help in data acquisition for the 3D X-ray micro-computed tomography.

CONTENTS OF PAPER IV

ABSTRACT

High-throughput vials permit fitting more formulations inside a freeze dryer than traditional serum vials, accelerating formulation screening for vaccine development. Translating freeze-drying cycles developed using high-throughput vials (research scale) into cycles for serum vials (pilot or production scale) requires heat and mass transfer models to ensure that the product reaches the same temperature during primary drying in both vial types. This work innovatively investigated how the vial type affects the dried product resistance to mass transfer (R_P), which is one of the most importat parameters affecting process duration and product quality. R_P of a 5% sucrose solution was determined in high-throughput and serum vials by a pressure rise test method. Results were interpreted considering the nucleation temperature (T_n; affected by the addition of a nucleating agent) measured with a thermal camera, the pore diameter of the dried product determined through 3D X-ray micro-computed tomography, and the shape of the sublimation front upon visual inspection. R_P values were roughly 60% lower in high-throughput vials than in serum vials when T_n was low (-7 °C, results without a nucleating agent) and 30% lower when T_n was high (-1.5 °C, results with a nucleating agent). R_P values could not be directly explained by the pore diameter as commonly seen in the literature but only considering also the shape of the sublimation front.

KEYWORDS

Freeze-drying/Lyophilisation; Vaccines; Up-scale; High-throughput vial; Serum vial; Freezing; Nucleation temperature; pressure rise test; X-ray micro-computed tomography.

INTRODUCTION

Vaccines are produced to protect a subject against viral or bacterial infections by triggering immune responses through particular ingredients known as "antigens" (Siegrist, 2008). Certain antigens can be damaged if the vaccines are not kept at low temperatures during their storage and transportation, e.g. -20 °C for the smallpox vaccine (Pipkin and Minor, 1998). These low temperatures are difficult to ensure all along the chain and could require expensive freezing equipment and high energy consumption. Therefore, vaccines are commonly dried after production to stabilize the antigen, to allow storage and transportation at temperatures over 2 °C (World Health Organisation, 2000). Freeze-drying is the most common technique to dry vaccines in the pharmaceutical industry, and consists of three consecutive steps: (i) a freezing step, (ii) a sublimation step (primary drying), and (iii) a desorption step (secondary drying). During the freezing step, approximately 80% of the water molecules form ice crystals, and the rest of the molecules remain sorbed to the product (Patel et al., 2010b). Then, ice crystals are removed by sublimation during primary drying, leaving a porous matrix consisted of the partially dried product and sorbed water (dried product layer). Finally, sorbed water is removed during secondary drying by desorption, resulting in a product with a final moisture content of less than 3% (May, 2010).

The three freeze-drying steps are commonly performed in a piece of equipment known as a "freeze dryer", presenting a drying chamber with shelves. Vials are filled with the vaccine and placed on the shelves of the freeze dryer. The quality attributes of a freeze-dried vaccine (e.g. appearance, reconstitution time, moisture content; Awotwe-Otoo and Khan, 2015; Patel et al., 2017; World Health Organization, 2011) depend on the product temperature during primary drying. Indeed, the dried product layer collapses when heated above a critical temperature known as collapse temperature (Fonseca et al., 2004; Pikal and Shah, 1990b). The freeze dryer cannot directly fix the product temperature; instead, the shelf temperature and the drying chamber pressure are the two operating conditions that can be set. Mathematical models are commonly used to relate the operating conditions with the product temperature, so the process could be designed to prevent product collapse and excessive drying durations (Koganti et al., 2011; Nail and Searles, 2008; Pikal, 2000; Scutellà et al., 2017a). Such mathematical models involve the heat transfer coefficient between the shelves and the vial (K_V), and the dried product resistance to the mass transfer from the sublimation from to the drying chamber (R_P). Previous works concluded that K_V values can vary among vials (Brülls and Rasmuson, 2002; Pisano et al., 2011; Scutellà et al., 2017a), and R_P values depend on the vaccine formulation and the freezing protocol (Hottot et al., 2005; Konstantinidis et al., 2011; Patel et al., 2009; Searles et al., 2001).

The most common containers used to freeze-dry vaccines are tubular glass vials with a total volume of over 3 mL (Brülls and Rasmuson, 2002; Pikal et al., 2016b; Pisano et al., 2011; Scutellà et al., 2017b), known as serum vials. Recently, smaller tubular glass vials with a total volume of 1 mL (or less), known as high-throughput vials, have been proposed to accelerate the development of new freeze-dried vaccines

(Buceta et al., 2021; von Graberg, 2011). The smaller high-throughput vials allow users to test more formulations per freeze-drying cycle since more vials could be fit inside the freeze dryer. Moreover, high-throughput vials are placed in aluminium well plates before being charged inside the freeze dryer. These well plates are compatible with most robots used to prepare formulations, simplifying the researcher's manual labour (Peterman et al., 2014; Stangegaard et al., 2011; Taylor et al., 2002). Buceta et al. (2021) highlighted that K_V is different for high-throughput and serum vials, suggesting the product temperature may differ when performing tests in high-throughput vials at a laboratory scale or serum vials at a pilot scale. Therefore, for a certain operating condition in the freeze dryer (i.e. shelf temperature and chamber pressure), the conclusions on the product quality obtained using high-throughput vials may not be valid when using serum vials.

Buceta et al. (2021) proposed a graphic tool to "translate" the operating conditions between high-throughput and serum vials to obtain the same product temperature, considering – for the sake of an example – the same R_P value in both vial types. However, there is no evidence confirming or denying this assumption for the R_P value. R_P depends on the pore diameter of the dried product layer and on the mass transfer area (Konstantinidis et al., 2011; Pikal, 2000). Pores in the dried product layer correspond to the ice crystals obtained during freezing; thus, for a given formulation, the pore diameter may vary depending on the container's geometry (Rosa et al., 2016) and the nucleation temperature (associated to the freezing protocol) (Oddone et al., 2016). The mass transfer area considered to determine R_P is the inner cross-section area of the container. Previous authors noted that the sublimation front tends to curve when the radial heat flow reaching the vial is not negligible (Nam and Song, 2005; Sheehan and Liapis, 1998), which is expected to be the case for high-throughput vials seated in aluminium wells. In this case, the mass transfer area may differ considerably from the inner cross-section area.

This work aimed at determining R_P in high-throughput and serum vials, and interpreting the results considering the pore diameter of the dried product layer and the shape of the sublimation front (as an indicator of the mass transfer area). In this way, the present work serves as a step forward to translate the operating conditions between vial types by focusing on mass transfer, in addition to previous studies mainly dealing with heat transfer (Buceta et al., 2021; Section 4.4.2).

MATERIALS AND METHODS

Vials

Two types of containers were used in this study: (i) the *96-Well Freeze-Drying System* manufactured by VirTis (SP Scientific, Stone Ridge, NY, USA) consisting of aluminium well plates and glass high-throughput vials with a maximal filling volume of 1 mL; and (ii) glass serum vials with a maximal filling volume of 3 mL provided by Müller + Müller (Holzminden, Germany). High-throughput vials were cleaned before each experiment by rinsing six times with deionised water and drying at 300 °C for 9 hours. Serum vials were pre-treated according to two procedures: (i) cleaned in the same way as high-throughput vials, or (ii) siliconized.

Solutions

A 5% (w/w) sucrose aqueous solution was employed in this work as a "model" product. The solution was prepared with ultra-pure water (Milli-Q, Millipore Corporation, Burlington, MA, USA) and crystalline sucrose (Fluka Analytical, Sigma-Aldrich, Germany), then filtered using a membrane with a pore size of 0.22 μm. In some cases, a nucleating agent commercially known as snomax ® (Snomax LLC, Englewood, CO, USA) was added after filtration, so the concentration of the nucleating agent was 0.1% (w/w).

The filling volume (V_{fill}) used with high-throughput vials was 0.6 mL (filling depth = 16 mm), and with serum vials was 1.8 mL (filling depth = 11 mm). Vials were filled in a laminar flow cabinet and covered with a plastic film during storage and transportation.

Freeze-drying cycles

The freeze-drying process was performed in a REVO laboratory-scale freeze dryer (Millrock Technology, Kingston, NY, USA). The freeze dryer presented a drying chamber of 0.12 m^3 containing three temperature-controlled shelves. Moreover, two pressure gauges monitored the pressure inside the drying chamber: (i) a capacitance manometer, and (ii) a thermal conductivity gauge (Pirani). The chamber was connected to a condenser by a butterfly valve.

Five experimental conditions summarised in Table 4.4-1 were tested. Experimental conditions varied depending on: (i) the vial type (i.e. high-throughput or serum vial), (ii) the use of a nucleating agent or not, and (iii) the pre-treatment of the surface (i.e. non-siliconized or siliconized). Before freeze-drying, 768 high-throughput vials or 385 serum vials were placed on the shelf according to the arrangement shown in Figure 4.4-1. The temperature of eight selected vials (red dots in Figure 4.4-1) was registered by eight thermocouples with a diameter of less than 1 mm.

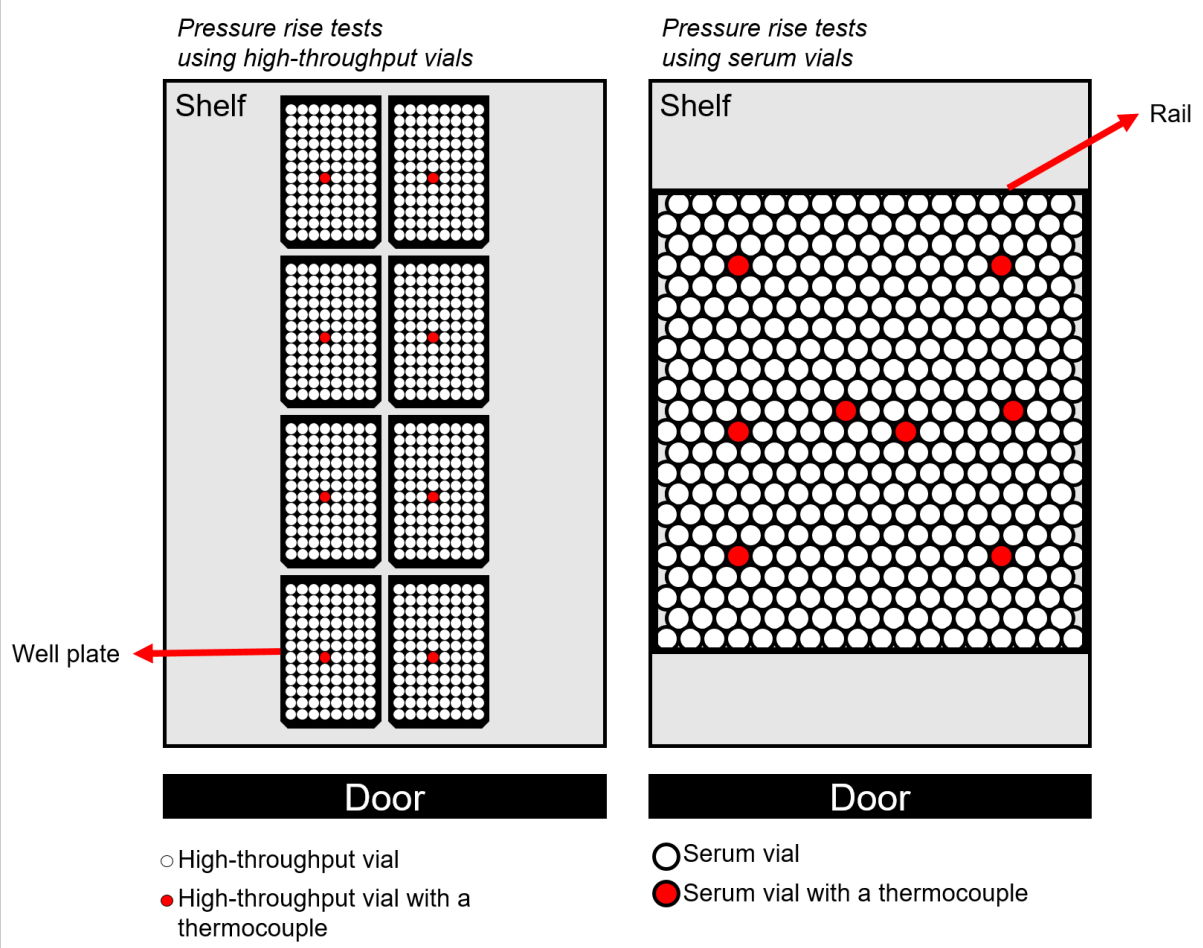

Figure 4.4-1 – View from the top of the disposition during pressure rise tests.

Table 4.4-1 – Experimental conditions studied.

		nucleating agent	
		No	**Yes**
vial type	**H**igh-throughput vial	**Hv-Nn**	**Hv-Yn**
	Serum vial (non-siliconized)	**Sv-Nn**	**Sv-Yn**
	Serum vial (**Siliconized**)	**Sv-Nn-S**	Not studied in this work

Once the vials were placed on the shelf, the freeze dryer was closed, and the freeze-drying cycle was launched. Two types of freeze-drying cycles were performed: (i) short cycles consisting of freezing and primary drying steps, and (ii) complete cycles consisting of freezing, primary drying, and secondary drying steps. The operating conditions set during each step are represented in Figure 4.4-2a (shelf temperature) and Figure 4.4-2b (chamber pressure).

The freezing step consisted of a temperature ramp at -1 °C.min^{-1} from ambient temperature (approximately 20 °C) to -50 °C. After the freezing step, the shelf temperature was maintained at -50 °C for 1 hour to ensure all the samples were completely frozen.

The primary drying step started by reducing the chamber pressure to 10 Pa and increasing the shelf temperature from -50 °C to -25 °C at 1 °C.min^{-1}. Short freeze-drying cycles were abruptly stopped after 9, 19 or over 43 hours of primary drying by breaking the vacuum inside the drying chamber. Then, the shelf temperature was rapidly lowered from -25 to -50 °C at -5 °C.min^{-1}. In contrast, during complete freeze-drying cycles, primary drying lasted for 48 hours of sublimation.

A secondary drying step was performed after primary drying during complete freeze-drying cycles. The secondary drying step began by quickly decreasing the chamber pressure from 10 to 4 Pa and increasing the shelf temperature from -25 °C to +25 °C at 0.25 °C.min^{-1}. Finally, the cycle was stopped after 12 hours by breaking the vacuum inside the drying chamber. Vials were quickly stoppered (manually) and preserved in vacuum-sealed bags at -45 °C.

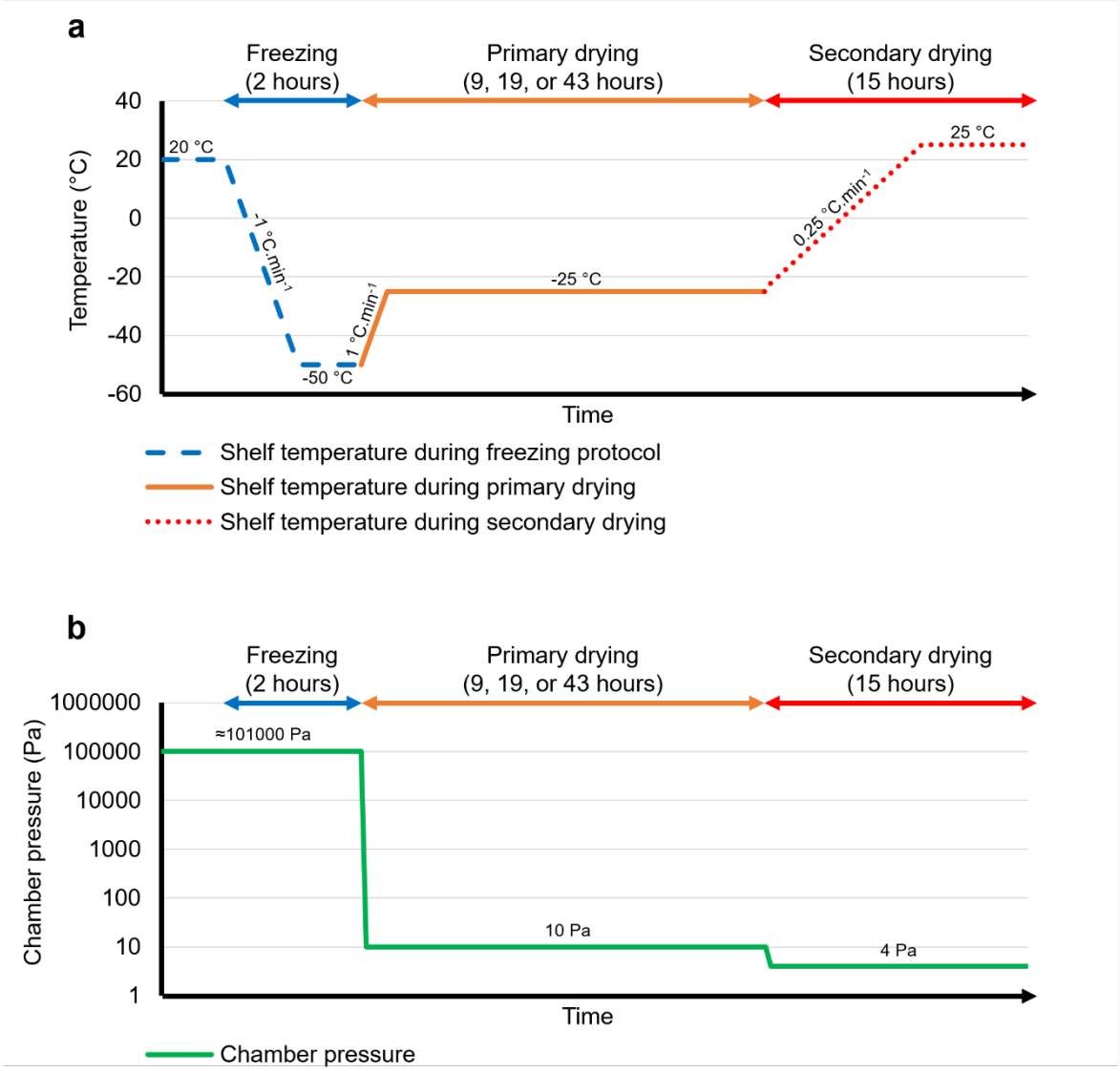

Figure 4.4-2 – Schemes of the operating conditions set during the freezing, the primary drying, and the secondary drying steps of freeze-drying. (a) Shelf temperature. (b) Chamber pressure. Time is not in scale.

Determination of the nucleation temperature

The nucleation temperature (T_n) was determined during freezing in the REVO laboratory-scale freeze dryer. Figure 4.4-3 shows the experimental device used. During experiments with high-throughput vials, one well plate containing 96 vials was placed on the bottom shelf, while during experiments with serum vials, 44 vials were placed on the bottom shelf. The middle and upper shelves were moved to the top of the drying chamber, so a thermal camera Testo 885-2 (Distrame S.A., Paris, France) could be placed over the bottom shelf and pointing downwards towards the vials. The camera was sustained by a tripod that kept it in the same place throughout the tests.

The five experimental conditions reported in Table 4.4-1 were tested. Experimental conditions using high-throughput vials (**H**v-**Y**n and **H**v-**N**n) were repeated three times (288 vials tested per experimental condition), and experiments using serum vials (**S**v-**Y**n, **S**v-**N**n, and **S**v-**N**n-**S**) were repeated six times (264 vials tested per experimental condition). The freezing protocol consisted in a continuous temperature ramp from ambient temperature to -50 °C at -1 °C.min^{-1}.

The image acquisition of the thermal camera was set to take pictures every 5 seconds. Thermal images obtained with the camera were expressed as matrices of 320×240 pixels, where each pixel contained a temperature value. These thermal images were treated using an in-house code developed in MATLAB R2017a (The MathWorks, Inc, Natick, MA, USA) to obtain the product surface temperature values as a function of time. A detailed description of the image treatment is presented in Appendix 4.4-A. Furthermore, the calibration of the surface temperature values to reduce the camera's noise due to the auto-calibration, and the constant biases due to the camera's angle with the surfaces is described in Appendix 4.4-B. Finally, for each vial, T_n was considered to be the value before the surface temperature of the content registered a sharp increase until the freezing-point depression temperature for a 5% (w/w) sucrose solution (-0.28 °C; Kiyosawa, 1988).

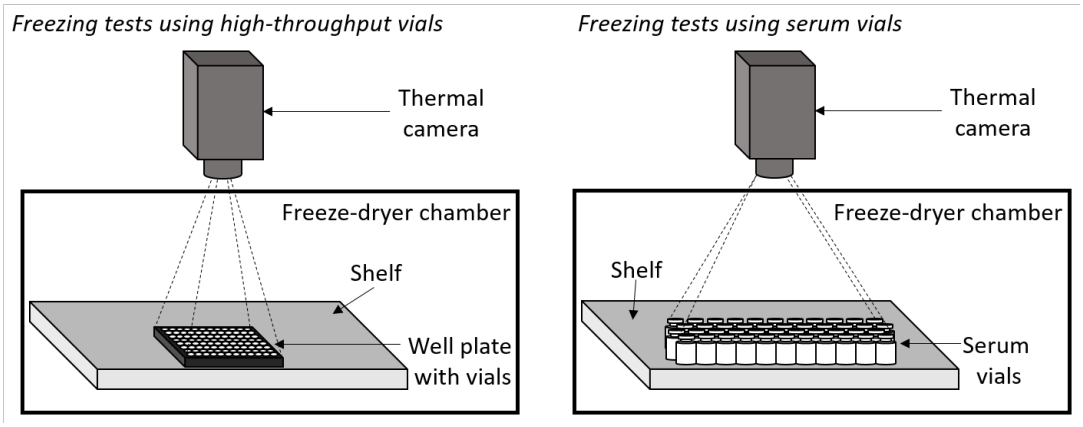

Figure 4.4-3 – Scheme of the experimental device during nucleation temperature (T_n) measurements using the thermal camera.

X-ray micro-computed tomography of the freeze-dried product

Completely freeze-dried samples (after freezing, primary drying, and secondary drying) were analysed by X-ray micro-computed tomography using a DeskTom 130 scanner (RXSolution, Chavanod, France). Five samples (vials) were analysed per experimental condition (Table 4.4-1). Samples were selected during freezing by measuring the nucleation temperature (T_n) with a thermal camera as described in Section *Determination of the nucleation temperature*, so their T_n differed by less than 0.5 °C from the average T_n value of the experimental condition.

Figure 4.4-4 shows a diagram of the image acquisition by tomography and image processing through different software. Inside the tomograph, there was a chamber presenting an X-ray source, detector, and a rotating cylinder in between. Sampled vials were taped on the rotating cylinder. The X-ray source was set to a current intensity of 160 µA and a voltage of 50 kV. For each sample, all the product was analysed with a voxel size of 8.98 µm. Samples were rotated 360°, capturing 1440 projection images (2D longitudinal).

The projection images were treated by the XAct 2 software (RX Solution, Chavanod, France) using a filtered back-projection algorithm to obtain a 3D volume (Hussani and Hayani, 2014; Mulot et al., 2019). This 3D volume was filtered using XAct 2 to correct possible ring artefacts due to the non-linear response of the tomograph's detector (Hsieh, 2003; Masselot et al., 2021). Over 1100 2D horizontal cuts of each 3D volume were exported using XAct 2 with an 8-bits resolution (pixel values between 0 and 255).

The 3D volume was re-reconstructed in Avizo 9.2.0 software (FEI VSG, Bordeaux, France) from the 2D horizontal cuts. In Avizo, a threshold filter was applied to the 3D re-reconstructed volume, distinguishing between the dried product phase and the pores. The threshold filter took the voxels initially in a grayscale (values between 0 and 255) and segmented them into a binary scale where the possible values were: product or gas. Pores (filled with gas) in the binary structure were identified using the H-maxima module (Avizo), and the equivalent pore diameter of each pore was measured using the Label Analysis module (Avizo).

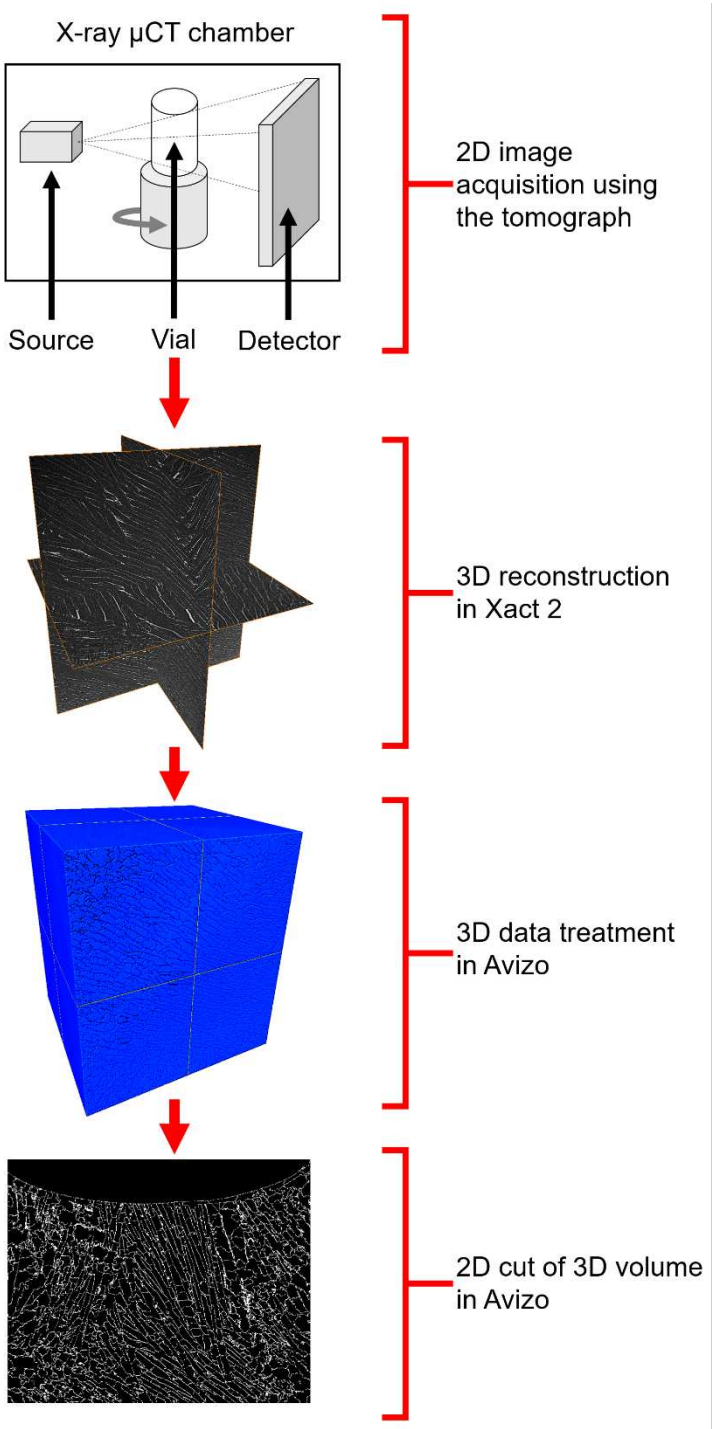

Figure 4.4-4 – Data processing scheme of the X-ray micro-computed tomography (µCT).

Visual inspection of the sublimation front

Short cycles, consisting of a freezing and primary drying step (see Section *Freeze-drying cycles* of this Paper IV), were performed for each experimental condition described in Table 4.4-1. Samples obtained after 9 and 19 hours of primary drying were quickly removed from the freeze dryer, placed inside a polystyrene box containing liquid nitrogen, and transported to a controlled temperature room at -20 °C. It is to note that the dried product layer spontaneously shrunk and separated from the frozen product layer when vials were removed from the freeze dryer. The top surface of the frozen layer (surface exposed to the air once the dried product separated) was considered to be the sublimation front. The shape of the sublimation front was visually inspected for all vials inside the controlled temperature room at -20 °C to ensure the frozen layer did not melt.

Pressure Rise Tests

One of the most common methods to determine the vial-averaged mass flow rate during primary drying is the pressure rise tests (e.g. Liapis and Sadikoglu, 1998; Milton et al., 1997; Pikal et al., 2005; Tang et al., 2005). In this work, pressure rise tests were performed every hour during the primary drying step of short freeze-drying cycles (see Section *Freeze-drying cycles*). Each pressure rise test consisted in closing the butterfly valve connecting the chamber and the condenser for 30 seconds, and registering the capacitance manometer's pressure every 0.1 seconds (Scutellà et al., 2018a). The capacitance manometer's pressure values were treated to obtain the vial-averaged sublimation mass flow rate as described in Section *Determination of the sublimation mass flow rate based on the pressure rise tests*.

The five experimental conditions reported in Table 4.4-1 were tested. Pressure rise tests during experimental conditions regarding high-throughput vials (**H**v-**Y**n and **H**v-**N**n) were repeated three times. In contrast, pressure rise tests during experimental conditions concerning serum vials (**S**v-**Y**n, **S**v-**N**n, and **S**v-**N**n-**S**) were performed once and results were compared with previous tests carried out by Scutellà et al. (2018).

THEORETICAL FRAMEWORK

A lumped-variable steady-state model was considered in this study for the heat and mass transfer during primary drying. This model considered a one-directional heat flow from the bottom shelf to the sublimation front and a one-directional mass flow from the sublimation front to the freeze-drying chamber.

Heat and mass transfer equations

Heat transfer

The heat flow received by the vials ($\dot{Q}$, W) was calculated based on the effective heat transfer coefficient between the shelves and the vial bottom (K_V, W.m^{-2}.K^{-1}):

$$\dot{Q} = A_V K_V \left(T_{shelf} - T_b\right) \qquad \text{Equation 4.4-1}$$

where A_V (m^2) is the vial bottom area, T_{shelf} (K) is the shelf surface temperature, and T_b (K) is the temperature at the bottom of the vial. K_V was determined by gravimetric analysis using an analytical scale (± 0.0001 g) during sublimation tests using vials (Figure 4.4-1) filled with ultra-pure water at chamber pressure 10 Pa and shelf temperature -25 °C, as described by Scutellà et al. (2017).

Assuming pseudo-steady state and heat transfer essentially from the vial bottom towards the sublimation front, $\dot{Q}$ was also considered equal to the heat flow going through the frozen layer and calculated as:

$$\dot{Q} = \frac{A_V \lambda_f}{l_f} (T_b - T_{sat}) \qquad \text{Equation 4.4-2}$$

where λ_f (W.m^{-1}.K^{-1}) is the thermal conductivity of the frozen layer, l_f (m) is the thickness of the frozen layer, and T_{sat} (K) is the temperature at the sublimation front. The numerical values of vial dimensions and coefficients are reported in Table 4.4-2.

Mass transfer

The area-normalised product resistance to mass transfer (R_P, Pa.s.m^2.kg^{-1}) was used to calculate the sublimation mass flow rate ($\dot{m}$, kg.s^{-1}). R_P relates the $\dot{m}$ and the pressure drop within the product as:

$$\dot{m} = \frac{A_{in}}{R_P} (P_{sat} - P_C) \qquad \text{Equation 4.4-3}$$

where A_{in} (m^2) is the inner vial cross-section area, P_C (Pa) is the chamber pressure, and P_{sat} (Pa) is the pressure at the sublimation front. Equation 4.4-3 considers no pressure drop within the chamber and no partially inserted vial stopper (Scutellà et al., 2018c).

Table 4.4-2 – Vial dimensions, physical properties and parameters used in this study.

Parameter	Significance	Value	Units	Reference
A_{in} (high-throughput vials)	Inner vial cross-section area	4.08×10^{-5}	m^2	(Buceta et al., 2021)
A_{in} (serum vials)	Inner vial cross-section area	1.78×10^{-4}	m^2	(Scutellà et al., 2017a)
A_V (high-throughput vials)	Outer bottom area of the vial	6.10×10^{-5}	m^2	(Buceta et al., 2021)
A_V (serum vials)	Outer bottom area of the vial	2.07×10^{-4}	m^2	(Scutellà et al., 2017a)
K_V (high-throughput vials)	Effective vial heat transfer coefficient	24.6	$W.m^{-2}.K^{-1}$	This work
K_V (serum vials)	Effective vial heat transfer coefficient	16.0	$W.m^{-2}.K^{-1}$	This work
ΔH_{sub}	Latent heat of sublimation	2.763×10^{6}	$J.kg^{-1}$	(Scutellà et al., 2017a)
λ_f	Thermal conductivity of the frozen layer	2.23	$W.m^{-1}.K^{-1}$	(Scutellà et al., 2017a)
ρ_f	Frozen product density	921*	$kg.m^{-3}$	(Harvey, 2018)
ρ_w	Liquid product density	997*	$kg.m^{-3}$	(Fierro and Nyer, 2007)

*Values for pure water

R_P was related to the dry layer thickness (l_d) through a generic formula (Kuu et al., 2006):

$$R_P = R_{P,0} + \frac{R_{P,1} \times l_d}{1 + R_{P,2} \times l_d} \quad \text{Equation 4.4-4}$$

where $R_{P,0}$ (Pa.s.m^2.kg^{-1}), $R_{P,1}$ (Pa.s.m.kg^{-1}) and $R_{P,2}$ (m^{-1}) are coefficients dependent on the structure of the dried product layer.

Coupling heat and mass transfer

The temperature (T_{sat}) and the pressure (P_{sat}) at the sublimation front were related through the Clausius-Clapeyron relation (Perry and Green, 2008):

$$T_{sat} = \frac{T_t}{1 - \frac{RT_t}{\widetilde{\Delta H_{sub}}} ln\left(\frac{P_{sat}}{P_t}\right)} \quad \text{Equation 4.4-5}$$

where T_t (273.16 K) and P_t (611.66 Pa) are the triple point temperature and pressure of the water respectively, R (8.3144 J.K^{-1}.mol^{-1}) is the ideal gas constant, and $\widetilde{\Delta H_{sub}}$ (51.1 kJ.mol^{-1}) is the molar enthalpy of sublimation. The heat and mass transfer are coupled by the following equation when considering that $\dot{Q}$ is responsible for the ice sublimation:

$$\dot{Q} = \dot{m}\, \Delta H_{sub} \quad \text{Equation 4.4-6}$$

were ΔH_{sub} (J.kg^{-1}) is the latent heat of sublimation reported in Table 4.4-2.

Estimation of the dried product layer thickness and frozen product layer thickness

The dried product layer thickness (l_d, m) and the frozen product layer thickness (l_f) are related by the following equation:

$$\frac{V_{fill}}{A_{in}} = \frac{\rho_f}{\rho_w} \times \left[l_f(t) + l_d(t)\right] \quad \text{Equation 4.4-7}$$

where V_{fill} (m^3) is the filling volume, ρ_f (kg.m^{-3}) is the frozen product density, and ρ_w (kg.m^{-3}) is the liquid product density – numerical values are reported in Table 4.4-2. Note that l_d and l_f vary in time, and l_d can be estimated for a certain time (t, s) as:

$$l_d(t) = \frac{1}{A_{in}\rho_f} \int_{t_{initial}}^{t} \dot{m}\ dt \quad \text{Equation 4.4-8}$$

where $t_{initial}$ (s) is the time when the sublimation begins.

Determination of the sublimation mass flow rate based on the pressure rise tests

Pressure rise tests were used to determine a vial-averaged sublimation mass flow rate ($\dot{m}_{PRT}$, kg.s^{-1}). The pressure evolution in the drying chamber during each pressure rise test (registered with the capacitance manometer) was fitted to a 6-degree polynomial, so the first-order coefficient ($\dot{P}_0$, Pa.s^{-1}) is the first derivate

of the pressure evaluated at the beginning of the test. Examples of the pressure evolution during pressure rise tests are presented in Appendix 4.4-C. $\dot{m}_{PRT}$ was obtained based on the ideal gas law:

$$\dot{m}_{PRT} = \dot{P}_0 \frac{M_W V_C}{R T_{shelf} n_V} \qquad \text{Equation 4.4-9}$$

where M_W (18 kg.kmol^{-1}) is the molar weight of the water vapour, V_C (0.12 m^3) is the volume of the drying chamber, and n_V is the total number of vials in the drying chamber (Pisano et al., 2011; Scutellà et al., 2018c). The total water mass removed during the freeze-drying cycle (Δm_{total}, kg) was measured by gravimetric analysis (Pisano et al., 2011; Scutellà et al., 2017a), and compared to the integral of the mass flow rate ($\dot{m}_{PRT}$) during primary drying. The mass loss factor (M_L) was defined as:

$$M_L = \frac{\Delta m_{total} - n_V \int \dot{m}_{PRT} dt}{\Delta m_{total}} \times 100\% \qquad \text{Equation 4.4-10}$$

Δm_{total} (kg) was calculated as the sum of the variation of all the vial's weights, and $\int \dot{m}_{PRT} dt$ (kg) was calculated using the experimental $\dot{m}_{PRT}$ and the trapezoidal integration formula (Perry and Green, 2008).

Comparison between calculated product temperature values and experimental values

The product temperature at the vial bottom (T_b) was calculated as a function of the dried product layer thickness (l_d) using Equation 4.4-1 to Equation 4.4-8. Furthermore, each vial thermal history registered by a thermocouple was expressed as a function of l_d to be compared with the calculated T_b. To do so, for each vial equipped with a thermocouple, we determined a particular starting time of primary drying and a particular finishing time of primary drying (t_{final}, s). $t_{initial}$ was considered as the time when the measured temperature was greater than the calculated initial T_b (for l_d = 0), and t_{final} was considered as the time when a temperature jump (+1 °C in less than 0.5 min) was registered – marking the beginning of secondary drying. Based on $t_{initial}$ and t_{final}, and assuming a constant mass flow during primary drying, a time-dependent dry layer thickness ($\widehat{l_d}$, m) was specifically calculated for each vial with an inserted thermocouple:

$$\widehat{l_d}(t) = \frac{V_{fill}}{A_{in}} \times \frac{\rho_w}{\rho_f} \times \frac{t - t_{initial}}{t_{final} - t_{initial}} \qquad \text{Equation 4.4-11}$$

RESULTS AND DISCUSSIONS

Nucleation temperature

The nucleation temperature (T_n) has been traditionally associated with the ice crystal size obtained during freezing (Fennema, 1973; Geidobler and Winter, 2013; Nakagawa et al., 2006; Searles et al., 2001). Nucleation is a stochastic process, hence T_n aleatory varies among vials causing differences in the ice crystal size. In the absence of product collapse, the ice crystal size is the same as the pore size obtained during primary drying, which affects the mass transfer through the dried product layer. Therefore, T_n variations among vials could cause differences in the coupled heat and mass transfer, as well as variations in the product temperature. In this vein, this work determined T_n as a first step to understanding how T_n impacts the mass transfer.

Five experimental conditions listed in Table 4.4-1 were considered; differing in the vial type (i.e. high-throughput vial or serum vial), the addition of a nucleating agent, and siliconizing the vial internal surfaces. For each experimental condition (Table 4.4-1), Figure 4.4-5 shows the vial content's surface temperature during freezing for the first vial (grey line) and the last vial to nucleate (green line), as well as a vial that nucleated at an intermediate time (blue line). Furthermore, Figure 4.4-5 presents the surface temperatures of the shelf and well plate (in the case of high-throughput vials). In the case of high throughput vials (**H**v-**Y**n and **H**v-**N**n in Figure 4.4-5), the well plate temperature did not follow a linear ramp like the shelf temperature after nucleation occurred in some vials. The heat released by the high-throughput vials in which nucleation occurred heated the well plate, ultimately affecting the rest of the high-throughput vials' temperature profile. This is opposed to the case of serum vials positioned directly on the freeze dryer's shelf, where the thermal interaction between vials was limited.

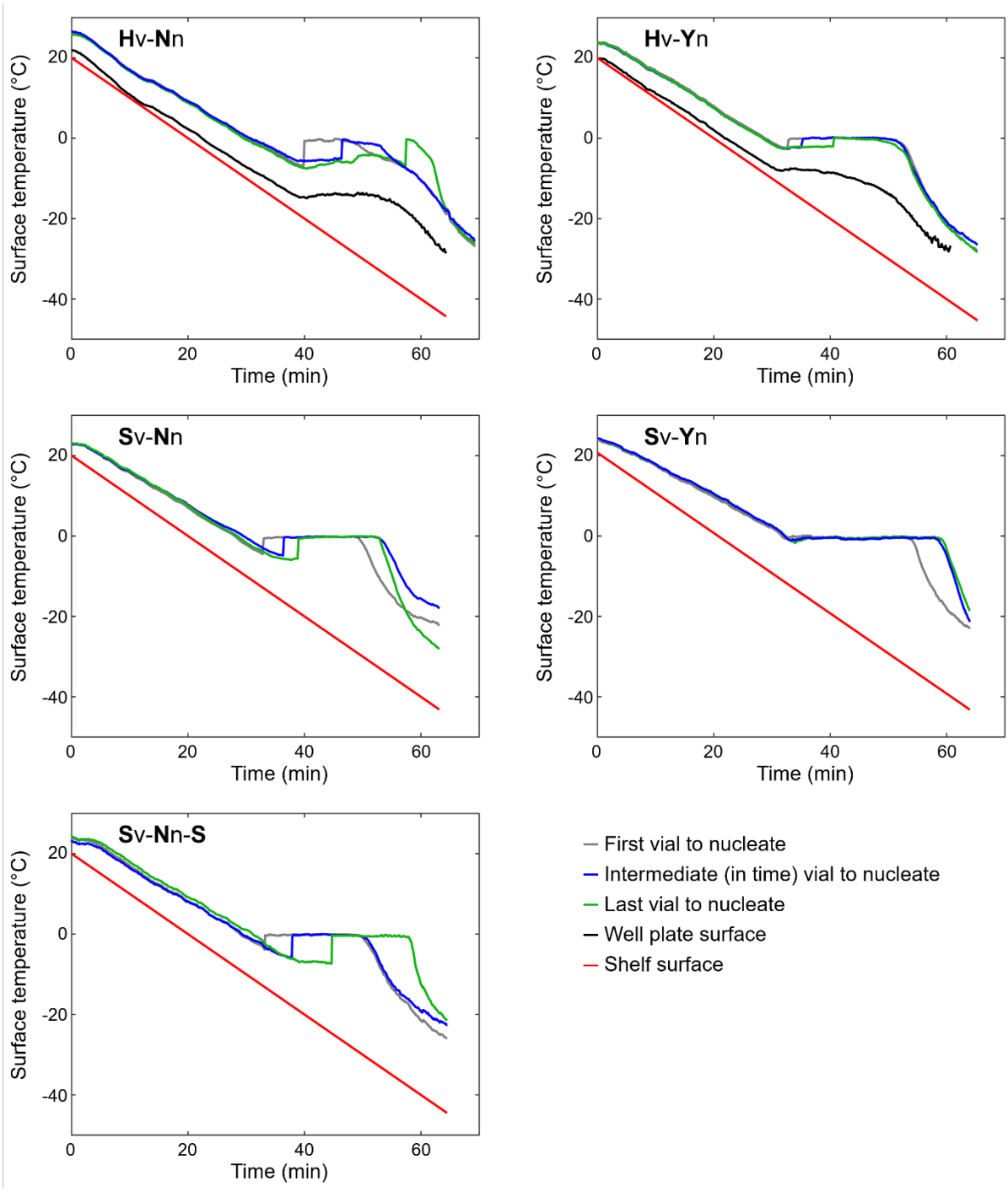

Figure 4.4-5 – Surface temperature profiles. Hv-Nn, Hv-Yn, Sv-Nn, Sv-Yn, and Sv-Nn-S are the experimental conditions described in Table 4.4-1.

T_n was determined for each vial based on the surface temperature profiles, as described in Appendix 4.4-A and Appendix 4.4-B. The T_n histograms of each experimental condition (Table 4.4-1) are presented in Figure 4.4-6. The impact of the vial type on T_n was negligible, since T_n results of experimental conditions using high-throughput and serum vials were not significantly different according to the ANOVA1 test ($p > 0.05$) (**H**v-**N**n vs **S**v-**N**n, and **H**v-**Y**n vs **S**v-**Y**n in Figure 4.4-6). In contrast, the nucleating agent impacted T_n by increasing the average value (approximately from -7 °C to -1.5 °C in Figure 4.4-6) and decreasing the standard deviation (approximately from 1 °C to 0.5 °C in Figure 4.4-6, confirming visual observations in Figure 4.4-5). The impact of siliconizing the vial surface was unimportant, T_n results using siliconized (**S**v-**N**n-**S** in Figure 4.4-6) or non-siliconized (**S**v-**N**n in Figure 4.4-6) serum vials were not significantly different (ANOVA1 test, $p > 0.05$).

T_n was also determined considering the product temperatures measured using the eight thermocouples inserted in the eight vials indicated in Figure 4.4-1. Values are expressed as black crosses in Figure 4.4-6. The range of the T_n values measured using thermocouples and the thermal camera overlapped, reassuring the accuracy of both methods.

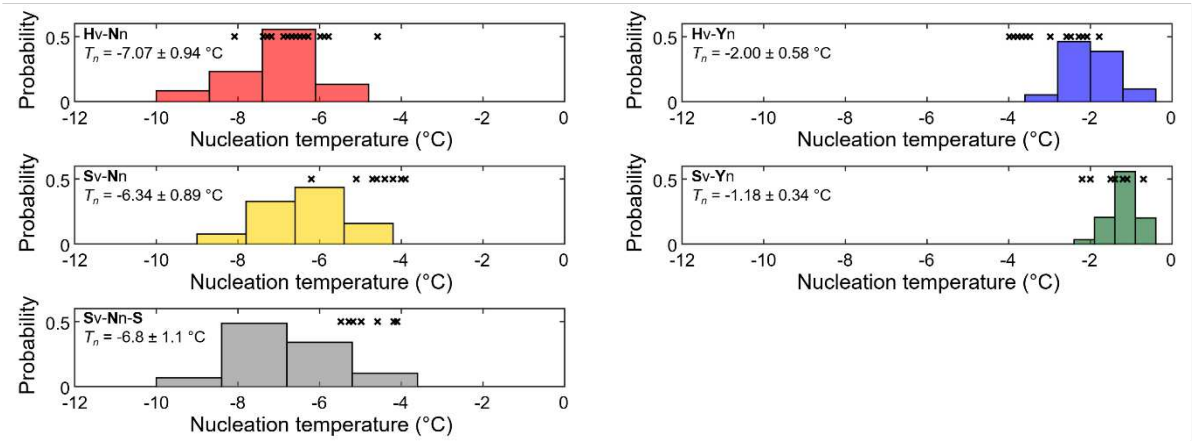

Figure 4.4-6 – Distribution of the nucleation temperature (T_n) determined using a thermal camera. Hv-Nn, Hv-Yn, Sv-Nn, Sv-Yn, and Sv-Nn-S are the experimental conditions described in Table 4.4-1. The mean value ± standard deviation of T_n is reported next to the histogram for each experimental condition – values based on 288 vials in Hv-Nn and Hv-Yn, and 264 vials in Sv-Nn, Sv-Yn, and Sv-Nn-S. T_n values determined using thermocouples are marked as black crosses on top of the histograms.

Pore structure observed through X-ray micro-computed tomography

The sublimation mass flow going through the dried product layer depends on the characteristics of the dried product structure, e.g. the pore diameter, the tortuosity, the porosity, and the connectivity, among others (Konstantinidis et al., 2011; Pikal, 2000; Pisano et al., 2017). The structure of the freeze-dried product was studied through X-ray micro-computed tomography to observe the variations due to the vial type (i.e. high-throughput or serum), the addition of a nucleating agent, and siliconizing the vials. Figure 4.4-7 shows the vertical cuts of the entire product structure (in white) and pores (in black) for all experimental conditions (Table 4.4-1), which were obtained after treating X-ray micro-computed tomography images. The impact of the vial type without a nucleating agent was not visually remarkable, and pores did not have a particular orientation in high-throughput or serum vials (**H**v-**N**n vs **S**v-**N**n in Figure 4.4-7); also, siliconizing the vials had no impact (**S**v-**N**n vs **S**v-**N**n-**S** in Figure 4.4-7). However, the impact of the vial type with a nucleating agent was very clear. In high-throughput vials (**H**v-**Y**n in Figure 4.4-7), pores were larger than without a nucleating agent, while pores were larger and elongated in serum vials (**S**v-**Y**n in Figure 4.4-7). Similar results to those shown in Figure 4.4-7 were obtained consistently in other cuts and repetitions of the same experimental conditions.

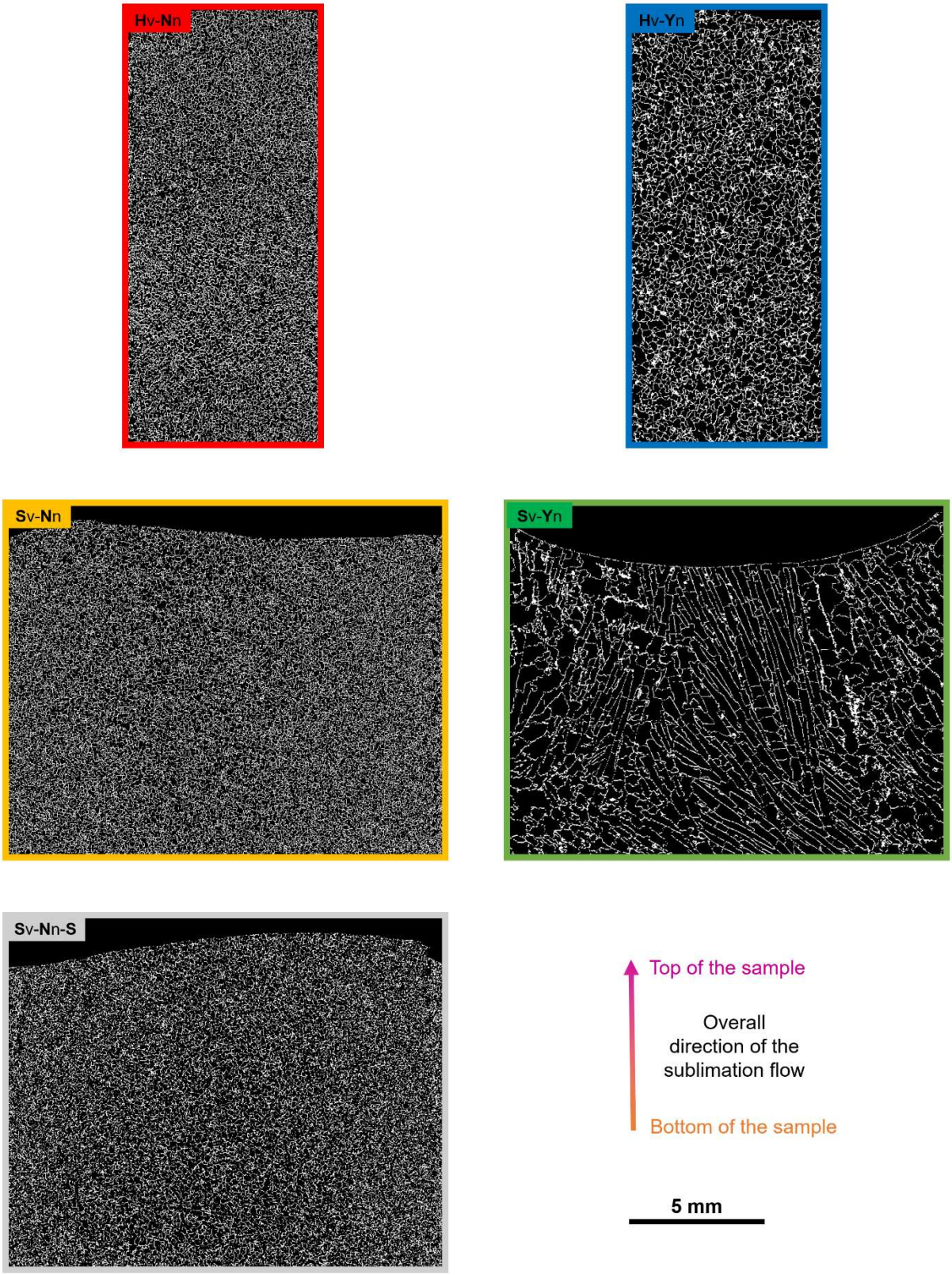

Figure 4.4-7 – Tomography images of the entire freeze-dried product. Vertical cuts. In white are the product structures, and in black are the pores. Hv-Nn, Hv-Yn, Sv-Nn, Sv-Yn, and Sv-Nn-S are the experimental conditions described in Table 4.4-1.

The values of the pore diameters were calculated using the Avizo software. Figure 4.4-8 shows the pore diameter determined for each repetition, plotted as a function of the nucleation temperature (T_n) of the sample. Each repetition provided an average of 50,000 pore diameter values. Due to the large size of the data packages, traditional statistic tests such as ANOVA and Kruskal-Wallis could detect significant differences between the pore diameter values of each repetition. However, differences between repetitions were deemed insignificant for our purposes since the mean values of all repetitions differed by less than the standard deviation; this could be observed in Figure 4.4-8 since all the error bars overlapped for each experimental condition. Table 4.4-3 reports the average pore diameters (results considering five repetitions) and their standard deviation. The impact of the vial type when not adding a nucleating agent was negligible, as pore diameters differed by less than the standard deviation (**H**v-**N**n vs **S**v-**N**n in Figure 4.4-8, Table 4.4-3). However, when adding a nucleating agent, pores were larger in high-throughput vials than in serum vials (**H**v-**N**n vs **S**v-**N**n in Figure 4.4-8, Table 4.4-3); the average pore diameter increased from 195 µm in high-throughput vials to 300 µm in serum vials (Table 4.4-3).

Overall, the mean pore diameter increased with T_n, as previously noticed by other authors (Geidobler and Winter, 2013; Konstantinidis et al., 2011; Nakagawa et al., 2006). For high-throughput vials, adding a nucleating agent increased the average pore diameter from 88 to 195 µm (Table 4.4-3). Interestingly, the impact of the nucleating temperature on the dried product structure was more dramatic in serum vials than in high-throughput vials. For serum vials, adding a nucleating agent increased the average pore diameter from 96 to 300 µm (**S**v-**N**n vs **S**v-**Y**n in Figure 4.4-8, Table 4.4-3) and radically changed the appearance of the pores by causing elongated and sharp shapes (**S**v-**N**n vs **S**v-**Y**n in Figure 4.4-7). Therefore, it is expected that mass transfer differences among vials will be less remarkable in high-throughput than serum vials. Furthermore, siliconizing the vial surface did not affect the pore size (**S**v-**N**n vs **S**v-**N**n-**S** in Figure 4.4-7, Figure 4.4-8, and Table 4.4-3).

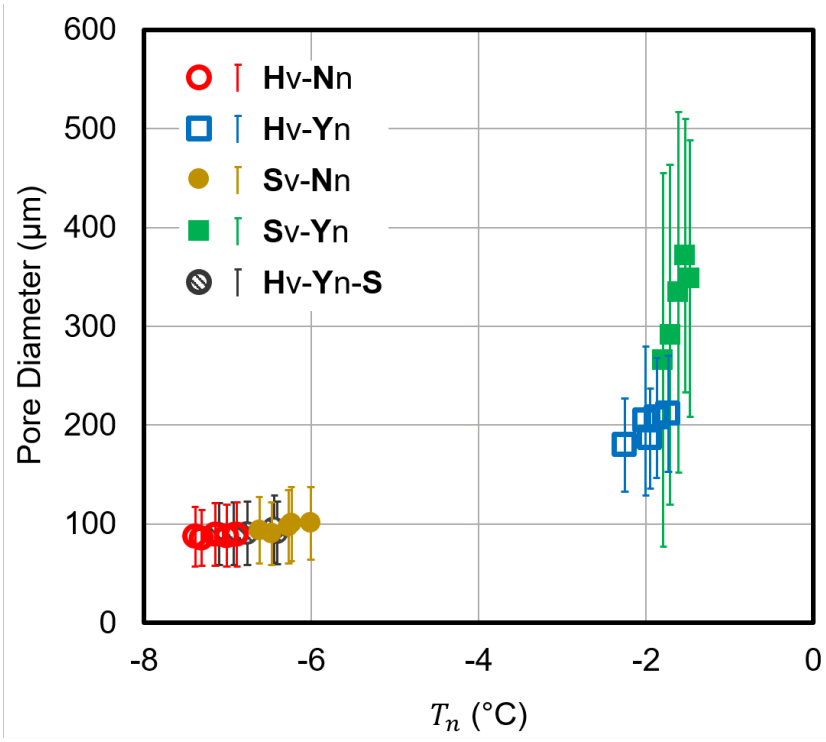

Figure 4.4-8 – Pore diameters as a function of the nucleation temperature (T_n). Each mark represents the mean pore diameter value and T_n for a sample (repetition). Error bars represent the standard deviations.

Table 4.4-3 – Pore diameter (mean values ± standard deviations). Results considering five repetitions per experimental condition.

		nucleating agent	
		No	**Yes**
vial type	**H**igh-throughput vial	88 µm ± 31 µm	195 µm ± 59 µm
	Serum vial (non-siliconized)	96 µm ± 36 µm	300 µm ± 174 µm
	Serum vial (**Siliconized**)	91 µm ± 32 µm	Not studied in this work

Shape of the sublimation front

The classic lumped-variable steady-state model of heat and mass transfer during primary drying (Pikal, 2000; Scutellà et al., 2017a; Velardi and Barresi, 2008), described in Section *Heat and mass transfer equations*, considers the mass transfer area equal to the inner vial cross-section area (A_{in}). However, previous work using 2D transient-state modelling indicated that this is not necessarily the correct mass transfer area when using some vials (Nam and Song, 2005; Sheehan and Liapis, 1998). In this work, the shape of the sublimation front was visually observed to study the validity of assuming the mass transfer area equal to A_{in}.

Figure 4.4-9 shows pictures of samples after 9 and 19 hours of primary drying. The dried product layers contracted when vials were removed from the freeze dryer, thus being separated from the frozen layer. The frozen layers are the structures marked with a blue snowflake symbol in Figure 4.4-9, and the dried layers are marked with a red circle. Some dried layers were removed using small tweezers so the frozen layers could be better observed.

Regarding the impact of the vial type in experimental conditions without a nucleating agent (**H**v-**N**n and **S**v-**N**n in Figure 4.4-9), sublimation fronts were curved in high-throughput vials (**H**v-**N**n) and rather flat in serum vials (**S**v-**N**n). Previous work using 2D transient heat and mass transfer models (Nam and Song, 2005; Sheehan and Liapis, 1998) proved that radial heat flows received by the vial tend to curve the shape of the sublimation front. Therefore, the curved sublimation fronts in high-throughput vials indicate a considerable contribution of radial heat flows from the well plate pillars and wall (Section 4.2.3), and the flatter sublimation fronts in serum vials suggest a lateral symmetry condition between vials (negligible radial heat flow) (Scutellà et al., 2017b).

Comparing results using different vial types with a nucleating agent (**H**v-**Y**n and **S**v-**Y**n in Figure 4.4-9), sublimation fronts in high-throughput vials (**H**v-**Y**n) were rather flat, while sublimation fronts in serum vials (**S**v-**Y**n) presented sharp peaks – particularly after 19 hours. These sharp peaks in serum vials with a nucleating agent are reminiscent of the elongated pores observed by X-ray micro-computed tomography (**S**v-**Y**n in Figure 4.4-7), suggesting that the product matrix coated the sharp ice crystals. For a given dried product layer thickness, the pores containing the sharp ice peaks were less connected to the sublimation front than the rest, so they dried more slowly. Under this assumption, sharp peaks imply large and not well-connected pores, so the "effective" sublimation front's area (where sublimation occurs, not the area of the frozen peaks) was smaller than A_{in}.

When using high-throughput vials (**H**v-**N**n and **H**v-**Y**n in Figure 4.4-9), adding a nucleating agent (**H**v-**Y**n) decreased the curvature of the sublimation front compared to the experimental condition without a nucleating agent (**H**v-**N**n). Results in high-throughput vials put forward that the pore shape and size might alter the shape of the sublimation front, emphasizing the coupling between heat and mass transfer.

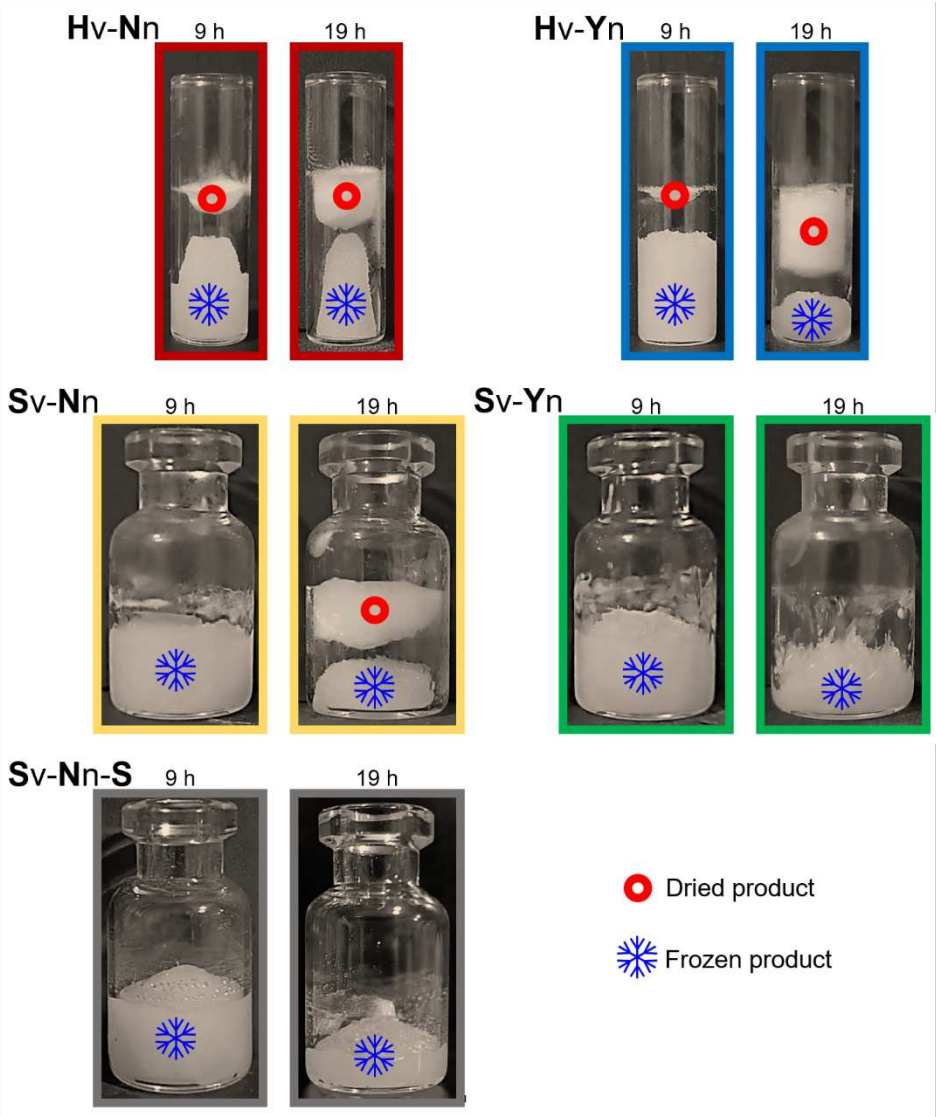

Figure 4.4-9 – Pictures of vials at intermediate points of primary drying taken after 9 or 19 hours of freeze-drying. Hv-Nn, Hv-Yn, Sv-Nn, Sv-Yn, and Sv-Nn-S are the experimental conditions described in Table 4.4-1.

The impact of siliconizing the vials appeared negligible (**S**v-**N**n vs **S**v-**N**n-**S** in Figure 4.4-9). Sublimation fronts observed in siliconized serum vials (**S**v-**N**n-**S**) presented a central cone with a height of approximately 4 mm, which was not observed in non-siliconized serum vials (**S**v-**N**n). However, a cone of 4 mm would only increase the sublimation front's area in serum vials by 13% compared to a flat surface. Therefore, such central curvature is not expected to impact the mass transfer significantly.

Overall, assuming A_{in} as the sublimation area was probably rather valid when using high-throughput vials with a nucleating agent (**H**v-**Y**n) or serum vials without a nucleating agent (**S**v-**N**n and **S**v-**N**n-**S**). For high-throughput vials without a nucleating agent (**H**v-**N**n), the sublimation area was greater than A_{in} due to the curved sublimation front. For serum vials with a nucleating agent (**S**v-**Y**n), the effective sublimation area may have been different to A_{in} due to the sharp ice peaks in the sublimation front.

Dried product resistance to mass transfer

The mass transfer through the dried product layer during primary drying is introduced in most lumped-variable steady-state models using the area-normalised product resistances to the mass transfer (R_P) (e.g. Koganti et al., 2011; Konstantinidis et al., 2011; Pikal, 1985; Pisano et al., 2013). In this vein, this work calculated R_P based on experimental mass flow rates ($\dot{m}_{PRT}$) determined during each pressure rise test for the five experimental conditions reported in Table 4.4-1. Figure 4.4-10 presents the $\dot{m}_{PRT}$ values expressed as a function of the dried product layer thickness (l_d). For all experimental conditions and repetitions, the mass loss factors (M_L) were less than 6%, suggesting that the calculations of $\dot{m}_{PRT}$ were in agreement with the overall mass loss measured gravimetrically.

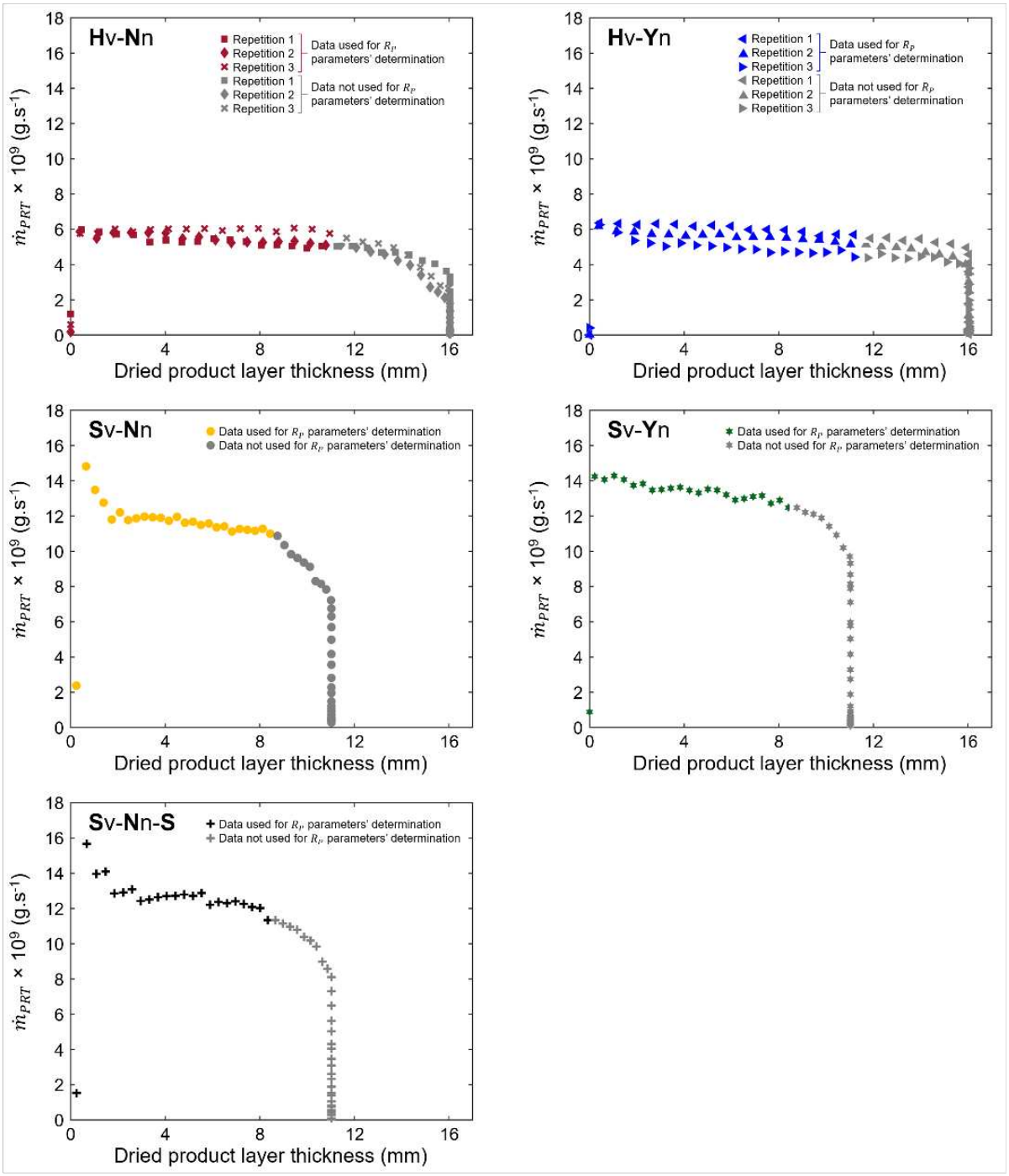

Figure 4.4-10 – Evolution of the vial-averaged mass flow rates ($\dot{m}_{PRT}$) with the dried product layer thickness (l_d). Vial-averaged $\dot{m}_{PRT}$ values were determined by the pressure rise test method using Equation 4.4-9. Hv-Nn, Hv-Yn, Sv-Nn, Sv-Yn, and Sv-Nn-S are the experimental conditions described in Table 4.4-1.

Symbols in Figure 4.4-11 show the R_P values obtained using Equation 4.4-1 to Equation 4.4-3 and Equation 4.4-5 to Equation 4.4-8, while the curves are R_P vs l_d fitted according to Equation 4.4-4. The coefficients in Equation 4.4-4 (i.e. $R_{P,0}$, $R_{P,1}$ and $R_{P,2}$) were fitted using R_P values calculated when all thermocouples indicated vials were going through ice sublimation (see Section *Comparison between calculated product temperature values and experimental values*, which corresponded to l_d values lower than 11 mm in high-throughput vials and lower than 9 mm in serum vials. It is to note that when some vials were no longer going through ice sublimation, the number of vials assumed to calculate R_P (n_V in Equation 4.4-9) was incorrect, leading to the reduction of the total flow and an overestimation of the R_P values. The values of the coefficients in Equation 4.4-4 are reported in Table 4.4-4. Note that the R_P curves for experimental conditions concerning serum vials (**S**v-**N**n, **S**v-**Y**n, and **S**v-**N**n-**S** in Figure 4.4-11) were close to the range of the results published by Scutellà et al. (2018), represented as purple streaked areas in Figure 4.4-11.

Table 4.4-4 – Calibrated coefficients $R_{P,0}$ (kPa.s.m2.kg-1), $R_{P,1}$ (MPa.s.m.kg-1), and $R_{P,2}$ (m^{-1}) from Equation 4.4-4.

		nucleating agent	
		No	**Y**es
vial type	**H**igh-throughput vial	$R_{P,0}$ = 10.0 ± 3.1 $R_{P,1}$ = 17.9 ± 3.0 $R_{P,2}$ = 147 ± 41	$R_{P,0}$ = 11.3 ± 3.3 $R_{P,1}$ = 10.5 ± 2.0 $R_{P,2}$ = 52 ± 25
	Serum vial (non-siliconized)	$R_{P,0}$ = 45.2 ± 14.4 $R_{P,1}$ = 75 ± 26 $R_{P,2}$ = 409 ± 144	$R_{P,0}$ = 2.2 ± 6.6 $R_{P,1}$ = 104 ± 26 $R_{P,2}$ = 813 ± 216
	Serum vial (**Siliconized**)	$R_{P,0}$ = 33.5 ± 21.2 $R_{P,1}$ = 103 ± 49 $R_{P,2}$ = 575 ± 255	Not studied in this work

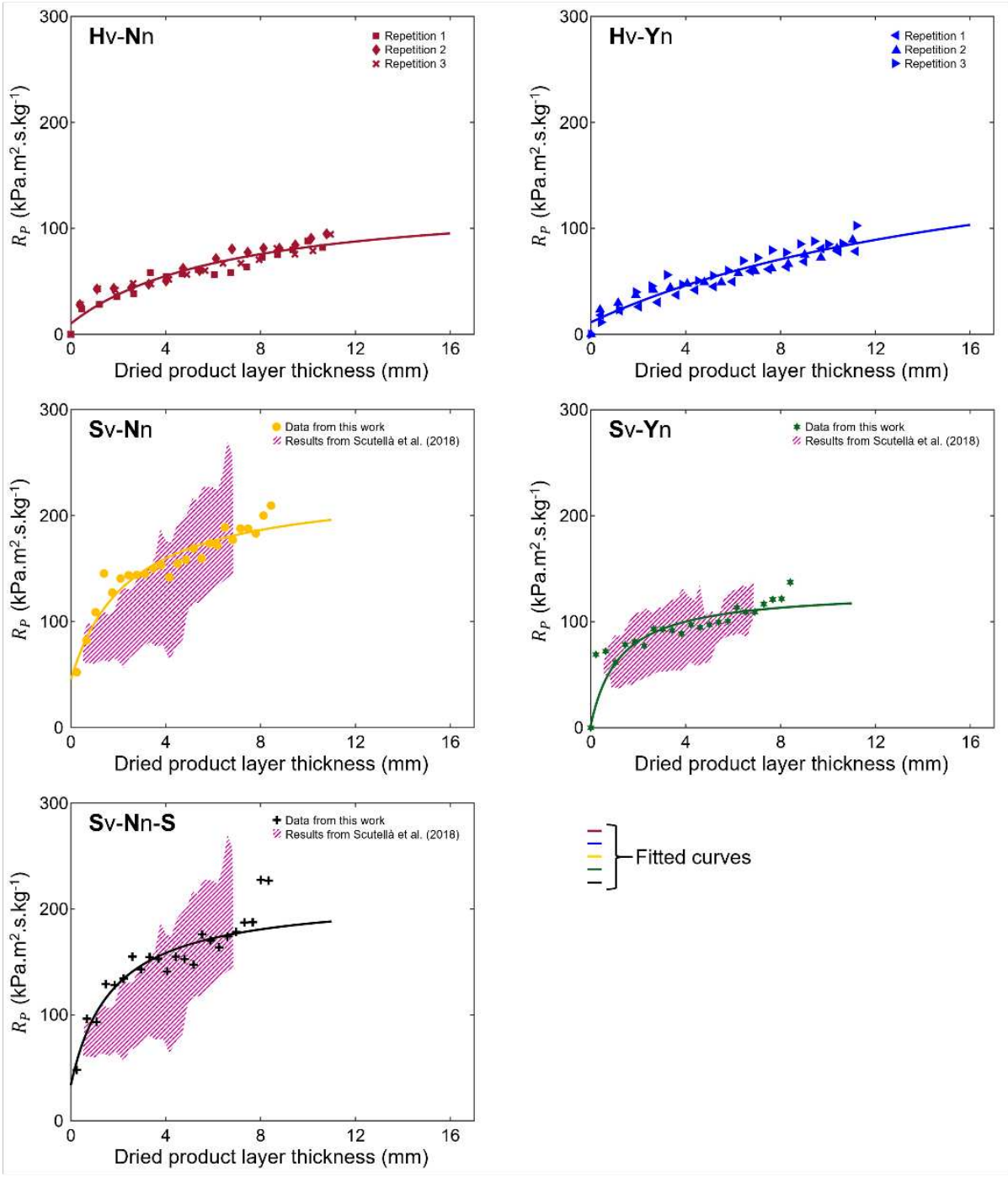

Figure 4.4-11 – Evolution of the area-normalised product resistance to mass transfer (R_P) with the dried product layer thickness (l_d). Solid lines are the curves obtained fitting R_P with Equation 4.4-4. Purple dashed areas represent the ranges of R_P values obtained by Scutellà et al. (2018) using serum vials filled with a 5% sucrose solution, without (Nn) and with (Yn) 0.1% snomax as a nucleating agent. Hv-Nn, Hv-Yn, Sv-Nn, Sv-Yn, and Sv-Nn-S are the experimental conditions described in Table 4.4-1.

For the sake of an example to compare the effect of the vial type on R_P, Figure 4.4-12a presents the ratio of R_P values at l_d of 5 mm using high-throughput vials to R_P values using serum vials. The ratio of R_P values using high-throughput vials to serum vials without a nucleating agent (R_P(**H**v-**N**n) / R_P(**S**v-**N**n) bar in Figure 4.4-12a) was approximately 0.4 – similar results were obtained at different l_d values. Thus, R_P for high-throughput vials was lower (roughly 60%) than for serum vials. R_P is defined as the resistance per vial cross-section area (A_{in}) (Equation 4.4-3), under the assumption that this is the mass transfer area. Given that the dried product structure was similar in both containers (**H**v-**N**n vs **S**v-**N**n in Figure 4.4-7), the variations on R_P values between high-throughput and serum vials could be explained by an effective mass transfer area in high-throughput vials greater than A_{in}, as suggested by the shape of the sublimation front (**H**v-**N**n in Figure 4.4-9).

Similarly, the ratio of R_P values at l_d of 5 mm using high-throughput vials to serum vials with a nucleating agent (R_P(**H**v-**Y**n) / R_P(**S**v-**Y**n) bar in Figure 4.4-12a) was approximately 0.7 – similar results were obtained at different l_d values. Hence, R_P values were lower (roughly 30% lower) in high-throughput than serum vial. When adding a nucleating agent, pores in the dried product structure were smaller in high-throughput vials than in serum vials (**H**v-**Y**n vs **S**v-**Y**n in Figure 4.4-7), so a higher R_P value would be expected for high-throughput vials than for serum vials (Pikal, 2000), contrary to what was observed. The lower R_P values in high-throughput vials compared to serum vials may be explained by a better connectivity between pores in high-throughput vials.

To observe the effect of adding a nucleating agent on R_P, Figure 4.4-12b shows the ratio of R_P values at l_d of 5 mm with a nucleating agent to R_P values without a nucleating agent. The overall impact of adding a nucleating agent on R_P was small for high-throughput vials (R_P(**H**v-**Y**n) / R_P(**H**v-**N**n) bar in Figure 4.4-12b was over 0.8, and similar results were obtained at different l_d values). Adding a nucleating agent increased the pore diameter of the dried product structure (which tends to decrease R_P) (Figure 4.4-7, Table 4.4-3) and reduced the curvature of the sublimation front (which tends to increase R_P) (Figure 4.4-9) in high-throughput vials. Thus, the impact of the pore diameter on R_P was counterbalanced by the shape of the sublimation front.

Concerning serum vials, adding a nucleating agent increased the pore diameter (which tends to decrease R_P) (Figure 4.4-7, Table 4.4-3) and reduced the sublimation front's area (which tends also to decrease R_P) (Figure 4.4-9). Thus, the ratio of R_P for serum vials with a nucleating agent to serum vials without a nucleating agent (R_P(**S**v-**Y**n) / R_P(**S**v-**N**n) bar in Figure 4.4-12b) was approximately 0.4.

Finally, the impact of siliconizing the vials on R_P was negligible (e.g. for l_d = 5 mm, R_P decreased less than 10% from **S**v-**N**n to **S**v-**N**n-**S** in Figure 4.4-11), as expected given the similar dried product structure (**S**v-**N**n vs **S**v-**N**n-**S** in Figure 4.4-7) and shape of the sublimation front (**S**v-**N**n vs **S**v-**N**n-**S** in Figure 4.4-9).

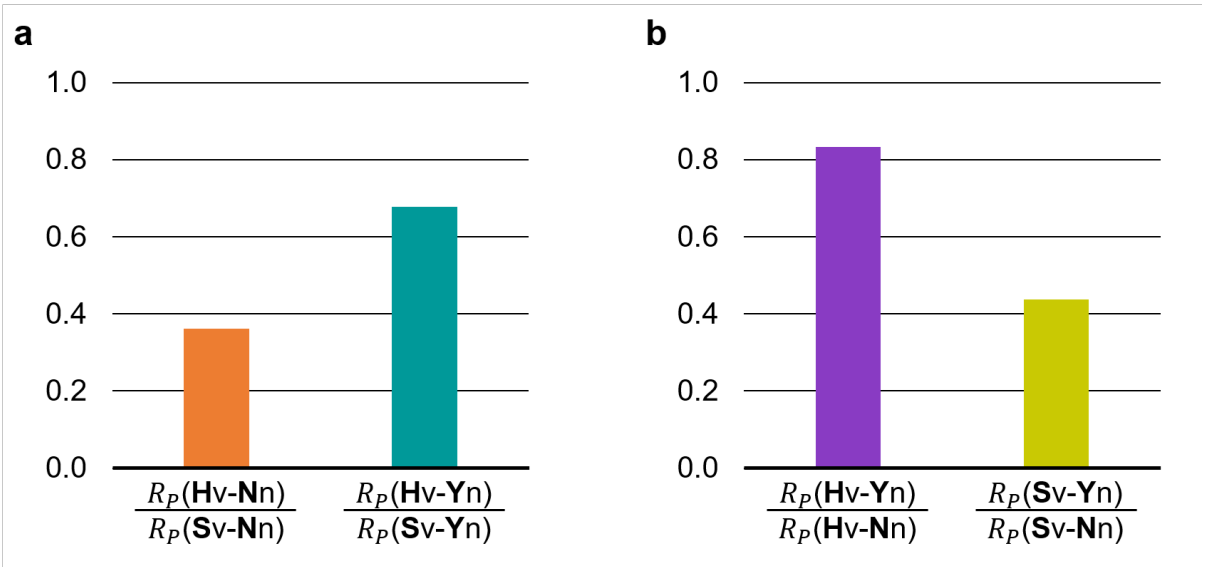

Figure 4.4-12 – Ratio of the area-normalised product resistance to mass transfer (R_P) for dried product layer thickness (l_d) of 5 mm between experimental conditions (a) using different vial types and (b) with and without a nucleating agent. Hv-Nn, Hv-Yn, Sv-Nn, Sv-Yn, and Sv-Nn-S are the experimental conditions described in Table 4.4-1.

The nucleating temperature (T_n) is commonly used to explain (or at least indicate) variations in the size distribution of the ice crystals obtained during freezing, hence the pore size distribution and R_P (e.g. Fennema, 1973; Geidobler and Winter, 2013; Konstantinidis et al., 2011; Nakagawa et al., 2006; Searles et al., 2001). To this end, Figure 4.4-13 shows the value of R_P at a dried product layer thickness of 5 mm against T_n (Figure 4.4-6) for each experimental condition (Table 4.4-1). For high-throughput vials, experimental conditions with different T_n values presented similar R_P values (e.g. R_P decreased by 20% from **H**v-**N**n to **H**v-**Y**n in Figure 4.4-13). Due to the contrary effects of the pore size and shape of the sublimation front, varying T_n by 5 °C in high-throughput vials did not considerably affect R_P. In contrast, increasing T_n by 5 °C in serum vials reduced the R_P value in half (Figure 4.4-12b and Figure 4.4-13).

Pikal (2000) stated that the pore size is inversely proportional to R_P. Adding a nucleating agent increased the pore size two times in high-throughput vials (Table 4.4-3), and should have reduced R_P by two times. However, the observed reduction of R_P when adding the nucleating agent in high-throughput vials was smaller than predicted by Pikal (2000) (R_P(**H**v-**Y**n) / R_P(**H**v-**N**n) bar in Figure 4.4-12b was higher than 0.5); probably due to mass transfer area variations, as suggested by the curved sublimation fronts in vials without the nucleating agent (**H**v-**Y**n in Figure 4.4-9). Similarly, for serum vials, adding a nucleating agent increased the pore size three times (Table 4.4-3), and should have reduced R_P by three. Nevertheless, the experimental R_P reduction was not as remarkable (R_P(**S**v-**Y**n) / R_P(**S**v-**N**n) bar in Figure 4.4-12b was greater than 0.33); possibly because of a low connectivity between pores when adding the nucleating agent.

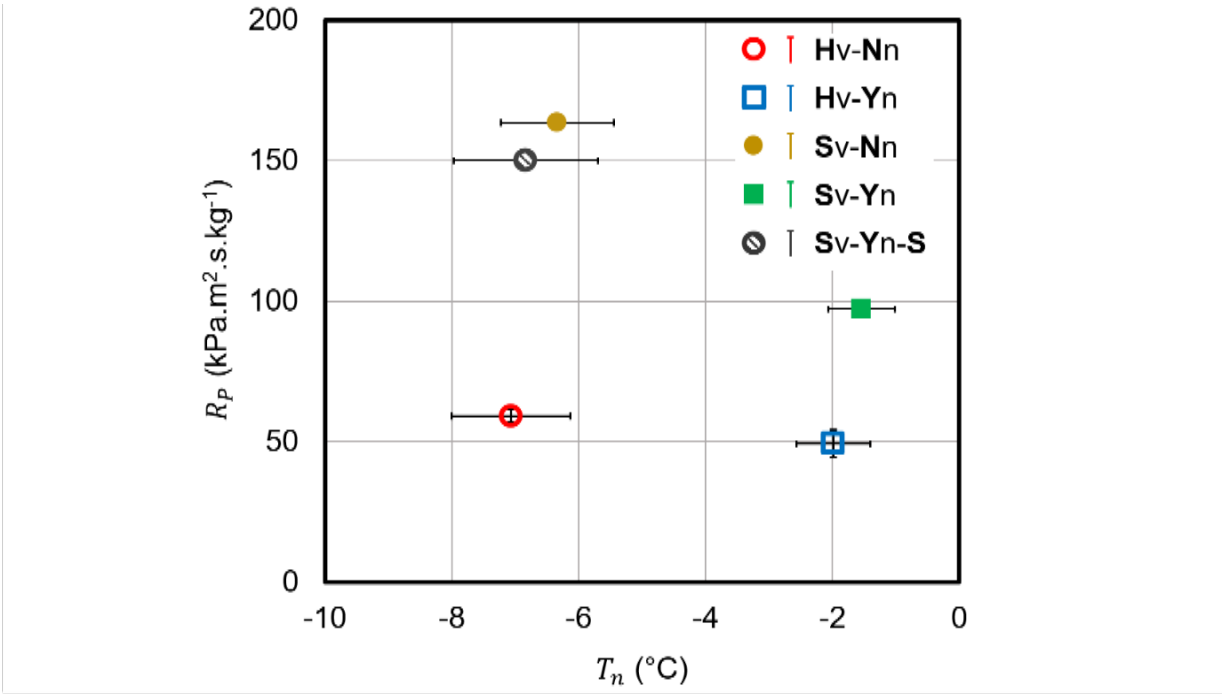

Figure 4.4-13 – R_P values at l_d = 5 mm expressed as a function of the nucleation temperature (T_n) determined using a thermal camera (Figure 4.4-6). Error bars in the R_P-axis are the R_P standard deviations of the three repetitions when using high-throughput vials (Figure 4.4-11). Error bars in the T_n-axis are the standard deviations (Figure 4.4-6). Hv-Nn, Hv-Yn, Sv-Nn, Sv-Yn, and Sv-Nn-S are the experimental conditions described in Table 4.4-1.

Impact of the vial type and nucleation temperature on the product temperature during primary drying

The evolution of the measured product temperature and the calculated value (T_b) for each experimental condition (Table 4.4-1) are presented in Figure 4.4-14. Experimental product temperatures (grey areas in Figure 4.4-14) increased at the beginning of primary drying and reached a pseudo-stationary value when the dried product layer thickness (l_d) was (approximately) greater than 4 mm. T_b values calculated with Equation 4.4-1 to Equation 4.4-8 remained mostly within the measured standard deviation. Hence, the heat and mass transfer model used in this work appears valid to calculate T_b.

Considering experimental conditions without a nucleating agent, the calculated T_b values for high-throughput vials (**H**v-**N**n in Figure 4.4-14) and serum vials (**S**v-**N**n in Figure 4.4-14) differed by less than 0.3 °C for l_d greater than 2 mm. To understand this observation, we must recall how small pores obtained without a nucleating agent (diameter approximately 90 µm, Table 4.4-3) entailed curved sublimation fronts in high-throughput vials (**H**v-**N**n in Figure 4.4-9) that reduced the apparent dried product resistance to mass transfer per inner vial cross-section (R_P) compared to serum vials (R_P(**H**v-**N**n) / R_P(**S**v-**N**n) bar in Figure 4.4-12a). Ultimately, T_b was similar for high-throughput and serum vials since the increase in the ability to transfer mass through the dried product layer ($R_P{}^{-1}$) in high-throughput vials compared to serum vials was compensated by the increase in the ability to transfer heat from the freeze-dryer (K_V; Table 4.4-2).

When adding a nucleating agent, the calculated T_b values for high-throughput vials (**H**v-**Y**n in Figure 4.4-14) were 2.3 °C higher than T_b values for serum vials (**S**v-**Y**n in Figure 4.4-14) by the end of primary drying. This could be physically explained by the similar ability to transfer mass through the dried product layer ($R_P{}^{-1}$) in both vial types (R_P(**H**v-**Y**n) / R_P(**S**v-**Y**n) bar in Figure 4.4-12a), and the higher ability to transfer heat from the freeze dryer for high-throughput vials (K_V; Table 4.4-2).

Comparing high-throughput vials, adding a nucleating agent had no impact on T_b because R_P was similar with and without the nucleating agent (R_P(**H**v-**Y**n) / R_P(**H**v-**N**n) bar in Figure 4.4-12b was close to 1). This similar R_P values are explained by an increase in the pore diameter when adding a nucleating agent (Table 4.4-3) that was compensated by the decrease in the mass transfer area (Figure 4.4-9). On the contrary, for serum vials, adding a nucleating agent decreased T_b by 2.4 °C by the end of primary drying. Hence, differences on the dried product structure could entail variations in the final product appearance. As a practical outcome, the nucleation process should be more carefully controlled in serum vials than in high-throughput vials to obtain a homogeneous batch.

The impact of siliconizing vials on T_b was negligible. Calculated T_b of for non-siliconized and siliconized serum vials differed on average less than 1 °C, as it was expected due to the similar R_P values (**S**v-**N**n vs **S**v-**N**n-**S** in Figure 4.4-11). Besides, the experimental range of T_b values of non-siliconized and siliconized serum vials overlapped (grey areas of **S**v-**N**n and **S**v-**N**n-**S** in Figure 4.4-14).

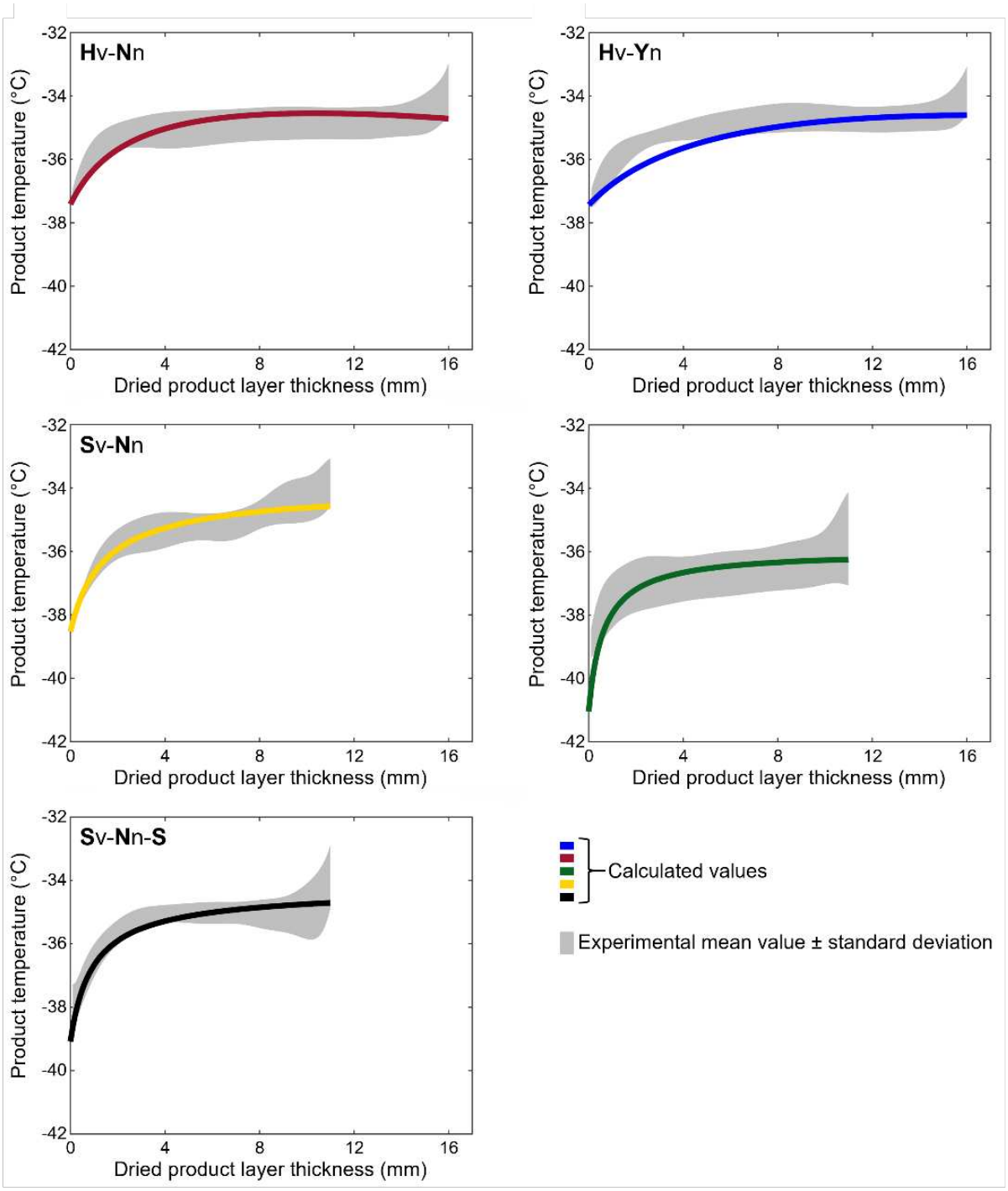

Figure 4.4-14 – Evolution of the product temperature with the dried product layer thickness (l_d). Grey areas are the represent the mean values ± standard deviations of the temperatures measured using the eight thermocouples, and coloured lines are the calculated temperatures using the area-normalised product resistance (R_P) and Equation 4.4-1 to Equation 4.4-8. Hv-Nn, Hv-Yn, Sv-Nn, Sv-Yn, and Sv-Nn-S are the experimental conditions described in Table 4.4-1.

CONCLUSIONS

This work delved into how the vial type (i.e. high-throughput or serum vials) could affect the mass transfer during primary drying by focusing on the product resistance to mass transfer (R_P) normalized by the vial cross-section area (A_{in}). The impact of the vial type on R_P was interpreted based on: (i) the pore diameter, and (ii) the shape of the sublimation front and the connectivity of the pores, even if they were not measured quantitatively. Furthermore, a lumped-variable steady-state model for heat and mass transfer during primary drying was used to evaluate the consequences of R_P variations between vial types on the product temperature (a critical process parameter).

A "model" product (5% w/w sucrose aqueous solution) was considered in this work, and the impact of the nucleation temperature (T_n) was evaluated by, in some cases, adding a nucleating agent in a small concentration (0.1% w/w). Regardless of the vial type, adding the nucleating agent increased T_n from approximately -7 °C to -1.5 °C. When T_n was close to -7 °C, the pore diameter was similar in both vial types (close to 92 μm), and the sublimation front was curved in high-throughput vials and flat in serum vials. Therefore, effective R_P was smaller in high-throughput vials than in serum vials since, in high-throughput vials, the effective mass transfer area was greater than A_{in} (area considered to normalize R_P). When T_n was close to -1.5 °C, the pore diameter was smaller in high-throughput vials (195 μm) than in serum vials (300 μm), yet the R_P values were similar in high-throughput and serum vials. Additionally, siliconizing of serum vials had no significant effect on any of the assessed variables.

As a practical outcome, when T_n was close to -7 °C, the product temperatures at the end of primary drying differed by less than 0.5 °C in both vial types. This mild difference in product temperature occurred because the differences in R_P between vial types were compensated by the differences in the heat transfer coefficient from the shelves to the vials (K_V). However, when T_n was close to -1.5 °C, product temperatures were over 2 °C greater in high-throughput vials than in serum vials due to differences on K_V. In this case, freeze-drying cycles should be re-designed when using different vial types to avoid product collapse while operating close to the maximum admissible product temperature (process optimization).

APPENDIX 4.4-A

To determine the nucleation temperature (T_n) of the vials, the thermal camera was set to take pictures of the vials every 5 seconds during freezing tests, as described in *Section Determination of the nucleation temperature* of this Paper IV. Thermal images were loaded into a computer, and then each image was exported as a matrix of 320×240 pixels (.xlsx file; Microsoft Excel, Microsoft Corporation, WA, USA) using the IRSoft software provided by Testo (Testo SE & co, Lenzkirch, Germany). Each pixel of each matrix contained a surface temperature value. For each experimental run, matrices were loaded in MATLAB R2017a (The MathWorks, Inc, Natick, MA, USA) and plotted as colour maps. Figure 4.4-15a shows a colour map based on a thermal image obtained during tests with high-throughput vials, and Figure 4.4-15b with serum vials. These colour maps served to visually identify the pixels corresponding to the surfaces of the vial content, the shelf, and the well plate (in the case of tests with high-throughput vials). Figure 4.4-15c and Figure 4.4-15d schematise Figure 4.4-15a and Figure 4.4-15b, respectively, to better understand the surfaces observed in the thermal images.

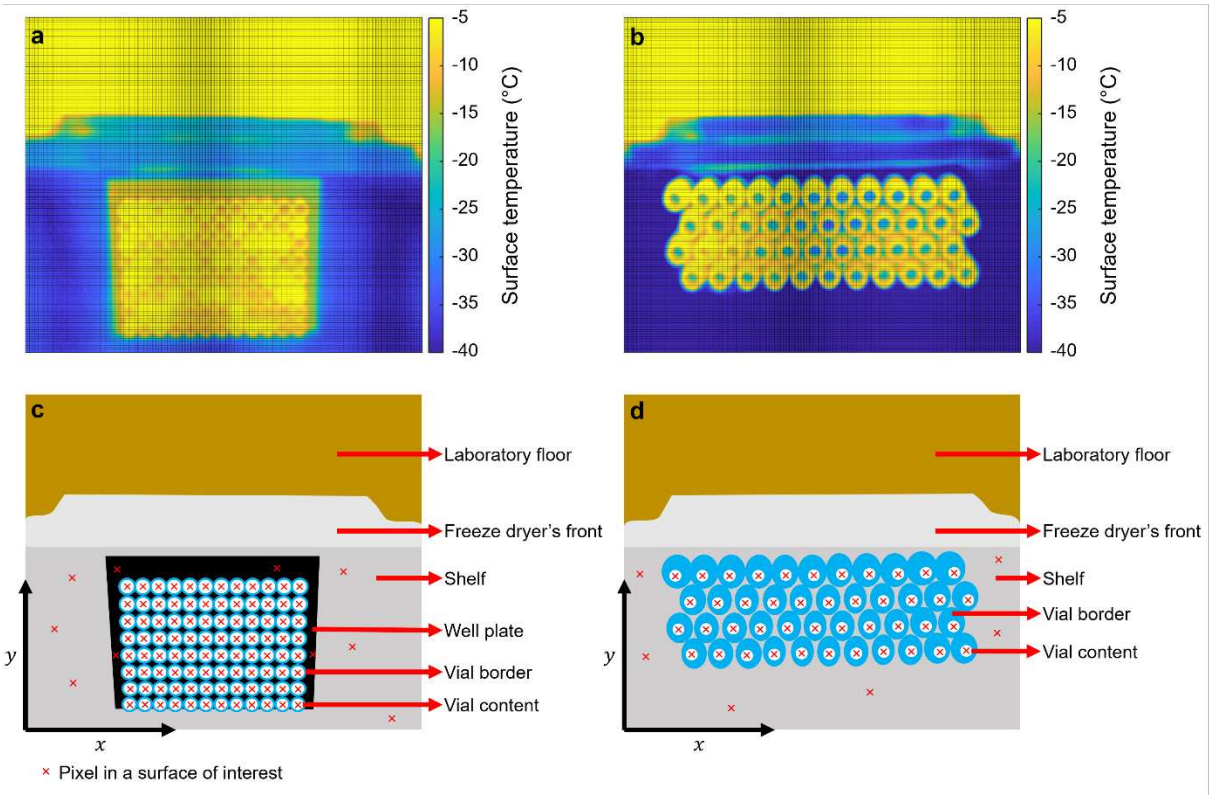

Figure 4.4-15 – Image treatment. (a) Thermal image (colour map) during freezing with high-throughput vials. (b) Thermal image (colour map) during freezing with serum vials. (c) Scheme of the surfaces observed in (a). (d) Scheme of the surfaces observed in (b). x and y are the directions of the axis in the colour maps used to identify the pixels. Red 'X' represent the positions of pixels used for data treatment of the surface temperature.

A MATLAB code was developed to treat the thermal images and obtain the surface temperature values of the vial contents, the shelf, and the well plate Table 4.4-5 presents a scheme of logic behind the MATLAB code. The inputs of the code were: (i) the thermal images expressed as matrices ($Image_1$, $Image_2$, …, $Image_n$ in Table 4.4-5), and (ii) the coordinates of the pixels corresponding to the surfaces of interest (Π_V^m for the mth vial content, Π_S for the shelf, and Π_{WP} for the well plate in Table 4.4-5). For each thermal image, 1 pixel in the centre of the vial content surface, 6 pixels of the shelf (ramdomly selected), and 4 pixels of the well plate (randomly selected) were considered (red 'X' in Figure 4.4-15c and Figure 4.4-15d). The coordinates of the pixels were expressed as a matrix (Π_V^m, Π_S, or Π_{WP}), in which the rows corresponded the each pixel's coordinates (using directions x and y in Figure 4.4-15c and Figure 4.4-15d). Note that the same pixel positions were used for all pictures within the same experimental run (the camera's position was fixed using a tripod). The output of the code are vectors listing the surface temperature values corresponding to successive times (every 5 seconds) for each vial content (T_V^m), the shelf (T_S), and the well plate (T_{WP}, only in the case of tests with high-throughput vials). The vectors (T_V^m, T_S, and T_{WP}) were built by identifying the temperature of the pixels corresponding to the surfaces of interest (listed in Π_V^m, Π_S, and Π_{WP}) in each thermal image ($Image_1$, $Image_2$, …, $Image_n$). In the case of the well plate and shelve surfaces, temperature values in each thermal image were averaged among the pixels.

Table 4.4-5 – Logic behind the MATLAB code to identify the surface temperatures.

	Meaning	Code Interpretation
Inputs	Thermal images expressed as temperature matrices ($Image$)	$Image_1, Image_2, \ldots, Image_n$
	Matrix of pixel coordinates corresponding to the vial contents (Π_V^m), the shelf (Π_S), and the well plate (Π_{WP}).	$\Pi_V^m = \begin{bmatrix} y_{V\_1} & x_{V\_1} \end{bmatrix}$; $\Pi_S = \begin{bmatrix} y_{S\_1} & x_{S\_1} \\ y_{S\_2} & x_{S\_2} \\ \vdots & \vdots \\ y_{S\_8} & x_{S\_8} \end{bmatrix}$; $\Pi_{WP} = \begin{bmatrix} y_{WP\_1} & x_{WP\_1} \\ y_{WP\_2} & x_{WP\_2} \\ \vdots & \vdots \\ y_{WP\_8} & x_{WP\_8} \end{bmatrix}$ m is the vial number, going from 1 to 96 in tests with high-throughput vials and 1 to 44 in tests with serum vials. y and x are the column and row numbers. V_i refers to the of the ith pixel of the vial content's surface. S_i refers to the of the ith pixel of the vial content's surface. V_i refers to the of the ith pixel of the vial content's surface.
Outputs	Matrix of surface temperatures in time of the vial contents (T_V^m), and vectors of surface temperatures in time of the shelf (T_S) and the well plate (T_{WP}).	$T_V^m = \begin{bmatrix} T_V^m \; at \; t = 0 \\ T_V^m at \; t = 5 \\ \vdots \\ T_V^m at \; t = 5(n-1) \end{bmatrix}$; $T_S = \begin{bmatrix} T_S \; at \; t = 0 \\ T_S \; at \; t = 5 \\ \vdots \\ T_S \; at \; t = 5(n-1) \end{bmatrix}$; $T_{WP} = \begin{bmatrix} T_{WP} \; at \; t = 0 \\ T_{WP} \; at \; t = 5 \\ \vdots \\ T_{WP} \; at \; t = 5(n-1) \end{bmatrix}$ m is the vial number, going from 1 to 96 in tests with high-throughput vials and 1 to 44 in tests with serum vials. t is the time (in seconds, s) since the first thermal image was registered.
Body	For each thermal image taken every 5 seconds ($Image_j$) ...	For j = 1 to n (at $t = 5(n-1)$)
	… the surface temperature of the vial contents ($T_V^m(j)$), the shelf ($T_S\ (j)$), and the well plate ($T_{WP}(j)$) is the average temperature of the pixels involved.	$T_V^m(j) = Image_j(y_{S\_i}, x_{S\_i})$; $T_S(j) = \frac{1}{6}\sum_{i=1}^{6} Image_j(y_{S\_i}, x_{S\_i})$; $T_{WP}(j) = \frac{1}{4}\sum_{i=1}^{4} Image_j(y_{WP_i}, x_{WP_i})$

APPENDIX 4.4-B

Two calibration steps were performed to remove (i) the noise and (ii) constant biases of the surface temperature values.

Surface temperature signals presented noise due to the ambient radiation and the auto-calibration of the camera. The first calibration step was aimed at removing the noise. To do so, the surface temperature of the shelf was fitted to straight lines (different lines for the ramps and plateaus). For example, Figure 4.4-16a presents a shelf's surface temperature with noise (non-calibrated). At the same time, Figure 4.4-16b shows a straight line obtained by fitting the experimental data of Figure 4.4-16a to a one-degree polynomial. The difference between the fitted shelf's surface temperature (e.g. Figure 4.4-16b) and the measured shelf's surface temperature (e.g. Figure 4.4-16a) was attributed to noise and was subtracted from the surface temperature of the well plate and vial contents. For example, Figure 4.4-16c presents a vial content's surface temperature with noise (non-calibrated), and Figure 4.4-16d shows the same signal after removing the noise.

A second calibration step removed the constant biases of the surface temperatures of the vial contents by following the method described in Harrison et al. (2018). This method required identifying, for each vial, when the content's surface temperature registered a sharp increase until close to 0 °C. For example, a temperature value after this sharp increase is represented as a grey dotted line in Figure 4.4-16e. The difference between this value after the sharp increase and the freezing-point depression temperature (-0.28 °C for a 5% sucrose solution; Kiyosawa, 1988; black dashed line in Figure 4.4-16e) was considered as a constant bias and removed from the vial content's surface temperature. Finally, a calibrated vial content's surface temperature was obtained, as shown in Figure 4.4-16f. The nucleation temperature (T_n) in each vial was considered as the signal value before the temperature increment until the freezing-point, represented in Figure 4.4-16f by a green dashed line.

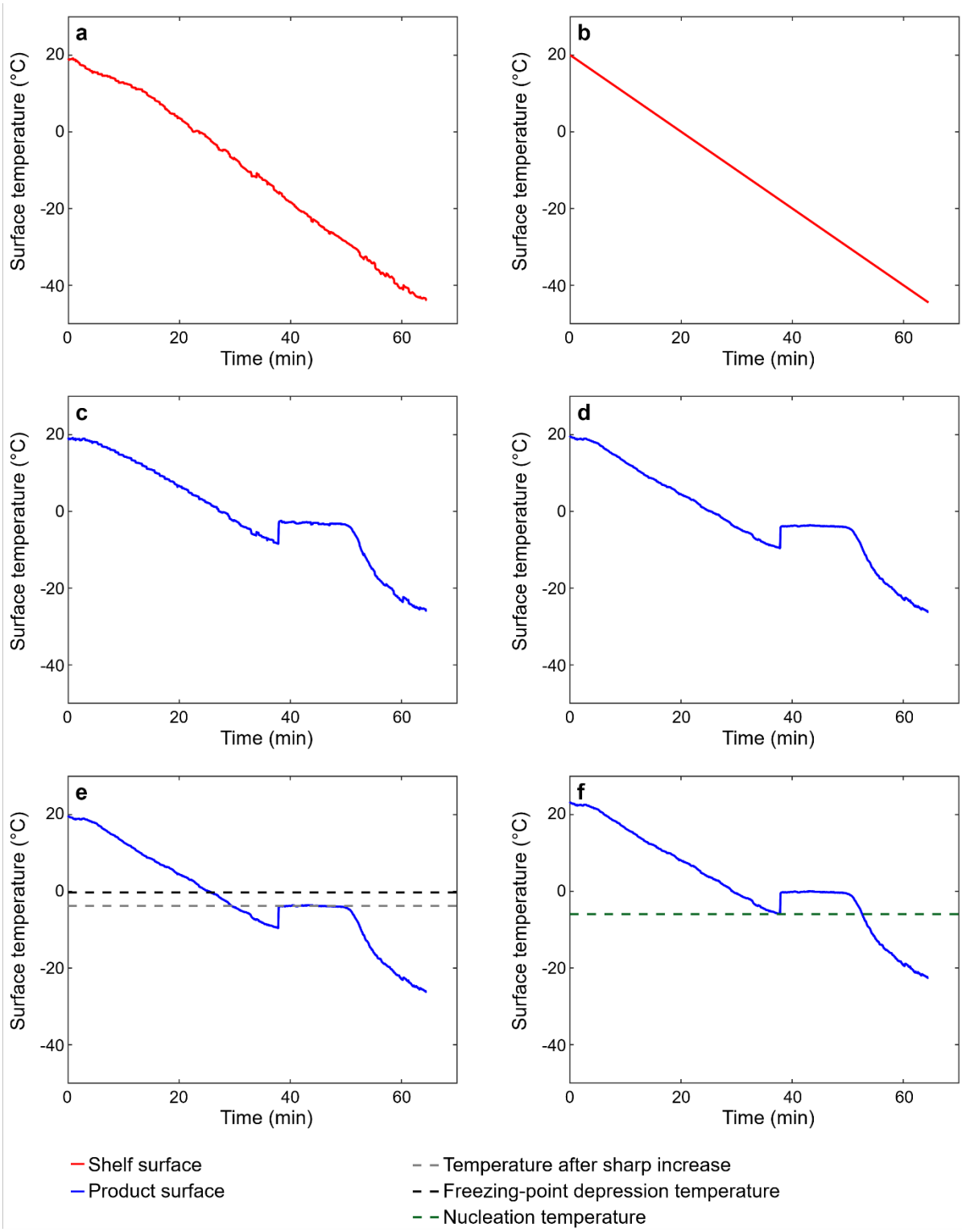

Figure 4.4-16 – Calibration of a surface temperature. (a) Non-calibrated shelf surface temperature. (b) Line obtained by fitting the data of (a) to a one-degree polynomial. (c) Non-calibrated vial content's surface temperature. (d) Data obtained after removing the noise from Figure (c). (e) Identification of the difference between the temperature after the sharp increase (grey dashed line) and the freezing-point depression temperature (black dashed line). (f) Data obtained after calibration and determined nucleation temperature (green dashed line).

APPENDIX 4.4-C

Figure 4.4-17 presents examples of the chamber pressure registered during the pressure rise tests (red dots in Figure 4.4-17) and the fitted curves obtained considering a 6-degree polynomial (black curves in Figure 4.4-17).

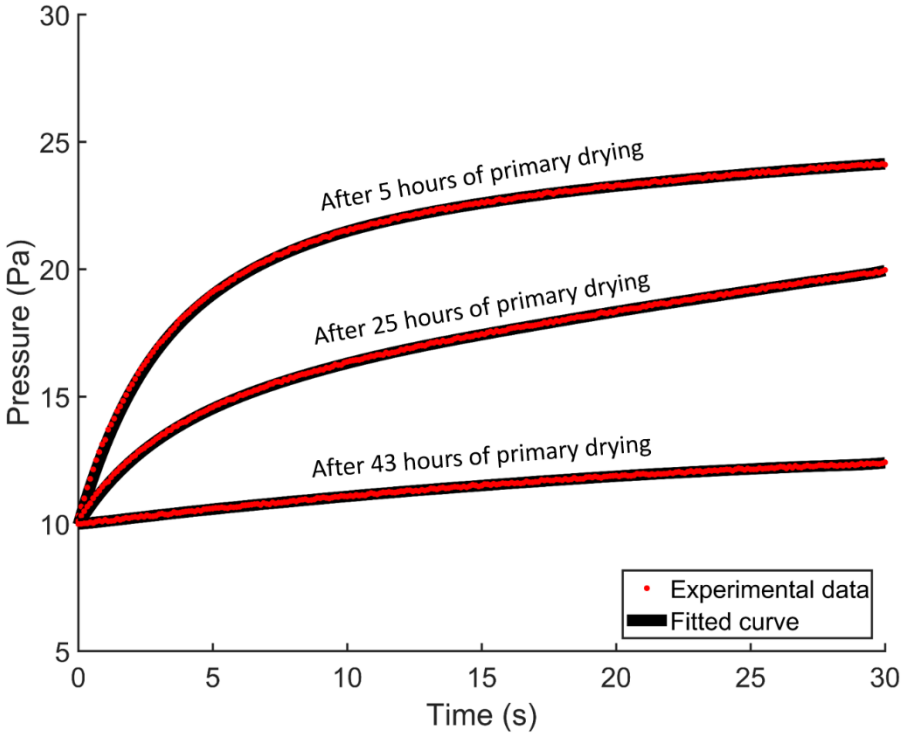

Figure 4.4-17 – Examples of the pressure evolution registered with the capacitance manometer during pressure rise tests performed at 5, 25, and 43 hours of primary drying. Fitted curves in black are the 6-degree polynomial obtained by adjusting the experimental data in red.

4.4.4. Take-Home Message

This section addressed the area-normalized product resistance to mass transfer (R_P*), which is one of the most important parameters in vial freeze-drying. The dry product pore size and shape, as determined by X-ray micro-computed tomography, interacted in a complex way with the shape of the sublimation front to produce an effective* R_P*, suitable for calculation of the mass flow rate and product temperature.*

When the nucleation temperature (T_n*) was lower (e.g. -7 °C, without use of a nucleating agent), the pore diameter was similar in high-throughput and serum vials (close to 92 mm), but the sublimation front was curved in high-throughput vials and flat in serum vials. Thus,* R_P *was lower in high-throughput vials than in serum vials, since a greater mass transfer area per inner vial cross-sectional area reduces* R_P*. Regarding the coupled heat and mass transfer, the product temperature differed by less than 0.5 °C in both container types at the end of primary drying because the* R_P *tendencies were counterbalanced by the heat transfer (*K_V*) differences.*

When T_n *was higher (e.g. -1.5 °C, in presence of a nucleating agent),* R_P *was similar in high-throughput and serum vials since the pore connectivity compensated the variations in pore size. Given the heat transfer (*K_V*) differences, product temperatures were over 2 °C higher in high-throughput vials than in serum vials, which may represent a significant product quality risk when the process is run close to the maximum admissible product temperature.*

5. General Discussion

Vaccination is one of the pillars that sustains healthcare systems, prevents several transmissible diseases, and controls epidemics. The active principle of a vaccine should be stabilized during transportation and storage, so the vaccine will cause the desired effect when administered to the subject. Freeze-drying is widely used in the pharmaceutical industry to stabilize active principles (Hansen et al., 2015; Izutsu, 2018). Most active principles are heat-sensitive, so the low product temperatures encountered during freeze-drying make it the drying method of choice (World Health Organization, 2006).

Freeze-dried vaccines must comply with different standards to preserve the active principle's quality. During vaccine development, candidate formulations are selected based on their potency and appearance after freeze-drying. Identifying the best formulation is a time-consuming work. Traditionally, candidate formulations are screened using tubular vials with a volume of 3 mL or more, commonly known as serum vials, which are the same used at the production scale (Pikal, 2000; Pisano et al., 2011; Scutellà et al., 2017a). Smaller vials with a volume of 1 mL or less, known as high-throughput vials, could accelerate the formulation screening since more vials could be fit in the freeze dryer (than when using serum vials), and more formulations could be tested per freeze-drying cycle. Furthermore, high-throughput vials simplify the laboratory labour since they are carried in 96-well plates compatible with most robots used for preparing and filling formulations (Peterman et al., 2014; Stangegaard et al., 2011; Taylor et al., 2002).

The vaccine's quality parameters, particularly the appearance of the dried cake, are related to the temperature of the formulation during drying. Heat and mass transfer during drying vary between high-throughput and serum vials due to the geometry differences (see Sections 2.2.2.1 and 2.3.2.5) and the presence of a well plate (see Section 2.2.2.3). Therefore, the product temperature may vary between high-throughput vials at the laboratory scale and serum vials at the production scale, impacting on the appearance of the dried cake. In this vein, this thesis focused on "translating" the results obtained with high-throughput vials at a serum vial scale, using mathematical modelling of the heat and mass transfer during sublimation (primary drying). Two interrelated scientific questions were addressed:

- *Question 1: How could we identify the operating conditions that entail the same product temperature during primary drying in high-throughput systems and serum vials?*
- *Question 2: What are the main factors responsible for product quality variations during primary drying in high-throughput systems?*

The following Sections 5.1 and 5.2 detail the general conclusions on Questions 1 and 2, respectively. Moreover, Section 5.3 presents perspectives for future research after this thesis.

5.1. Question 1: Translation of the Operating Conditions

The product temperature during primary drying is a critical process parameter (Fonseca et al., 2004; Overcashier et al., 1999; Pikal and Shah, 1990a) which depends on the heat and mass transfer while ice crystals are removed by sublimation (Pikal, 2000). Variations in the heat and mass transfer between vial types (e.g. high-throughput and serum vials) could entail different product temperatures, possibly resulting in different product qualities. In this vein, Table 5.1-1 lists the main results of this thesis concerning the variations in the heat and mass transfer during primary drying when using either high-throughput or serum vials.

The following Section 5.1.1 presents the conclusions when comparing the heat transfer in high-throughput or serum vials, and similarly, Section 5.1.2 introduces the conclusions when comparing the mass transfer. Finally, Section 5.1.3 presents the conclusions on the impact of the coupled heat and mass transfer.

Table 5.1-1 – Main results of this thesis concerning the variations in the heat and mass transfer during primary drying when using high-throughput or serum vials.

Question 1: "How could we identify the operating conditions that entail the same product temperature during primary drying in high-throughput systems and serum vials?"	
Heat transfer	At chamber pressures lower than 12 Pa, the effective heat transfer coefficient between the shelves and the vial (K_V) was almost three times greater for high-throughput vials than for serum vials. The high K_V value in high-throughput vials was due to the efficient heat transfer between the shelf and the well plate bottom by contact conduction and gas conduction, and between the wells and the vials by contact conduction. (Section 4.1)
Mass transfer	The mass transfer was studied using a 5% sucrose aqueous solution. At low nucleation temperature (approx. -7 °C, obtained without a nucleating agent), the effective dried product resistance to the mass transfer (R_P) was close to two times smaller in high-throughput vials than in serum vials because, in high-throughput vials, the effective mass transfer area was greater than the geometric cross-section area. At high nucleation temperature (approx. -1.5 °C, obtained with a nucleating agent), R_P was similar in high-throughput and serum vials, because the opposite effects of the pore diameter and pore connectivity were counterbalanced. (Section 4.4)

5.1.1. Heat Transfer

During primary drying, the freeze dryer's shelves are considered the main heat source for the containers placed in the centre of each shelf surrounded by other vials (Sheehan and Liapis, 1998; Velardi and Barresi, 2008). Under this hypothesis, the effective heat transfer coefficient between the shelves and the vial (K_V) is commonly used to model the heat transfer. In this thesis, only high-throughput vials in the centre of a well plate (surrounded by other vials) in the centre of the shelf (at more than 10 cm of the shelf's edge) and serum vials in the centre of the shelf were initially considered to comply with this hypothesis, and therefore, were considered to answer Question 1.

For both container types (i.e. high-throughput and serum vials), K_V values mainly depended on the chamber pressure (studied range from 4 to 65 Pa), as many other authors previously observed (e.g. Pikal et al., 1984; von Graberg, 2011). The pressure dependence of K_V (during freeze-drying) is commonly attributed to the heat transfer through the gas trapped between adjacent surfaces (e.g. Pikal, 2000; Pisano et al., 2011; Velardi and Barresi, 2008). In the case of serum vials, the pressure dependence of K_V was due to the variation in the heat transfer by conduction through the gas trapped between the shelf and the serum vial. High-throughput vials are not placed directly on the shelf, instead go inside well plates; consequently, K_V was modelled considering two heat transfer coefficients in series: (i) one from the shelves to the well plates (K_{WP}), and (ii) another from the well plates to the vials (K_{HV}). K_{WP} was pressure dependent; however, K_{HV} was not. This suggested that the pressure dependency of K_V in high-throughput vials was due to the gas trapped between the shelf and the well plate, which is included in K_{WP}. The pressure dependence of K_{HV}, even if theoretically expected, was not put in evidence in our study. A possible reason is that K_{HV} was not limiting for heat transfer due to the good thermal contact between the vial and the surrounding well.

Comparing container types, K_V values were close to 3 times higher in high-throughput than in serum vials at chamber pressures lower than 12 Pa (range used in the pharmaceutical industry). Therefore, the heat transfer from the shelves to the well plate and then to the high-throughput vials was more effective than from the shelves to serum vials. Indeed, K_{WP} and K_{HV} (expressed relatively to the high-throughput vial bottom area) were over 2 and 9 times higher than K_V for serum vials (Scutellà et al., 2017a), respectively. The main mechanisms in the heat transfer to the high-throughput vials were the conduction through the gas trapped between the shelf and the well plate bottom (over 60% of K_{WP}) and the contact conduction between the wells and the vials (over 70% of K_{HV}).

From the heat transfer's perspective, high-throughput vials are expected to present higher product temperatures than serum vials due to their higher K_V values (all other conditions being equal). However, the impact of the container type on the product temperature also depends on the mass transfer, which will be discussed in the following Section 5.1.2.

5.1.2. Mass Transfer

The heat received by the vials provides the energy to sublimate the ice crystals during primary drying. As primary drying occurs, the sublimation front moves through the vial content leaving a dried product layer (containing the product and sorbed water) behind. The sublimated vapour flow goes through the dried product layer before escaping from the vial to the drying chamber. Several authors pointed out that the main mass transfer resistance is that of the dried product layer (Rambhatla et al., 2004; Scutellà et al., 2018a; Tang et al., 2006), and it is commonly modelled as an area-normalized resistance (R_P) considering the vial inner cross-sectional area as the mass transfer area (A_{in}). R_P depends on the geometry of the pores in the dried product layer (e.g. pore size, connectivity) (Konstantinidis et al., 2011; Pikal, 2000), which could vary due to the container geometry (Nam and Song, 2005; Rosa et al., 2016).

For both container types, R_P values increased as sublimation advanced and the dried product layer thickness increased, as expected. The nucleation temperature (T_n) – modified in this study by the introduction of a nucleating agent – played a key role when comparing R_P values in different container types. At low T_n (close to -7 °C, without a nucleating agent), both container types presented similar pore diameters (close to 92 μm), yet the sublimation front was curved in high-throughput vials and flat in serum vials. The curved sublimation front in high-throughput vials overall improved the mass transfer, so the effective R_P appeared smaller than in serum vials. When T_n was high (close to -1.5 °C, with a nucleating agent), the pore diameter was smaller in high-throughput vials (195 μm) than in serum vials (310 μm). However, the R_P values were similar in both container types, presumably since the pore connectivity was worse in serum vials.

The product temperature depends on the coupled heat and mass transfer. The translation of the operating conditions will be discussed in Section 5.1.3, considering the variations of R_P and K_V between container types.

5.1.3. Coupling Heat and Mass Transfer

A graphic tool was presented in Section 4.1.3, embodying the solution of the heat and mass transfer equations during sublimation in high-throughput and serum vials. This graphic tool allows us to identify the operating conditions that entail the same temperature in both container types, also referred to as "translating" the operating conditions. It is to note that heat and mass transfer equations are solved considering steady-state. However, in reality, the product temperature increased during primary drying. Therefore, the product temperature should be considered by the end of primary drying to translate the operating conditions, assuming this is the worst case for product collapse in both vial types.

This thesis considered two sizes of high-throughput vials differing in the maximal volume (500-µL or 1000-µL), and two types of well plates varying in their surface finish (A-type well plate with brilliant black surfaces, and B-type well plate with matte black surfaces). For the sake of an example, K_V values of 1000-µL high-throughput vials in a B-type well plate (determined in Section 4.1.3) and 3-mL serum vials (determined by Scutellà et al. 2017a) were studied. Furthermore, R_P values of a "model" product (5% w/w sucrose aqueous solution, determined in Section 4.4.3) were evaluated at the end of primary drying for each container, for a dried layer thickness (l_d) of: (i) 16 mm in 1000-µL high-throughput vials, and (ii) 11 mm in serum vials. R_P values depended on T_n, and so did the graphic tools obtained; Figure 5.1-1a presents the graphic tool to translate the operating conditions considering a T_n close to -1.5 °C in both vial types, and Figure 5.1-1b considering a T_n close to -7 °C.

- For a T_n close to -1.5 °C, the product temperature in high-throughput vials was higher than in serum vials. In general, one should increase the shelf temperature and decrease the chamber pressure when using serum vials (compared to high-throughput vials) to achieve the same product temperature while increasing the sublimation mass flow (optimizing the process design). For example, in Figure 5.1-1a, the product temperature is the same (-36 °C) when using high-throughput vials at a chamber pressure of 10 Pa and shelf temperature of -30 °C or serum vials at a shelf temperature of +20 °C and a chamber pressure of 5 Pa (black square in Figure 5.1-1a).
- For a T_n close to -7 °C, variations between container types in the mass transfer resistance (R_P) and the heat transfer coefficients (K_V) counterbalanced, and product temperatures were similar. Regardless, Figure 5.1-1b suggests that increasing the shelf temperature and decreasing the chamber pressure when using serum vials is convenient to increase the sublimation mass flow to optimize the process. As an example, in Figure 5.1-1b, the product temperature is the same (-36 °C) when using high-throughput vials at a chamber pressure of 10 Pa and shelf temperature of -30 °C or serum vials at a shelf temperature of -10 °C and a chamber pressure of 5 Pa (black square in Figure 5.1-1b).

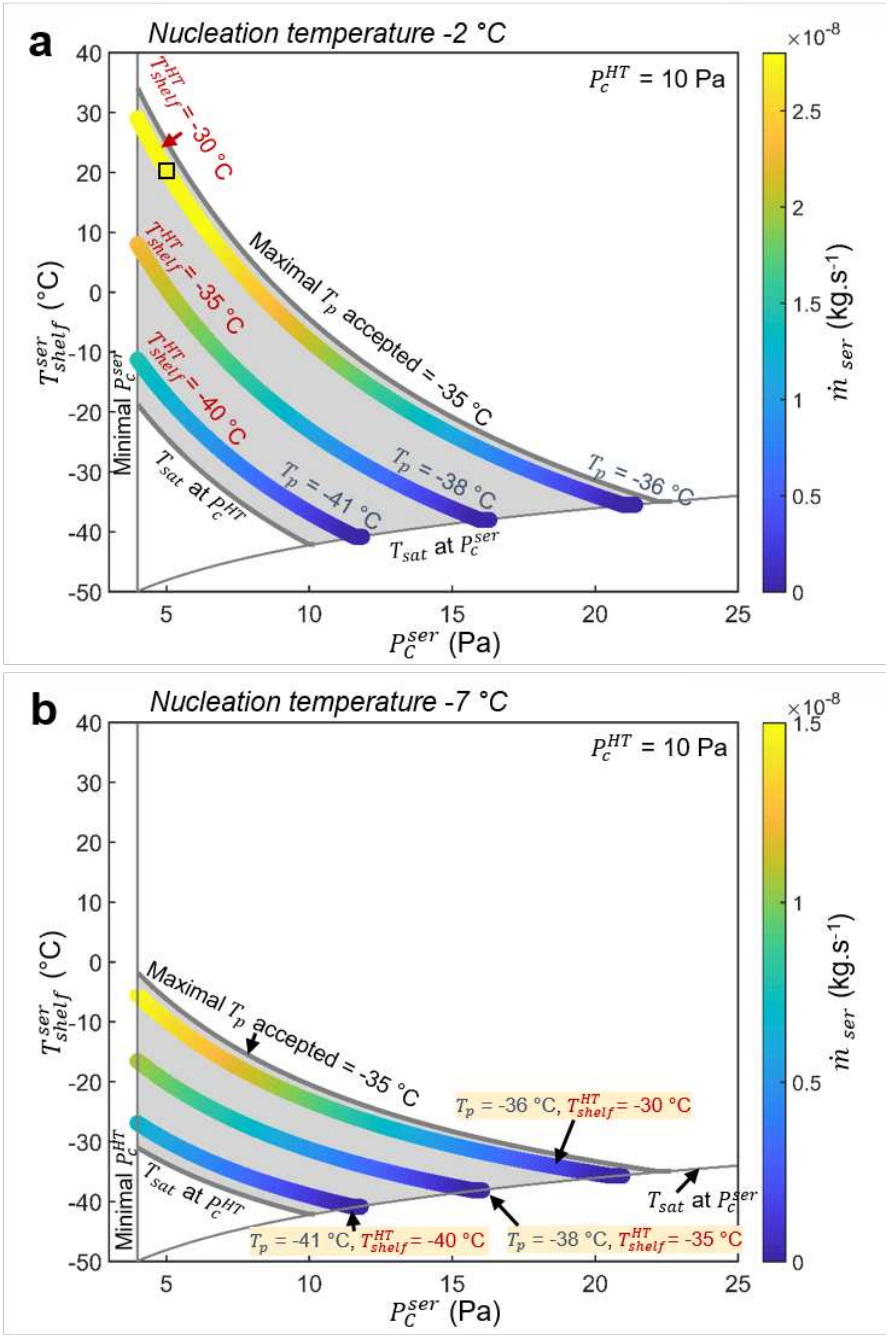

Figure 5.1-1 – Primary drying design spaces of a 5% sucrose solution calculated for high-throughput to serum vials, with a nucleation temperature of approximately (a) -1.5 °C, and (b) -7 °C. P_C^{HT} and T_{shelf}^{HT} are the chamber pressure and shelf temperature during primary drying performed with high-throughput vials, respectively. P_C^{ser}, T_{shelf}^{ser}, and $\dot{m}_{ser}$ are the chamber pressure, shelf temperature and sublimation mass flow rate during primary drying performed with serum vials, respectively. T_{sat} is the ice-vapour equilibrium temperature. T_p is the product temperature, and the maximal T_p allowed for this product was -35 °C. The grey areas represent the safe zone of the process where T_p is lower than -35 °C. Linear colour maps represent iso-T_p curves. Calculations were performed considering the global heat transfer coefficient between the shelf and the vial bottom for 1000-µL vials in B-type well plates.

Regardless of T_n, formulations that did not collapse in high-throughput vials should not collapse when using serum vials under the same operating conditions, but the primary drying times may be unnecessarily long. Results and conclusions considering A-type well plates or 500-µL high-throughput vials (maximal l_d of 11 mm) were similar to those of 1000-µL in a B-types well plate (data not shown). It is to note that conclusions may change in the case of using different filling depths in one of the vial types, since R_P could drastically vary. However, the approach presented in this work remains valid and useful to translate the operating conditions.

5.1.4. Take-Home Message

The use of high-throughput vials to accelerate the development of freeze-dried vaccines requires heat and mass transfer models to translate the results from high-throughput to serum vials. Moreover, in some cases, the opposite translation from serum to high-throughput vials might also be useful. For this thesis, translating the results implied identifying the operating conditions that entail the same product temperature in both container types. A lumped-variable (0D) steady-state model was used for such translation, and the model's results were presented as a graphic tool. The main parameters to build the design space were the heat transfer coefficient between the shelves and the vials (K_V*) and the dried product resistance to mass transfer (*R_P*). The nucleation temperature (*T_n*) was an important factor when translating the operating conditions via its influence on* R_p*. Results suggest that formulations that did not collapse in high-throughput vials should not collapse in serum vials under the same operating conditions. However, the process operation might be suboptimal, leading to excessively long primary drying times.*

5.2. Question 2: Factors Responsible for Product Quality Variations

Different factors could affect the heat and mass transfer during primary drying, altering the product temperature, and ultimately, the product quality. After reviewing the literature (Sections 2.2.2 and 2.3.2), five factors were considered in this work: (i) the variability of the well plate bottom and well surfaces; (ii) the variability of the high-throughput vial bottom geometry; (iii) the position of the vials in the well plate; (iv) the position of the well plate on the shelf; and (v) the variability of the nucleation temperature. The impact of these factors on the heat and mass transfer was evaluated using lumped-variable (0D) and 3D steady-state models. As a reminder, Table 5.2-1 briefly lists the main results of this thesis concerning the variation in the heat and mass transfer during primary drying within high-throughput vials.

Table 5.2-1 – Main results of this thesis concerning the variation in the heat and mass transfer during primary drying within high-throughput vials.

Question 2: What are the main factors responsible for product quality variations during primary drying in high-throughput systems?	
Heat transfer	Variations in the well plate bottom finish and the well surface caused variations in K_V among well plates. (Section 4.1)
	Variations in the high-throughput vial bottom explained variations in K_V among vials in the centre of a well plate. (Section 4.1)
	High-throughput vials at the edge of the well plate (next to a well plate edge) may receive a heat flow up to 25% greater than those in the centre of the well plate (surrounded by other vials). The impact of the vial position in the well plate diminishes as primary drying proceeds and a dried product layer forms. (Section 4.2)
	At the beginning of primary drying, high-throughput vials in a well plate near a chamber wall or door received a heat flow up to 31% greater than those in a well plate in the centre of the shelf. The impact of the well plate position on the shelf may increase up to 42% as primary drying advances and a dried product layer forms. (Section 4.3)
Mass transfer	Variations in the nucleation temperature (from -7 to -1.5 °C, caused by the presence of a nucleating agent) did not affect R_P in high-throughput vials because the differences in the pore diameter and the shape of the sublimation front were counterbalanced. (Section 4.4)

5.2.1. Factors Related to the Heat Transfer

During primary drying, the sublimation front moves through the vial content, increasing the dry product layer thickness and decreasing the frozen product layer thickness. From a modelling perspective, primary drying is a transient phenomenon when the sublimation front moves "slowly" (hours or days) and could be studied as a succession of heat and mass transfer equilibria. Therefore, heat and mass transfer equations were solved in steady-state at different positions of the sublimation front to introduce the notion of time passing. The beginning of primary drying was modelled as vials containing a frozen layer only. In contrast, an advanced point of primary drying was modelled considering a frozen and a dried product layer of a "model" product (5% w/w sucrose aqueous solution).

Two types of well plates were used in this thesis, differing in their surface finish: brilliant black (A-type well plate) and matte black (B-type well plate). At the beginning of primary drying, high-throughput vials in A-type well plates received heat flows close to 13% higher than those in B-type well plates (chamber pressures lower than 12 Pa). 0D modelling suggested that this heat flow variation was due to the conduction through the gas trapped between the shelf and the well plate bottom, the contact conduction between the shelf and the well plate bottom, and the contact conduction between the wells and the vials. A-type well plates presented circular marks on the bottom surface and the internal surface of the well bottoms, while B-type well plate bottoms and well bottoms were mostly flat. The surface reliefs in A-type well plates decreased the heat transfer to the vials compared to B-type well plates. 3D models indicated that as sublimation advances, the heat flow variation between well plate types decreases until close to 7% (chamber pressures lower than 12 Pa, R_P = 1.248×10^5 Pa.s.m^2.kg^{-1}). Regarding the product temperature during primary drying (critical quality parameter), the well plate type could cause a variation in the product temperature between 0.3 and 0.7 °C.

Concerning the high-throughput vials in the centre of a well plate (surrounded by other vials), 3D modelling proved that the heat flow from the wells to the vials occurred mostly by contact conduction. Furthermore, 0D modelling suggested that variations in the contact area of the vial bottoms (affecting contact conduction) were the main factor responsible for heat transfer variations at chamber pressures lower than 12 Pa. As a practical outcome of the variation between central vials, a safety margin of 3 °C is recommended when selecting the operating conditions during primary drying based on the vial-averaged product temperature (considering R_P = 1.248×10^5 Pa.s.m^2.kg^{-1}).

The high-throughput vial position in the well plate affects the heat flow from the chamber wall or door. At the beginning of primary drying, heat flows received by high-throughput vials next to a well plate edge were up to 25% greater than that of vials in the centre of the well plate (surrounded by other vials). As sublimation occurs and a dried product layer forms in the vials (considering R_P = 1.248×10^5 Pa.s.m^2.kg^{-1}), the variation on the heat flow received by different vial positions in a well plate drops to 4%. Furthermore, the product temperature differed by less than 1 °C between vial positions in the well plate.

When selecting the operating conditions during primary drying, the safety margin of 3 °C previously recommended (due to the variations in the vial bottom geometry) seemed to cover any heat transfer variation due to the vial position in the well plate.

Regarding the impact of the well plate position on the shelf at the beginning of primary drying, placing a well plate near the chamber door increased the heat flow received by the vials compared to a well plate in the centre of the shelf, on average by 23% at chamber pressures lower than 12 Pa and shelf temperatures -40 and -15 °C. Meanwhile, placing a well plate near the chamber wall increased the heat flow received by the vials (on average by 19%) at only low shelf temperatures (-40 °C). The higher surface emissivity of the door (0.88) compared to the chamber wall (0.13) increased the heat transfer to the vials and the well plate by radiation, explaining the greater impact of placing a well plate near the chamber door than a wall. When primary drying advances and the dried product layer imposes a mass transfer resistance (considering R_P = 1.248×10^5 Pa.s.m^2.kg^{-1}), the vials in well plates near the chamber door could receive a heat flow up to 42% greater than those in a well plate in the centre of the shelf. Therefore, the impact of the heat flow from the chamber door could increase throughout primary drying. 3D mathematical modelling indicated that the heat flow from the chamber door becomes relatively more important as the dried product layer resistance increases, explaining the greater variation between well plate positions compared to the beginning of primary drying. This variation of the relative importance of the heat flows from the chamber could not be predicted by traditional 0D models (e.g. Pikal, 2000; Scutellà et al., 2017a; Velardi and Barresi, 2008), and a safety margin for the product temperature of 2 °C is recommended when using such simplified models. Overall, placing a well plate near the chamber door increased the product temperature by 1 to 2 °C compared to a well plate in the centre of the shelf. The impact of the chamber wall remained lower than that of the chamber door as sublimation advanced; the increase in the product temperature was close to 1 °C.

5.2.2. Factors Related to the Mass Transfer

The mass transfer from the sublimation front to the condenser is mainly determined by the transfer through the dried product layer in the vials. Furthermore, variations in the dried product layer could entail mass transfer variations that ultimately affect the product temperature among the vials. According to the literature, the nucleation temperature (T_n) is commonly highlighted as a key indicator of the mass transfer variations between vials (Section 2.3.2.2), affecting the ice crystal size, the pore size, and eventually the dried product resistance to mass transfer (R_P). Nucleation is a stochastic process; therefore the T_n value varies from vial to vial. A "model" product (5% w/w sucrose aqueous solution) was considered in this work, and the average T_n was artifitially modifided in some cases by adding a nucleating agent in a small concentration (0.1% w/w). Adding the nucleating agent increased T_n from close to -7 °C to -1.5 °C, and the pore diameter increased on average from 88 to 195 µm. Commonly, an increase of the pore diameter should be associated with a lower R_P value, but this was not the case in high-throughput vials, as R_P values were similar regardless of the pore diameter. R_P is an area-normalized resistance defined for the vial inner cross-sectional area (A_{in}), assuming this is the mass transfer area. This assumption was utterly false when pores were smaller (T_n close to -7 °C), as suggested by curved sublimation fronts observed at intermediate points of primary drying. Instead, when pores were greater (T_n close to -1.5 °C), sublimation fronts were flat. The curved sublimation fronts when pores were smaller tended to increase the mass transfer area, improved the mass transfer and counterbalanced the effect of smaller pore size on R_P. Therefore, in the case of our "model" product, the impact of T_n variations between vials could be neglected due to two opposite phenomena (i.e. the pore size's effect vs the mass transfer area's effect).

5.2.3. Take-Home Message

Variations in the heat transfer between high-throughput vials could affect the product temperature and quality. Safety margins for the product temperature are useful to design primary drying based on the average values temperature values. In this vein, a safety margin of 3 °C is suggested to account for the heat transfer variations between high-throughput vials in a well plate. Comparing well plates, a safety margin of 0.7 °C is recommended when using *different well plate types, of 2 °C when placing a well plate near the chamber door, and of 1 °C when placing well plate near the chamber wall at low shelf temperatures (-40 °C). Variations in the nucleation temperature did not affect the mass transfer in high-throughput vials filled with a 5% w/w sucrose solution due to mutually compensating effects.*

5.3. Perspectives

5.3.1. Short Term

5.3.1.1. Heat and Mass Transfer Modelling of the Primary Drying in High-Throughput Vials Containing Different Formulations in the Same Well Plate

A 0D transient-state model was developed to predict the product temperature of different high-throughput vials containing different products and situated on the same well plate. Overall, this model is a variation of the 0D steady-state model of Section 4.1.3, additionally including thermal energy accumulation in the vials and well plate. In the 0D transient-state model, each vial has assigned a specific relationship between the dried product layer thickness (l_d) and the dried product resistance to mass transfer (R_P). Even if this model has been developed, it requires obtaining further experimental data to: (i) adjust the function relating l_d with R_P for other formulations (besides a 5% sucrose solution, as presented in Section 4.4.3), and (ii) compare the predicted product temperatures with experimental data (analogous to Section 4.4.3).

5.3.1.2. Use of Cryo-Microscopy to Determine the Water Vapour Diffusion Coefficient Through the Dried Product Layer

When developing a freeze-dried vaccine, certain R_P values could be preferred to avoid high product temperatures during primary drying. However, determining R_P could take days. Theoretically, R_P could be mathematically related to the water vapour diffusion coefficient ($\overline{D}_{H20}^{Kn}$) through the dried product layer (Section 2.3.1.1), which could be determined within hours. An internship project was carried out during the PhD programme aiming at evaluating the relation between $\overline{D}_{H20}^{Kn}$ and R_P, in view of using $\overline{D}_{H20}^{Kn}$ as a selection criterion for candidate vaccine formulations. $\overline{D}_{H20}^{Kn}$was determined by freeze-drying microscopy for five model products (i.e. sucrose and mannitol aqueous solutions with different concentrations), and compared to R_P values taken from the literature. R_P and $1/\overline{D}_{H20}^{Kn}$ values were directly proportional for small l_d values (less than 0.5 mm). For greater l_d values, other factors (provably canalisations among pores, pore shape, connectivity) affected the direct proportionality of R_P and $\overline{D}_{H20}^{Kn}$. Thus, while $\overline{D}_{H20}^{Kn}$ could be an indicator of R_P, it does not replace the need of determining R_P to build mathematical models capable of predicting the product temperature by the end of primary drying (l_d greater than 0.5 mm). To confirm these observations, more $\overline{D}_{H20}^{Kn}$ and R_P data should be collected.

5.3.1.3. Develop of a User-Friendly Software Interface to Build the Graphic Tool for Translating the Operating Conditions between Container Types

Building the graphic tool for translating the operating conditions between container types requires coding skills to solve the heat and mass transfer equations and plot the figure (e.g. Figure 5.1-1). A user-friendly software interface shall be developed to simplify the task for future researchers.

5.3.2. Long Term

5.3.2.1. Compare the Mass Transfer in High-Throughput and Serum Vials Using Other Model Products

The results obtained in this thesis refer to a particular "model" product (5% w/w sucrose aqueous solution). However, other model products should be studied to confirm the results and conclusions of this thesis. For example, using other sucrose concentrations, sugars that present different R_P values (e.g. maltodextrin), or sugars that create crystalline product matrixes (e.g. mannitol).

5.3.2.2. Develop a 2D Transient Model of the Heat and Mass Transfer in High-Throughput Vials

The shape of the sublimation front proved to be extremely important to model the mass transfer in high-throughput vials, considerably affecting R_P. Therefore, developing a 2D (or 3D) transient model of the heat and mass transfer in high-throughput vials could help understand why the sublimation front could be curved or flat depending on the dried product structure, ultimately contributing to a better translation of the operating conditions between vial types. Such model could integrate the actual pore size, shape and connectivity. Other modelling techniques based on particle motion rather than continuous equations could be investigated for this purpose.

5.3.2.3. Study the Secondary Drying in High-Throughput Vials

This thesis focused on the primary drying step of freeze-drying (ice sublimation). Similarly, it would be useful to translate the operating conditions between high-throughput and serum vials during secondary drying (water desorption).

This thesis contributes to a faster vaccine development using high-throughput systems. However, this research is only a modest step towards using high-throughput vials, compared to the huge body of literature devoted to serum vials.

Scientific progress requires a constant revaluation of the established technology. This thesis is an open invitation to question the established freeze-drying techniques and consider new containers.

Ultimately, by accelerating the development of freeze-dried pharmaceuticals, this work aims at improving our current health care systems and everyone's wellbeing.

6. Résumé en Français

Contexte

Les maladies infectieuses sont causées par des organismes appelés « agents pathogènes » (par exemple, certains virus ou bactéries). Lorsqu'un agent pathogène rentre dans l'organisme d'un sujet, son système immunitaire produit des molécules appelées « anticorps » qui reconnaissent l'agent pathogène et tentent de le neutraliser. Les vaccins vivants-atténués contiennent des agents pathogènes affaiblis ou inactivés capables de déclencher la production d'anticorps sans provoquer de maladie. De cette manière, ces vaccins préparent le système immunitaire d'un sujet vacciné contre une future exposition à l'agent pathogène. La partie de l'agent pathogène inactivé qui provoque la formation d'anticorps est « l'antigène ». Pour que la vaccination soit efficace, la capacité thérapeutique de l'antigène doit être préservée pendant le stockage et le transport du vaccin ; à cette fin, de nombreux vaccins vivants-atténués sur le marché nécessitent une étape de séchage pour préserver l'antigène.

La lyophilisation est le procédé de séchage le plus couramment utilisé pour les vaccins. Pendant la lyophilisation, les températures des vaccins sont particulièrement basses (inférieures à 0°C), ce qui est essentiel pour ne pas dégrader l'antigène. Le processus de lyophilisation se compose de trois étapes, qui sont : (i) la congélation, au cours de laquelle plus de 80 % de l'eau est transformée en cristaux de glace et le reste de l'eau reste chimiquement lié au produit ; (ii) le séchage primaire, au cours duquel les cristaux de glace sont éliminés par sublimation ; et (iii) le séchage secondaire, au cours duquel la majeure partie de l'eau chimiquement liée au produit est éliminée par désorption. En raison des étapes de congélation et de séchage, l'antigène peut être endommagé de manière irréversible lors de la lyophilisation, c'est pourquoi les vaccins contiennent d'autres ingrédients pour protéger l'antigène.

Pour caractériser la qualité d'un vaccin lyophilisé, trois attributs sont généralement pris en compte : (i) l'activité biologique, (ii) la teneur en eau finale, et (iii) l'apparence. L'activité biologique du produit fait référence à la conservation de l'intégrité de la composition du produit, de sorte que le vaccin continue à remplir son rôle biologique après la lyophilisation. La teneur en eau finale du produit doit être suffisamment réduite pour stabiliser l'antigène pendant le stockage et le transport. L'apparence du produit sec final fait référence à l'état de surface général et à la forme du produit lors d'une inspection visuelle, et c'est peut-être l'attribut de qualité qui implique les normes les plus subjectives. Le produit final sec doit avoir un aspect extérieur « lisse » et présenter des pores intérieurs; le contraire d'un produit « effondré ». Lorsque le produit s'effondre, il peut y avoir des parties qui n'ont pas séché correctement, ce qui peut entraîner une détérioration de l'antigène pendant le stockage et le transport. De plus, un produit effondré est plus difficile à dissoudre avant l'injection, ce qui peut affecter le dosage du patient. En pratique, l'apparence est donc un critère de routine essentiel pour l'évaluation de la qualité des vaccins lyophilisés.

La température du produit doit rester inférieure à la température d'effondrement pendant le séchage primaire pour obtenir un produit sec conforme. Cependant, un lyophilisateur ne peut pas régler directement la température du produit. Les lyophilisateurs disposent d'une chambre de séchage avec des étagères où sont placés les récipients contenant le produit pendant tout le processus de lyophilisation. Un lyophilisateur

peut contrôler deux conditions opératoires: (i) la température des étagères, et (ii) la pression à l'intérieur de la chambre de séchage. La température du produit dépend des phénomènes de transfert de chaleur et de matière qui se produisent simultanément. Pendant le séchage primaire, la majeure partie du flux de chaleur va des étagères aux flacons, et le transfert de matière le plus critique est celui de la vapeur d'eau s'échappant du front de sublimation vers l'intérieur de la chambre de séchage à travers la couche de produit sec. La compréhension des phénomènes de transfert de chaleur et de matière est la clé pour contrôler la température du produit à travers des conditions opératoires afin d'obtenir un produit sec élégant.

Une proposition d'amélioration pour le développement de vaccins

La température à laquelle le produit s'effondre (température d'effondrement) varie selon les formulations. Par conséquent, lors de la mise au point d'un vaccin lyophilisé, il est primordial de choisir une formulation qui a le plus de chances de produire un produit sec élégant (non effondré). La sélection d'une telle formulation nécessite l'analyse de plusieurs formulations potentielles de vaccins pendant la lyophilisation. Les récipients les plus courants pour l'analyse sont des flacons tubulaires d'un volume généralement supérieur à 3 mL, appelés « flacons à sérum ». Ces flacons sont les mêmes conteneurs que ceux utilisés pour la production de vaccins, et constituent le conteneur final pour le stockage et le transport. La sélection d'une formulation de vaccin qui protège l'antigène et ne s'effondre pas au cours du séchage implique de nombreux tests de lyophilisation et constitue une tâche laborieuse et longue. Afin de tester les formulations plus rapidement, l'utilisation de plaques d'aluminium à 96 puits contenant de petits flacons tubulaires (moins de 1 mL), appelés flacons « à haut débit », a récemment été proposée.

D'une part, les petits flacons à haut débit permettent de placer plus de récipients à l'intérieur du lyophilisateur (l'équipement utilisé pour la lyophilisation), par rapport aux grands flacons à sérum. Par conséquent, les flacons à haut débit réduisent le nombre de cycles de lyophilisation nécessaires pour analyser les formulations candidates. De plus, la disposition en 96 puits est compatible avec la plupart des robots utilisés pour préparer et doser les solutions à cribler, ce qui simplifie la préparation des échantillons et réduit les erreurs de manipulation.

D'autre part, l'utilisation de flacons à haut débit entraîne des difficultés pour interpréter les résultats et les transposer à l'échelle des flacons à sérum. Les flux de chaleur et de matière dépendent (entre autres facteurs) de la géométrie des récipients. Par conséquent, le transfert de chaleur et de matière ne sera pas le même si l'on utilise des flacons à haut débit ou des flacons à sérum, de sorte que la température du produit peut également varier. En pratique, cela signifie que, pour une condition opératoire donnée, l'aspect du produit obtenu avec les flacons à haut débit peut être différent de l'aspect du produit obtenu avec les flacons à sérum. Pour obtenir les mêmes températures de produit lors du séchage primaire dans les flacons à haut débit et les flacons à sérum, il faudrait modifier les conditions opératoires, ce que l'on appellera la « traduction » des conditions opératoires.

En raison de l'utilisation limitée des flacons à haut débit dans le passé, il n'y a pas de recherche précédente publiée avec ces flacons sur les facteurs possibles affectant le transfert de chaleur et de matière pendant le séchage primaire, causant des hétérogénéités entre les flacons. Ces facteurs doivent être pris en compte lors de l'acceptation ou du rejet d'une formulation, afin de ne pas biaiser la prise de décision.

Objectifs de la thèse

L'objectif de ce travail était de mettre en valeur les résultats obtenus avec des flacons à haut débit.

Tout d'abord, la traduction des conditions opératoires a été étudiée pour pouvoir obtenir les mêmes résultats avec des flacons à haut débit et des flacons à sérum. La première question scientifique était donc: « comment identifier les conditions opératoires impliquant la même température du produit lors du séchage primaire dans les flacons à haut débit et dans les flacons à sérum ? ».

Ensuite, l'accent a été mis sur les variations du transfert de chaleur et de matière entre les flacons à haut débit, car ces variations peuvent biaiser la sélection des formulations. C'est pourquoi la deuxième question scientifique était: « quels sont les principaux facteurs responsables des variations de la qualité du produit lors du séchage primaire en flacons à haut débit ? ».

Principaux résultats

Comment identifier les conditions opératoires impliquant la même température du produit lors du séchage primaire dans les flacons à haut débit et dans les flacons à sérum ?

Pendant le séchage primaire, le coefficient de transfert de chaleur effectif entre les étagères et le flacon (K_V) est généralement utilisé pour modéliser le transfert de chaleur, et le transfert de matière est modélisé en fonction de la résistance imposée par la couche de produit sec (R_P).

En ce qui concerne le transfert de chaleur, pour les deux types de récipients (c'est-à-dire les flacons à haut débit et les flacons à sérum), les valeurs de K_V dépendaient de la pression de la chambre (étudiée ici entre 4 et 65 Pa). Dans le cas des flacons à sérum, la dépendance de K_V par rapport à la pression était due à la variation du transfert de chaleur par conduction à travers le gaz piégé entre l'étagère et le flacon. Dans le cas des flacons à haut débit, la dépendance de K_V avec la pression était due au gaz piégé entre l'étagère et la plaque. En comparant les types de récipients, les valeurs de K_V étaient presque 3 fois plus élevées dans les flacons à haut débit que dans les flacons à sérum à des pressions de chambre inférieures à 12 Pa (plage de pression utilisée dans l'industrie pharmaceutique). La chaleur des étagères a été transférée plus efficacement aux flacons à haut débit qu'aux flacons à sérum car le coefficient de transfert de chaleur de l'étagère aux plaques (K_{WP}) et des plaques aux flacons à haut débit (K_{HV}) était très élevé (plus de 2 et 9 fois supérieur au K_V pour les flacons à sérum, respectivement). Les principaux mécanismes de transfert de chaleur étaient la conduction par le gaz piégé entre l'étagère et le fond de la plaque (plus de 60% de K_{WP}) et la conduction par contact entre les puits et les flacons (plus de 70% de K_{HV}). Du point de vue du transfert

de chaleur, on s'attend à ce que les flacons à haut débit aient des températures de produit plus élevées que les flacons à sérum en raison de leurs valeurs K_V plus élevées (toutes conditions égales par ailleurs).

En ce qui concerne le transfert de matière, il faut noter que R_P est défini en fonction de la surface de la section transversale du flacon (A_{in}), en supposant qu'il s'agit de l'aire de transfert de matière. Cependant, cette hypothèse concernant l'aire de transfert de matière peut ne pas être vraie pour tous les types de récipients. De plus, R_P augmente lorsque les pores sont plus petits ou moins connectés. Par conséquent, R_P dépend de la valeur réelle de l'aire de transfert de matière et de la géométrie des pores dans la couche de produit sec (par exemple, la taille et la forme des pores, leur connectivité). Pour les deux types de récipients, les valeurs R_P ont augmenté au fur et à mesure que la sublimation progressait et que l'épaisseur de la couche de produit sec augmentait. La température de nucléation (T_n) a joué un rôle clé dans la comparaison des valeurs R_P pour les différents types de contenants. À faible T_n (environ -7 °C, obtenue sans ajout d'agent nucléant), les deux types de récipients avaient des diamètres de pores similaires (environ 92 mm), mais le front de sublimation était incurvé dans les flacons à haut débit et plat dans les flacons à sérum. Le front de sublimation incurvé dans les flacons à haut débit a généralement amélioré le transfert de matière, de sorte que R_P apparent était plus faible que dans les flacons à sérum. Lorsque T_n était proche de -1.5 °C (avec ajout d'agent nucléant), le diamètre des pores était plus petit dans les flacons à haut débit (195 mm) que dans les flacons à sérum (310 mm). Cependant, les valeurs de R_P étaient similaires dans les deux types de récipients, car la connectivité des pores était moins bonne dans les flacons à sérum, comme l'indiquent les pics aigus observés au niveau du front de sublimation.

En ce qui concerne le transfert couplé de chaleur et de matière, cette thèse présente un outil graphique qui intègre la solution des équations de transfert pendant le séchage primaire dans des flacons à haut débit et des flacons à sérum, permettant la traduction des conditions opératoires. En considérant une solution aqueuse de saccharose à 5% comme le produit « modèle », les résultats de la traduction des conditions opératoires dépendent de T_n. Lorsque T_n est proche de -1.5 °C, la température du produit dans les flacons à haut débit était plus élevée que dans les flacons à sérum. Dans ce cas, nous devrions augmenter la température de l'étagère et diminuer la pression de la chambre lorsque nous utilisons des flacons à sérum (par rapport aux flacons à haut débit) pour obtenir la même température de produit et augmenter le flux massique de sublimation (optimisation du procédé). Lorsque T_n est proche de -7 °C, les variations de R_P et de K_V entre les deux dypes de flacons se sont compensées mutuellement, et les températures des produits étaient similaires. Indépendamment de T_n, les formulations qui ne se sont pas effondrées dans les flacons à haut débit ne devraient pas s'effondrer lorsqu'on utilise des flacons à sérum dans les mêmes conditions opératoires mais le procédé pourrait être fortement sous-optimal, avec des temps de dessication primaire inutilement longs.

Quels sont les principaux facteurs responsables des variations de la qualité des produits lors du séchage primaire des flacons à haut débit ?

Sur la base des facteurs étudiés dans les flacons à sérum, cette thèse s'est focalisée sur l'impact sur le transfert de chaleur et de matière : (i) des variations des surfaces des plaques, (ii) des variations des surfaces des flacons, (iii) de la position des flacons sur la plaque, (iv) de la position de la plaque sur l'étagère, et (v) de la variation de la température de nucléation. Au fur et à mesure que le séchage primaire avance, le front de sublimation se déplace à travers le contenu du flacon, augmentant l'épaisseur de la couche de produit sec et diminuant l'épaisseur de la couche de produit congelé. Le début du séchage primaire a été modélisé comme des flacons contenant une couche gelée (uniquement). En revanche, un point avancé de séchage primaire a été modélisé en considérant une couche congelée et une couche sèche d'un produit « modèle » (solution aqueuse de saccharose à 5%) dans les flacons.

Deux types de plaques ont été utilisés pour maintenir les flacons à haut débit, différant par leur finition de surface : noir brillant (plaque type A) ou noir mat (plaque type B). Au début du séchage primaire, les flacons à haut débit sur les plaques de type A ont reçu des flux de chaleur environ 13 % plus élevés que ceux sur les plaques de type B (à des pressions de chambre inférieures à 12 Pa). Les plaques de type A présentaient des marques circulaires sur la surface du fond et sur la surface intérieure des fonds de puits, alors que dans les plaques de type B, les fonds de plaques et les fonds de puits étaient pratiquement plats. Les reliefs de surface des plaques de type A ont diminué le transfert de chaleur vers les flacons par rapport aux plaques de type B. La modélisation à variables concentrées (0D) a suggéré que cette variation était due à la conduction par le gaz piégé entre l'étagère et le fond de la plaque, à la conduction par contact entre l'étagère et le fond de la plaque, et à la conduction par contact entre les puits et les flacons. Les modèles 3D ont indiqué que, au fur et à mesure que la sublimation progresse, la variation du flux thermique entre les types de plaques diminue pour atteindre près de 7 % (pressions de la chambre inférieures à 12 Pa, en considérant une épaisseur de couche de produit sec de 5 mm). En ce qui concerne la température du produit pendant le séchage primaire (paramètre de qualité critique), le type de plaque peut entraîner une variation de la température du produit entre 0,3 et 0,7 °C.

Pour les flacons à haut débit situés au centre d'une plaque (entourés d'autres flacons), la modélisation 3D a montré que le flux de chaleur des puits vers les flacons se faisait principalement à travers de la conduction par contact. De plus, la modélisation 0D a suggéré que les variations de la surface de contact des fonds de flacons (affectant la conduction de contact) était le principal facteur responsable de la variation du transfert de chaleur entre flacons à des pressions de chambre inférieures à 12 Pa. En raison de la variation constatée entre les flacons centraux, une marge de sécurité de 3 °C est recommandée lors de la sélection des conditions opératoires pendant le séchage primaire sur la base de la température moyenne du produit entre tous les flacons.

La position des flacons à haut débit sur la plaque affecte le flux de chaleur provenant de la paroi ou de la porte de la chambre. Au début du séchage primaire, les flux de chaleur reçus par les flacons à haut

débit situés près d'un bord de la plaque étaient jusqu'à 25 % plus élevés que ceux des flacons situés au centre de la plaque (entourés d'autres flacons). Au fur et à mesure que la sublimation se produit et qu'une couche de produit sec se forme sur les flacons, la différence de flux thermique reçu par les différentes positions des flacons sur une plaque diminue jusqu'à 4%, et la température du produit diffère de moins de 1 °C. Lors du choix des conditions opératoires pendant le séchage primaire, la marge de sécurité de 3 °C recommandée ci-dessus (en raison des variations de la géométrie du fond du flacon) semble couvrir toute variation du transfert de chaleur due à la position du flacon sur la plaque.

En ce qui concerne l'impact de la position de la plaque sur l'étagère au début du séchage primaire, le fait de placer une plaque près de la porte de la chambre a augmenté le flux de chaleur reçu par les flacons par rapport à une plaque au centre de l'étagère (en moyenne) de 23 % pour des pressions de chambre inférieures à 12 Pa et des températures d'étagère de -40 et -15 °C. En revanche, le fait de placer une plaque près de la paroi de la chambre a augmenté le flux de chaleur reçu par les flacons (en moyenne de 19 %) uniquement aux basses températures d'étagère (-40 °C). L'émissivité plus élevée de la surface de la porte (0,88) par rapport à la paroi de la chambre (0,13) a augmenté le transfert de chaleur vers les flacons et la plaque par rayonnement, ce qui explique l'impact plus important du placement d'une plaque près de la porte de la chambre que près de la paroi. Lorsque le séchage primaire progresse et que la couche de produit sec impose une résistance au transfert de matière, les flacons placés dans des plaques près de la porte de la chambre pourraient recevoir jusqu'à 42 % de flux thermique en plus par rapport à ceux placés sur une plaque au centre de l'étagère. Par conséquent, l'impact du flux thermique provenant de la porte de la chambre pourrait augmenter tout au long du séchage primaire. Dans l'ensemble, le fait de placer une plaque près de la porte de la chambre a augmenté la température du produit de 1 à 2 °C par rapport à une plaque placée au centre de l'étagère. L'impact de la paroi de la chambre a augmenté la température du produit d'environ 1 °C.

En considérant un produit modèle (solution aqueuse de saccharose à 5%), l'ajout de l'agent de nucléation a augmenté la T_n d'environ -7 °C à -1.5 °C, et le diamètre des pores a augmenté en moyenne de 88 à 195 µm. En général, une augmentation du diamètre des pores devrait être associée à une valeur R_P plus faible, mais ce n'était pas le cas dans les flacons à haut débit, car les valeurs R_P étaient similaires quel que soit le diamètre des pores. R_P est une résistance normalisée en fonction de la surface de la section transversale interne du flacon (A_{in}), en supposant qu'il s'agit de l'aire de transfert de matière. Cette hypothèse était fausse lorsque les pores étaient plus petits (T_n proche de -7 °C), comme le suggèrent les fronts de sublimation incurvés observés aux points intermédiaires du séchage primaire. En revanche, lorsque les pores étaient plus grands (T_n proche de -1.5 °C), les fronts de sublimation étaient plats. Les fronts de sublimation incurvés lorsque les pores sont plus petits ont eu tendance à augmenter l'aire de transfert de matière, améliorant le transfert de matière et contrebalançant l'effet de la plus petite taille des pores sur R_P. Par conséquent, dans le cas de notre produit « modèle », l'impact des variations de T_n entre les flacons est apparu négligeable en raison de la compensation entre deux phénomènes opposés.

Perspectives

À court terme, il serait intéressant d'étudier l'effet de placer des flacons avec des formulations différentes sur la même plaque. De plus, il serait utile de développer de nouvelles techniques pour prédire plus rapidement la valeur de R_P, par exemple par cryomicroscopie. En même temps, le développement d'une interface interactive permettant d'obtenir facilement les outils graphiques pour traduire les conditions opératoires serait un moyen d'intégrer cette approche dans la pratique quotidienne des chercheurs.

À long terme, le transfert de chaleur et de matière dans les flacons à haut débit devrait être étudié avec autres « produits modèles » (par exemple, mannitol, tréhalose). Pour mieux comprendre l'effet de l'aire de transfert de matière, il faudrait réaliser un modèle 2D (ou 3D) qui tienne compte du déplacement du front de sublimation et de l'évolution de sa forme en fonction du transfert de chaleur latéral. Etudier l'écoulement du gaz en régime moléculaire dans des pores de forme irrégulière permettrait de mieux comprendre l'effet de leur taille, forme et connectivité. Finalement, il serait important d'étudier le séchage secondaire (désorption) dans des flacons à haut débit pour comprendre l'ensemble du processus de lyophilisation.

7. References

33 World Health Assembly, 1980. Thirty-third World Health Assembly, Geneva, 5-23 May 1980: resolutions and decisions, annexes.

Abdelwahed, W., Degobert, G., Fessi, H., 2006. Freeze-drying of nanocapsules: Impact of annealing on the drying process. International Journal of Pharmaceutics, Selected papers from the 15th International Microencapsulation Symposium 324, 74–82. https://doi.org/10.1016/j.ijpharm.2006.06.047

Adams, G., 2007. The Principles of Freeze-Drying, in: Day, J.G., Stacey, G.N. (Eds.), Cryopreservation and Freeze-Drying Protocols, Methods in Molecular Biology™. Humana Press, Totowa, NJ, pp. 15–38. https://doi.org/10.1007/978-1-59745-362-2_2

Adams, G.D.J., Irons, L.I., 1993. Some implications of structural collapse during freeze-drying using Erwinia caratovoraL-asparaginase as a model. Journal of Chemical Technology & Biotechnology 58, 71–76. https://doi.org/10.1002/jctb.280580110

Akers, M.J., 2016. Sterile Drug Products: Formulation, Packaging, Manufacturing and Quality. CRC Press.

Alexeenko, A.A., Ganguly, A., Nail, S.L., 2009. Computational Analysis of Fluid Dynamics in Pharmaceutical Freeze-Drying. Journal of Pharmaceutical Sciences 98, 3483–3494. https://doi.org/10.1002/jps.21862

Amorij, J.-P., Meulenaar, J., Hinrichs, W.L.J., Stegmann, T., Huckriede, A., Coenen, F., Frijlink, H.W., 2007. Rational design of an influenza subunit vaccine powder with sugar glass technology: Preventing conformational changes of haemagglutinin during freezing and freeze-drying. Vaccine 25, 6447–6457. https://doi.org/10.1016/j.vaccine.2007.06.054

Arsiccio, A., Barresi, A., De Beer, T., Oddone, I., Van Bockstal, P.-J., Pisano, R., 2018. Vacuum Induced Surface Freezing as an effective method for improved inter- and intra-vial product homogeneity. European Journal of Pharmaceutics and Biopharmaceutics 128, 210–219. https://doi.org/10.1016/j.ejpb.2018.04.002

Assegehegn, G., Brito-de la Fuente, E., Franco, J.M., Gallegos, C., 2019. The Importance of Understanding the Freezing Step and Its Impact on Freeze-Drying Process Performance. Journal of Pharmaceutical Sciences 108, 1378–1395. https://doi.org/10.1016/j.xphs.2018.11.039

Awotwe-Otoo, D., Khan, M.A., 2015. Lyophilization of Biologics: An FDA Perspective, in: Varshney, D., Singh, M. (Eds.), Lyophilized Biologics and Vaccines: Modality-Based Approaches. Springer, New York, NY, pp. 341–359. https://doi.org/10.1007/978-1-4939-2383-0_15

Barley, J., 2009. Freeze Drying / Lyophilization Information: Basic Principles [WWW Document]. URL https://www.spscientific.com/freeze-drying-lyophilization-basics/ (accessed 12.17.20).

Barresi, A.A., Ghio, S., Fissore, D., Pisano, R., 2009. Freeze Drying of Pharmaceutical Excipients Close to Collapse Temperature: Influence of the Process Conditions on Process Time and Product Quality. Drying Technology 27, 805–816. https://doi.org/10.1080/07373930902901646

Berny, J.-F., Hennebert, G.L., 1991. Viability and Stability of Yeast Cells and Filamentous Fungus Spores During Freeze-Drying: Effects of Protectants and Cooling Rates. Mycologia 83, 805–815. https://doi.org/10.1080/00275514.1991.12026086

Bosca, S., Barresi, A.A., Fissore, D., 2013. Use of a soft sensor for the fast estimation of dried cake resistance during a freeze-drying cycle. International Journal of Pharmaceutics 451, 23–33. https://doi.org/10.1016/j.ijpharm.2013.04.046

Bourlés, E., de Lannoy, G., Scutellà, B., Fonseca, F., Tréléa, I.C., Passot, S., 2019. Scale-Up of Freeze-Drying Cycles, the Use of Process Analytical Technology (PAT), and Statistical Analysis: New Technologies and Approaches, in: Methods in Pharmacology and Toxicology. pp. 215–240. https://doi.org/10.1007/978-1-4939-8928-7_10

Boylston, A., 2013. The origins of vaccination: myths and reality. J R Soc Med 106, 351–354. https://doi.org/10.1177/0141076813499292

Brülls, M., Rasmuson, A., 2002. Heat transfer in vial lyophilization. Internation journal of pharmaceutics 246, 1–16.

Buceta, J.P., Tréléa, I.C., Scutellà, B., Bourlés, E., Fonseca, F., Passot, S., 2021. Heat transfer during freeze-drying using a high-throughput vial system in view of process scale-up to serum vials. Journal of Pharmaceutical Sciences. https://doi.org/10.1016/j.xphs.2020.11.029

Cannon, A., Shemeley, K., 2004. Statistical Evaluation of Vial Design Features That Influence Sublimation Rates During Primary Drying. Pharmaceutical Research volume 21.

Carrigy, N.B., Pant, L.M., Mitra, S., Secanell, M., 2012. Knudsen Diffusivity and Permeability of PEMFC Microporous Coated Gas Diffusion Layers for Different Polytetrafluoroethylene Loadings. J. Electrochem. Soc. 160, F81. https://doi.org/10.1149/2.036302jes

Chouvenc, P., Vessot, S., Andrieu, J., Vacus, P., 2004. Optimization of the Freeze-Drying Cycle: A New Model for Pressure Rise Analysis. Drying Technology - DRY TECHNOL 22, 1577–1601. https://doi.org/10.1081/DRT-200025605

Christensen, D., Foged, C., Rosenkrands, I., Nielsen, H.M., Andersen, P., Agger, E.M., 2007. Trehalose preserves DDA/TDB liposomes and their adjuvant effect during freeze-drying. Biochimica et Biophysica Acta (BBA) - Biomembranes 1768, 2120–2129. https://doi.org/10.1016/j.bbamem.2007.05.009

Corning® 96-well UV-Transparent Microplates | 96 Well Microplates | Assay Microplates | Microplates | Life Sciences EU Other Consumer Site | Corning [WWW Document], n.d. URL https://ecatalog.corning.com/life-sciences/b2c/EUOther/en/Microplates/Assay-Microplates/96-Well-Microplates/Corning%C2%AE-96-well-UV-Transparent-Microplates/p/corning96WellUVMicroplates?clear=true (accessed 8.3.20).

Cunningham, R., Williams, R.J.J., 1980. Diffusion in Gases and Porous Media. Springer US. https://doi.org/10.1007/978-1-4757-4983-0

Darcy, H., 1856. Les fontaines publiques de la ville de Dijon: exposition et application ... Victor Dalmont.

D'Arrigo, J.S., 1978. Screening of membrane surface charges by divalent cations: an atomic representation. American Journal of Physiology-Cell Physiology 235, C109–C117. https://doi.org/10.1152/ajpcell.1978.235.3.C109

Dinc, G., Ulman, Y.I., 2007. The introduction of variolation 'A La Turca' to the West by Lady Mary Montagu and Turkey's contribution to this. Vaccine 25, 4261–4265. https://doi.org/10.1016/j.vaccine.2007.02.076

Elder, D., 2014. What does quality mean to you? European Pharmaceutical Review https://www.europeanpharmaceuticalreview.com/article/25973/foreword-quality-mean/.

Emteborg, H., Zeleny, R., Charoud-Got, J., Martos, G., Lüddeke, J., Schellin, H., Teipel, K., 2014. Infrared Thermography for Monitoring of Freeze-Drying Processes: Instrumental Developments and Preliminary Results. Journal of Pharmaceutical Sciences 103, 2088–2097. https://doi.org/10.1002/jps.24017

European Medicines Agency, 2009. ICH Q8 (R2) Pharmaceutical development. European Medicines Agency.

Evans, R.B., Watson, G.M., Mason, E.A., 1962. Gaseous Diffusion in Porous Media. II. Effect of Pressure Gradients. J. Chem. Phys. 36, 1894–1902. https://doi.org/10.1063/1.1701287

Fan, T.-H., Li, J.-Q., Minatovicz, B., Soha, E., Sun, L., Patel, S., Chaudhuri, B., Bogner, R., 2019. Phase-Field Modeling of Freeze Concentration of Protein Solutions. Polymers 11, 10. https://doi.org/10.3390/polym11010010

Feng, Y., Ping Tan, C., Zhou, C., Yagoub, A.E.A., Xu, B., Sun, Y., Ma, H., Xu, X., Yu, X., 2020. Effect of freeze-thaw cycles pretreatment on the vacuum freeze-drying process and physicochemical properties of the dried garlic slices. Food Chemistry 324, 126883. https://doi.org/10.1016/j.foodchem.2020.126883

Fennema, O.R., 1973. Low-temperature preservation of foods and living matter. Dekker.

Fierro, P., Nyer, E.K. (Eds.), 2007. The Water Encyclopedia: Hydrologie Data and Internet Resources, 3rd ed. CRC Press, Boca Raton. https://doi.org/10.1201/9781420012583

Fissore, D., Pisano, R., 2015. Computer-Aided Framework for the Design of Freeze-Drying Cycles: Optimization of the Operating Conditions of the Primary Drying Stage. Processes 3, 406–421. https://doi.org/10.3390/pr3020406

Fissore, D., Pisano, R., Baressi, A.A., 2010. On the Methods Based on the Pressure Rise Test for Monitoring a Freeze-Drying Process. Drying Technology An International Journal 29, 73–90.

Fissore, D., Pisano, R., Barresi, A.A., 2011. Advanced approach to build the design space for the primary drying of a pharmaceutical freeze-drying process. Journal of Pharmaceutical Sciences 100, 4922–4933. https://doi.org/10.1002/jps.22668

Fonseca, F., Cenard, S., Passot, S., 2015. Freeze-Drying of Lactic Acid Bacteria, in: Wolkers, W.F., Oldenhof, H. (Eds.), Cryopreservation and Freeze-Drying Protocols, Methods in Molecular Biology. Springer, New York, NY, pp. 477–488. https://doi.org/10.1007/978-1-4939-2193-5_24

Fonseca, F., Passot, S., Cunin, O., Marin, M., 2004. Collapse Temperature of Freeze-Dried Lactobacillus bulgaricusSuspensions and Protective Media. Biotechnology Progress 20, 229–238. https://doi.org/10.1021/bp034136n

Franks, F., 1998. Freeze-drying of bioproducts: putting principles into practice. European Journal of Pharmaceutics and Biopharmaceutics 45, 221–229. https://doi.org/10.1016/S0939-6411(98)00004-6

Gan, K.H., Bruttini, R., Crosser, O.K., Liapis, A.I., 2005. Freeze-drying of pharmaceuticals in vials on trays: effects of drying chamber wall temperature and tray side on lyophilization performance. International Journal of Heat and Mass Transfer 48, 1675–1687. https://doi.org/10.1016/j.ijheatmasstransfer.2004.12.004

Geddes, A.M., 2006. The history of smallpox. Clinics in Dermatology 24, 152–157. https://doi.org/10.1016/j.clindermatol.2005.11.009

Geidobler, R., Winter, G., 2013. Controlled ice nucleation in the field of freeze-drying: Fundamentals and technology review. European Journal of Pharmaceutics and Biopharmaceutics, SI: EJPB Freeze Drying (Invited only) 85, 214–222. https://doi.org/10.1016/j.ejpb.2013.04.014

Gieseler, H., Kramer, T., Pikal, M.J., 2007. Use of manometric temperature measurement (MTM) and SMART™ freeze dryer technology for development of an optimized freeze-drying cycle. Journal of Pharmaceutical Sciences 96, 3402–3418. https://doi.org/10.1002/jps.20982

Giordano, A., Barresi, A.A., Fissore, D., 2011. On the Use of Mathematical Models to Build the Design Space for the Primary Drying Phase of a Pharmaceutical Lyophilization Process. Journal of Pharmaceutical Sciences 100, 311–324. https://doi.org/10.1002/jps.22264

Glynn, I., Glynn, J., 2004. The Life and Death of Smallpox. New York, NY.

Greco, K., Mujat, M., Galbally-Kinney, K.L., Hammer, D.X., Ferguson, R.D., Iftimia, N., Mulhall, P., Sharma, P., Kessler, W.J., Pikal, M.J., 2013. Accurate Prediction of Collapse Temperature using Optical Coherence Tomography-Based Freeze-Drying Microscopy. Journal of Pharmaceutical Sciences 102, 1773–1785. https://doi.org/10.1002/jps.23516

Hansen, L.J.J., Daoussi, R., Vervaet, C., Remon, J.-P., De Beer, T.R.M., 2015. Freeze-drying of live virus vaccines: A review. Vaccine 33, 5507–5519. https://doi.org/10.1016/j.vaccine.2015.08.085

Harrison, A.D., Whale, T.F., Rutledge, R., Lamb, S., Tarn, M.D., Porter, G.C.E., Adams, M.P., McQuaid, J.B., Morris, G.J., Murray, B.J., 2018. An instrument for quantifying heterogeneous ice nucleation in multiwell plates using infrared emissions to detect freezing. Atmospheric Measurement Techniques 11, 5629–5641. https://doi.org/10.5194/amt-11-5629-2018

Harvey, A.H., 2018. Properties of Ice and Supercooled Water. CRC Handbook of Chemistry and Physics; CRC Press, Boca Raton, FL.

Hasselstrom, A.K.J., Nilsson, U.E., 2012. Thermal contact conductance in bolted joints. Diploma work No. 85/2012. Department of Materials and Manufacturing Technology; Chalmers University of Technology; Sweden.

Haynes, W.M. (Ed.), 2014. CRC Handbook of Chemistry and Physics, 95th Edition, 95 edition. ed. CRC Press, Boca Raton; London; New York.

Hays, J.N., 2005. Epidemics and Pandemics: Their Impacts on Human History. ABC-CLIO.

Heitz, W.L., Westwater, J.W., 1971. Critical Rayleigh Numbers for Natural Convection of Water Confined in Square Cells With L/D From 0.5 to 8. Journal of Heat Transfer 93, 188–195. https://doi.org/10.1115/1.3449783

Heldman, D.R., Moraru, C.I., 2010. Encyclopedia of Agricultural, Food, and Biological Engineering. CRC Press.

Hoffman, D., Singh, B., Thomas III, J., 1997. Handbook of Vacuum Science and Technology, 1st ed. Academic Press, Elsevier.

Hopkins, D.R., 2002. The Greatest Killer: Smallpox in History. University of Chicago Press.

Horn, J., Schanda, J., Friess, W., 2018. Impact of fast and conservative freeze-drying on product quality of protein-mannitol-sucrose-glycerol lyophilizates. European Journal of Pharmaceutics and Biopharmaceutics 127, 342–354. https://doi.org/10.1016/j.ejpb.2018.03.003

Hottot, A., Andrieu, J., Hoang, V., Shalaev, E., Gatlin, L., Ricketts, S., 2009a. Experimental Study and Modeling of Freeze-Drying in Syringe Configuration. Part II: Mass and Heat Transfer Parameters and Sublimation End-Points. Drying Technology - DRY TECHNOL 27, 49–58. https://doi.org/10.1080/07373930802565814

Hottot, A., Andrieu, J., Vessot, S., Shalaev, E., Gatlin, L., Ricketts, S., 2009b. Experimental Study and Modeling of Freeze-Drying in Syringe Configuration. Part I: Freezing Step. Drying Technology - DRY TECHNOL 27, 40–48. https://doi.org/10.1080/07373930802565806

Hottot, A., Peczalski, R., Vessot, S., Andrieu, J., 2007. Freeze-Drying of Pharmaceutical Proteins in Vials: Modeling of Freezing and Sublimation Steps. Drying Technology 24.

Hottot, A., Vessot, S., Andrieu, J., 2005. Determination of Mass and Heat Transfer Parameters During Freeze-Drying Cycles of Pharmaceutical Products. PDA Journal of Pharmaceutical Science and Technology 59, 138–153.

Hottot, A., Vessot, S., Andrieu, J., 2004. A Direct Characterization Method of the Ice Morphology. Relationship Between Mean Crystals Size and Primary Drying Times of Freeze-Drying Processes. Drying Technology 22, 2009–2021. https://doi.org/10.1081/DRT-200032717

Howell, J.R., Mengüc, M.P., Daun, K., Siegel, R., 2020. Thermal Radiation Heat Transfer. CRC Press.

Hsieh, J., 2003. Computed Tomography: Principles, Design, Artifacts, and Recent Advances. SPIE Press.

Hussain, A.S., 2003. Quality by Design: Next Steps to Realize Opportunities?

Hussani, M.T.A., Hayani, M.H.A.A., 2014. The Use of Filtered Back projection Algorithm for Reconstruction of tomographic Image. Al-Nahrain Journal for Engineering Sciences 17, 151–156.

Izutsu, K., 2018. Applications of Freezing and Freeze-Drying in Pharmaceutical Formulations, in: Iwaya-Inoue, M., Sakurai, M., Uemura, M. (Eds.), Survival Strategies in Extreme Cold and Desiccation: Adaptation Mechanisms and Their Applications, Advances in Experimental Medicine and Biology. Springer, Singapore, pp. 371–383. https://doi.org/10.1007/978-981-13-1244-1_20

Juran, J.M., 1992. Juran on Quality by Design, The New Steps for Planning Quality into Goods and Services. Free press, New York, NY.

Kasper, J.C., Friess, W., 2011. The freezing step in lyophilization: Physico-chemical fundamentals, freezing methods and consequences on process performance and quality attributes of biopharmaceuticals. European Journal of Pharmaceutics and Biopharmaceutics, Unmet Needs in Protein Formulation Science 78, 248–263. https://doi.org/10.1016/j.ejpb.2011.03.010

Kawasaki, H., Shimanouchi, T., Kimura, Y., 2019. Recent Development of Optimization of Lyophilization Process [WWW Document]. Journal of Chemistry. https://doi.org/10.1155/2019/9502856

Kiyosawa, K., 1988. The Volumes of Hydrated Glucose, Sucrose and Raffinose Molecules, and the Osmotic Pressures of These Aqueous Saccharide Solutions as Measured by the Freezing-Point-Depression Method. BCSJ 61, 633–642. https://doi.org/10.1246/bcsj.61.633

Knudsen, M., 1909. The law of molecular flow and viscosity of gases moving through tubes. Ann. Phys 28.

Koganti, V.R., Shalaev, E.Y., Berry, M.R., Osterberg, T., Youssef, M., Hiebert, D.N., Kanka, F.A., Nolan, M., Barrett, R., Scalzo, G., Fitzpatrick, G., Fitzgibbon, N., Luthra, S., Zhang, L., 2011. Investigation of Design Space for Freeze-Drying: Use of Modeling for Primary Drying Segment of a Freeze-Drying Cycle. AAPS PharmSciTech 12, 854–861. https://doi.org/10.1208/s12249-011-9645-7

Konstantinidis, A.K., Kuu, W., Otten, L., Nail, S.L., Sever, R.R., 2011. Controlled nucleation in freeze-drying: Effects on pore size in the dried product layer, mass transfer resistance, and primary drying rate. Journal of Pharmaceutical Sciences 100, 3453–3470. https://doi.org/10.1002/jps.22561

Kramer, M., Sennhenn, B., Lee, G., 2002. Freeze-drying using vacuum-induced surface freezing. J. Pharm. Sci. 91, 433–443. https://doi.org/10.1002/jps.10035

Krokida, M.K., Panagiotou, N.M., Maroulis, Z.B., Saravacos, G.D., 2001. Thermal conductivity: literature data compilation for foodstuffs. International Journal of Food Properties 4, 111–137.

Kuila, U., Prasad, M., Kazemi, H., 2012. Application of Knudsen flow in modeling gas-flow in shale reservoirs.

Kurz, W., Fisher, D.J., 1989. Fundamentals of solidification.

Kuu, W.Y., 2014. Optimization of nucleation and crystallization for lyophilization using gap freezing. US8689460B2.

Kuu, W.Y., Hardwick, L.M., Akers, M.J., 2006. Rapid determination of dry layer mass transfer resistance for various pharmaceutical formulations during primary drying using product temperature profiles. International Journal of Pharmaceutics 313, 99–113. https://doi.org/10.1016/j.ijpharm.2006.01.036

Kuu, W.Y., Nail, S.L., 2009. Rapid freeze-drying cycle optimization using computer programs developed based on heat and mass transfer models and facilitated by tunable diode laser absorption spectroscopy (TDLAS). Journal of Pharmaceutical Sciences 98, 3469–3482. https://doi.org/10.1002/jps.21813

Kuu, W.Y., O'Bryan, K.R., Hardwick, L.M., Paul, T.W., 2011. Product mass transfer resistance directly determined during freeze-drying cycle runs using tunable diode laser absorption spectroscopy (TDLAS) and pore diffusion model. Pharmaceutical Development and Technology 16, 343–357.

Levi, G., Karel, M., 1995. Volumetric shrinkage (collapse) in freeze-dried carbohydrates above their glass transition temperature. Food Research International 28, 145–151. https://doi.org/10.1016/0963-9969(95)90798-F

Liapis, A.I., Bruttini, R., 1994. A theory for the primary and secondary drying stages of the freeze-drying of pharmaceutical crystalline and amorphous solutes: comparison between experimental data and theory. Separations Technology 4, 144–155. https://doi.org/10.1016/0956-9618(94)80017-0

Liapis, A.I., Litchfield, R.J., 1979. Optimal control of a freeze dryer—I Theoretical development and quasi steady state analysis. Chemical Engineering Science 34, 975–981. https://doi.org/10.1016/0009-2509(79)85009-5

Liapis, A.I., Sadikoglu, H., 1998. Dynamic Pressure Rise in the Drying Chamber as a Remote Sensing Method for Monitoring the Temperature of the Product During the Primary Drying Stage of Freeze Drying. Drying Technology 16, 1153–1171. https://doi.org/10.1080/07373939808917458

Lienhard, J.H.I., Lienhard, J.H.V., 2017. A Heat Transfer Textbook, 4th ed. Phlogiston Press, Cambridge, MA, USA.

Lim, J.Y., Lim, D.G., Kim, K.H., Park, S.-K., Jeong, S.H., 2018. Effects of annealing on the physical properties of therapeutic proteins during freeze drying process. International Journal of Biological Macromolecules 107, 730–740. https://doi.org/10.1016/j.ijbiomac.2017.09.041

Lombard, M., PASTORET, P.-P., Moulin, A.M., 2007. A brief history of vaccines and vaccination. Revue scientifique et technique (International Office of Epizootics) 26, 29–48. https://doi.org/10.20506/rst.26.1.1724

Lopez-Quiroga, E., Antelo, L.T., Alonso, A.A., 2012. Time-scale modeling and optimal control of freeze–drying. Journal of Food Engineering 111, 655–666. https://doi.org/10.1016/j.jfoodeng.2012.03.001

Lu, X., Pikal, M.J., 2004. Freeze-Drying of Mannitol–Trehalose–Sodium Chloride-Based Formulations: The Impact of Annealing on Dry Layer Resistance to Mass Transfer and Cake Structure. Pharmaceutical Development and Technology 9, 85–95. https://doi.org/10.1081/PDT-120027421

M. S. van Dusen, 1929. International Critical Tables of Numerical Data, Physics, Chemistry and Technology. NAP, Washington, DC.

MacKenzie, A.P., 1975. Collapse during freeze drying--qualitative and quantitative aspects. Freeze Drying and Advanced Food Technology. S. A. Goldblith, L. Rey & W. W. Rothmayr, eds.

Mascarenhas, W.J., Akay, H.U., Pikal, M.J., 1997. A computational model for finite element analysis of the freeze-drying process. Computer Methods in Applied Mechanics and Engineering 148, 105–124. https://doi.org/10.1016/S0045-7825(96)00078-3

Masselot, V., Bosc, V., Benkhelifa, H., 2021. Analyzing the microstructure of a fresh sorbet with X-ray micro-computed tomography: Sampling, acquisition, and image processing. Journal of Food Engineering 292, 110347. https://doi.org/10.1016/j.jfoodeng.2020.110347

Matejtschuk, P., Rafiq, S., Johnes, S., Gaines Das, R., 2005. A comparison of vials with ampoules for the storage of biological reference materials. Biologicals 33, 63–70. https://doi.org/10.1016/j.biologicals.2004.12.002

May, J.C., 2010. Regulatory Control of Freeze-Dried Products: Importance and Evaluation of Residual Moisture, in: Freeze-Drying/Lyophilization of Pharmaceutical and Biological Products. CRC Press.

Meister, E., Gieseler, H., 2009. Freeze-Dry Microscopy of Protein/Sugar Mixtures: Drying Behavior, Interpretation of Collapse Temperatures and a Comparison to Corresponding Glass Transition Data. Journal of Pharmaceutical Sciences 98, 3072–3087. https://doi.org/10.1002/jps.21586

Millman, M.J., Liapis, A.I., Marchello, J.M., 1985. An analysis of the lyophilization process using a sorption-sublimation model and various operational policies. AIChE Journal 31, 1594–1604. https://doi.org/10.1002/aic.690311003

Millrock Technology Inc, n.d. Opti dry software. Millrock Technology, Inc. URL https://www.millrocktech.com/wp-content/uploads/2020/02/opti-dry-2-v2.jpg (accessed 11.24.20).

Milstien, J.B., Gibson, J.J., 1990. Quality control of BCG vaccine by WHO: a review of factors that may influence vaccine effectiveness and safety. Bull World Health Organ 68, 93–108.

Milton, N., Pikal, M.J., Roy, M.L., Nail, S.L., 1997. Evaluation of Manometric Temperature Measurement as a Method of Monitoring Product Temperature During Lyophilization. PDA Journal of Pharmaceutical Science and Technology 51, 7–16.

Miyamoto-Shinohara, Y., Imaizumi, T., Sukenobe, J., Murakami, Y., Kawamura, S., Komatsu, Y., 2000. Survival Rate of Microbes after Freeze-Drying and Long-Term Storage. Cryobiology 41, 251–255. https://doi.org/10.1006/cryo.2000.2282

Monchau, J., Candau, Y., Ibos, L., 2013. Device for measuring the emissivity or reflectivity of a surface. FR20120051476.

Morris, G., Acton, E., 2012. Controlled ice nucleation in cryopreservation - A review. Cryobiology 66. https://doi.org/10.1016/j.cryobiol.2012.11.007

Morris, M.D., 1991. Factorial Sampling Plans for Preliminary Computational Experiments. Technometrics 33, 161–174.

Mortier, S.T.F.C., Van Bockstal, P.-J., Corver, J., Nopens, I., Gernaey, K.V., De Beer, T., 2016. Uncertainty analysis as essential step in the establishment of the dynamic Design Space of primary drying during freeze-drying. European Journal of Pharmaceutics and Biopharmaceutics 103, 71–83. https://doi.org/10.1016/j.ejpb.2016.03.015

Moy, J.H., Chan, K.-C., Dollar, A.M., 1971. Bound Water in Fruit Products by the Freezing Method. Journal of Food Science 36, 498–499. https://doi.org/10.1111/j.1365-2621.1971.tb06398.x

Mulot, V., Fatou-Toutie, N., Benkhelifa, H., Pathier, D., Flick, D., 2019. Investigating the effect of freezing operating conditions on microstructure of frozen minced beef using an innovative X-ray micro-computed tomography method. Journal of Food Engineering 262, 13–21. https://doi.org/10.1016/j.jfoodeng.2019.05.014

Murphy, D.M., Koop, T., 2005. Review of the vapour pressures of ice and supercooled water for atmospheric applications. Q J R Meteorol Soc 131, 1539–1565. https://doi.org/10.1256/qj.04.94

Naik, S.P., Zade, J.K., Sabale, R.N., Pisal, S.S., Menon, R., Bankar, S.G., Gairola, S., Dhere, R.M., 2017. Stability of heat stable, live attenuated Rotavirus vaccine (ROTASIIL®). Vaccine 35, 2962–2969. https://doi.org/10.1016/j.vaccine.2017.04.025

Nail, S., Searles, J., 2008. Elements of quality by design in development and scale-up of freeze parenterals. BioPharm International 21, 44–52.

Nail, S.L., Gatlin, L.A., 2010. Freeze-drying: principles and practice, in: Pharmaceutical Dosage Forms - Parenteral Medications. CRC Press.

Nakagawa, K., Hottot, A., Vessot, S., Andrieu, J., 2007. Modelling of Freezing Steps During Freeze-Drying of Drugs in Vials. AIChE Journal 53, 1362–1372. https://doi.org/10.1002/aic.11147

Nakagawa, K., Hottot, A., Vessot, S., Andrieu, J., 2006. Influence of controlled nucleation by ultrasounds on ice morphology of frozen formulations for pharmaceutical proteins freeze-drying. Chemical Engineering and Processing: Process Intensification 45, 783–791. https://doi.org/10.1016/j.cep.2006.03.007

Nam, J.H., Song, C.S., 2005. An Efficient Calculation of Multidimensional Freeze-Drying Problems Using Fixed Grid Method. Drying Technology 23, 2491–2511. https://doi.org/10.1080/07373930500341757

Oddone, I., Van Bockstal, P.-J., De Beer, T., Pisano, R., 2016. Impact of vacuum-induced surface freezing on inter- and intra-vial heterogeneity. Eur. J. Pharm. Biopharm. 103, 167–178.

Oslan, S.N.H., Halim, M., Ramle, N.A., Saad, M.Z., Tan, J.S., Kapri, M.R., Ariff, A.B., 2017. Improved stability of live attenuated vaccine gdhA derivative Pasteurella multocida B:2 by freeze drying method for use as animal vaccine. Cryobiology 79, 1–8. https://doi.org/10.1016/j.cryobiol.2017.10.004

Otero, L., Sanz, P.D., 2000. High-Pressure Shift Freezing. Part 1. Amount of Ice Instantaneously Formed in the Process. Biotechnology Progress 16, 1030–1036. https://doi.org/10.1021/bp000122v

Overcashier, D.E., Patapoff, T.W., Hsu, C.C., 1999. Lyophilization of protein formulations in vials: Investigation of the relationship between resistance to vapor flow during primary drying and small-scale product collapse. J. Pharm. Sci. 88, 688–695. https://doi.org/10.1021/js980445+

Page, M., Wilkinson, D.E., Mattiuzzo, G., Efstathiou, S., Minor, P., 2017. Developing biological standards for vaccine evaluation. Future Virology 12, 431–437. https://doi.org/10.2217/fvl-2017-0003

Pant, L.M., Mitra, S.K., Secanell, M., 2012. Absolute permeability and Knudsen diffusivity measurements in PEMFC gas diffusion layers and micro porous layers. Journal of Power Sources 206, 153–160. https://doi.org/10.1016/j.jpowsour.2012.01.099

Passot, S., Cenard, S., Douania, I., Tréléa, I.C., Fonseca, F., 2012a. Critical water activity and amorphous state for optimal preservation of lyophilised lactic acid bacteria. Food Chemistry, 6th International Conference on Water in Food 132, 1699–1705. https://doi.org/10.1016/j.foodchem.2011.06.012

Passot, S., Fonseca, F., Cenard, S., Tréléa, I.C., 2012b. Developing smart control strategies of freeze-drying of lactic acid bacteria, in: 5th International Conference on Lyophilization and Freeze Drying. Bologne, Italy.

Passot, S., Tréléa, I.C., Marin, M., Galan, M., Morris, G.J., Fonseca, F., 2009. Effect of Controlled Ice Nucleation on Primary Drying Stage and Protein Recovery in Vials Cooled in a Modified Freeze-Dryer. J Biomech Eng 131. https://doi.org/10.1115/1.3143034

Patel, A., Erb, S.M., Strange, L., Shukla, R.S., Kumru, O.S., Smith, L., Nelson, P., Joshi, S.B., Livengood, J.A., Volkin, D.B., 2018. Combined semi-empirical screening and design of experiments (DOE) approach to identify candidate formulations of a lyophilized live attenuated tetravalent viral vaccine candidate. Vaccine, Vaccine Technology VI 36, 3169–3179. https://doi.org/10.1016/j.vaccine.2017.04.086

Patel, S.M., Bhugra, C., Pikal, M.J., 2009. Reduced Pressure Ice Fog Technique for Controlled Ice Nucleation during Freeze-Drying. AAPS PharmSciTech 10. https://doi.org/10.1208/s12249-009-9338-7

Patel, S.M., Chaudhuri, S., Pikal, M.J., 2010a. Choked flow and importance of Mach I in freeze-drying process design. Chemical Engineering Science, Pharmaceutical Engineering Science- A Key for Tomorrow's Drugs 65, 5716–5727. https://doi.org/10.1016/j.ces.2010.07.024

Patel, S.M., Doen, T., Pikal, M.J., 2010b. Determination of End Point of Primary Drying in Freeze-Drying Process Control. AAPS PharmSciTech 11, 73–84. https://doi.org/10.1208/s12249-009-9362-7

Patel, S.M., Jameel, F., Pikal, M.J., 2010c. The Effect of Dryer Load on Freeze Drying Process Design. Journal of Pharmaceutical Sciences 99, 4363–4379. https://doi.org/10.1002/jps.22132

Patel, S.M., Nail, S.L., Pikal, M.J., Geidobler, R., Winter, G., Hawe, A., Davagnino, J., Rambhatla Gupta, S., 2017. Lyophilized Drug Product Cake Appearance: What Is Acceptable? Journal of Pharmaceutical Sciences 106, 1706–1721. https://doi.org/10.1016/j.xphs.2017.03.014

Patel, S.M., Pikal, M.J., 2013. Lyophilization Process Design Space. Journal of Pharmaceutical Sciences 102, 3883–3887. https://doi.org/10.1002/jps.23703

Patel, S.M., Pikal, M.J., 2011. Emerging freeze-drying process development and scale-up issues. AAPS PharmSciTech 12, 372–378. https://doi.org/10.1208/s12249-011-9599-9

Peiren, J., Hellemans, A., De Vos, P., 2016. Impact of the freeze-drying process on product appearance, residual moisture content, viability, and batch uniformity of freeze-dried bacterial cultures safeguarded at culture collections. Appl Microbiol Biotechnol 100, 6239–6249. https://doi.org/10.1007/s00253-016-7359-1

Perry, R.H., Green, D.O., 2008. Perry's chemical engineers' handbook, 8th ed. McGraw-Hill.

Peterman, S., Niederkofler, E.E., Phillips, D.A., Krastins, B., Kiernan, U.A., Tubbs, K.A., Nedelkov, D., Prakash, A., Vogelsang, M.S., Schoeder, T., Couchman, L., Taylor, D.R., Moniz, C.F., Vadali, G., Byram, G., Lopez, M.F., 2014. An automated, high-throughput method for targeted quantification of intact insulin and its therapeutic analogs in human serum or plasma coupling mass spectrometric immunoassay with high resolution and accurate mass detection (MSIA-HR/AM). PROTEOMICS 14, 1445–1456. https://doi.org/10.1002/pmic.201300300

Petitti, M., Barresi, A., Marchisio, D., 2013. CFD modelling of condensers for freeze-drying processes. Sadhana 38. https://doi.org/10.1007/s12046-013-0155-z

Pikal, M.J., 2000. Heat and mass transfer in low pressure gases: applications to freeze-drying, in: Transport Processes in Pharmaceutical Systems. Marcel Dekker, Inc., New York, pp. 611–686.

Pikal, M.J., 1999. Mechanisms of protein stabilization during freeze-drying and storage: The relative importance of thermodynamic stabilization and glassy state relaxation dynamics. Freeze-Drying/Lyophilization of Pharmaceutical and Biological Products 96, 161–198. https://doi.org/10.1201/9780203021323.ch3

Pikal, M.J., 1994. Freeze-Drying of Proteins, in: Formulation and Delivery of Proteins and Peptides, ACS Symposium Series. American Chemical Society, pp. 120–133. https://doi.org/10.1021/bk-1994-0567.ch008

Pikal, M.J., 1985. Use of laboratory data in freeze drying process design: heat and mass transfer coefficients and the computer simulation of freeze drying. J. Parenter. Sci. Technol. 39, 115–139.

Pikal, M.J., Bogner, R., Mudhivarthi, V., Sharma, P., Sane, P., 2016a. Freeze-Drying Process Development and Scale-Up: Scale-Up of Edge Vial Versus Center Vial Heat Transfer Coefficients, Kv. J Pharm Sci 105, 3333–3343. https://doi.org/10.1016/j.xphs.2016.07.027

Pikal, M.J., Bogner, R., Mudhivarthi, V., Sharma, P., Sane, P., 2016b. Freeze-Drying Process Development and Scale-Up: Scale-Up of Edge Vial Versus Center Vial Heat Transfer Coefficients, Kv. Journal of Pharmaceutical Sciences 105, 3333–3343. https://doi.org/10.1016/j.xphs.2016.07.027

Pikal, M.J., Dellerman, K., Roy, M.L., 1992. Formulation and stability of freeze-dried proteins: effects of moisture and oxygen on the stability of freeze-dried formulations of human growth hormone. Dev Biol Stand 74, 21–37; discussion 37-38.

Pikal, M.J., Dellerman, K.M., Roy, M.L., Riggin, R.M., 1991. The Effects of Formulation Variables on the Stability of Freeze-Dried Human Growth Hormone. Pharm Res 8, 427–436. https://doi.org/10.1023/A:1015834724528

Pikal, M.J., Roy, M.L., Shah, S., 1984. Mass and Heat Transfer in Vial Freeze-Drying of Pharmaceuticals: Role of the Vial. Journal of Pharmaceutical Sciences 73, 1224–1237. https://doi.org/10.1002/jps.2600730910

Pikal, M.J., Shah, S., 1990a. The collapse temperature in freeze drying: Dependence on measurement methodology and rate of water removal from the glassy phase. International Journal of Pharmaceutics 62, 165–186. https://doi.org/10.1016/0378-5173(90)90231-R

Pikal, M.J., Shah, S., 1990b. The collapse temperature in freeze drying: Dependence on measurement methodology and rate of water removal from the glassy phase. International Journal of Pharmaceutics 62, 165–186. https://doi.org/10.1016/0378-5173(90)90231-R

Pikal, M.J., Shah, S., Roy, M.L., Putman, R., 1990. The secondary drying stage of freeze drying: drying kinetics as a function of temperature and chamber pressure. International Journal of Pharmaceutics 60, 203–207. https://doi.org/10.1016/0378-5173(90)90074-E

Pikal, M.J., Shah, S., Senior, D., Lang, J.E., 1983. Physical Chemistry of Freeze-drying: Measurement of Sublimation Rates for Frozen Aqueous Solutions by a Microbalance Technique. Journal of Pharmaceutical Sciences 72, 635–650. https://doi.org/10.1002/jps.2600720614

Pikal, M.J., Tang, X., Nail, S.L., 2005. Automated process control using manometric temperature measurement. US6971187B1.

Pipkin, P.A., Minor, P.D., 1998. Studies on the loss of infectivity of live type 3 poliovaccine on storage. Biologicals 26, 17–23. https://doi.org/10.1006/biol.1997.0118

Pisano, R., Baressi, A.A., Fissore, D., 2011. Heat transfer in freeze-drying apparatus, in: Developments in Heat Transfer. Rijeka, Croatia, pp. 91–114.

Pisano, R., Barresi, A.A., Capozzi, L.C., Novajra, G., Oddone, I., Vitale-Brovarone, C., 2017. Characterization of the mass transfer of lyophilized products based on X-ray micro-computed tomography images. Drying Technology 35, 933–938. https://doi.org/10.1080/07373937.2016.1222540

Pisano, R., Capozzi, L.C., 2017. Prediction of product morphology of lyophilized drugs in the case of Vacuum Induced Surface Freezing. Chemical Engineering Research and Design 125, 119–129. https://doi.org/10.1016/j.cherd.2017.07.004

Pisano, R., Fissore, D., Barresi, A., 2012. Quality by Design in the Secondary Drying Step of a Freeze-Drying Process. Drying Technology 30, 1307–1316. https://doi.org/10.1080/07373937.2012.704466PLEASE

Pisano, R., Fissore, D., Barresi, A.A., Brayard, P., Chouvenc, P., Woinet, B., 2013a. Quality by design: optimization of a freeze-drying cycle via design space in case of heterogeneous drying behavior and influence of the freezing protocol. Pharmaceutical Development and Technology 18, 280–295. https://doi.org/10.3109/10837450.2012.734512

Pisano, R., Fissore, D., Barresi, A.A., Rastelli, M., 2013b. Quality by Design: Scale-Up of Freeze-Drying Cycles in Pharmaceutical Industry. AAPS PharmSciTech 14, 1137–1149. https://doi.org/10.1208/s12249-013-0003-9

Plett, P.C., Schmidt, J.G., 2006. Peter Plett und die übrigen Entdecker der Kuhpockenimpfung vor Edward Jenner. Sudhoffs Archiv 90, 219–232.

Ponsá, S., Bolzonella, D., Colón, J., Deshusses, M., Fonts, I., Gil-Lalaguna, N., Komilis, D., Lyberatos, G., Pérez-Elvira, S., Sánchez, J.L., 2017. Recovering energy from sludge. https://doi.org/10.2166/9781780407876_0325

Rahman, M., 2004. State Diagram of Date Flesh Using Differential Scanning Calorimetry (DSC). International Journal of Food Properties - INT J FOOD PROP 7. https://doi.org/10.1081/JFP-200032930

Rambhatla, S., Pikal, M.J., 2003. Heat and mass transfer scale-up issues during freeze-drying, I: Atypical radiation and the edge vial effect. AAPS PharmSciTech 4, 22–31. https://doi.org/10.1208/pt040214

Rambhatla, S., Ramot, R., Bhugra, C., Pikal, M.J., 2004. Heat and mass transfer scale-up issues during freeze drying: II. Control and characterization of the degree of supercooling. AAPS PharmSciTech 54–62.

Renaud, T., Briery, P., Andrieu, J., Laurent, M., 1992. Thermal properties of model foods in the frozen state. Journal of food engineering.

Rohsenow, W.M., Hartnett, J.P., Cho, Y.I. (Eds.), 1998. Handbook of heat transfer, 3rd ed. ed, McGraw-Hill handbooks. McGraw-Hill, New York.

Roos, Y.H., 2005. Frozen state transitions in relation to freeze drying. Journal of Thermal Analysis and Calorimetry 48, 535–544. https://doi.org/10.1007/bf01979500

Rosa, M., Tiago, J.M., Singh, S.K., Geraldes, V., Rodrigues, M.A., 2016. Improving Heat Transfer at the Bottom of Vials for Consistent Freeze Drying with Unidirectional Structured Ice. AAPS PharmSciTech 17, 1049–1059. https://doi.org/10.1208/s12249-015-0437-3

Rowe, T.D., 1990. A Technique for the Nucleation of Ice.

Schneid, S., Gieseler, H., 2008. Evaluation of a New Wireless Temperature Remote Interrogation System (TEMPRIS) to Measure Product Temperature During Freeze Drying. AAPS PharmSciTech 9, 729–739. https://doi.org/10.1208/s12249-008-9099-8

Schneid, S.C., Stärtzel, P.M., Lettner, P., Gieseler, H., 2011. Robustness testing in pharmaceutical freeze-drying: Inter-relation of process conditions and product quality attributes studied for a vaccine formulation. Pharmaceutical Development and Technology 16, 583–590. https://doi.org/10.3109/10837450.2011.581287

Schneider, W.H., 2009. Smallpox in Africa during Colonial Rule. Medical History 53, 193–227. https://doi.org/10.1017/S002572730000363X

Scutellà, B., 2017. Freeze-drying of vaccines: Contribution of mathematical modelling for assessing product heterogeneity and scale-up risks. PhD thesis from Université Paris-Saclay prepared at AgroParisTech -- Institut des sciences et industries du vivant et de l'environnement, Doctoral School n° 581 : Agriculture, alimentation, biologie, environnement et santé (ABIES).

Scutellà, B., Passot, S., Bourlés, E., Fonseca, F., Tréléa, I.C., 2017a. How Vial Geometry Variability Influences Heat Transfer and Product Temperature During Freeze-Drying. Journal of Pharmaceutical Sciences 106, 770–778. https://doi.org/10.1016/j.xphs.2016.11.007

Scutellà, B., Plana-Fattori, A., Passot, S., Bourlés, E., Fonseca, F., Flick, D., Tréléa, I.C., 2017b. 3D mathematical modelling to understand atypical heat transfer observed in vial freeze-drying. Appl. Therm. Eng. 126, 226–236.

Scutellà, B., Tréléa, I.C., Bourlès, E., Fonseca, F., Passot, S., 2018a. Determination of the dried product resistance variability and its influence on the product temperature in pharmaceutical freeze-drying. Eur J Pharm Biopharm 128, 379–388. https://doi.org/10.1016/j.ejpb.2018.05.004

Scutellà, B., Tréléa, I.C., Bourlés, E., Fonseca, F., Passot, S., 2018b. Use of a multi-vial mathematical model to design freeze-drying cycles for pharmaceuticals at known risk of failure, in: IDS 2018. 21st International Drying Symposium Proceedings. Presented at the IDS 2018. 21st International Drying Symposium Proceedings, Editorial Universitat Politècnica de València, pp. 315–322. https://doi.org/10.4995/IDS2018.2018.7421

Searles, J.A., 2004. Freezing and annealing phenomena in lyophilization, in: Freeze-Drying/Lyophilization of Pharmaceutical and Biological Products. pp. 109–145.

Searles, J.A., Carpenter, J.F., Randolph, T.W., 2001a. Annealing to optimize the primary drying rate, reduce freezing-induced drying rate heterogeneity, and determine T'g in pharmaceutical lyophilization. Journal of Pharmaceutical Sciences 90, 872–887. https://doi.org/10.1002/jps.1040

Searles, J.A., Carpenter, J.F., Randolph, T.W., 2001b. The ice nucleation temperature determines the primary drying rate of lyophilization for samples frozen on a temperature-controlled shelf. J. Pharm. Sci. 90, 860–871. https://doi.org/10.1002/jps.1039

Sheehan, P., Liapis, A.I., 1998. Modeling of the primary and secondary drying stages of the freeze drying of pharmaceutical products in vials: Numerical results obtained from the solution of a dynamic and spatially multi-dimensional lyophilization model for different operational policies. Biotechnology and Bioengineering 60, 712–728. https://doi.org/10.1002/(SICI)1097-0290(19981220)60:6<712::AID-BIT8>3.0.CO;2-4

Shi, A.-M., Wang, L.-J., Li, D., Adhikari, B., 2012. The effect of annealing and cryoprotectants on the properties of vacuum-freeze dried starch nanoparticles. Carbohydrate Polymers 88, 1334–1341. https://doi.org/10.1016/j.carbpol.2012.02.013

Shukla, S., 2011. Freeze-drying process: a review. International Journal of Pharmaceutical Sciences and Research 2.

Siegrist, C.-A., 2008. Vaccine immunology, in: Vaccines. Elsevier Health Sciences, pp. 17–36.

Smith, D.S., Alzina, A., Bourret, J., Nait-Ali, B., Pennec, F., Tessier-Doyen, N., Otsu, K., Matsubara, H., Elser, P., Gonzenbach, U.T., 2013. Thermal conductivity of porous materials. Journal of Materials Research 28, 2260–2272. https://doi.org/10.1557/jmr.2013.179

Smith, K.F., Acevedo-Whitehouse, K., Pedersen, A.B., 2009. The role of infectious diseases in biological conservation. Animal Conservation 12, 1–12. https://doi.org/10.1111/j.1469-1795.2008.00228.x

Stangegaard, M., Hansen, A.J., Frøslev, T.G., Morling, N., 2011. A Simple Method for Validation and Verification of Pipettes Mounted on Automated Liquid Handlers. JALA: Journal of the Association for Laboratory Automation 16, 381–386. https://doi.org/10.1016/j.jala.2009.06.004

Stärtzel, P., Gieseler, H., Gieseler, M., Abdul-Fattah, A.M., Adler, M., Mahler, H.-C., Goldbach, P., 2015. Freeze-Drying of l-Arginine/Sucrose-Based Protein Formulations, Part 2: Optimization of Formulation Design and Freeze-Drying Process Conditions for an l-Arginine Chloride-Based Protein Formulation System. Journal of Pharmaceutical Sciences 104, 4241–4256. https://doi.org/10.1002/jps.24658

Tang, X. (Charlie), Pikal, M.J., 2004. Design of Freeze-Drying Processes for Pharmaceuticals: Practical Advice. Pharm Res 21, 191–200. https://doi.org/10.1023/B:PHAM.0000016234.73023.75

Tang, X., Nail, S.L., Pikal, M.J., 2006. Evaluation of manometric temperature measurement, a process analytical technology tool for freeze-drying: Part I, product temperature measurement. AAPS PharmSciTech 7, E95–E103. https://doi.org/10.1208/pt070114

Tang, X.C., Nail, S.L., Pikal, M.J., 2006. Evaluation of manometric temperature measurement, a process analytical technology tool for freeze-drying: Part II measurement of dry-layer resistance. AAPS PharmSciTech 7, E77–E84. https://doi.org/10.1208/pt070493

Tang, X.C., Nail, S.L., Pikal, M.J., 2005. Freeze-drying process design by manometric temperature measurement: design of a smart freeze-dryer. Pharm. Res. 22, 685–700. https://doi.org/10.1007/s11095-005-2501-2

Tariq, A., Asif, M., 2016. Experimental investigation of thermal contact conductance for nominally flat metallic contact. Heat Mass Transfer 52, 291–307. https://doi.org/10.1007/s00231-015-1551-1

Taylor, P.B., Ashman, S., Baddeley, S.M., Bartram, S.L., Battle, C.D., Bond, B.C., Clements, Y.M., Gaul, N.J., McAllister, W.E., Mostacero, J.A., Ramon, F., Wilson, J.M., Hertzberg, R.P., Pope, A.J., Macarron, R., 2002. A Standard Operating Procedure for Assessing Liquid Handler Performance in High-Throughput Screening. J Biomol Screen 7, 554–569. https://doi.org/10.1177/1087057102238630

The College of Physicians of Philadelphia, 2020. History of Vaccines [WWW Document]. URL / (accessed 12.15.20).

Tréléa, I.C., Fonseca, F., Passot, S., 2016. Dynamic Modelling of the Secondary Drying Stage of Freeze-Drying Reveals Distinct Desorption Kinetics for Bound Water. Drying Technology 34, 335–345. https://doi.org/10.1080/07373937.2015.1054509

Tréléa, I.C., Fonseca, F., Passot, S., Flick, D., 2015. A binary gas transport model Improves the prediction of mass transfer in freeze drying. Drying Technology 33, 1849–1858. https://doi.org/10.1080/07373937.2015.1040025

Tréléa, I.C., Passot, S., Fonseca, F., Marin, M., 2007. An interactive tool for the optimization of freeze-drying cycles based on quality criteria. Drying technology.

Trnka, H., Rantanen, J., Grohganz, H., 2015. Well-plate freeze-drying: a high throughput platform for screening of physical properties of freeze-dried formulations. Pharmaceutical development and technology 20, 65–73.

US Department of Health and Human Services, 2008. Understanding vaccines: what they are, how they work. National Institute of Allergy and Infectious Diseases Website.

US Food and Drug Administration, 2009. Guidance for Industry: Q8(R2) pharmaceutical development. http://www.fda.gov/downloads/Drugs/.../Guidances/ucm073507.pdf (International Conference on Harmonization).

van Eck, R., Kelp, M., van Schijnde, J., 2016. Surface to surface radiation benchmarks, in: Comsol Conference. Presented at the Comsol Conference, Munich, Germany.

Vanbillemont, B., Nicolaï, N., Leys, L., De Beer, T., 2020. Model-Based Optimisation and Control Strategy for the Primary Drying Phase of a Lyophilisation Process. Pharmaceutics 12, 181. https://doi.org/10.3390/pharmaceutics12020181

Velardi, S.A., Barresi, A.A., 2008. Development of simplified models for the freeze-drying process and investigation of the optimal operating conditions. Chemical Engineering Research and Design 86, 9–22. https://doi.org/10.1016/j.cherd.2007.10.007

Velardi, S.A., Rasetto, V., Barresi, A.A., 2008. Dynamic Parameters Estimation Method: Advanced Manometric Temperature Measurement Approach for Freeze-Drying Monitoring of Pharmaceutical Solutions. Ind. Eng. Chem. Res. 47, 8445–8457. https://doi.org/10.1021/ie7017433

von Graberg, S., 2011. Freeze Drying from Small Containers: Heat and Mass Transfer and Implications on Process Design [WWW Document]. ResearchGate. URL https://www.researchgate.net/publication/296063173_Freeze_Drying_from_Small_Containers_Heat_and_Mass_Transfer_and_Implications_on_Process_Design (accessed 2.7.19).

Wagner, W., Saul, A., Pruss, A., 1994. International Equations for the Pressure Along the Melting and Along the Sublimation Curve of Ordinary Water Substance. Journal of Physical and Chemical Reference Data 23, 515–527. https://doi.org/10.1063/1.555947

Wang, D.Q., Hey, J.M., Nail, S.L., 2004. Effect of collapse on the stability of freeze-dried recombinant factor VIII and α-amylase. Journal of Pharmaceutical Sciences 93, 1253–1263. https://doi.org/10.1002/jps.20065

Wegiel, L., Ferris, S., Nail, S., 2018. Experimental Aspects of Measuring the Vial Heat Transfer Coefficient in Pharmaceutical Freeze-Drying. AAPS PharmSciTech 19. https://doi.org/10.1208/s12249-018-0998-z

White, F.M., 1984. Heat transfer, Addison-Wesley. ed.

Wiggan, O., Livengood, J.A., Silengo, S.J., Kinney, R.M., Osorio, J.E., Huang, C.Y.-H., Stinchcomb, D.T., 2011. Novel formulations enhance the thermal stability of live-attenuated flavivirus vaccines. Vaccine, Special Section - Universal Influenza Vaccination of Children: Food for Thought 29, 7456–7462. https://doi.org/10.1016/j.vaccine.2011.07.054

Woodcock, J., 2004. The concept of pharmaceutical quality. American Pharmaceutical Review 7, 10–15.

World Health Organisation, 2000. Vaccines and biologicals update. Department of vaccines and biologicals 35.

World Health Organization, 2015. WHO guidance note: vaccine diluents: the proper handling and use of vaccine diluents.

World Health Organization, 2011. WHO manual for the establishment of national and other secondary standards for vaccines (No. WHO/IVB/11.03).

World Health Organization, 2006. Temperature sensitivity of vaccines.

Yang, L., Ma, Y., Zhang, Y., 2007. Freeze-drying of live attenuated Vibrio anguillarum mutant for vaccine preparation. Biologicals 35, 265–269. https://doi.org/10.1016/j.biologicals.2007.03.001

Yu, L.X., 2008. Pharmaceutical Quality by Design: Product and Process Development, Understanding, and Control. Pharm Res 25, 781–791. https://doi.org/10.1007/s11095-007-9511-1

Zhai, S., Su, H., Taylor, R., Slater, N.K.H., 2005. Pure ice sublimation within vials in a laboratory lyophiliser; comparison of theory with experiment. Chemical Engineering Science 60, 1167–1176. https://doi.org/10.1016/j.ces.2004.09.078